8-2017

FUNDAMENTAL STUDY AND DEVELOPMENT OF TUNED ACTIVE FLOW CONTROL ACTUATORS

Brian A. Binkley
University of Tennessee, Knoxville, bbinkle1@vols.utk.edu

To the Graduate Council:

I am submitting herewith a dissertation written by Brian A. Binkley entitled "FUNDAMENTAL STUDY AND DEVELOPMENT OF TUNED ACTIVE FLOW CONTROL ACTUATORS." I have examined the final electronic copy of this dissertation for form and content and recommend that it be accepted in partial fulfillment of the requirements for the degree of Doctor of Philosophy, with a major in Aerospace Engineering.

Ahmad D. Vakili, Major Professor

We have read this dissertation and recommend its acceptance:

Trevor Moeller, Christian Parigger, William Baker

Accepted for the Council:
Dixie L. Thompson

Vice Provost and Dean of the Graduate School

(Original signatures are on file with official student records.)

FUNDAMENTAL STUDY AND DEVELOPMENT OF TUNED ACTIVE FLOW CONTROL ACTUATORS

A Dissertation Presented for the
Doctor of Philosophy
Degree
The University of Tennessee, Knoxville

Brian A. Binkley
August 2017

DEDICATION

To my wife

Amie

my son

Logan

and my daughter

Leila

ACKNOWLEDGEMENTS

I would like to thank my wife for her endless patience and her support to overcome life's challenges. I would like to thank Dr. Vakili for his patience, guidance and encouragement in overcoming the valleys of experimental research testing. I would also like to thank the UTSI lab facility staff for their support in setting up, debugging, and executing tests despite limited resources. I would like to thank my dissertation committee for their guidance and suggestions. Finally, I would like to thank the leadership at the USAF Arnold Engineering Development Complex for providing the resources necessary to complete this endeavor.

ABSTRACT

A novel, multi-level, flow-control actuator was developed using piezoceramic materials. Several actuators were fabricated in various shapes and sizes to produce a variety of effects for flow control applications. The actuators were studied in a quiescent-air bench test to understand the vibrations produced by various actuator shapes. The actuator flow-control effect was studied experimentally with flat-plate and cavity configurations, and was studied numerically using moving boundary conditions and dynamic meshing. The disturbances produced by the actuator couple with the cavity flow field producing increased cavity tones, increased vorticity, and sustainment of large-scale vorticity downstream of the cavity. The combined actuation result, from perturbations upstream of the cavity to increased vorticity downstream of the cavity, is the novel multi-level actuator developed and studied in this research.

The largest actuator was experimentally tested in boundary layers with free-stream Mach numbers from 0.1 to 0.5 and Reynolds numbers, based on momentum thickness, from approximately 800 to 3600. Actuator effects were measured using high-frequency-response pressure instrumentation in the floor downstream of the actuator. The actuator produced disturbances with amplitudes at least 30 dB above the noise floor and frequencies nine-times the actuator driving frequency. The disturbances created by the actuator coupled with the boundary layer flow and were observable up to 62 kHz. A time-dependent effect from changing actuation frequency was observed on the stability of the flow.

A compact, multi-actuator pack was designed to study multi-level flow control using experimental tests of a two-dimensional cavity flow at Mach numbers of 0.1, 0.2, and 0.3. Actuator operation did not produce amplified cavity oscillations at all Rossiter tones in the experiments. However, significant flow coupling occurred when the actuator driving frequency matched a Rossiter tone and a fundamental cavity acoustic tone. The cavity amplifications were stronger when the distance between the actuator and the cavity leading edge was increased. The numerical simulations showed that the actuator produced cavity flow amplifications at the first Rossiter tone about 8 dB higher amplitude than without actuation.

TABLE OF CONTENTS

LIST OF TABLES

LIST OF FIGURES

LIST OF ATTACHMENTS

NOMENCLATURE

Abbreviations

CFD	Computational Fluid Dynamics
DAQ	Data Acquisition
dB	Decibels
DNS	Direct Numerical Simulation
L/D	Ratio of cavity length (L) to depth (D)
LES	Large Eddy Simulation
OD	Outer Diameter
PIV	Particle Image Velocimetry
PK	Identifier for a high-response pressure instrument
RANS	Reynolds-averaged Navier-Stokes equations
RSM	Reynolds Stress Model
SPL	Sound Pressure Level
SST	Shear Stress Transport
UTSI	University of Tennessee Space Institute
VB	Vortex Breakdown

Symbols

A	Area (sq. in.), non-dimensional frequency for fundamental acoustics of cavity
D	Diameter (in), electric flux density in piezoelectric materials
d_{31}	Charge coefficient in piezoelectric materials
E	Electric field in piezoelectric materials
e	Internal energy, exponential
F	Body forces, function
f	Frequency (Hz or kHz)
f0	Frequency at resonance (Hz or kHz)
g	Gravity vector
h	Enthalpy
Hz, kHz	Frequency units in Hertz or kilohertz
K	Turbulence kinetic energy or units of Kelvin
k	Thermal conductivity

K_{act}	Non-dimensional frequency for actuator motion
k-ω	A two-equation turbulence model
k-ε	A two-equation turbulence model
ℓ	Largest turbulence length scale
n	Number of observations or number of items in a series
M	Mach number
m	Meter units
$\dot{m}$	Mass flow rate
mm	Millimeter units
P, p	Pressure (psi)
P0	Acoustic reference pressure
Pa	Pascal units
Pr	Prandtl number
psi	Units of pounds per square inch
Q	Quality factor
R	Gas constant, non-dimensional frequency for Rossiter cavity tones
Re	Reynolds number
S	Swirl number, mechanical strain in piezoelectric materials
s	Units of seconds
St	Strouhal number
T	Temperature (degrees F), mechanical stress in piezoelectric materials
t	Time, students-t statistic
U	Any mean flow-field variable, free-stream velocity
u’	Any fluctuating flow-field variable
u	Any total flow-field variable which is the sum of a mean and fluctuating component
$\boldsymbol{u}$	The velocity vector with components (u,v,w)
V	Velocity, Volts

Greek Letters

γ	Ratio of specific heats
δ_{99}	Boundary layer thickness (in)
δ*	Displacement thickness (in)

δf	Frequency bandwidth
δX	Displacement (in)
η	Smallest turbulence length scale
θ^*	Momentum thickness (in)
λ	Second coefficient of viscosity
μ	Dynamic viscosity
ν	Kinematic viscosity
ρ	Density
σ	Variance
τ_{ij}	Shear stress tensor
τ	Time scale
ω	Vorticity, complex frequency

Subscripts

abs	Absolute conditions
act	Actuator
gauge	Gauge conditions
op	Operating conditions
t	Total conditions

Coordinate Systems

(a,b)	Ellipse half height, a, and half width, b
(h,v)	Ellipse center coordinates
(L,D,W)	Rectangular cavity dimensions of length (L), depth (D), and width(W)
(r,θ,z)	Unit directions (radial, tangential, axial) in the cylindrical coordinate system
(u,v,w)	Velocity components in the unit directions
(u',v',w')	Fluctuating velocity components in the unit directions
(x,y,z)	The unit directions in the Cartesian coordinate system

CHAPTER ONE INTRODUCTION AND BACKGROUND

Introduction

Flow control is the ability to manipulate a fluid flow field to produce a desired effect. Ideally, successful flow control methodologies result in flow effects that are much larger than the energy input required to produce the effect. Typical effects that are desired by flow-control practitioners are production/prevention of turbulence, increased fluid mixing, attenuated/amplified hydrodynamic instabilities, increased/reduced heat transfer, and attenuated/amplified acoustic noise. Flow control applications include control of boundary layers, shear layers, cavity flows, wakes, and jets. Various flow control methods have been studied throughout the years and some of these methods are presented in the literature review. Flow control is a fundamental fluid dynamics instability problem because it is necessary to understand the governing physics of basic flows such as boundary layers, jets, and shear flows. Basic flow controls also have practical applications such as cavities in aircraft weapons bays and engine combustion chambers, jet nozzle flows, and boundary layer transition and separation. Flow control methods can take a variety of forms, but are generally categorized as passive, active or adaptive controls.

Passive flow control methods leverage geometrical aspects of a local flow field to excite or attenuate hydrodynamic instabilities to achieve desired local or global flow control effects. Passive control methods utilize static configurations and require no additional energy input as these methodologies utilize the energy in the flow itself to amplify or suppress desired flow features. Passive control methods can generate the desired effect at a single flow condition, or a small range of flow conditions. Active control methods, however, require some form of additional energy input to achieve the desired controlled flow effects, and therefore, can achieve effects over a larger range of operating conditions. Additionally, active control methods can be classified as open-loop (Sipp, 2012) or closed-loop (Takahashi et al., 2011). Closed-loop control methods rely on a feedback loop in which a sensor is used to measure some characteristic of the flow which is provided to a controller. The controller then perturbs the flow actuator to maximize or minimize the flow characteristic being measured. Open-loop control methods do not have a feedback control loop. Another method in flow control is adaptive control (Takahashi et al., 2011), where global flow variations are measured and used to make limited changes in the control variables. For example, as the free stream Mach number changes, flow actuation frequency or amplitude is adapted to obtain the desired outcome.

The purpose of this work is to document the process of scientific research and development of a novel, adaptive, multi-level, flow actuator, using piezoceramic materials as drivers, for custom configurations and flow actuation. The flow actuator could be miniaturized such that an array of actuators can produce flow disturbances tuned to the direction, amplitude, and frequency needed to resonate with or suppress large scale coherent structures and small scale turbulent features in the flow. The individual flow actuators could be independently controlled to produce desired actuation frequencies, amplitudes, and local vorticity to produce control authority for specific, larger-scale global flow outcomes. A numerical simulation of the flow configuration was also completed to use as a guide as well as trend analysis. Details of the flow features were visualized in images and used to compare and understand the flow physics.

A literature review was performed to understand the relevant state-of-the-art research in flow control in boundary layers, shear and cavity flows, vortex flows, and piezoelectric actuator designs. The literature review is presented in Chapter Two. The governing equations for fluid flow, relevant flow control flow regimes, and piezoelectric coupling equations are presented in Chapter Three. Details of the actuator development, designs, and bench tests are presented in Chapter Four. Details of the test facilities and test setup are presented in Chapter Five. Information on the Computational Fluid Dynamics (CFD) solver, mesh, and setup are provided in Chapter Six. Discussion of test and CFD results is presented in Chapter Seven. Finally, conclusions are provided in Chapter Eight.

Objectives

Greater quantitative and physical understanding of large-scale coherent structures, shear layers, and acoustic feedback mechanisms that drive fluid instabilities are needed to guide novel fluid actuator designs. Development of an innovative, multi-level flow actuation system is studied. A multi-level flow actuation system is one in which an actuator excites flow instabilities which then couple with a second flow field, which can then couple with other flow fields or produce desired flow control effects.

The proposed multi-level actuator could be applied to flows such as leading/trailing edge flows, nozzle flows, and cavity flows. Flow controls are often developed to suppress shear layer and acoustic resonance in cavity and jet flows, or to control boundary layer transition to turbulence, or to prevent boundary layer separation. However, the goal of this research is to study and understand a novel, multi-level, flow-control actuator, and to demonstrate flow control in a relevant environment. The desired flow-control outcome is to increase turbulence levels and improve flow mixing downstream of the actuator system.

Motivation

Recent research has highlighted the fact that unsteady and unstable flows are dominated by large-scale, coherent structures which interact, entrain, and resonate (amplify or attenuate) with other flow features, if designed and implemented appropriately. Detailed measurement and understanding of the flow physics that generate the large-scale coherent structures is desired. In-depth understanding of how active actuators interact with and produce large-scale structures is desired. Successfully forcing a flow to develop high order instabilities can increase turbulence and mixing in both subsonic and supersonic flows. Increased mixing capabilities can significantly benefit the performance, as well as environmental aspects, of propulsion applications by increasing fuel/oxidant residence time which could result in lower emissions and greater fuel economy. Heat transfer control applications can also benefit because of the potential for enhanced convection provided by turbulent flows which could result in more efficient heating or cooling processes. This research should increase understanding of a specific class of flow actuators. Studies of demonstrated production and control of turbulent structures using active actuators tuned to the flow environment will help progress towards research into robust flow control techniques.

Contributions to State of the Art

Historically, most flow control actuators have not been robust enough to be miniaturized for practical applications, especially in adverse flow environments. High pressure air, high-power electronics, or cumbersome mechanical devices are typically required to produce motion for

certain fluid actuators. Piezoelectric devices have improved the access, power, and dynamic range capabilities of advanced actuators. This research provides information on how piezoelectric actuators can be designed in such a way that they are robust, require relatively little power, and may be scaled to appropriate (miniature) sizes, while maintaining tuned response to a dynamic flow environment.

Furthermore, it will be shown that cavity flow field excitation can be easily controlled with minimal energy input and small-scale actuators when the actuators are operated at the appropriate frequency. Authors have published analytical models in the literature and claimed that coupling between cavity natural-acoustic modes and the classical Rossiter "edge-tones" can lead to an unstable and easily controlled, resonant cavity flow. This research will provide the first experimental data that verifies these assertions.

CHAPTER TWO LITERATURE REVIEW

The literature abounds with flow control research, especially from the past three decades. Some of the relevant literature will be reviewed in the following sections. The review is organized into sections according to the type of flow, such as boundary layers, shear layers, or cavities, all of which exhibit similar shear-flow instabilities.

Furthermore, each of these flow regimes will be important for the present research. Characterization of boundary layers is important for flow upstream of cavities and jets. Coupling of boundary layer flows with cavity acoustic resonances will be key to controlling large-scale flow structures, enhanced mixing, and turbulence generation.

Boundary Layer Flow Control

Boundary layer flow manipulation methods include passive techniques such as cylindrical rods placed in cross-flow, and vanes or vortex generators placed in the flow to generate vorticity or control the pressure gradient. Some of these devices are for flow management; that is, they change the kinetic energy distribution of the local flow to overcome flow separation. These devices use large-scale flow interactions and do not couple with flow instabilities to amplify the interaction effects. Other active flow control methods include plasma actuation, surface vibration via mechanical or piezoelectric devices, mass addition/subtraction via blowing/suction at the surface, or acoustic forcing.

Passive boundary layer control has been a focus of research for many years. Examples include control by cylindrical rods, vanes, or vortex generators (White, 1991). Vortex generators can be used to control flow separation by imparting momentum into the boundary layer to delay the onset of flow separation. Static vortex generators have been applied to upper wing surfaces and engine-inlets to delay boundary layer separation. These applications typically consist of the classical vortex generator pairs (Smith, 1975) which exchange high-momentum flow from outside the boundary layer with low-momentum flow inside the boundary layer using counter-rotating, streamwise vortex pairs. The streamwise vortex pairs are three-dimensional and create the spanwise flow needed to control shear-layer instabilities (Gutmark, 1997).

It has been shown that laminar boundary layers exposed to pressure gradients in the direction of the flow can have increased stability if the pressure gradient is favorable or decreased stability if the gradient is adverse (White, 1991). It is also well known that adverse pressure gradients can lead to boundary-layer separation in laminar flows.

Schubauer and Skramstad (Schubauer & Skramstad, 1948) were the first to characterize the effects of active flow control on boundary layers. They demonstrated control of the location of boundary layer transition from 10 to 25 percent of the natural transition location on a flat plate using a variable-frequency loudspeaker placed in the wall of a wind tunnel. Furthermore, Schubauer and Skramstad studied the effects of pressure gradient in the flow direction. Since the experiment was performed in the wind tunnel (as many experiments are), the pressure drop across the wind tunnel test section could be used to study the effect of pressure gradient on the flow stability. For Schubauer and Skramstad's experiment, the tunnel walls could be moved to increase (or decrease) the axial pressure gradient by diverging (converging) the walls to the point where the tunnel flow decelerates (accelerates) enough to generate the necessary pressure gradient. Their results showed

that the instabilities were always amplified in adverse pressure gradients and were always damped in favorable pressure gradients regardless of the driving frequency or the Reynolds number. The independence of driving frequency or Reynolds number may have been because the adverse pressure gradient changes the slope of the boundary-layer profile at or near the wall, which is a key Kelvin-Helmholtz instability requirement.

Another popular form of active flow control is by fluidic jets in crossflow (Chiekh, Bera, & Sunyach, 2011; Raman, 1997). These types of active flow control fall under the mass addition/subtraction flow-control category. Addition of mass generates vortical structures near the wall that can excite hydrodynamic instabilities and modify the turbulent boundary layer profile. Likewise, suction through a porous wall can also modify the boundary layer velocity profile, oftentimes to stabilize the boundary layer. White (White, 1991) maintains that the asymptotic suction velocity profile provides great stability to boundary layer flows. Indeed, the asymptotic suction velocity profile meets the stable-flow requirement of lack of an inflection point in the velocity profile theorized by Rayleigh.

Schubauer and Skramstad were also able to control instability waves using a thin, bronze ribbon mounted near the surface of the flat plate. The ribbon was mounted close enough to the surface of the flat plate that the ribbon did not create instabilities when it was stationary. The ribbon was oscillated by "passing a current through it in the presence of a strong magnetic field from a large electromagnet on the opposite side of the flat plate" (Schubauer & Skramstad, 1948).

It is also possible that the stability of a boundary layer can be controlled using compliant boundaries. White references the results of Kaplan and Kramer who studied the effect of compliant boundaries on boundary layer stability. Kaplan studied the stability of Tollmien-Schlichting (T-S) waves and Kelvin-Helmholtz waves with a compliant membrane surface and a Blasius boundary layer. He showed that the T-S waves would become unstable at ~40 percent higher Reynolds number than the rigid wall case. Unfortunately, physical realization of a compliant wall has not been reliable, and this method of controlling transition has not been popular in recent history.

Piezoelectric fluidic actuators have become popular in recent years for blowing/sucking at boundary layer surfaces because of their simplicity and low power input requirements. Piezoelectric fluidic actuators are typically called synthetic jets or Zero-Net-Mass-Flux (ZNMF) actuators in modern literature (Batikh, Baldas, Caen, Ghozlani, & Kourta, 2010; Jabbal, Liddle, Potts, & Crowther, 2012). Batikh showed experimentally that synthetic jets (piezoelectric actuator jets) are effective at reattaching boundary layer flows downstream of separated boundary layers on a flat plate as well as a plate sloped 28 degrees relative to the free stream. Batikh measured the effect of the synthetic jets on the boundary layer flow using hot-wire and Particle Image Velocimetry (PIV) techniques in 21.3 ft/s flow. Batikh's results showed that the synthetic jet was more efficient than constant or pulsed jets relative to the increase in velocity near the wall. Batikh claimed that the “vortical structures generated by the [synthetic jet] actuator … induce a periodical momentum injection in the boundary layer”. This may be true for the synthetic jet actuator, but would also be true for the pulsed jet, and perhaps, the continuous jet actuators. Batikh’s evidence that the synthetic jet actuator is only supported by an increase in the velocity in the near wall zone using the synthetic jet actuator.

Piezoceramic electro-mechanical actuators have also been used to excite or attenuate instabilities in shear and boundary layer flows. Piezoceramics are desirable for their robustness, low power

requirements, and wide range of frequency operation. Control of a turbulent boundary layer using an array of 16 cantilevered, piezoelectric actuator beams was demonstrated by (Bai et al., 2014). Each beam was approximately 0.0787 inches (2 mm) in width and 0.787 inches (20 mm) in length. The beams were placed adjacently in the cross-stream direction separated by 0.002 inches (0.05 mm). Each actuator could be independently controlled such that a sinusoidal wave could be produced in the cross-stream direction. Tests were conducted at free-stream velocities of 7.9 and 13.1 ft/s and measurements were taken using hot-wire and PIV instruments. Bai showed that the transverse travelling wave created a layer of streamwise vortices that interfered with turbulence production and ultimately reduced skin friction drag on the flat plate. Bai also demonstrated an increase in the linear part of the sublayer of up to 100 percent over the uncontrolled boundary layer.

Blackwelder demonstrated similar results to Bai using a surface piezoelectric actuator shaped like a delta wing (Blackwelder, Liu, & Jeon, 1998; Jeon & Blackwelder, 2000). Blackwelder used unimorph and bimorph piezoelectric devices to drive a flexible spring steel cut in the shape of a triangle. The active triangular geometry created near-wall vorticity on the order of the viscous sub-layer thickness. Experiments were completed to measure the streamwise velocity upstream and downstream of the actuators using a hot-wire. Blackwelder demonstrated that a single actuator produced a spanwise velocity in the viscous region near the wall and decreased the magnitude of the streamwise turbulent fluctuations by 10 to 30 percent. Blackwelder also tested multiple actuators simultaneously. However, only limited results were provided, and details on the orientation of each actuator relative to its neighbors were not provided. Nevertheless, the limited results for the multiple-actuator case showed comparable results to the single actuator case.

Jacobson (Jacobson & Reynolds, 1998) also used a piezoelectric actuator to control turbulent boundary layer flows. Jacobson's actuator consisted of a rectangularly shaped, cantilever with a single piezoceramic layer bonded to a single stainless-steel substrate which was mounted flush to the flow boundary. The actuator was 0.016 inches (0.41 mm) thick and 0.787 inches (20 mm) long with the free-end of the cantilever oriented in the downstream direction. Tests were completed in a water tunnel, so the actuator was encapsulated in an insulating epoxy to prevent electrical shorting between the actuator and the water. A single actuator was tested at a free stream velocity of 0.787 ft/s at a Reynolds number, based on length, of approximately 110,000. The single actuator was shown to produce significant disturbances which controlled boundary layer transition. The flow was visualized with a fluorescent dye and velocity measurements were taken using a Laser Doppler Anemometer (LDA) system. The resulting experiments showed transition could be delayed by 40 displacement thicknesses. The actuator produced a pair of streamwise vortices that decayed downstream within a few displacement thicknesses. Jacobson alluded to the use of an array of these types of actuators for localized boundary layer control distributed over a surface, but did not perform or report any multi-actuator experimental results.

Shear Layer and Cavity Flow Control

Shear layers occur when two fluids of different velocity and/or density are flowing with parallel mean velocity. The different velocity and/or density creates viscous shear stress at the interface of the two fluids resulting in production of vorticity. Examples of shear flows are backward facing steps, the wake of a flat plate, the wake and entrainment around a jet nozzle, and cavity flows. The shear layer over a cavity can cause large pressure oscillations, and sometimes, undesired effects.

Since this research is focused on the control of turbulence inside and downstream of a cavity, most of the literature review and equations presented on shear layers in this document will be focused on cavity flows. Per (A. D. Vakili & Gauthier, 1991), cavity flows can be classified into 3 categories:

- Closed cavity flows occur when the shear layer attaches to the bottom of the cavity. This is common for large length/depth (L/D) cavity geometries.
- Open cavity flows occur when the shear layer spans the length of the cavity and does not attach to the bottom. This behavior is common for small L/D cavity geometries.
- Transitional cavity flows occur when the flow alternates between open or closed flow types.

This research will be further narrowed to the open cavity because open cavities generally exhibit both normal and longitudinal modes of pressure oscillations which are of interest in the present research.

Some examples of passive flow control methods for cavity flows include leading-edge spoilers (Perng & Dolling, 2001), cylindrical rods placed near the leading-edge (Fowler, 2010; Givogue, Fowler, & Vakili, 2011; Loewen, 2008; A. Vakili et al., 2014), and sloped aft cavity walls (Freitas, 2014).

Perng performed experiments to study a variety of passive cavity flow controls including vented upstream and downstream walls, inclined and swept downstream walls, spoilers, and vortex generators. Perng's research was focused on suppressing pressure fluctuations in cavities with L/D from 3 to 5 in Mach 5 flow. Perng's results indicated that the inclined downstream cavity wall was the best passive-suppression mechanism reducing mean and root-mean-square (RMS) pressures near the downstream wall/floor junction by as much as 35% and 40%, respectively.

Low Mach number, high Reynolds number experiments by Zhang (Zhang & Naguib, 2008), using unsteady pressure and hotwire measurements, showed that self-sustaining oscillations were sensitive to the cavity width. He showed that self-sustained oscillations only occur for narrow cavities in which W/L is approximately less than 1. He hypothesized that the attenuation of the self-sustained oscillations for wide cavities is caused by reduction in hydrodynamic feedback mechanism because of three-dimensional recirculation effects.

Experiments by Ma (Ma, Slaboch, & Morris, 2009) using PIV measurements showed that a Helmholtz resonator cavity could hydrodynamically force the shear layer into resonance over a range of flow speeds.

Lada (Lada & Kontis, 2010, 2011) performed experiments to study the effect of cavity leading-edge sweep as a mechanism to alter the position of the shear layer impingement inside the cavity. Leading-edge sweep angle was changed by inserting triangular-shaped blocks of various angles into the cavity. Oil-flow was used to qualitatively observe the effects of the triangular blocks and surface pressures were used to quantitatively measure changes in cavity flow response. Various L/D configurations were tested at transonic and supersonic Mach numbers. Changing the leading-edge sweep resulted in a notable change in pressure gradient in the cavity for closed cavity cases (i.e. shallow cavities with L/D>13 where the shear layer attaches to the cavity floor). Leading-edge sweep changes resulted in no change for transitional and open cavity cases (i.e. deep cavities with L/D<10 where the shear layer does not attach to the cavity floor).

Acoustic forcing is a popular method for active control of cavity flows. Acoustic forcing was researched by Bechert (Bechert, 1982) and Zaman (Zaman & Hussain, 1980). Bechert studied excitation of waves in shear layers by using acoustic sources placed in various positions upstream and downstream of the trailing edge of a flat plate. Bechert showed analytically and experimentally that near the trailing-edge of the flat plate, the pressure field dominates the control of the shear layer if "the excitation field has a stagnation point at the plate edge or the excitation is directly located at the plate edge itself". Furthermore, Bechert demonstrated that when the excitation source was located downstream of the plate edge, the excitation was very inefficient requiring much more energy to excite the shear layer waves than a source placed upstream. Bechert applied these conclusions to the effect of turbulence in the shear layer stating that downstream turbulence has a weak effect on the stability of the upstream shear layer. If the pressure excitation source is placed upstream of the plate edge, then Bechert claimed that the excitation was "orders of magnitude" more efficient than a downstream pressure excitation.

Microjets, or leading-edge blowing is also a common method of cavity control. Zhuang (Zhuang, 2006) showed experimentally that supersonic microjets placed upstream of the cavity leading edge could attenuate the primary cavity instability tone at Mach 2. Zhuang demonstrated up to 20 decibel reductions in cavity tones using shadowgraphs, unsteady pressure measurements, and Particle Image Velocimetry (PIV). Furthermore, Vakili (A. Vakili & Gauthier, 1994) demonstrated cavity shear layer control using upstream mass injection at supersonic Mach numbers. Cavity oscillations were reduced by up to 27 dB because of the thickening of the shear layer caused by the upstream mass injection. By modifying the shear layer, the shear layer instability characteristics were changed and control was achieved using various mass injection distributions and strengths.

Similarly, open-cavity tone attenuation was achieved by use of a spanwise 2-dimensional cylinder placed upstream of the cavity in supersonic flow (Givogue et al., 2011). The vortex shedding from the cylinder interacted with the cavity shear layer, modifying the shear layer stability properties. Various positions and shapes of the spanwise cylinder were tested experimentally. Cavity acoustics were measured using high-response pressure instrumentation and the flow field was measured using PIV. Cavity tones were suppressed by as much as 9 dB in the broadband and 18.7 dB in the 2^{nd}-mode cavity resonant frequency.

Flaherty (Flaherty, 2013) demonstrated passive cavity flow control using a spoiler, large triangular-shaped steps at the leading edge, ridges at the leading edge, and a rod-in-crossflow. Flaherty's experiments were focused on cavity tone attenuation at Mach 0.7 and 1.5. Unsteady pressure sensitive paint was used to measure and visualize the cavity pressure response. Flaherty reported that the rod-in-crossflow showed the largest peak suppression, followed by the spoiler, then the triangular steps. No cavity tone suppression was reported for the ridged leading edge.

Others have attempted to attenuate cavity instabilities by sloping the aft cavity walls (Bruce & Mundell, 2003). Chaplin showed via computations and comparison to experimental results that a 60-degree sloped aft wall would attenuate the acoustic instabilities of the weapons bay cavity of the UCAV 1303 vehicle by 5 to 6 decibels (dB). Also of interest were the results that showed Chaplin's computations were very sensitive to the time step used in the solver. For large time-steps (1.82×10^{-5} seconds), the primary cavity instability tone from the CFD did not match wind tunnel test data at the peak Sound-Pressure-Level (SPL) or the frequency at which the peak occurred.

Solutions using much smaller time steps ($9.1x10^{-6}$ and $4.55x10^{-6}$ seconds) showed that the peak SPL and the corresponding frequency from the CFD approached the test data as the time step was reduced. These results, of course, depend on the free stream conditions which drive the convective velocity of the vortices across the cavity, and thereby the cavity tones. This implies that to accurately capture cavity flow physics in a CFD simulation, a small time-step is required in addition to the usual high-density grid in high-gradient regions near walls and in shear layers.

Vortex Flow Control

Much effort has been accomplished in recent history to control various aspects of vortex flow such as the size, shape, strength, stability and direction. Vortex flows can be categorized as free-vortices, such as wing tip vortices in which there is no radial pressure gradient, or forced-vortices such as a confined vortex with pressure gradients imposed by the containing walls.

In forced vortices, the fluid particles have the same angular velocity and the fluid body rotates about an axis as if it were a solid body. In free vortices, every fluid particle moves in a circular fluid path with different angular velocities. A Rankine vortex is a combination of free and forced vortex where the inner portion of the vortex behaves in a "forced" manner and the outer portion behaves in a "free" manner.

Nearly all vortex control research is completed using a confined vortex because of the ability to control the experiment. Much research has been accomplished to understand the breakdown of vortices into turbulence. Recent literature has focused on the physics of multiple, confined-vortex cells, i.e. where there are multiple layers of vortices around a single axis with different axial and rotational velocities. It has been shown that generation of multiple cells leads to vortex instability (M. Khorrami & Grosch, 1989).

The processes by which vortex breakdown (VB) occurs are fundamental to the understanding of confined swirling flows and the control thereof. The literature includes work that was accomplished to understand the controlling factors that cause confined vortices to breakdown into pure turbulence. In all literature that was reviewed, the primary variables controlling VB are the Reynolds number and the circulation number (Hussein, Shtern, & Hussain, 1997; Nakamura, Leonard, & Spalart, 1985; Saprkaya, 1995). Additionally, changing the Reynolds number or circulation number will not only change the VB, but will also change the properties that define whether the flow is multicellular.

Hall (J. L. Hall, 1985) presents a concise history of vortex breakdown studies up to 1985 (which include literature from many of the authors cited herein). Hall notes that no complete description of vortex breakdown exists, but that the actual breakdown process includes elements of all theories such as Benjamin’s criticality theory (Benjamin, 1962) (the flow is supercritical upstream of the VB and subcritical downstream of the VB), Hall's quasi-cylindrical theory (M. G. Hall, 1967) (assume that the axial gradients are much smaller than the radial gradients in a vortex core then the VB occurs where this assumption fails in numerical simulations), and the hydrodynamic instability theory (Jones, 1960; Ludweig, 1961) (VB results from hydrodynamic instability of the vortex core caused by asymmetric disturbances).

In the mid-to-late 1990’s, Knuth and co-workers performed experiments (Knuth, Crawford, & Litchford, 1993; Knuth, Gramer, Chiaverini, & Sauer, 1998a, 1998b, 2002) and CFD (Knuth,

Gramer, Chiaverini, Sauer, et al., 1998; Trinh, Knuth, & Michaels, 2000) to develop a hybrid rocket engine that utilizes the 2-cell vortex. Two U.S. patents currently exist for a hybrid rocket engine that implements the 2-cell vortex flow field and both are held by Knuth and co-workers (Knuth, Chiaverini, & Gramer, 2001, 2003). The 2-cell vortex is desirable for rocket propulsion because the burn rate and combustion efficiency can be improved by the enhanced mixing, increased residence time of the fuel/oxidant, and enhanced heat transfer properties provided by the swirling 2-cell vortex (Knuth, Gramer, Chiaverini, Sauer, et al., 1998). Another desirable property of the 2-cell vortex is the potential ability of the secondary vortex to shield the chamber wall from high-temperature combustion that takes place in the primary vortex. Knuth and coworkers demonstrated that when the oxidizer is tangentially injected at the outlet end of the vortex chamber and the fuel is injected axially at the head end of the chamber, the wall temperatures were kept lower than normally observed with typical liquid rocket engines (Trinh et al., 2000).

Hoyt (Hoyt et al., 2013) performed a series of experiments, CFD simulations and analytical model calculations of single and multi-phase liquid/gas cyclonic separator flows (2-cell vortex devices) and described the relations between the primary vortex radius, the characteristic swirl velocity and the vortex pressure field. Factors affecting the swirl strength are important not only for increasing the velocity and the convective heat transfer coefficient, but also for preventing vortex breakdown. The primary variable for controlling the swirl velocity is the injection port velocity, but as with internal pipe flows, the injection port velocity is a function of the Reynolds number of the incoming flow. His results indicated that the non-dimensional radius of the primary vortex and the non-dimensional characteristic swirl velocity do not change unless the skin friction coefficient changes. Hoyt empirically related the skin friction coefficient to the Reynolds number of the incoming flow so that the two primary non-dimensional values (radius and swirl velocity) are a function of the Reynolds number only. Hoyt showed that when the injection velocity is increased, the primary vortex core radius increases because the increased radial pressure gradients in the secondary vortex force the secondary vortex to have a thinner annular cross-section.

Sarpkaya (Saprkaya, 1995) performed a series of experiments for various types of VB in non-cavitating, swirling flows. Sarpkaya showed that the vortex core size could be decreased by increasing Reynolds number at a constant circulation number, which has the effect of increasing the vorticity and the axial velocity in the vortex core as well as delaying vortex core burst (A. Vakili, Eramo, & Tennent, 1993). Sarpkaya listed four flow field properties that trigger VB:

- Increased asymmetry of circumferential vorticity distribution
- Disruption of outer radius flow
- Deflection of the stagnation point away from the vortex core axis
- Intensification of core deceleration due to stretching of azimuthal vorticity

Another common occurrence in VB was the oscillating behavior of the vortex core along the vortex axis with amplitude dependent on asymmetric fluctuations (Faler & Leibovich, 1978; Saprkaya, 1995). The oscillating behavior of the vortex core occurs in single-cell flows, but was also observed in the multicell flow and was observed by Vakili in his experimental investigation of the water-tunnel model arc-heater (A. D. Vakili, 1993).

Hussain (Hussein et al., 1997) showed that VB could be controlled using an additional swirl source at the axis of the primary swirling flow. Hussain experimented with a cylindrical device with one

end wall stationary, one end-wall rotating and a solid rod along the axis of the tube that could be rotated independently of the rotating end-wall. The rotation of the solid rod along the axis was varied in both co-rotating and counter-rotating modes. Hussain's experiment showed that weak forcing of the rod at the vortex axis had strong effect on VB.

Vakili (A. Vakili, Tennent, & Panchapakesan, 1996; A. D. Vakili, 1993) performed a series of experiments in a water-tunnel model of the AEDC H-1 arc heater (Felderman, Chapman, Jacocks, Horn, & Bruce, 1996) to study the vortex flow structure and to understand the effect of various types of periodic forcing on the vortex breakdown. Vakili's studies were focused on prevention of VB using suction and/or blowing (either axially or tangentially) at various stations along the confined vortex tube. The oscillatory behavior of the vortex core along the vortex axis was observed in Vakili's experiments, but he found that the oscillatory behavior could be controlled using axial “forcing”, i.e. suction or blowing along the axis. The experiments included steady forcing, in which the oscillatory motion had longer wavelengths and included periodic forcing where the wavelength of the oscillatory motion corresponded to the forcing frequency (A. Vakili et al., 1993). Vortex burst could be delayed with high frequency forcing and the vortex breakdown position was dependent on the non-dimensional frequency of forcing. Quantitative measurements of the velocity flow field were obtained using hot film anemometry and a single-component, radially traversing velocity probe. Qualitative flow visualizations were accomplished using a fluorescing dye injected into the flow field at various radial locations. The experiments were focused on researching various methods for controlling the vortex core burst, however, Vakili was able to identify single and three-cell vortex structures inside the arc-heater model and validate the single and multicell vortex results against similar, prior experiments performed by Rigney (Rigney, 1988). While Vakili's experiments were focused on controlling VB, forcing may be necessary to produce multicell vortex behavior in some cases (M. Khorrami & Grosch, 1989).

Piezoelectric Devices

In 1880, Jacques and Pierre Curie discovered that certain naturally occurring crystals create electrical charges when a mechanical strain is applied. The Curie brothers called this effect the "piezoelectric effect" where the prefix "piezo" is the Greek word for "push" or "pressure". Naturally occurring piezoelectric crystals are quartz, tourmaline, topaz, and Rochelle salt. For many years, quartz was used for piezoelectric research and applications because it exhibited the best piezoelectric effect. Recently, synthetic materials called piezoceramics have become popular because of their ability to be tailored to applications. (D. Inman, 2011; PiezoTechnology, 2014)

When a force is applied to a piezoelectric or piezoceramic material, the internal stresses displace the electrical dipoles resulting in an electrical field (PiezoTechnology, 2014). A constant force would produce a constant electric field, or a DC voltage. An oscillating force would create an alternating electric field, or an AC voltage. The effect is reversible. When a DC voltage is applied to the piezoelectric material, the material will assume a constant state of deformation until the voltage is removed. When an AC voltage is applied, the material will vibrate or oscillate.

Since the piezoelectric effect is reversible, the material can be used as either a sensing device or an actuator. When used as a sensor, an applied mechanical force to the piezoelectric material creates a voltage across the material which can be measured. When used as an actuator, the piezoelectric material is subjected to an electrical potential causing the material to deform (D.

Inman, 2011). Piezoelectric actuators (or sensors) typically fall into one of several types of construction with one of two types of wiring as shown in Figure 1 (note that all figures are located in the appendix).

Most piezoelectric devices are the bimorph type which simply means that there are two layers of piezoelectric material. Typically, the two layers are bonded to a third layer (substrate) of ductile material such as steel. Bimorph actuators have greater potential for larger deflections because each piezoelectric layer can be driven independently if wired in parallel. In all bimorph designs, the contact bond between layers must be electrically conductive so that the driving (or sensing) circuit can be completed. piezoelectric material is very brittle and can shatter if too much stress is applied. Bonding the piezoelectric material to a substrate greatly increases the device robustness making the unimorph and bimorph designs with substrates a popular construction technique. Furthermore, the substrate and piezoelectric material are not required to be the same geometric shape and size. A small amount of piezoelectric material can induce enough stress in a lengthy substrate to produce significant tip deflections in cantilever arrangements. Single crystal devices do not produce much tip deflection, but can still be driven at high frequencies which will produce a significant acoustic or ultrasonic signal. Piezoelectric materials are used in a variety of applications such as accelerometers; pressure or sound sensing; actuators for pneumatic pumps and valves; energy generators for spark ignition or solid-state batteries; and ultrasonic medical applications.

Literature Review Summary

Some common recurring topics can be found in flow control literature. First, understanding of the production, evolution and breakdown of large-scale coherent structures is paramount for achieving flow control. The large-scale coherent structures can be present in laminar or turbulent flow and promote mixing and entrainment of surrounding fluid. Second, the stability characteristics of the flow govern how the large-scale coherent structures grow, evolve, dissipate, or break down. Flow fields which are inherently stable require much energy input via some perturbation mechanism to amplify or attenuate instabilities that change the flow state. Conversely, unstable flow fields may require very little perturbation to achieve control. Third, the direction of flow perturbation used to achieve control is important. Much of the literature indicates that perturbations and growth in the cross-stream direction (or azimuthal direction for axisymmetric flow) tends to be the direction in which growth of fluid instability is sensitive. Indeed, this can be seen in many natural transition experiments where vortex formation and breakdown are evident prior to full transition.

Furthermore, most of the literature is focused on attenuation of cavity instabilities. Using the instability of the shear layer and cavity feedback mechanisms, large-scale mixing enhancement can be achieved via amplification of cavity instabilities. This research is focused on leveraging these flow control fundamentals to demonstrate how the proposed multi-level actuator can be used to actively control production of large-scale coherent structures and couple with cavity flows.

CHAPTER THREE GOVERNING EQUATIONS

Introduction

All fluid flow problems begin with the Navier-Stokes (N-S) equations. However, there are fundamental flow fields that are related to flow control problems for which the N-S equations can be simplified. There are three primary flow fields that will be reviewed here - the boundary layer, shear flows, and vortex flow. Understanding of these three fundamental flow fields is required for any type of flow control design or application. Furthermore, governing equations are also reviewed for turbulence and one-dimensional gas dynamics.

Boundary layers are present in every real flow. The stability of the boundary layer is an important feature of the flow that governs how the flow transitions to turbulence. The N-S equations can be reduced to a set of 2-D equations that describe most boundary layer flows.

Shear flows are also common flow fields that have been studied in detail. Shear layers are produced in the wake of bodies, or at the leading edge of an aft-facing step or cavity. A cavity has a leading surface on which a boundary layer grows. The leading edge of the cavity can behave like a backward facing step in which a free-shear layer is formed. Therefore, the cavity flow field consists of a boundary layer coupled with a shear layer. Instabilities in the upstream boundary layer could affect the cavity shear layer, and hence, the cavity resonant tones. Cavity geometry is usually defined in two-dimensions (either rectangular or axisymmetric) having dimensions of length (L) and depth (D). Despite typical cavity flows having geometric descriptions in two-dimensions (2D), their actual flow physics are always three-dimensional (3D).

Vortex flows are also common and have significant importance for flow over a cavity. The leading edge of a cavity produces a shear layer that eventually produces vortices. These vortices travel across the cavity opening and impact the aft-wall of the cavity. The vortices are broken up by the aft wall of the cavity and a pressure wave is created that travels upstream. The travelling pressure wave interacts with and resonates with the vortex production at the leading edge of the cavity.

The governing equations are presented in this chapter for each of these flow types. Additionally, the piezoelectric equations are presented at the end of the chapter, but no attempt has been made to couple the piezoelectric equations with the fluid flow equations.

Navier-Stokes Equations

The continuity equation, the N-S equations, and the energy equation for a compressible, viscous fluid where body forces are assumed negligible are (White, 1991)

$$\frac{\partial \rho}{\partial t} + \nabla \cdot (\rho \boldsymbol{u}) = 0 \tag{1}$$

$$\rho\left(\frac{\partial \boldsymbol{u}}{\partial t} + \boldsymbol{u}(\nabla \cdot \boldsymbol{u})\right) = \rho \boldsymbol{g} - \nabla P + \frac{\partial}{\partial x_j}\left[\mu\left(\frac{\partial u_i}{\partial x_j} + \frac{\partial u_j}{\partial x_i}\right) + \delta_{ij}\lambda \nabla \cdot \boldsymbol{u}\right] \tag{2}$$

$$\rho\left(\frac{\partial h}{\partial t}+h(\nabla\cdot h)\right)=\left(\frac{\partial P}{\partial t}+\boldsymbol{u}(\nabla P)\right)+\nabla\cdot(k\nabla T)+\Phi\,. \tag{3}$$

The λ term is the second coefficient of viscosity (often taken as either 0 or $-2/3\mu$, h is the enthalpy, and the last term of the energy equation, Φ, is the viscous dissipation of energy caused by work done on the fluid by shear stresses and is given by

$$\begin{aligned}\Phi=\mu\Bigg[2\left(\frac{\partial \mathrm{u}}{\partial \mathrm{x}}\right)^2+2\left(\frac{\partial \mathrm{v}}{\partial \mathrm{y}}\right)^2+\left(\frac{\partial \mathrm{w}}{\partial \mathrm{z}}\right)^2+\left(\frac{\partial \mathrm{v}}{\partial \mathrm{x}}+\frac{\partial \mathrm{u}}{\partial \mathrm{y}}\right)^2+\left(\frac{\partial \mathrm{w}}{\partial \mathrm{y}}+\frac{\partial \mathrm{v}}{\partial \mathrm{z}}\right)^2\\+\left(\frac{\partial \mathrm{u}}{\partial \mathrm{z}}+\frac{\partial \mathrm{w}}{\partial \mathrm{x}}\right)^2\Bigg]+\lambda(\nabla\cdot\mathbf{u})^2\,.\end{aligned} \tag{4}$$

The vector $\boldsymbol{u}=(u,v,w)$ represents the (x,y,z) velocity components in the Cartesian coordinate system or the (r,θ,z) velocity components in the cylindrical coordinate system. However, the equations take a different form in the cylindrical coordinate system than the Cartesian form shown here. The equation of state is also required to solve the equations for a compressible fluid. If the fluid is assumed to be incompressible, e.g. for gases at low Mach numbers or liquids, then the continuity equation becomes

$$\nabla\cdot\boldsymbol{u}=0\,, \tag{5}$$

and the Navier-Stokes equation becomes

$$\frac{\partial \boldsymbol{u}}{\partial t}+u(\nabla\cdot\mathbf{u})=-\frac{1}{\rho}\nabla \mathrm{P}+\frac{\mu}{\rho}\nabla^2 u\,. \tag{6}$$

Vorticity

Vorticity is defined as the curl of the velocity (cross product of the gradient operator with the velocity vector),

$$\omega=\nabla\times\boldsymbol{u}\,. \tag{7}$$

Being a vector cross-product, vorticity has three components which are functions of the local velocity gradients. Vorticity is a measure of the local rotational motion of a fluid flow field. Vorticity is always generated by viscosity. A flow is irrotational if it has zero vorticity. Vorticity does not imply a vortex is present in the flow. A vortex is a global flow phenomenon that can be present in irrotational flow such as the free vortex.

The vorticity equation can be derived by taking the curl of the momentum equation.

$$\nabla\times\frac{\partial \boldsymbol{u}}{\partial t}+\nabla\times\big(\boldsymbol{u}(\nabla\cdot\mathbf{u})\big)=-\nabla\times\left(\frac{1}{\rho}\nabla \mathrm{P}\right)+\nabla\times\left(\frac{\mu}{\rho}\nabla^2\mathbf{u}\right) \tag{8}$$

The first term on the left side of equation (8) is the unsteady component of vorticity and can be written as

$$\nabla\times\frac{\partial \boldsymbol{u}}{\partial t}=\frac{\partial}{\partial t}(\nabla\times\boldsymbol{u})=\frac{\partial \omega}{\partial t}. \tag{9}$$

Since we have assumed incompressible flow, the first term on the right-hand side of equation (8) vanishes because of the following vector identity

$$\nabla\times\nabla\cdot scalar=0. \tag{10}$$

The last term on the right-hand side of equation (8) is the viscous diffusion of vorticity and becomes

$$\nabla\times\left(\frac{\mu}{\rho}\nabla^2\mathbf{u}\right)=\frac{\mu}{\rho}\nabla^2\boldsymbol{\omega} \tag{11}$$

The second term on left hand side of equation (8) is the convective transport of vorticity and can be written as

$$\nabla\times\big(\boldsymbol{u}(\nabla\cdot\mathbf{u})\big)=(\boldsymbol{u}\cdot\nabla)\boldsymbol{\omega}-(\boldsymbol{\omega}\cdot\nabla)\boldsymbol{u}+\boldsymbol{\omega}(\nabla\cdot\boldsymbol{u})+\boldsymbol{u}(\nabla\cdot\boldsymbol{\omega}) \tag{12}$$

but,

$$\boldsymbol{u}(\nabla\cdot\boldsymbol{\omega})=\boldsymbol{u}\big(\nabla\cdot(\nabla\times\boldsymbol{u})\big)=0$$

because of the vector identity, and

$$\boldsymbol{\omega}(\nabla\cdot\boldsymbol{u})=0$$

because of the incompressible assumption. Finally, putting all terms together and re-ordering, we arrive at the vorticity equation as shown in equation (13).

$$\frac{\mathrm{D}\boldsymbol{\omega}}{\mathrm{D}t}=\frac{\partial\boldsymbol{\omega}}{\partial t}+(\boldsymbol{u}\cdot\nabla)\boldsymbol{\omega}=(\boldsymbol{\omega}\cdot\nabla)\boldsymbol{u}+\frac{\mu}{\rho}\nabla^2\boldsymbol{\omega} \tag{13}$$

The first term on the right side represents the change in moment of inertia caused by stretching of a fluid element, and the second term represents the torque on the fluid element caused by viscosity. Stretching a fluid element reduces the moment of inertia thereby increasing the angular velocity of the element much like the increase in angular velocity an ice skater achieves by detracting their arms while spinning.

Following Davidson (Davidson, 2015), consider vorticity in the two-dimensional *x-y* plane. Only the z-component of vorticity remains in the *x-y* plane because there is no z-component of velocity. There can be no vortex stretching in the x-y plane, so the first term on the right side is zero and the vorticity is only a function of the viscous forces as shown in equation (14).

$$\frac{\mathrm{D}\omega_z}{\mathrm{D}t}=\frac{\partial\omega_z}{\partial t}+u\frac{\partial\omega_z}{\partial x}=\nu\nabla^2\omega_z \tag{14}$$

This equation is synonymous with the governing equation for temperature diffusion in a fluid where the vorticity can be replaced by temperature, *T*, and the viscosity can be replaced by the thermal diffusivity, α. So, by analogy, planar vorticity behaves like heat and can be convected with the flow ($u\ \partial\omega_z/\partial x$) or can be diffused in the flow ($\nu\nabla^2\ \omega_z$) by viscosity. There is no vorticity generation term in the equation. Vorticity is generated from surfaces on which the no-slip boundary condition imposes shear forces and a velocity gradient, e.g. the boundary layer. The velocity in the

boundary layer is much lower than the free stream, and therefore, the convection of vorticity is small but the diffusion of vorticity is large in the boundary layer. The vorticity diffuses through the boundary layer and into the free stream flow where it is then convected and diffused throughout the flow field.

Vortex Definition

A vortex is described simply as "the flow of fluid along a curved path or the flow of a rotating mass of fluid" (Bansal, 2005). The two basic classifications of vortices are the "free vortex" and the "forced vortex".

In a "forced vortex", all fluid particles follow a curved path around a central point but also rotate locally with varying degrees of velocity. The tangential velocity of the vortex is proportional to the distance from the axis of rotation, equation (15). The fluid particles in a forced vortex are in shear, and therefore have vorticity.

$$\frac{V_t}{r} = \text{constant} \tag{15}$$

A free vortex, however, is one in which all fluid particles in a body of fluid follow a curved path around a central point without local fluid-particle rotation. The tangential velocity decays as a function of distance from the axis of rotation. Free vortices follow the relation between radius and tangential velocity shown in equation (16). Free vortices can be irrotational since the fluid particles travel a circular path, but do not rotate themselves. Furthermore, if the free vortex is inviscid and irrotational it can be classified as a potential vortex because it can be defined by potential flow theory. Free vortices are not shear flows because the fluid elements do not rotate locally, and therefore, do not have vorticity despite the circular streamlines.

$$rV_t = \text{constant} \tag{16}$$

Vortices can also be compound free and forced where an inner portion of the vortex behaves like forced motion, and the outer portion of the vortex behaves like free motion. These types of flow are often called "Rankine" vortices after their discoverer.

Vortex Stability

Like boundary layer and shear flow stability analyses, the most common method for determining stability for vortex flow is to assume some form for the small disturbances, substitute them into the governing fluid motion equations, and linearize the results. The linearized disturbance equations are presented in this section and are largely reproduced from Khorrami (M. Khorrami & Grosch, 1989; M. R. Khorrami, 1989). Assume that the disturbance quantities *(u,v,w,p)* have a helical wave form:

$$(u, v, w, p) = i[F(r), G(r), H(r), P(r)]\exp[i(\alpha Z + \eta\theta - \omega t)], \tag{17}$$

where α is the axial wavenumber, η is the circumferential wavenumber, ω is the temporal frequency (as distinguished from the vorticity ω in this case), and *(F, G, H, P)* are the complex disturbance eigenfunctions. The assumed waveform can be substituted into the governing equations and can be linearized by ignoring the quadratic terms.

There are two types of mechanisms that can cause instabilities in swirling flows, classical centrifugal inviscid instability, and viscous instabilities imposed by confining walls or from the shear stresses between different layers of fluid. For inviscid fluid motion, Lord Rayleigh deduced criteria for centrifugal instability: "An inviscid rotating flow is unstable if the square of its circulation decreases outward" (White, 1991). This is described mathematically in equation (18).

$$\frac{\mathrm{d}}{\mathrm{dr}}(\mathrm{rv})^2 < 0, \mathrm{unstable} \tag{18}$$

Rayleigh's criterion for centrifugal instability only applies to a vortex without axial velocity. Howard and Gupta showed that the stability criteria can be modified for a vortex with axial component of velocity and must be satisfied everywhere in the flow field (M. R. Khorrami, 1989), or described mathematically as:

$$\frac{1}{\mathrm{r}^3}\frac{\mathrm{d}(\mathrm{rv})^2}{\mathrm{dr}} \Big/ \left(\frac{\mathrm{dW}}{\mathrm{dr}}\right)^2 < \frac{1}{4}. \tag{19}$$

Gostintsev (Gostintsev, 1968) reviewed the analytical work of Rayleigh, Howard and Gupta and used experiments on vortex tubes to demonstrate that the effect of axial velocity (and hence axial shear between layers) has a significant effect on flow stability and that the stability criteria is better described by Howard and Gupta's criteria than with Rayleigh's results.

Up to this point, both stability criteria assume axisymmetry. Rayleigh's stability criterion is only a function of the gradient of circulation in the radial direction. Howard and Gupta's stability criteria is a function of the gradient of circulation in the radial direction and the gradient of axial velocity in the radial direction. Stability results for non-axisymmetric assumptions were detailed by Vladimirov (Vladimirov, 1983).

Instabilities can also be self-excited in some cases. It has been shown experimentally, numerically, and theoretically that self-excitation of the global swirling flow field can be caused by resonance (Paschereit, Terhaar, ĆOsiĆ, & Oberleithner, 2014). Paschereit describes situations in which the self-excited instabilities are present in cold-flow applications, but are not present in similar hot-flow or reacting flow fields. Paschereit showed analytically using linear stability theory and experimentally that the density stratification present in reacting flows can dampen the self-excited instabilities.

Khorrami (M. Khorrami & Grosch, 1989; M. R. Khorrami, 1989), Nolan (Nolan, 2012), and Paschereit (Paschereit et al., 2014) used a spectral collocation technique to solve the linear stability equations for a three-dimensional, swirling vortex flow. Khorrami presented stability results for the two-cell vortex with a mean profile selected from Donaldson and Sullivan's (C. Donaldson & Sullivan, 1962; C. D. Donaldson, 1960) three-dimensional similarity solutions for swirling flow in a porous pipe. Khorrami solves the three-dimensional, linearized stability equations using a staggered spectral collocation method for multiple values of the axial wavenumber for the axisymmetric circumferential wavenumber $\eta=0$ as well as asymmetric circumferential wavenumbers $\eta=+/-1$. His work showed that there is a broad range of axial wavenumbers that increase the frequency of oscillation for the flow rates shown. The results also indicate there is a small effect from the flow rate and a negligible effect from the Reynolds number. The lack of

significant effect of Reynolds number might indicate the instability is not driven by viscous forces. These results might also indicate that an axial pulsing at the centerline of the vortex to maintain symmetry could be used to control the stability of the two-cell vortex flow. Khorrami also demonstrated that there are multiple modes of instability for the asymmetric ($\eta = +/-1$) circumferential disturbances. The $\eta = 1$ disturbance caused a small, but insignificant second mode of instability. However, the $\eta = -1$ disturbance showed up to three significant instability modes. Khorrami's work also proved that the growth rate of a single-cell vortex is more stable than a two-cell vortex.

Boundary Layer Flow

The boundary layer is the viscous flow region where shear stress is imparted to the flow by bounding surfaces causing the flow to slow down. The boundary layer is thin if the time it takes for a fluid particle to travel (U) the length of a surface (L) is much less than the time needed for the viscous effects (v) to diffuse across the boundary layer. These quantities are often combined into the dimensionless Reynolds number. The boundary layer is thin when the Reynolds number is large. The Reynolds number can be defined by a streamwise length scale or by a transverse length scale such as the boundary layer thickness, momentum thickness, or displacement thickness. A large Reynolds number has different meaning for each of the definitions with different length scales. Most boundary layer analyses assume high enough Reynolds number that the boundary layer is thin, and therefore, the entire flow field is not dominated by viscous effects.

The boundary layer is usually laminar (meaning in layers) near the beginning of the surface. As the Reynolds number becomes large further downstream, the boundary layer thickens and the stability of the boundary layer decreases until the laminar flow transitions to turbulence. Much research has been accomplished to understand the transitional physics between laminar and turbulent flows. Flow control applications are often targeted toward preventing or promoting boundary layer transition to turbulence. Typical boundary layer equations and stability analyses are presented next.

Boundary Layer Equations

While laminar boundary layers often exhibit two-dimensional behavior, turbulent boundary layers are always three-dimensional. Nevertheless, simplifying the N-S equations to two-dimensions results in a set of solvable equations that accurately represent most boundary layers. Other approximating assumptions that are generally made for boundary layer analysis are:

- the Reynolds number is large,
- the buoyancy force and free-convection are negligible, and
- the transverse pressure gradient is negligible.

The resulting two-dimensional boundary layer equations (White, 1991) for a compressible, laminar, perfect gas are:

Continuity:
$$\frac{\partial \rho}{\partial t} + \frac{\partial}{\partial x}(\rho u) + \frac{\partial}{\partial y}(\rho v) = 0 \tag{20}$$

x-momentum:
$$\rho\left(\frac{\partial u}{\partial t}+u\frac{\partial u}{\partial x}+v\frac{\partial u}{\partial y}\right)=-\frac{\partial P}{\partial x}+\frac{\partial}{\partial y}\left(\mu\frac{\partial u}{\partial y}\right) \tag{21}$$

y-momentum:
$$\frac{\partial P}{\partial y}\approx 0 \tag{22}$$

Energy:
$$\rho\left(\frac{\partial h}{\partial t}+u\frac{\partial h}{\partial x}+v\frac{\partial h}{\partial y}\right)\approx u\frac{\partial P}{\partial x}+\frac{\partial}{\partial y}\left(k\frac{\partial T}{\partial y}\right)+\mu\left(\frac{\partial T}{\partial y}\right)^2 . \tag{23}$$

The term $h = e + P/\rho$ is the fluid enthalpy. A fifth equation of state is needed in compressible flows to complete the coupling between the energy and momentum equations. The most common equation of state for non-reacting gas flows is the ideal gas law:

$$P = \rho RT . \tag{24}$$

Some additional, useful equations that define the boundary layer thickness parameters were derived by Von Karman using an integral control-volume analysis. The equations for the boundary layer displacement thickness, δ^*, and the momentum thickness, θ, are given by equations (25) and (26), respectively.

$$\delta^* = \int_0^{Y\to\infty}\left(1-\frac{u}{U}\right)dy \tag{25}$$

$$\theta = \int_0^{Y\to\infty}\frac{u}{U}\left(1-\frac{u}{U}\right)dy \tag{26}$$

The upper limit of integration, $Y\to\infty$, is often taken as the 99-percent boundary layer thickness, δ_{99}, which is simply the distance from the bounding surface at which the velocity is 99-percent of the free stream velocity.

Similarity solutions are often used to solve the system of differential equations for boundary layer flow. The Blasius solution is a well-known similarity solution for incompressible flow. The Blasius similarity parameter is

$$\eta = y\sqrt{\frac{U}{2\nu x}}, \tag{27}$$

and the stream function is

$$\psi = \sqrt{2\nu U x}f(\eta) . \tag{28}$$

Substituting these into the momentum equations results in the Blasius equation for flat-plate incompressible boundary layer flow:

$$f''' + ff' = 0, \tag{29}$$

with the no-slip and freestream merge conditions:

$$f'(0) = f(0) = 0 \tag{30}$$

$$f'(\infty) = 1\,.$$

Tabulations of the solution to the non-linear Blasius equation are found in many textbooks (Schlichting & Gersten, 1999; White, 1991).

The boundary layer thickness parameters can be estimated by solving the Blasius equation for the velocity profile. The estimated parameters for laminar flows are:

$$\begin{aligned}\frac{\delta_{99}}{x} &\approx \frac{5.0}{\sqrt{Re_x}}\\ \frac{\delta^*}{x} &\approx \frac{1.7208}{\sqrt{Re_x}}\\ \frac{\theta}{x} &\approx \frac{0.664}{\sqrt{Re_x}}\,.\end{aligned} \tag{31}$$

The definitions of boundary layer thickness parameters are the same for turbulent flow and laminar flow if time-averaged quantities are used. A momentum-integral analysis could be used to evaluate the boundary layer thickness parameters for turbulent flow. However, Prandtl's 1/7th power-law profile has been held for many years as the best fit to experimental data since Prandtl's 1921 paper. The 1/7th power law for turbulent flows is

$$\begin{aligned}\frac{\bar{u}}{U} &= \left(\frac{y}{\delta}\right)^{1/7},\\ \frac{\theta}{\delta} &\approx \frac{7}{72}\,.\end{aligned}$$

where the overbar indicates time-averaged quantities. The Reynolds number based on displacement thickness and the Reynolds number based on momentum thickness can be defined for laminar or turbulent flows as,

$$\begin{aligned}Re_{\delta^*} &= \frac{U\delta^*}{\nu}\\ Re_\theta &= \frac{U\theta}{\nu}\,.\end{aligned} \tag{32}$$

Boundary Layer Stability

The goals of stability theory are to determine if a flow field can withstand a small disturbance and still return to the original state (White, 1991) while "one tries to infer whether this perturbation increases, decreases, or remains the same" (Parhi & Nath, 1997). Boundary layer flow stability is often studied using linearized stability theory in which a disturbance is added to the governing equations, the governing equations are then linearized, and the resulting simplified equations are solved. The disturbances that are added to the governing equations are called Tollmien-Schlichting waves, or T-S waves, and typically take the form

$$(\hat{u}, \hat{v}, \hat{w}, \hat{p}) = [u(y), v(y), w(y), p(y)]\exp[i\alpha(x\cos\phi + z\sin\phi - ct)]\,, \tag{33}$$

where *i* is the imaginary number, φ is the direction of the disturbance relative to the horizontal axis, α is the wave number of the disturbance, and *c* is the propagation speed of the disturbance. When a disturbance of this type is substituted into the incompressible N-S equations, a set of two-dimensional disturbance equations in the plane of the disturbance can be written. Further assuming the basic flow is two-dimensional, the Orr-Sommerfeld (O-S) relation can be derived,

$$(\mathrm{U}-\mathrm{c})(\mathrm{v}''-\alpha^2\mathrm{v})-\mathrm{U}''\mathrm{v}+\frac{\mathrm{i}\nu}{\alpha}(\mathrm{v}''''-2\alpha^2\mathrm{v}''+\alpha^4\mathrm{v}), \tag{34}$$

where the prime notation denotes differentiation with respect to *y*. The Orr-Sommerfeld equation can be nondimensionalized using the following transformations:

$$\phi=\frac{\mathrm{v}}{\mathrm{U_e}},\quad \mathrm{U}^*=\frac{\mathrm{U}}{\mathrm{U_e}},\quad \mathrm{c}^*=\frac{\mathrm{c}}{\mathrm{U_e}},\quad \alpha_\delta=\alpha\delta,\quad \mathrm{Re}_\delta=\frac{\mathrm{U_e}\delta}{\nu}. \tag{35}$$

The non-dimensional form of the Orr-Sommerfeld equation is

$$(\mathrm{U}^*-\mathrm{c}^*)\left(\frac{\mathrm{d}^2\phi}{\mathrm{dy}^2}-\alpha_\delta^2\right)-\frac{\mathrm{d}^2\mathrm{U}^*}{\mathrm{dy}^2}\phi+\frac{\mathrm{i}}{\alpha_\delta\mathrm{Re}_\delta}\left(\frac{\mathrm{d}^4\phi}{\mathrm{dy}^4}-2\alpha_\delta^2\frac{\mathrm{d}^2\phi}{\mathrm{dy}^2}+4\alpha_\delta^4\phi\right)=0. \tag{36}$$

The O-S equation has been widely used to study stability of various flows such as internal duct flow, boundary layer flow, and free-shear layers (each of these requires a different boundary condition but is governed by the same stability equation). The boundary conditions for flat-plate flow are

$$\begin{aligned}\mathrm{v}(0)&=\mathrm{v}'(0)=0\\ \mathrm{v}(\infty)&=\mathrm{v}'(\infty)=0\,.\end{aligned} \tag{37}$$

The eigenvalues define temporal or spatial stability. For temporal instability $c_i^*>0$, and for spatial instability $\alpha_{\delta i}<0$. Since the disturbance is a function of space (α) and time (c), stability curves are typically generated either for temporal or spatial stability, but not both simultaneously. Stability curves for the growth of disturbances in Blasius flat-plate boundary layer flow are shown in Figure 2 and Figure 3.

In Figure 2, the curves are lines of constant temporal amplification (c_r for real, c_i for imaginary components). The $c=0$ line is the neutral stability curve. The curves are shown as a function of the Reynolds number based on δ^*. A point inside the neutral stability curve has amplified disturbances, i.e. the flow is unstable. A point outside of the neutral stability curve has attenuated disturbances, i.e. the flow is stable. Moving inside the curve will promote transition to turbulence. This can be accomplished by increasing the Reynolds number (increasing δ*, increasing velocity, or reducing viscosity). Similarly, the curves in Figure 3 are lines of constant spatial amplification. These curves can be used as reference to determine where the flow characteristics reside relative to the neutral stability curve at a given location in the wind tunnel, perhaps where flow control will be applied.

Stability analysis of laminar flows is useful for predicting when a small disturbance will become unstable. However, the stability analysis does not predict when or how the unstable laminar flow will transition into turbulence. We can only know that when a laminar flow remains in the unstable region, the flow will transition as Reynolds number is increased. Furthermore, the linearized stability theory only considers two-dimensional flow stability, but nearly all real flows are three-dimensional in nature, especially turbulent flow. Experiments and flow visualization have

provided insight to the behavior of transitional flow and fully turbulent flow, but there is still no theoretical solution for transition or turbulence. However, flow visualization and experimental techniques have provided insight to the transition process in recent years. The unstable laminar flow develops into T-S waves which are still part of the linear growth regime and are difficult to visualize because the displacements are small. The T-S waves quickly develop secondary and tertiary instabilities where vorticity develops and the flow becomes three-dimensional. White (White, 1991) refers to the experiments of Klebanoff which revealed that "a shear layer in the unstable region has a strong ability to amplify any slight three-dimensionality".

The onset of this three-dimensionality is where the linearized disturbance theory begins to break down and transition to turbulence cannot be predicted. Finally, at some critical Reynolds number for transition (Re_{tr}), a region of mixed laminar flow and turbulent spots form, beginning the transition process to fully turbulent flow further downstream. The important note here is that spanwise vorticity gradients begin to appear during the transition process. If one desires to force transition to turbulence using small perturbations, then introducing spanwise vorticity, and subsequently three-dimensionality, to the flow may be key.

The linearized stability equations are sensitive to the shape of the velocity profile of the basic flow, *U(y)*. Following White (White, 1991), the boundary layer equation at the wall, now for a fluid with non-constant viscosity $\mu = \mu(T)$ and a heated wall, is

$$\mu_w \frac{\partial^2 y}{\partial y^2}(0) = \frac{dP}{dx} + \left[\rho v_w \frac{d\mu}{dT}\frac{\partial T}{\partial y}(0)\right]\frac{\partial u}{\partial y}(0), \tag{38}$$

where the ρv_w term is added for non-zero velocity at the wall. Per White, the following features make the right-hand side more negative resulting in a more stable velocity profile:

- favorable pressure gradient: $dP/dx < 0$
- wall suction: $v_w < 0$
- reduction of viscosity - Cooling of gases: $d\mu/dT > 0$, $\partial T/\partial y > 0$
- reduction of viscosity - Heating of liquids: $d\mu/dT < 0$, $\partial T/\partial y < 0$
- active control by wave cancellation
- active control by arrays of piezoelectric actuators.

Favorable pressure gradients can be created by confining walls or by design. Wall suction can be inefficient if a large pressure gradient is needed to provide the proper suction. Heating/cooling can be inefficient if much energy is needed to heat/cool the surface. Wave cancellation uses a system that detects instability waves and generates cancelling waves of the same magnitude as the disturbance, but 180 degrees out of phase. Piezoelectric actuators can be used to generate vorticity to suppresses/amplify growing T-S waves.

Shear Flow

The free-shear layer is shown in Figure 4. Free-shear flows occur in the wake of an airfoil, in the wake of an aft-facing step, or at the leading edge of a cavity. Assume that the velocity in the z-direction (out of the page) is negligible and the shear layer is developing in two-dimensions as shown in the figure. The two streams have velocity profiles U_1 and U_2. The velocity gradient creates a shear stress in the fluid and generates a z-component of vorticity at the interface of the

two streams. This vorticity generation is important for mixing of two streams. The viscous forces smooth out the large-scale discontinuities in velocity profiles and convert kinetic energy into thermal energy through dissipation at the smallest scales (White, 1991). For cavity flows, the production of vorticity at the leading edge of the cavity is a defining feature for the shear layer across the cavity.

The flow develops from left to right in the figure until at some point it is fully developed. Furthermore, it is assumed that both streams have constant properties and are incompressible. Fully developed free-shear flows are like the two-dimensional boundary layer when the dominant component of velocity is in the x direction, there is no pressure gradient in the y-direction, and the Reynolds number is large. This is important because many studies on laminar flow stability have been performed for the flat-plate case. Similar behavior allows one to apply the same principles from flat-plate boundary layer experiments to free-shear flows.

For the case shown in Figure 4, the pressure gradient in the x-direction is also zero because there are no confining walls. This is not a necessary condition for free-shear flows, but pressure gradient in the x-direction has shown to significantly change the stability of the flow. For cavity flows, the forward and aft walls of the cavity impress an x-direction pressure gradient on the flow and the cavity floor impresses a y-direction pressure gradient.

It is assumed that the two streams are initially laminar and transition to turbulence at some point downstream of the initial disturbance. Disturbances can be pressure, velocity or both. Typical analyses assume that transition occurs at some Reynolds number greater than the critical Reynolds number. The difficulty becomes in how the Reynolds number is defined. For free-shear flows, there is no characteristic length and there are two velocities to choose from. One choice for defining the Reynolds number would be to use the difference in velocities $U_c=U_1 - U_2$ as the characteristic velocity and the momentum thickness of the upstream boundary layer as the characteristic length (Jimenez, 2013).

Flow visualization from Jimenez's experiments for laminar and turbulent shear flows are shown in Figure 5. For both cases, the instabilities in the shear layer take the form of large coherent structures that resemble the Kelvin-Helmholtz instabilities of a vorticity layer and agree well with two-dimensional laminar stability analysis (Jimenez, 2013). Also, following the work of Jimenez, if the large coherent structures are approximately the width of the shear layer, θ, then the time-scale for internal shear deformation of the structure is, approximately θ/u' where u' is the x-component of the perturbation velocity. The time scale related to the bulk flow is $\theta/\delta U$. The perturbation velocity is much smaller than the bulk velocity and the difference in velocity of the two streams in the free-shear flow which indicates that the time scale for the internal deformation of the large structures is much larger than the time scale of the bulk flow processes. This means that large-structure dynamics are dominated by the "linear processes due to the mean flow, instead of by their non-linear deformation" (Jimenez, 2013). This is true for both the turbulent and laminar cases shown in Figure 5 and is the reason why linear stability theory is so successful for analyzing these types of flows. Finally, the mixing of two fluids is minimal for the laminar case because the large-scale structures are essentially without vorticity until they break down into turbulence. The laminar entrained fluid mixes on a bulk level but not on a molecular level that can be achieved by the small-scale turbulent structures (Gutmark, 1997).

Shear Flow Equations

For the two-dimensional shear flow, the dominant velocity component is in the x direction and it is assumed that the Reynolds number is large enough that the developed velocity profiles are similar with boundary layer profiles. The plane shear flow can be modeled by the flat plate equations without a pressure gradient term because of the lack of confining walls, as shown in equations (39). The assumptions implicit in these equations are incompressible, laminar flow with constant properties and no buoyancy effects.

$$\frac{\partial u}{\partial x}+\frac{\partial v}{\partial y}=0$$
$$u\frac{\partial u}{\partial x}+v\frac{\partial u}{\partial y}\approx \nu\frac{\partial^2 u}{\partial y^2} \tag{39}$$

If one considers the developed region of the shear flow, a Blasius-type similarity variable for each stream can be defined, per White (White, 1991), as

$$\eta_j = y\sqrt{\frac{U_1}{2x\nu_j}}$$
$$f_j' = \frac{u_j}{U_1},\ \ j=1,2\,. \tag{40}$$

Substituting the similarity variables, equation (40), into the continuity and momentum equations, (39), results in a single, ordinary differential equation for each shear layer,

$$f_j''' + f_j f_j'' = 0,\quad j=1,2, \tag{41}$$

with three boundary conditions, the first being asymptotic behavior away from the shear layer due to the lack of confining walls,

$$f_1'(+\infty)=1,\quad f_2'(-\infty)=\frac{U_2}{U_1}, \tag{42}$$

the second boundary condition is kinematic equality at the interface,

$$f_1(\eta=0) = f_2(\eta=0)=0$$
$$f_1'(\eta=0) = f_2'(\eta=0)\neq 0, \tag{43}$$

and the third boundary condition being equal shear stress at the interface of the two streams

$$\mu_1\frac{\partial u_1}{\partial y}(0)=\mu_2\frac{\partial u_2}{\partial y}(0). \tag{44}$$

Shear Flow Stability

Shear flows can be efficiently controlled by introducing small perturbations upstream of the flow because shear flows are inherently unstable. The small perturbations grow until the onset of transition to turbulence. If the perturbations are too large they can overcome the small instabilities

and transition the flow to turbulence too soon, perhaps with less desirable outcomes. Transition to turbulence is a key factor for controlling and enhancing mixing of single or multiphase flows.

Per Rayleigh, a requirement for instability in laminar flows is an inflection point in the velocity profile. This requirement is readily satisfied by shear flows because they always have strong curvature and at least one inflection point (Figure 4). Furthermore, assuming parallel flow and two-dimensional profiles, shear layers are unconditionally unstable for all Reynolds numbers (White, 1991).

If the mean flow velocity profiles are known, perhaps from the Blasius type solution, the stability of the free-shear layer can be analyzed by first assuming the flow is disturbed by small perturbations of form of the Tollmien-Schlichting (T-S) waves. The stability equations are obtained by adding the perturbed quantities ($\hat{u}, \hat{v}$) to the bulk flow quantities (U, V), substituting into the governing equations, and linearizing the results by removing higher-order terms. The resulting linearized disturbance equations for the free-shear flow, not including pressure gradient terms due to the lack of confining walls, are

$$\frac{\partial \hat{u}}{\partial x} + \frac{\partial \hat{v}}{\partial y} = 0 \tag{45}$$

$$\frac{\partial u}{\partial t} + U\frac{\partial \hat{u}}{\partial x} + \hat{u}\frac{\partial U}{\partial x} + V\frac{\partial \hat{u}}{\partial y} + \hat{v}\frac{\partial U}{\partial y} \approx \nu\nabla^2\hat{u} \tag{46}$$

$$\frac{\partial v}{\partial t} + U\frac{\partial \hat{v}}{\partial x} + \hat{u}\frac{\partial V}{\partial x} + V\frac{\partial \hat{v}}{\partial y} + \hat{v}\frac{\partial V}{\partial y} \approx \nu\nabla^2\hat{v}\,. \tag{47}$$

Following White, the equations can be reduced to the classical Orr-Sommerfeld equation with the boundary conditions for free-shear layers

$$v(\pm\infty) = \frac{dv}{dy}(\pm\infty) = 0\,. \tag{48}$$

White states that free-shear flows are unstable for all Reynolds numbers, i.e. Re_{crit}=0, for all wavenumbers, α. This phenomenon was demonstrated by Cumbo (Cumbo, 1996) by analyzing a finite domain of length L along the x-direction. Cumbo analyzed the stability of the free-shear layer for increasing values of L and showed that as $L\rightarrow\infty$, $Re_{crit}\rightarrow 0$. The unstable nature of free-shear flows facilitates the transition from laminar to turbulent flow. Therefore, shear flows are important for mixing and were early candidates for improving mixing for combustion applications.

Cavity Flow

In general, cavity flows are fully three-dimensional, whether the geometry is rectangular or axisymmetric, because of strong regions of re-circulation near the leading-edge and trailing-edge walls. However, most cavity flows can be adequately approximated by assuming two-dimensional geometry, i.e. the lateral velocity is zero for Cartesian cavities or the swirl (azimuthal) velocity is zero for axisymmetric cavities.

Because of the viscous nature of all fluids, a boundary layer will form upstream of the cavity leading-edge. The characteristics of the upstream boundary layer (such as boundary layer thickness, displacement thickness, and momentum thickness) define the shear layer at the leading-

edge of the cavity. All shear layers are inherently unstable because of the inflection point in their velocity profile, but can have different receptivity to disturbances because of the boundary layer thickness at the leading-edge. Therefore, cavity flows can be separated into several fundamental flow types.

Upstream of the cavity is the approaching viscous, boundary-layer flow. Here, it is assumed that the approaching boundary layer is fully-developed and two-dimensional. Next, the boundary layer reaches the leading-edge of the cavity. Just downstream of the cavity face, the flow is similar to free-shear flow where the boundary layer flow and the flow inside the cavity are moving at different velocities. However, cavity flows differ from free-shear flows because cavity flows have a pressure gradient caused by the presence of the cavity walls and floor. If the cavity is shallow, then the shear flow will attach to the floor of the cavity until it reaches the aft wall. As the flow approaches the aft wall of the cavity, the pressure increases because of the presence of the wall and the flow is expelled from the cavity. Once the flow is expelled, the pressure decreases and fluid from the front of the cavity replaces the expelled fluid. If the cavity is deep, the shear flow may not attach to the floor of the cavity and be convected downstream to the aft wall of the cavity. Large-scale vortices are shed from the leading edge of the cavity. The vortices are convected with the shear layer until they reach the corner of the trailing-edge wall. At this point, the vortices are broken down and a pressure wave is generated that travels upstream in the cavity. The pressure wave couples with the vortex generating mechanism at the leading-edge and the shear layer resonates with self-sustaining oscillations. The cyclical pressure fluctuations are typically called Rossiter tones, Rossiter modes, or edge-tones, all of which may be used interchangeably.

Flow over an open cavity at subsonic and transonic speeds was studied extensively by (Rossiter, 1966). Rossiter's experiments were important for identifying the random and periodic fluctuating components of cavities and for identifying the acoustic coupling that can drive cavity resonance. Rossiter 's empirical equation was the standard for identifying resonance modes in cavities until it was modified for supersonic flow by Heller (Heller, Holmes, & Covert). Rossiter's equation is

$$\mathrm{St} = \frac{\mathrm{fL}}{\mathrm{U}} = \frac{\mathrm{m} - \mathrm{a}}{\frac{1}{\mathrm{k}} + \mathrm{M}}, \tag{49}$$

where *St* is the Strouhal number, *L* is the characteristic length which is usually the cavity length, *f* is the frequency in Hz, *k* is the ratio of vortex convection speed to the free-stream flow speed *U*, *M* is the free-stream Mach number, *a* is a phase-shift constant, and the cavity resonant modes are *m=1,2,3...* (Heller et al., 1971). The *k*-constant is generally taken to be 0.57. Rossiter used the *a* constant to fit the model to his experimental results. Rossiter's phase constant, *a*, ranged from 0.25 to 0.58 for *L/D* 4 to 10, respectively.

Heller improved on Rossiter's formula by assuming the cavity sound speed is equal to the free-stream sound speed based on stagnation temperature for higher Mach numbers (Heller et al., 1971). Heller's modification to Rossiter's formula is

$$\mathrm{St} = \frac{\mathrm{fL}}{\mathrm{U}} = \frac{\mathrm{m} - \mathrm{a}}{\frac{\mathrm{M}}{\left(1 + \frac{\gamma - 1}{2}\mathrm{M}^2\right)^{1/2}} + \frac{1}{\mathrm{k}}}. \tag{50}$$

Given a mode shape, *m*, these equations provide a means to determine the Strouhal number, and therefore, the resonance frequency of the fluctuating pressure in the cavity. These frequencies could then be used to drive cavity resonance using some active or passive control method. Unfortunately, Rossiter's model only predicts the cavity edge-tone frequencies (the frequency with which vortex shedding occurs from the leading edge and acoustic waves return from the trailing edge). Rossiter's model does not predict the broadband acoustic SPL, nor does it predict the amplitude associated with each of the edge-tones.

Dix and Bauer (Bauer & Dix, 1991a; Dix & Bauer, 1993, 2000) developed engineering models of cavity acoustics that accurately predict the amplitudes of the broadband acoustics, as well as the frequency and amplitudes of the Rossiter edge tones. Dix and Bauer used an extensive wind tunnel database to validate their work which included cavity acoustic data at subsonic and transonic Mach numbers. Their engineering model includes effects caused by upstream boundary layer characteristics as well as modifications for leading-edge spoilers and mass-injection. Bauer and Dix used the modified Rossiter equation to estimate the frequencies of the tones in the cavity. A single-stream, turbulent, mixing-layer model (derived using similarity solutions) was used to predict the pressure amplitudes on the back wall of the cavity. The engineering model accurately described the broadband cavity acoustics at subsonic Mach numbers, but did not match wind tunnel data as well at supersonic conditions. Bauer and Dix also determined a correlation for Rossiter's phase shift constant that accounted for the effects of Mach number in addition to the cavity L/D geometry. However, Rossiter's original phase constant is generally used in the literature despite Bauer and Dix's successful definition.

Furthermore, Bauer and Dix distinguish between the Rossiter edge-tones, and the fundamental acoustic tones of the cavity. Bauer showed that a theoretical model for the cavity acoustics can be developed by assuming the cavity behaves like an open organ pipe in which the maximum pressure occurs at both ends. Bauer then shows that the fundamental relationship for wave motion results in frequency estimates of

$$f_L = \frac{a_t}{2L},$$

$$f_W = \frac{a_t}{2W},$$

$$f_D = \frac{a_t}{4D},$$

where a_t is the speed of sound in the cavity, and the three frequencies are for the natural acoustic modes of the length (*L*), width (*W*), and depth (*D*).

Similar results were obtained by Rona (Rona, 2007). Rona investigated acoustic resonance in rectangular and cylindrical cavities by analytically solving the acoustic wave equation. The solid walls of the cavity were modeled as no-slip boundary conditions and an acoustic reflecting boundary condition was imposed at the open end of the cavity. A general solution was obtained by assuming the solutions were functions of orthogonal Fourier series. The resulting Strouhal numbers for the length (*L*), width (*W*) and depth (*D*) modes was shown to be

$$St_{l,m,n} = \frac{f_{l,m,n}L}{U_\infty} = \frac{\left(1 + \frac{\gamma - 1}{2} M_\infty^2\right)^{1/2}}{M_\infty} \left[\left(\frac{l}{2}\right)^2 + \left(\frac{m}{2}\frac{L}{W}\right)^2 + \left(\frac{n}{2}\frac{L}{D}\right)^2 \right]^{1/2}, \quad (51)$$

where *n,m,l* are the integer mode numbers of the length, width, and depth modes. Rona claimed that "The necessary condition for a Rossiter mode to be reinforced by the cavity acoustic resonance is that the Strouhal number of a cavity acoustic resonance mode matches one component of the harmonic series of any Rossiter mode, that is $St_{l,m,n} = oSt_h$, where *o* is an arbitrary integer". The arbitrary integer, *o*, indicates harmonics of the Rossiter mode. Rona's conclusion is that the natural acoustic modes of the cavity couple with the Rossiter edge-tones to create cavity resonances. These assertions were studied in detail using the experimental data obtained in this research.

Turbulence

There is no single theory of turbulence that can predict the behavior of turbulent flows. In fact, it is difficult to provide a succinct and accurate definition of turbulence even though most flows of interest are turbulent or become turbulent at high Reynolds numbers. Turbulence can be present in compressible or incompressible flows. It can manifest as large-coherent structures that are convected with the flow or micro-scale eddies that appear to behave randomly – all in the same flow field. Most fluid flows naturally become turbulent; laminar flows are the exception to nature. Flows can transition to turbulence in two different ways (Davidson, 2015):

- Instabilities in laminar boundary layers are naturally amplified until small regions of turbulent motion appear. The turbulent patches grow until the flow becomes fully turbulent.
- The flow is perturbed to an unstable state at which point turbulence develops uniformly throughout the fluid.

Fluid flows are generally unstable meaning that once perturbed, they do not return to their original state. Studies have shown that at the beginning of laminar-to-turbulent transition, the localized turbulent spots contain cross-stream components of fluctuating velocity (White, 1991) indicating that transition to turbulence, and turbulence itself, is a highly three-dimensional phenomenon.

Characteristics of Turbulence

Since there is no rigorous definition of turbulence, and certainly no exact theory, turbulence is best described by some common characteristics (Davidson, 2015; Tennekes & Lumley, 1972) such as:

- the velocity field fluctuates randomly in time, is highly distorted and irregular
- the velocity field exhibits a wide range of length scales
- the velocity field is unstable such that a minor change to initial conditions will lead to substantial changes in the fluid motion
- velocity fluctuations are rapidly spread throughout the fluid, i.e. the turbulence is diffusive
- the Reynolds number is high
- elevated levels of fluctuating vorticity are present in the flow, and
- turbulent flows are dissipative, requiring continuous supply of energy to prevent rapid dissipation.

Turbulence is not a property of the fluid such as density or viscosity. Turbulence is a characteristic state of a fluid flow. Flows are turbulent, laminar, or transitional, and the flow state is determined

by the Reynolds number. Higher Reynolds numbers are almost always turbulent. As will be shown later, the length, time, and velocity scales associated with turbulence are dependent upon the Reynolds number. As the Reynolds number increases, the difference between the largest scales and the smallest scales becomes larger (Tennekes & Lumley, 1972). (A turbulent jet at relatively low Reynolds number has various large and small scale turbulent structures, but a similar turbulent jet at a very high Reynolds number contains much smaller-scale turbulence.) Most turbulent flows have an asymptotic limit to the size of the smallest-scale, turbulent structures at high Reynolds numbers.

There are many ways that turbulence has been described. Davidson uses the term "eddy" to define a turbulent structure and defines an "eddy" as a fluid element containing vorticity (Davidson, 2015). Tennekes only provides characteristics of turbulence, but notes that "turbulence is rotational and three-dimensional" and "turbulent flows always exhibit elevated levels of fluctuating vorticity" (Tennekes & Lumley, 1972). White also describes turbulence by its characteristics such as "fluctuations in velocity and pressure", "eddies or fluid packets that intermingle", or "coherent structures" (White, 1991). White does not directly tie turbulence to vorticity, but since vorticity is defined by the curl of the velocity field, a spatially fluctuating velocity field would also result in fluctuating vorticity satisfying White's definition of turbulence being equivalent to fluctuating velocity. At any rate, vorticity appears to be fundamental to the idea of turbulence.

As shear forces perform work on the fluid, vorticity is generated in the fluid and turbulent structures are formed from "large-scale, coherent" to small-scale sizes. These turbulent structures are rotational (having vorticity), are convected with the flow, and are diffused by viscosity. If the turbulent structures are large enough, e.g. the Reynolds number based on the eddy length scale is large, then the viscous forces working on the large-scale structures is insignificant compared to the inertia of the turbulent structure. These large structures can persist, being convected through the flow and entraining fluid, or can be broken up in to smaller eddies by inertial and viscous instabilities. Eventually, the smallest structures are created at boundaries or break-down from larger structures by instability driven forces. The break-down process continues until the length scale of the smallest eddies is small enough that viscous stresses become significant. Once the length scale is small enough viscosity "smears-out" (dissipates) the small eddies and their turbulent kinetic energy is transformed into heat. This "energy cascade" was first introduced by Richardson and later expanded upon by Kolmogorov (Davidson, 2015).

Length scales can be categorized as diffusive (viscous), η, or convective (inertial), ℓ (Tennekes & Lumley, 1972). In boundary layer flows, the diffusive length scale is a transverse length scale representing the diffusion of momentum loss across the boundary layer and the upper bound for large turbulent eddy size in the boundary layer. The convective length scale is the stream-wise scale representing the length that turbulent structures are convected with the flow. Assuming that Reynolds number is proportional to the ratio of these two length scales, we see that as η becomes small or ℓ becomes large, the ratio ℓ/η becomes large which is the expected result for thin boundary layers at high Reynolds number. At high enough Reynolds numbers, the large turbulent eddies transfer momentum deficit away from the boundary because of the diffusivity characteristic of turbulence.

The smaller turbulent eddies get smeared out by viscosity. Viscous terms in the governing equations prevent the generation of infinitely small eddies in the energy cascade by dissipating the small-scale energy into heat (Tennekes & Lumley, 1972). Furthermore, small-scale eddies have small time scales which become increasingly more independent of the large-scale turbulence and the mean flow. Therefore, the net energy in small-scale motion depends only upon the energy provided by the breakdown of the large-scale eddies and the energy converted into heat by viscous dissipation (Tennekes & Lumley, 1972). This is Kolmogorov's universal equilibrium theory.

Equations for Turbulent Flow

First, the Reynolds decomposition is used to define the mean velocity (U_i), the turbulent fluctuating velocity (u_i') and the total velocity vector (u_i). Bold text indicates vector quantities, and indices represent principal directions.

$$\mathrm{u_i} = \mathrm{U_i} + \mathrm{u_i}' \tag{52}$$

Substituting the Reynolds decomposition into the Navier-Stokes equations results in the governing equations for turbulent flow. Note that the governing equations for turbulent flow are the same as the governing equations for laminar flow with the only difference being how the velocity term is defined.

Continuity
$$\nabla \cdot (\rho \mathbf{u}) = 0 \tag{53}$$

Momentum
$$\rho \frac{\partial \mathrm{u_i}}{\partial \mathrm{t}} + \rho(\mathbf{u} \cdot \nabla)\mathrm{u_i} = -\frac{\partial \mathrm{P}}{\partial \mathrm{x_i}} + \frac{\partial \tau_{\mathrm{ij}}}{\partial \mathrm{x_j}} \tag{54}$$

The stress term (τ_{ij}) in the momentum equations is shown in equation (55) where the S_{ij} term is the rate of strain tensor. The diagonal terms of τ_{ij} are normal stresses, or pressures, and the off-diagonal terms are shear stresses.

$$\tau_{\mathrm{ij}} = 2\mu \mathrm{S_{ij}} = \mu \left[\frac{\partial \mathrm{u_i}}{\partial \mathrm{x_j}} + \frac{\partial \mathrm{u_j}}{\partial \mathrm{x_i}} \right] \tag{55}$$

The time average of the velocity components gives the mean-value of the fluctuating total velocity, is denoted by an overbar, and is defined by equation (56). The time-averaged value of the fluctuating component, u_i', is zero by-definition. In practice, it is not possible to sample turbulent flow fields for an infinite amount of time, and a finite time duration is used to time-average turbulent quantities.

$$\overline{\mathrm{u_i}} = \mathrm{U_i} = \lim_{\mathrm{T}\to\infty} \frac{1}{\mathrm{T}} \int_{\mathrm{t0}}^{\mathrm{to+T}} \mathrm{u_i}\, \mathrm{dt} \tag{56}$$

Time averaging the momentum equation results in an equation for the mean velocity and pressure fields, equation (57).

$$\rho(\overline{\mathbf{u}} \cdot \nabla)\overline{\mathrm{u_i}} = -\frac{\partial \overline{\mathrm{P}}}{\partial \mathrm{x_i}} + \frac{\partial}{\partial \mathrm{x_j}} \left[\tau_{\mathrm{ij}} - \rho \overline{\mathrm{u_i}' \mathrm{u_j}'} \right] \tag{57}$$

The additional stress term $-\rho\overline{u_i' u_j'}$ is a result of the non-linear product $(\mathbf{u}\cdot\nabla)u_i$, which couples the mean flow to the turbulent fluctuations. The additional $-\rho\overline{u_i' u_j'}$ terms are called the Reynolds stresses and are often denoted as τ_{ij}^R. Averages of products of quantities, such as the Reynolds stresses, are generally called correlated terms if they are non-zero or uncorrelated if they are zero.

Furthermore, time averaging the continuity equation results in two distinct continuity equations, one for the mean velocity field and one for the turbulent fluctuating velocity field. This indicates that turbulence obeys the law of mass conservation for incompressible flow. When considering compressible flow, the density fluctuations must also be accounted for and the $\rho\overline{u_i' u_j'}$ term would couple the continuity equations for mean and fluctuating terms (White, 1991). The Reynolds stresses are an additional set of unknowns that must be solved in addition to the field variables. However, no new equations have been formulated that can be used to provide solutions for the new Reynolds stresses. This is called the closure problem for turbulent flows.

Turbulence Closure Problem

The Reynolds stresses resulting from the time average of the Navier-Stokes equations are interesting because they couple the mean flow and the turbulent fluctuations. However, the Reynolds stress tensor introduces a new set of unknowns into the system of equations for fluid motion. The Reynolds stress tensor is symmetric about the diagonal, and therefore, there are 6 unique unknowns that must be solved in addition to the pressure and velocity field. This is typically called the "turbulence closure problem" for which there is no general solution in existence today. Many researches have attempted, with varying levels of success, to close the turbulence problem by estimating the Reynolds stresses. Prandtl devised the earliest attempt at closing turbulence using the mixing length model. Prandtl developed an analogy to the kinetic theory of gasses for packets of turbulent fluid. Prandtl theorized that packets of turbulent fluid exchanged momentum between different layers of fluid and this momentum exchange was a function of the convective velocity and a mixing length scale. This theory might be sufficient for a flow in which a single length scale exists, but fails to account for the multiple length (or velocity) scales that are always present in turbulent flow (Tennekes & Lumley, 1972). Turbulence models have improved significantly since Prandtl's work, but still fall short of closing the turbulence problem.

Scales in Turbulence

The sizes of turbulent structures in high-Reynolds number flow vary dramatically from the large-scale structures produced by the mean flow (of size ℓ) to the smallest-scale structure that can withstand viscous dissipation (of size η). The largest scale, ℓ, is often called the integral scale and represents turbulent structures that are driven primarily by inertial instabilities and the extent of the region over which velocities are correlated (Davidson, 2015). Let u and v be the velocity quantities associated with the large- and small-scale structures, respectively. The large structures created by inertial instabilities in the mean flow break down into smaller-scale turbulent structures passing their energy in the process. The new smaller-scale turbulent structures eventually break down into smaller structures, and so on, until the scale of the turbulent structure is small enough that viscosity become significant compared to the length scale of the turbulent structure. At this point, viscosity converts the turbulence into heat. This "cascade" of energy was first theorized by Richardson.

A turbulent structure breaks down over a span of time on the order of ℓ/u which is called the turnover time which provides a frequency associated with the integral length scale. If statistically stationary processes are considered, then the energy transferred down from the large scales, ℓ, must equal the energy dissipated by viscosity at the smallest scales, η. The energy transferred from the largest scales is

$$u^2/_{(\ell/u)} = u^3/_{\ell} = \epsilon\,, \tag{58}$$

and the energy dissipated by viscosity is

$$\nu\ v^2/_{\eta^2}\,. \tag{59}$$

The Reynolds number based on the smallest length scale is

$$v\eta/_{\nu} \sim 1, \tag{60}$$

where v and η are the Kolmogorov microscales of turbulence. Combining the microscales and the integral scale results in the following useful relations:

Length scale $$\eta \sim \ell\ Re^{-3/4} \tag{61}$$

Velocity scale $$v \sim u\ Re^{-1/4} \tag{62}$$

Time scale $$\tau \sim \frac{\ell}{u} Re^{-1/2}\,. \tag{63}$$

These relations provide an estimate of the smallest scale and velocity of turbulence as a function of the largest-scale Reynolds number. To put these relations into perspective, the UTSI transonic blow down wind tunnel operating at Mach 0.53 with a cavity of length L=0.75-inches in the floor of the test section has smallest-scale structures on the order of 6.2e-5 inches and turnover times on the order of 2e-7 seconds! Measuring the turbulent structures down to the Kolmogorov scale would require data-acquisition sample rates on the order of 5 MHz, which introduces significant data acquisition and storage difficulties. Furthermore, CFD simulations attempting to capture turbulent structures at the Kolmogorov scale would require maximum grid sizes less than 6.2e-5 inches.

These relations also provide insight into an important trend in turbulence. As Reynolds number is increased, the turbulence becomes finer and finer containing structures with smaller length scales. Furthermore, it turns out that the relations provided above are somewhat general in nature and apply to many types of turbulent flows such as wakes, jets, shear layers, and boundary layers. Kolmogorov suggested that there is a part of the energy cascade spectrum where there is statistical, universal equilibrium for which all turbulent flows should have similar energy transfer trends from larger to smaller structures.

A plot of the microscales as a function of the Reynolds number is shown in Figure 6. Here, the Reynolds number dependence of the smallest turbulent length, velocity, and time scales is shown. The microscales are shown normalized by the largest length, velocity, and time scales. As Reynolds number increases, the microscales approach an asymptotic limit. As Reynolds number increases, the difference between the large scales and the smaller scales becomes larger, until the

turbulence becomes so small that viscosity converts the kinetic energy into heat preventing further reduction in turbulence scales and resulting in the asymptotic limit shown in the figure.

The classical interpretation of Reynolds number is the ratio of inertial forces to viscous forces. This definition serves the purpose for undergraduate definitions, but Tennekes (Tennekes & Lumley, 1972) provides an alternate understanding of the role Reynolds number has in analysis of turbulence. Tennekes shows using dimensional analysis with the characteristic length and velocity that the Reynolds number can also be interpreted as the "ratio of a turbulence time or length scale to a diffusive time or length scale that would prevail in the absence of turbulence in a problem with the same time or length scale". For example, from Tennekes (Tennekes & Lumley, 1972), the equation for heat diffusion is

$$\frac{\partial \mathrm{T}}{\partial \mathrm{t}} = \alpha \frac{\partial^2 \mathrm{T}}{\partial \mathrm{x_i}\, \partial \mathrm{x_i}}.$$

Using dimensional analysis, the equation can be written as

$$\frac{\Delta \mathrm{T}}{\mathrm{t_d}} \sim \alpha \frac{\Delta \mathrm{T}}{\mathrm{L}^2},$$

or,

$$\mathrm{t_d} \sim \frac{\mathrm{L}^2}{\alpha},$$

where t_d is the time scale of diffusion. The time scale associated with large-scale turbulent fluid in motion, with characteristic velocity u, can be estimated by assuming the diffusivity can be replaced by an "eddy viscosity", K, which is of the order $K \sim uL$. The resulting time scale is,

$$\mathrm{t_t} = \frac{\mathrm{L}}{\mathrm{u}}.$$

The ratio of these time scales is,

$$\frac{\mathrm{t_t}}{\mathrm{t_d}} \sim \frac{\mathrm{L}}{\mathrm{u}} \frac{\alpha}{\mathrm{L}^2} = \frac{\alpha}{\mathrm{uL}}.$$

Furthermore, the Prandtl number for air is approximately unity and is the ratio of viscosity to diffusivity is,

$$\mathrm{Pr} = \frac{\nu}{\alpha} \sim 1.$$

Substituting the viscosity for the diffusivity results in,

$$\frac{\mathrm{t_t}}{\mathrm{t_d}} \sim \frac{\nu}{\mathrm{uL}} = \frac{1}{\mathrm{Re}},$$

which shows that for a given length scale, the ratio of a turbulence time scale to the diffusive time scale is proportional to the inverse of Reynolds number.

Conversely, the same logic can be applied to fluid motion with a fixed time scale and different length scales. Again, from Tennekes (Tennekes & Lumley, 1972), consider a laminar boundary

layer in which the length scale for diffusion can be determined from dimensional analysis of the diffusion equation and assuming the Prandtl number is ~1 so that $\alpha \sim \nu$,

$$L_d^2 \sim \nu t\,.$$

Like the previous example, the turbulent length scale is estimated using the eddy viscosity, K, resulting in the estimate,

$$L_t \sim u t\,.$$

Again, taking the ratio of these length scales results in an expression proportional to the Reynolds number,

$$\frac{L_t}{L_d} \sim \frac{u}{(\nu t)^{1/2}} = \left(\frac{u}{t\ell}\mathrm{Re}\right)^{1/2} = f\left(\mathrm{Re}^{\frac{1}{2}}\right),$$

where the function, *f*, is often observed empirically. For simple flows, this interpretation of Reynolds number is sufficient and complete. However, the more general turbulent flows encountered in most flows of interest contain multiple length scales, e.g. large eddy sizes are limited by the bounds of the flow field and small eddy sizes are bounded by the viscosity that they can withstand.

Comparing the large-scale turnover time, ℓ/u, to the small-scale turnover time, η/v, the small-scale time is much faster (e.g. a higher rate), and hence, more energetic than the large-scale turnover time. This is an indication that vorticity is concentrated in the small-scale turbulent structures. Furthermore, as small-scale turbulence is dissipated into heat, new small-scale turbulence must be generated from vorticity production at boundaries or from breakdown of large-scale structures. Otherwise, the turbulence would not be self-sustaining. Energy must be continually cascaded to the small-scale structures from larger structures to sustain the turbulence. This indicates that most of the kinetic energy in the flow is contained in large-scale structures while most of the vorticity in the flow is contained in small-scale structures (Tennekes & Lumley, 1972).

Turbulent Boundary Layers

Some characteristics of the turbulent boundary layer are, per White (White, 1991):

- three-dimensional pressure and velocity fluctuations,
- eddies of size from approximately the shear layer thickness to the Kolmogorov length scale that fill the shear layer,
- self-sustaining production of new turbulent eddies not related to the original instability mechanisms such as T-S waves, and
- stronger mixing than laminar flow caused by entrainment of the outer flow by the turbulent eddies. The mixing mechanism greatly enhances heat transfer, mass transfer, and friction.

For non-bounded regions, such as free-shear layers and the edge of the boundary layer, turbulent eddies may entrain fluid from outside the shear layer which may cause large coherent structures.

The turbulent inertia tensor term is always significant for turbulent flow. The components of the turbulent inertia tensor have been measured experimentally in the past (Klebanoff, 1955). Several observations from this experimental data will help understanding of how turbulent behavior might be controlled.

Because of the no-slip boundary condition at the wall, all velocity components should go to zero. The no-slip condition is clearly observed in typical turbulent velocity profiles, but the turbulent velocity fluctuations have significant non-zero values in the near-wall region. This indicates that the fluctuating velocity components have a steep slope near the wall. Compared to the mean flow profile, all three components of the turbulent fluctuations are large near the wall and resist the no-slip condition. For control purposes, this means that vorticity is introduced in the presence of surfaces because of the large velocity gradients. Furthermore, turbulent fluctuations are highest near the wall and using small perturbations for turbulence control in the free-stream flow would be much less efficient than introducing the same small perturbations near the wall.

Secondly, the turbulent fluctuations extend outside of the mean-flow boundary layer where $y/\delta \sim 1$. This region is commonly known as the superlayer and is the interface between the turbulent and nonturbulent fluids. This superlayer is the mechanism that drives the mixing of the two types of flows by the entrainment of the outer layer with the inner turbulent layer and the dissipation of turbulent eddies in the outer layer.

Finally, outside of $y/\delta \sim 0.8$, the fluctuating components, (u', v', w'), become equal and isotropic, or invariant with respect to direction. However, near the wall, the values of the fluctuating components are very different, or anisotropic and this "is the region where most of the production and dissipation of turbulence energy takes place" (White, 1991).

Relating Pressure Fluctuations to Velocity Fluctuations

Turbulence is often described as local fluctuations in velocity. In fact, as was previously shown, when the Reynolds decomposition is used to write the velocity in terms of mean and fluctuating components, the resulting Reynolds stress tensor is defined in terms of the fluctuating velocity components. Since there is no theory of turbulence, turbulence is often studied experimentally and measurements of fluctuating velocity components are measured using hot wire anemometry. The effect of turbulence can also be observed in high-response pressure instrumentation. When static pressure ports or total pressure probes can be sampled at a high enough rate, the instantaneous pressure fluctuations caused by turbulence can be observed. The question then becomes, how does a fluctuating pressure measurement relate to fluctuating velocity?

Liepmann and Roshko (Liepmann & Roshko, 1993) derive useful equations that provide some insight. If the continuity equation (1) is multiplied by the total energy quantity, which is the sum of internal energy and kinetic energy,

$$\left(\mathrm{e} + \frac{1}{2}\mathrm{u}^2\right),$$

and this term is subtracted from the energy equation (3), then the following energy equation results,

$$\frac{\mathrm{D}}{\mathrm{Dt}}\left(\frac{\mathrm{P}}{\rho}\right) + \frac{\mathrm{De}}{\mathrm{Dt}} + \frac{\mathrm{D}}{\mathrm{Dt}}\left(\frac{1}{2}\mathrm{u}^2\right) = \mathrm{q} + \boldsymbol{Fu} + \frac{1}{\rho}\frac{\partial \mathrm{P}}{\partial \mathrm{t}}.$$

Substituting the enthalpy,

$$\mathrm{h} = \mathrm{e} + \frac{\mathrm{P}}{\rho},$$

into the new energy equation results in a relation between the enthalpy, the heat transfer (q), the body forces (Fu), and the pressure (P) as shown in equation (64).

$$\frac{\mathrm{D}}{\mathrm{Dt}}\left(\mathrm{h}+\frac{1}{2}\mathrm{u}^2\right)=\mathrm{q}+\boldsymbol{Fu}+\frac{1}{\rho}\frac{\partial \mathrm{P}}{\partial \mathrm{t}} \tag{64}$$

Expanding the terms, assuming there is no heat transfer, and body forces are negligible, equation (64) can be re-written as

$$\frac{\partial \mathrm{h}}{\partial \mathrm{t}}+\boldsymbol{u}\cdot\nabla\left(\mathrm{h}+\frac{1}{2}\mathrm{u}^2\right)+\frac{1}{2}\frac{\partial \mathrm{u}^2}{\partial \mathrm{t}}=\frac{1}{\rho}\frac{\partial \mathrm{P}}{\partial \mathrm{t}}. \tag{65}$$

This equation shows an interesting relation between the time rate of change of pressure and the time rate of change of the square of velocity. If the Reynolds decomposition is used, and conditions are assumed to be stationary, i.e. no variation in the mean, then the time rate-of-change of velocity squared and the time rate of change of pressure represent the fluctuating components. Therefore, the fluctuating pressure is proportional to the square of the fluctuating velocity. This type of relationship has been proposed by other researchers also. Komerath (Komerath, Hegde, & Strahle, 1985) studied the relationship between fluctuating velocity and pressure in turbulent jets and proposed that, away from boundaries, the proportionality was,

$$\mathrm{P}'\sim\rho|\mathrm{U}|\mathrm{u}',$$

where U is the mean velocity. Tsai (Tsai & Yang, 1993) studied the correlation between fluctuating velocity and pressure in the wake of a two-dimensional v-gutter. He proposed that, outside of the recirculation zone, the correlation for wakes should be written as

$$\mathrm{P}'=\mathrm{C}\rho(|\mathrm{U}\mathrm{u}'|+|\mathrm{V}\mathrm{v}'|+\mathrm{u}'^2+\mathrm{v}'^2),$$

where C is a constant between 0.085 to 0.1. These results are consistent with the order-of-magnitude proportionality derived from the Liepmann and Roshko equations.

Turbulence Models

A full description of turbulence and modeling is beyond the scope of this paper, but some basic descriptions are presented here for better understanding of the difficulties associated with computational turbulence modeling.

Since there is no theory leading to the full prediction of turbulent flows, we are forced to study turbulence experimentally and model it in our use. There have been many turbulence models and new models are being developed every year. Turbulence models can be separated into one of three classes, each with advantages and disadvantages.

The first class of turbulence modeling is the zero-, one-, and two-equation models. The zero-equation models assume the turbulence can be modeled as an eddy viscosity or a mixing length and are the simplest turbulence models, but least accurate. One-equation models such as the Spalart-Allmaras model are popular for their ability to model turbulent cavity and shear-layer flows. Two-equation models such as the k-ε or k-ω models consider not only the turbulent kinetic energy (k), but also the rate of change of dissipation (ε), turbulence length scale (L) or the ratio of dissipation to turbulent kinetic energy (ω). The two equation models and the Spalart-Allmaras one-equation model are the most popular, and many variations and improvements have been made to

these models over the years. These models are often used for Reynolds-Averaged Navier Stokes (RANS) simulations. These approaches do not model small scale turbulence in boundary layers that could excite boundary layer instability. However, simple one- or two-equation turbulence models are computationally more efficient than the next two classes of models.

The second type of turbulence model is the Large-Eddy Simulation, or LES. LES can model smaller scale turbulent structures, but requires significantly more grid points and much smaller time scales to capture these effects. LES simulations are typically only performed on simple geometries because of the computational cost.

Finally, the third class of turbulence modeling is the Direct Numerical Simulation (DNS) which directly solves the turbulent Navier-Stokes equations without modeling. DNS simulations require an even larger amount of grid points to achieve the resolution required to capture the smallest perturbations in the flow that lead to turbulence. DNS solutions are reserved only to the simplest of problems (such as flat plate flows) on the largest supercomputers available at the time of this writing.

One-Dimensional and Quasi-One-Dimensional Flow Equations

The one-dimensional isentropic equations are some of the most useful equations in gas dynamic theory. These equations are often used to determine the bulk flow properties in internal and external flows where compressibility is of concern. These equations are only valid for isentropic and ideal gas flows. The isentropic equations are most useful for purely one-dimensional flow, but are applicable to quasi-one-dimensional flow where the area change is not drastic. Often, the lateral and cross-stream flow components can be ignored if they are small enough and two-dimensional or even some three-dimensional flows can be approximated well with the isentropic equations. The isentropic equations do not account for boundary layers, but are often used to estimate free-stream properties in external flows or centerline properties for internal flow. The isentropic equations will be used to determine flow quantities in the wind tunnel experiments in this research.

The isentropic flow equations are presented here without derivation. Derivations can be readily found in undergraduate text books, see (Liepmann & Roshko, 1993). Assume the working fluid is a perfect gas with constant specific heats and is adiabatic. Further assume that the flow is steady and inviscid in the free stream. The temperature, pressure and density can be related to Mach number by,

$$\frac{T_t}{T} = 1 + \frac{\gamma - 1}{2} M^2 \tag{66}$$

$$\frac{P_t}{P} = \left(1 + \frac{\gamma - 1}{2} M^2\right)^{\gamma/(\gamma-1)} \tag{67}$$

$$\frac{\rho_t}{\rho} = \left(1 + \frac{\gamma - 1}{2} M^2\right)^{1/(\gamma-1)}, \tag{68}$$

where the *t* subscripts denote the total conditions in which the flow is decelerated isentropically to rest. The mass flow rate through any one-dimensional cross section is given by the mass flow function,

$$\frac{\dot{m}\sqrt{T_t}}{AP_t}\sqrt{\frac{R}{\gamma}} = M\left(1+\frac{\gamma-1}{2}M^2\right)^{-\frac{\gamma+1}{2(\gamma-1)}}, \tag{69}$$

which conveniently expresses the mass flow through the system as a non-dimensional function of Mach number. A convenient reference condition is the sonic condition in which the flow is choked at the minimum area point. The sonic conditions are often written with a superscript *.

$$\frac{\dot{m}^*\sqrt{T_t}}{AP_t}\sqrt{\frac{R}{\gamma}} = \left(\frac{\gamma+1}{2}\right)^{-\frac{\gamma+1}{2(\gamma-1)}} \tag{70}$$

These equations provide a convenient way to express the Mach number of the flow relative to the cross-sectional area in the flow by taking the ratio of the two mass flow functions,

$$\frac{A}{A^*} = \frac{1}{M}\left(\frac{\gamma+1}{2}\right)^{-\frac{\gamma+1}{2(\gamma-1)}}\left(1+\frac{\gamma-1}{2}M^2\right)^{-\frac{\gamma+1}{2(\gamma-1)}}. \tag{71}$$

Sometimes, the flow variables are known and the Mach number is desired. For example, a Pitot-static probe in a wind tunnel measures total pressure and static pressure from which the Mach number can be calculated. Inverting the isentropic equation for pressure ratio results in equation (72).

$$M = \sqrt{\left[\left(\frac{P_t}{P}\right)^{\frac{\gamma-1}{\gamma}} - 1\right]\frac{2}{\gamma-1}} \tag{72}$$

Coupled Piezoelectric Equations

Piezoelectric materials are characterized by the basic relationships shown in equation (73) where *D* is the electric flux density, or dielectric displacement, *T* is the mechanical stress, *E* is the electric field, *S* is the mechanical strain or elastic deformation, *d* is the piezoelectric charge coefficient, ε^T is the dielectric permittivity for constant *T*, and s^E is the elastic coefficient for constant *E*.

$$\begin{aligned} D &= dT + \varepsilon^T E \\ S &= s^E T + dE \end{aligned} \tag{73}$$

These equations contain an inherent assumption that small electrical and mechanical inputs exist. Each of the terms in the equations are matrices, and are dependent on the coordinate system.

From (Hudec, 2013), the *s* matrix is related to the compliance of the material and the product *sT* is Hooke's stress law. The permittivity, *ε*, permits electric field behavior in dielectrics and a high value causes high electric flux in the material. The piezo electric charge coefficient, *d*, provides an indication of the strength of the piezoelectric effect of the material.

These equations may be easily solved analytically for a simple one-dimensional beam (Burke & Hubbard, 1987; Hudec, 2013), but more complex methods (Huang & Hu, 2013; Sullivan, Hubbard, & Burke, 1996) are needed for two-dimensional shapes such as the triangular or wedge shapes of interest in the present research. However, a simple math model was developed during the actuator

design phase of this research that can be used for any similarly shaped bi-morph actuator (this is discussed in a following chapter).

The simplest bimorph actuator is a cantilever beam with two layers of the same piezoelectric material such as shown in Figure 7. When a voltage is applied in series across the one-dimensional actuator, the coupled equations reduce to equation (74) (Shi, 2013).

$$\delta X = \frac{3L^2 V d_{31}}{2T^2} \tag{74}$$

The static tip deflection is given by δX and is only a function of the length of the beam, the voltage applied, the piezoelectric material properties, and the thickness of the beam. Although this equation only applies to the simplest of actuators, it can provide insight into important parameters that change the actuator response.

CHAPTER FOUR ACTUATOR DESIGN AND BENCH TEST

Introduction

This chapter describes the processes and test procedures that were used to design, fabricate, test, and apply the novel flow actuators. Actuator design and bench testing are covered in the first section. Test design is covered in the second section.

Actuator Design

Actuator shape and geometry were designed with the objective of obtaining 0.039 inches (1 mm) of tip deflection when driven near 1kHz frequency. This design point was selected to ensure there was enough tip deflection to interact with the viscous sub-layer and there was sufficient frequency range to drive the actuator at frequencies that would couple/interfere with natural flow frequencies such as with cavity tones or shedding frequencies.

Geometry was perturbed around the design point to determine how the tip deflection and natural frequency of the device scaled with geometry. The designs were bench tested in quiescent air so that the natural frequencies (modes) and tip deflection amplitude could be measured.

Actuator designs started with simple, rectangular, cantilever beams. An actuator similar to Blackwelder's design (Blackwelder et al., 1998), which uses bimorph layers with a triangular substrate, was manufactured to provide a reference point and control case. The triangular, bimorph actuator was then miniaturized and scaling relationships were developed. Several perturbations of the triangular substrate design were also studied. Details on the actuator design and test process are presented in the following sections.

Test Articles

All actuator test articles were manufactured from a piece of PZT5H4E sheet stock purchased from Piezo Systems, Inc. The piezoelectric material was 0.00752 inches (0.191 mm) thick with properties shown in Table 1. The piezoelectric shapes were manufactured by carefully cutting the material with light pressure using a razor blade along a straight edge positioned over the piezoelectric material. The material broke along the cut after 4 or 5 passes with a sharp razor. A schematic of a generic actuator and the important dimensions are shown in Figure 8.

Several single-crystal, unimorph, and bimorph designs were bench tested. The single-crystal designs are shown in Figure 9. All single-crystal test articles did not produce significant tip deflection, but could be driven in the 1kHz frequency range. The single-crystal test article designs were not studied further.

Unimorph actuators (Figure 10) were fabricated by bonding the single-crystal shapes to a flexible piece of shim steel of 0.003 inches thickness. The bond was created using electrically conductive superglue. The substrate added significant robustness to the actuator, but the actuator did not produce significant tip deflection. Furthermore, since the piezoelectric material was attached at the active end of the actuator, wire was required to run the length of the actuator to supply driving voltage to the piezoelectric material. The wires added to the stiffness of the actuator system and damped some of the oscillations produced by the active piezoelectric material. Therefore, the unimorph designs shown in Figure 10 were also abandoned.

Table 1. PZT5H4E Properties. Table reproduced from (PiezoTechnology, 2014).

Description	Symbol	Units	Value
Piezo Systems' Designation			PSI-5H4E
Industry Designations			Navy type VI, Industry Type 5H
Composition			Lead Zirconate Titanate (PZT)
Relative Dielectric Constant	$\boldsymbol{K_3^T}$		3800
"d" coefficients relate Strain Produced / Electric Field Applied	d_{33}	m/V	650 x 10^{-12}
	d_{31}	m/V	-320x10^{-12}
"g" coefficients relate Electric Field Produced / Stress Applied	g_{33}	V-m/N	19x10^{-3}
	g_{31}	V-m/N	-9.5x10^{-3}
Coupling Coefficients	k_{33}	ND	0.75
	k_{31}	ND	0.44
Density	ρ	kg/m^3	7800
Mechanical *Q*	*Q*	ND	30
Elastic Modulus	$\boldsymbol{Y_3^E}$	N/m^2	5.0x10^{10}
	$\boldsymbol{Y_1^E}$	N/m^2	6.2x10^{10}
Thermal Expansion Coefficient	β	m/m-K	3x10^{-6}
Curie Temperature		K	503

Several bimorph actuators were developed (Figure 11) that leveraged the bimorph concept with the flexible substrate like Blackwelder's design. These actuators produced a wide range of tip deflections and frequency ranges depending on the size/shape. Multiple variations were bench tested to arrive at the final test articles that were used as flow actuators.

A variation of the bimorph actuator was designed to provide additional tuning of the tip amplitude and resonant frequency. An example of the tunable actuator is shown in Figure 12. These tunable actuators were designed so that the clamping position could be varied producing a range of desired tip deflections. Lowering the clamping position on the device resulted in lower tip amplitudes for the 1st natural mode. Insignificant changes were observed in the 1st mode frequency when the clamping position was changed. Clamping the actuator below the piezoelectric material resulted in a need to run wires up the length of the unclamped substrate to the piezoelectric material. It is suspected that the 32-gauge wires provided significant damping to the test article during the bench test which contributes to the lack of trend in 1st mode resonant frequency with clamping position. Further design work would need to be accomplished to alleviate this wire damping effect.

Actuator Bench Tests

A simple bench test was devised to test the natural frequencies and tip deflections of the actuators for various driving frequencies and voltages. Each actuator test article was clamped in a bench vice and a laser was pointed at the tip of the actuator. Since the material used for the flapper mechanism was shim steel, the laser was reflected off the actuator and onto an observation surface where the vibration modes could be observed when the actuator was being driven. An example bench-test setup is shown in Figure 13.

Small movements of the actuator tip were amplified by the laser reflecting onto the observation surface making actuator vibration qualitatively observable. The driving voltage was set to a constant value (typically 21.6 VRMS) and the frequency was swept from 1 Hz to 10 kHz. As the frequency was increased, the laser reflection moved with the actuator vibration. As the frequency was increased to the natural frequencies of the actuator, the natural modes could easily be identified by the laser reflection. As the natural frequency was achieved, the amplitude and shape of the laser reflection changed dramatically. Natural mode frequencies were hand-recorded as the frequency sweep was accomplished. Actuator tip deflection was measured using a millimeter ruler at the natural frequencies where the tip deflection was visible (typically only the first mode). Actuator tip deflection was observed using the laser at all driving frequencies, regardless of whether the actuators were operating near resonance or the motion could be observed visually.

Driving signals for the piezo-actuators were generated using a Wavetek Model 180 function generator and a linear amplifier. The linear amplifier was purchased from Piezo Systems Inc. and had a maximum voltage output of +/- 200 volts with a frequency range from DC to 250 kHz. Leads were attached from the linear amplifier to the piezoelectric material on the actuator. For the bench-test only, the leads were attached to the piezoelectric material using electrical tape to facilitate rapid construction and testing of multiple designs. Once final designs had been selected for further wind tunnel testing, 32-gage wire leads were soldered directly to the actuators.

Exact replicas of Blackwelder's actuator were not fabricated because Blackwelder's piezoelectric material was not identified and the shim steel material was different. Furthermore, Blackwelder did not report detailed bench-test information related to actuator dynamics in quiescent air. However, Blackwelder did report that actuators of this type had a resonant frequency in the range of 100-300 Hz depending on the size and structural characteristics (Blackwelder et al., 1998). Blackwelder also reported tip deflections exceeding 10 viscous scale lengths when driven by a 10- to 20-volt signal (this results in tip deflections of about 0.0394 to 0.0787 inches (1 to 2 mm) for Blackwelder's conditions). A similar actuator was tested in this research and was found to have a first mode resonant frequency of about 150 Hz and tip deflections between 0.197 to 0.236 inches (5 to 6 mm).

Since Blackwelder's results are the only known, published results for piezo-actuators of this type, there are no direct comparisons that can be made to validate the present bench test. However, the trends between Blackwelder's results and the present bench-test results agree. Despite the dissimilar materials and thicknesses, the first mode frequency and tip deflection are comparable to Blackwelder's results.

Actuator Scaling Model

The simplest bimorph actuator is a rectangular cantilever beam of two layers of the same piezoelectric material. Inspection of equation (74) reveals four parameters that can be used to scale the actuator. A cantilever type actuator should scale linearly with the applied voltage and with the piezoelectric material property d_{31}. Also, deflection scales proportionally with the square of the actuator length and inversely proportional with the thickness of the actuator. This information was used to guide the development of a numerical scaling model for actuators like that shown in Figure 8. Since only one sheet of piezoelectric material was used during the bench test, the piezoelectric material properties and thickness were fixed. Therefore, two of the factors were eliminated and scaling studies were focused on the planform shape of the geometry and the applied voltage.

A single actuator was selected to study the effect of applied voltage. This fixed the geometry variable and allowed determination of how the tip deflection scaled with applied voltage for the actuator. Three peak driving voltages of 30.5, 24.9 and 17.8 (or V_{RMS} = 21.6, 17.6, and 12.6, respectively) were selected to produce enough tip deflection that could be easily measured. The results are shown in Figure 14 and prove that the tip deflection remains a linear function of the driving voltage even when the device is two dimensional and all the piezoelectric material is in the clamped position. Clamping position was also considered. By changing where the device was clamped in the bench vice, the tip deflection changed a small, but significant amount. By extending the device such that half of the piezoelectric material was unclamped in the bench vice, the tip deflection increased by 0.197 inches (5 mm), or about 10 percent increase over the fully clamped configuration.

Unfortunately, the piezoelectric material is very brittle and the material is susceptible to cracking when too much stress has been applied, either by bending the material or cycling the applied voltage. Bonding the piezoelectric material to a substrate helps to prevent cracking in the material, but a substrate does not fully eliminate the risk of failure by cracking. Furthermore, when the adhesive layer between the piezoelectric material and substrate is not completely uniform, the piezoelectric material does not deform uniformly under stress, which also leads to cracks. This was a particularly difficult problem because the adhesive required 8 hours of cure time before the actuator could be used. Also, the adhesive had to be applied very carefully to ensure that there was no adhesive spillage around the edges of the substrate layer that would cause a short circuit when each side of the actuator was connected to the driving signal. These difficulties resulted in many actuators that had short circuits caused by adhesive overrun, or adhesive layers that were not uniform and led to the piezoelectric material cracking under the smallest driving voltage load. The sensitivity of the material to stress and the corresponding cracking resulted in many failed actuators. An example of cracks in an actuator caused by over-stressing the piezoelectric material is shown in Figure 15. The effect of stress cracks on actuator performance were observed during the bench test. The actuator would still be operational even if a small crack was present in the piezoelectric material if the crack did not run completely through the entire surface of the material. Typically, actuators with small cracks could be operated with larger voltages to produce the same deflection as actuators without cracks. Unfortunately, once a crack begins, the life of the actuator is at risk every time the actuator is operated. Eventually, the crack (or cracks) spreads until the piezoelectric material is unable to produce enough stress in the substrate to drive the tip of the actuator.

For actuators operating near resonance, the Quality factor, or Q-factor, defines the resonators under-damped characteristics. Given an amplitude-frequency response curve, the Q-factor is defined as the ratio of the peak resonant frequency to the bandwidth of the resonance at half-amplitude. The Q-factor for test article 5 was estimated using the frequency response measurements from the bench test. The frequency response derived from bench test measurements for test article 5 are shown in Figure 16 for steady-state, driven forcing (note that the response would be different and the peak frequencies shifted for impulse or step-input forcing). This actuator was chosen because the frequency response was large enough to be measured with the techniques described in this section. Small actuators resonated at higher frequencies and lower amplitudes that could not be measured without more sophisticated devices. There are three curves that represent the frequency response at each of three driving voltages listed in the legend. The center frequency (f_0) for the resonance occurs at 150 Hz. The amplitude at the half-power level was calculated from the peak by $A_{half} = A_{peak}/\sqrt{2}$. The Q factor was computed for each driving voltage by using equation (75) where δf is the interval in frequency around the center frequency, f_0.

$$Q = \frac{f_0}{\delta f} \tag{75}$$

The average Q factor for test article 5 is 23.5. For underdamped systems, the Q-factor is 0.5 or higher. A higher value of Q would indicate that damping is reduced resulting in longer oscillations when the actuator is exposed to a step response. Q-values much higher than 0.5 have a high-peak and small bandwidth in frequency response at resonance. The peak and small bandwidth behavior is evident in the plots shown in Figure 16. For a damped harmonic oscillator, the frequency response is generally asymmetric unless the system is underdamped, as is the case for the actuators described herein. For largely underdamped systems (high Q-factor), the frequency response begins to show symmetry around the center frequency. The frequency response plots shown in Figure 16 show most of the characteristics of classical underdamped harmonic oscillators with large peaks at the resonant frequency and symmetry around the center frequency.

Several versions of test article 5 were directly scaled (i.e. no change in aspect ratio) and bench tested. Variations on the planform of test article 5 are shown in Figure 17. The planform dimensions (length and width, but not thickness) of test article 5 were halved to create test article 8. A one-fourth-scale test article was created by halving the planform dimensions of test article 8 to create test article 11. These three actuators were bench tested and the natural frequencies and amplitudes determined using the methods previously described in this chapter. Two off-nominal design were also created to determine the effects of changing the aspect ratio of the actuator while also miniaturizing the overall geometry. Data from all three scaled geometries were used to determine the numerical model of how the tip amplitude and first mode natural frequencies scale. The results are shown in Figure 18. The scaling results for the tip deflection is shown in the upper plot. The tip amplitude is proportional to the area of the shim steel (A_{Flap}) used as the cantilever beam being driven by the piezoelectric material. The three test articles with the same aspect ratio, but smaller scale, cover the range of areas that were feasible to manufacture in the lab. The two test articles with different aspect ratios are shown in orange color and fall on the numerical scaling curve. It should be noted that only three of the five points were used to fit the model. Given that the model is quadratic, the fit will exactly pass through the results for the three scaled devices (blue points). However, the off-nominal designs were used to cross-validate the quadratic fit of the

scaled geometries. The agreement of the off-nominal points with the fit curve indicates the model is accurate for any size of actuator with a similar shape.

The numerical scaling estimate for the 1st mode frequency is also shown. The frequency scales linearly with the inverse of the length of the cantilever (L_{Flap}). The scaled devices, as well as the off-nominal geometry with different aspect ratio, fall on the linear trend. Again, only the results for the scaled devices were used to develop the numerical model shown and the off-nominal shapes were used to cross-validate. As with the tip amplitude model, the numerical model for frequency scaling can accurately predict the natural frequencies of similarly shaped actuators.

These results are valid for a cantilever beam boundary condition. Changing the clamping location or mechanism could significantly change the response of the actuator and the natural frequency.

CHAPTER FIVE TEST FACILITIES

Introduction

The actuators were tested for their ability to control flow dynamics using the UTSI subsonic blow-down wind tunnel. The response of the flow to actuation was measured using high-response pressure measurements. Several configurations of test article geometry were tested in boundary-layer flow by gluing the test articles to the floor of the wind tunnel. The best actuators were selected to test upstream of a cavity in the floor of the test section.

An existing rectangular test section was used for testing the actuators. However, there was no wind-tunnel contraction or transition section to connect the test section to the wind tunnel. So, a circular-to-rectangular contraction nozzle was designed to connect the rectangular test section to the wind tunnel. The rectangular test section has cross section dimensions of 3.945 inches wide by 1.642 inches tall. The axial nozzle contours in the vertical and horizontal planes were developed using elliptical profiles to force the contours to tangency with the incoming and outgoing flow paths. The nozzle cross sections were designed using super ellipse equations to ensure a smooth round-to-rectangular transition. A mold of the nozzle was fabricated from ABS plastic using additive manufacturing techniques. The nozzle contour mold was placed in a standard bell-housing pipe reducer and the nozzle was cast using Smooth-On ® casting material. Simulations of the flow through the stilling chamber, contraction, and test section were completed using the Ansys Fluent Computational Fluid Dynamics (CFD) package. This chapter describes the wind tunnel facility, the wind tunnel and test section design, and the operation of the facility.

Historically, wind tunnel design has been more of an art than a detailed science (Batill & Hoffman, 1984b; Mikhail & Rainbird, 1978). Wind tunnel flows are often three-dimensional, viscous, and turbulent in nature. Prior to the advent of modern computational science, wind tunnel design was a trial and error process. Authors in the literature agree that the wind tunnel contraction is one of the most important, and challenging, steps in the wind tunnel design process (Hoghooghi, Ahmadabadi, & Manshadi, 2016; Lastra, Fernandez, & Vega, 2013). The wind tunnel contraction serves several purposes simultaneously. First, the contraction provides a smooth transition from a large circular chamber, to a smaller cross-section. The smaller cross-section can be circular, square, or rectangular. The flow path is axisymmetric for circular-to-circular contractions and only the axial variation of cross-sectional area need to be defined. However, circular-to-rectangular contractions have the additional requirement of corner shape transition that must be carefully considered. Second, the contraction accelerates the flow from low speed to high speed (Batill & Hoffman, 1984b) with uniform exit flow and low turbulence levels (Caylor & Batill, 1984). The flow acceleration is ideally accomplished with no flow separation while maintaining uniformity of the exit flow. Hoghooghi (Hoghooghi et al., 2016) noted that a high-contraction ratio can reduce flow turbulence in the test section and increase flow uniformity for axisymmetric geometry. This was also a known fact in earlier days where Mikhail (Mikhail & Rainbird, 1978) stated that “for fixed requirements the necessary contraction length decreases as the contraction ratio increases”. Furthermore, the contraction length can be shorter for high Reynolds numbers and low Reynolds numbers may be susceptible to re-laminarization (Mikhail & Rainbird, 1978). Additionally, the corner shape of circular-to-rectangular contractions induces three-dimensionality to the flow which must be considered in addition to one-dimensional gas dynamic and boundary layer effects.

Lastly, the boundary layer characteristics in the test section are influenced by the contraction design. The boundary layer can thicken significantly in low-speed flows which can result in an effective reduction in test section cross-sectional area. The boundary layer growth and stability through the contraction must be considered. There are two regions of adverse pressure gradient in a subsonic wind tunnel and they exist at the inlet and exit of the contraction (Bell & Metha, 1988; Mikhail & Rainbird, 1978). According to Mikhail, extensive studies have been performed to suggest that even if boundary layer separation occurs at the contraction inlet, "the exit region is safe from boundary-layer separation as long as the boundary layer stays turbulent."

Much of the literature focuses on the axisymmetric case or a rectangular-only contraction. Bell (Bell & Metha, 1988) reports that "attempts to derive axisymmetric contraction shapes from two-dimensional ones" have had "limited success" especially for large contraction ratio shapes. There have been many methods proposed in the literature to define the wall contour for wind tunnel nozzle contractions. Typically, the wall contour is defined by two curves with a turning point that connects the two curves smoothly (Batill & Hoffman, 1984a, 1984b; Hoghooghi et al., 2016). Batill developed a set of design charts for rectangular-to-rectangular contractions to aid the designer in selecting the proper wall curvature. Batill used cubic spline curves with a match point to define the wall curvature. Caylor and Batill evaluated several rectangular contraction designs using numerical methods (Batill & Hoffman, 1984a, 1984b) and using experimental methods (Caylor & Batill, 1984). Lastra (Lastra et al., 2013) developed a rectangular-to-rectangular contraction design using a logarithmic wall curvature profile instead of the classical polynomial definitions. Lastra performed Computational Fluid Dynamics (CFD) and experiments to validate his design and claims that the logarithmic profile produces less turbulence at the contraction exit and is more tolerant to boundary layer separation than the same nozzle designed by polynomial curves. Calautit (Calautit, Chaudhry, & Hughes, 2014) proposed a CFD-based design methodology which took into consideration the entire closed-loop wind tunnel. Calautit's wind tunnel included a circular-to-rectangular contraction upstream of the test section, but no details were provided about the design of the contraction. Hoghooghi (Hoghooghi et al., 2016) proposed a ball-spine inverse design method to optimize the contraction contour for a circular, axisymmetric contraction. Inverse design methods such as this have the capability to solve for the unknown wall contour geometry given a desired wall pressure distribution. High-order polynomials were used by Bell and Metha (Bell & Metha, 1988) and Sargison (Sargison, Walker, & Rossi, 2004) to define the wall contours for axisymmetric contraction nozzles. For definitions of this type, additional constraints must be applied to ensure tangency of the inlet flow path with the stilling chamber and the exit flow path with the test section. The coefficients for the constrained polynomial equations can be solved using a constrained least-squares approximation. Contraction design using higher-order simulation tools such as panel methods (Bell & Metha, 1988), finite difference methods (Batill & Hoffman, 1984a, 1984b), or CFD (Doolan, 2007) and CFD coupled with Design of Experiments (DOE) (Abdelhamed, 2015) are also common in the literature.

UTSI Subsonic Blow-Down Wind Tunnel

The UTSI subsonic blow-down wind tunnel is shown in Figure 19. The wind tunnel is a continuous blowdown type that is supplied by high pressure air. The wind tunnel is approximately 6.7 feet in length, without nozzle or test section, and has an outlet diameter of 8 inches. The tunnel is built from standard pipe lengths, reducers, and flanges allowing the use of many interchangeable

configurations. A stainless-steel flow conditioning screen is installed approximately 1 foot upstream of the inlet to the wind tunnel contraction nozzle. The flow conditioner (Figure 19) is located just upstream of the stilling chamber. The flow conditioner consists of a steel, honeycomb mesh supported by ¼-inch steel rods. The wind tunnel contraction is housed in a standard 8-inch to 6-inch bell-shaped pipe reducer. The bell-shaped reducer attaches to the wind tunnel stilling chamber outlet via standard pipe flanges and gaskets. The test section that was used for this effort is fabricated from ¼-inch steel plates, and is approximately 10-inches long with a rectangular cross-section of 1.642-inches tall by 3.945-inches wide. The test section bolts onto a standard pipe cap that has a rectangular cutout to match the cross-section of the test section.

The test section walls and floor are designed so that they can be removed and replaced with alternate parts to facilitate test article buildup and installation. The top of the test section has a rectangular cut-out that is covered with 0.3-inch thick glass that allows a laser to illuminate seeded flow for use with PIV. One side of the test section is fabricated from plexiglass so that a PIV camera can image the seeded flow. The internal surfaces of the tunnel walls and ceiling are flush throughout when each piece is properly installed.

The test section floor is also removable which allows the user to build up, easily remove, and install multiple test articles. The test section floor shown in Figure 20 is designed for testing of piezoelectric flow actuators and measurement of boundary layer perturbations using up to 18 flush-mounted, high-response pressure transducers. When properly installed, the test section floor is flush throughout the test section.

An exploded view of one of the test section floors with a test article installed is shown in Figure 21. The test article is securely glued to the shim plate to ensure that the top surface of the test article is flush with the upstream floor of the test section. The shim plate is secured to the floor using a small amount of glue and tape to ensure that the plate can be removed and other test articles can be installed onto a single test section floor. Tubes for holding the high-response pressure instrumentation are bonded into the floor section.

The test section mounts directly to the flange of the upstream wind tunnel nozzle contraction. The contraction section was housed in a standard, bell-shaped, 8-to-6-inch pipe reducer. Two standard pipe flanges were welded to the bell-reducer as shown in Figure 22. The total length of the bell reducer and flanges is approximately 6.5 inches. A mold of the internal lines of the contraction was used to cast the contraction insert. A section view is also shown in Figure 22 to illustrate how the contraction fits into the bell housing. The length of the contraction mold was equivalent to the length of the bell-reducer plus the butt-weld flange on the outlet side to ensure a smooth, continuous flow path from stilling chamber to test section. More details on how the contraction mold was manufactured are provided in the following section.

Wind Tunnel Nozzle Design and Fabrication

Since many of the components of the wind tunnel existed prior to the design and manufacture of the contraction, most of the typical design parameters for a wind tunnel contraction were fixed. The contraction inlet was fixed at nominally 8 inches (7.975 inches exactly) for the standard pipe diameter of the stilling chamber. The contraction cross-section at the exit was defined by the rectangular cross-section of the test section. This results in a contraction ratio of 7.71. The contraction length was fixed at 6.5 inches due to the length of the available contraction housing

(bell-reducer and flanges). Therefore, the only remaining degrees of freedom for design were the shape of the wall contours in the vertical and horizontal planes.

The shapes of the wall contours were defined by two ellipses centered at the inlet and exit planes and a single line that shares tangency between the two ellipses. The equation of an ellipse with center at (*h*,*v*) and half-width and half-height (*a*,*b*) is given by equation (76).

$$\frac{(x-h)^2}{a}+\frac{(y-v)^2}{b}=1 \tag{76}$$

The ellipses can be used to force tangency at the inlet when the ellipse is positioned with the h-coordinate equal to the x-coordinate of the leading edge of the inlet and the v-coordinate equal to the y-coordinate of the leading edge plus the half-height of the ellipse as shown in Figure 23. Similarly, tangency is forced at the exit of the contraction when a second ellipse has h-coordinate equal to the x-coordinate of the trailing edge of the exit and the v-coordinate equal to the y-coordinate of the outlet plus the half-height of the second ellipse, also shown in Figure 23.

The ellipses were sized such that the height was half of the width, e.g. $a_i=2b_i$ and $a_e=2b_e$. Furthermore, the half-width of the exit ellipse was sized such that the edge of the ellipse was located at half the contraction length. Since the contraction length was fixed, and the aspect ratios of the ellipses were fixed, the design variables were reduced to the half-width of the inlet ellipse. The common tangency line is defined by the two points on the pair of ellipses that share a common slope and intercept. These points are easily found by searching for the slope of the 4th quadrant of the exit ellipse that has the same slope as a point in the first quadrant of the inlet ellipse.

The equation of an ellipse can be implicitly differentiated to obtain the local slope, *dy/dx* as shown in equation (77).

$$\frac{dy}{dx}=\frac{b^2}{a^2}\frac{h-x}{y-v} \tag{77}$$

Furthermore, the tangent line to an ellipse that passes through the point (x_0,y_0) is given by equation (78), which has two unknowns, (x_0,y_0), which is the intercept point of the common tangent line.

$$\frac{(x-h)(x_0-h)}{a^2}+\frac{(y-k)(y_0-k)}{b^2}=1 \tag{78}$$

These equations for each ellipse can be solved simultaneously using standard algebraic techniques giving the equation of the tangent line connecting the two elliptical profiles. At this point, the wall contour has been algebraically defined for one plane, either vertical or horizontal. The process must be repeated to define the wall contour in the perpendicular plane if the outlet is a rectangle. For square outlets, one profile defines the wall contour in both vertical and horizontal plane. Blending the two wall profiles around the cross-section requires further mathematics.

Computer code was developed to parametrically study the effect of the size of the inlet elliptical half-width. Parametric studies were also completed to study the effect of the outlet elliptical half-width. However, it was decided to fix the outlet half width at 50 percent of the total contraction length to keep the exit contour as long and gradual as possible and to attempt to keep any separated flow in the inlet region anticipating that the turbulent flow will remain attached through the exit as reported by Mikhail (Mikhail & Rainbird, 1978). Since the contraction length is fixed and is

relatively short, small adjustments to the inlet length, a_i, have significant effects on the Mach number and pressure distribution. Example parametric studies are shown in Figure 24. The inlet ellipse half-width, a_i, was varied between 0.1 and 0.5 for both the vertical (upper left plot) and horizontal (upper right plot) planes. The distance from centerline to the wall is normalized by the stilling chamber radius (R_{inlet}) and is shown in the upper two plots of the figure. Once the horizontal and vertical plane wall contours are defined (and the cross-sections are defined), then one-dimensional gas dynamic equations can be used to estimate the centerline Mach number and centerline pressure distributions through the contraction. For the case shown in Figure 24, the stilling chamber pressure was about 18 psia and the exit pressure was ambient pressure. This resulted in a contraction exit Mach number of about 0.6 (lower left of figure) not accounting for the length of the test section behind the contraction. The centerline pressure distribution was normalized by the local centerline dynamic pressure and is shown in the lower right of the figure. The parametric studies indicated that the longer inlet ellipse lengths created a non-smooth pressure profile and the shorter inlet ellipse lengths created a steep pressure profile. Therefore, the chosen wall curvature was defined using a normalized inlet ellipse half-width, a_i/L, of approximately 0.3.

Once the wall profiles are known, a function to describe the corner geometry must be defined. A super ellipse function was used to define the transition from circular to rectangular cross-section through the contraction. The equation of a super ellipse centered at the origin with half-width a, and half-height b, is given by equation (79).

$$\left|\frac{x}{a}\right|^n + \left|\frac{y}{b}\right|^n = 1 \tag{79}$$

The ellipse shape exponent, n, defines the corners of the contraction. For $0<n<1$ the ellipse has concave sides. For $n=1$, the ellipse is shaped like a rhombus. For $1<n<2$, the sides of the rhombus appear to bulge. For $n=2$, the curve is a pure ellipse. For $n>2$, the curve begins to take rectangular shape with round corners. Since the contraction inlet was round, the equation of the super ellipse could easily be determined. For a circle, $a=b$ and $n=2$. For the rectangular contraction exit, the parameters of the super ellipse equation that matched the test section were a=3.945/2, b=1.642/2 and n=50. Matching the inlet and exit geometry provides the limits of the super ellipse exponent, n, from which a transition function can be determined. After the inlet, exit, and wall contour geometry were defined, 20 slices were used to determine the shape exponent in the super ellipse equation such that there was a smooth transition between circular inlet and rectangular outlet (Figure 25). Once the slices were determined, a set of (x,y,z) points was imported into a CAD program and surface lofts were used to create the three-dimensional solid model. Only one-quarter of the super ellipse points were used so that fine definition of the shape could be maintained while minimizing the number of points imported into the CAD program. Once imported into the CAD program, the quarter-tunnel geometry was mirrored across the horizontal and vertical planes to create a fully three-dimensional flow path.

Automated methods were attempted for determining the axial distribution of the shape exponent with respect to the contraction length. The automated methods failed to produce a smooth contraction corner shape. Ultimately, the author resorted to manually defining the shape exponent for each slice by manually editing the shape exponent for a slice and inspecting the distance between the corners of the current slice and surrounding slices to ensure there was approximately equal distance between each slice.

A mold for the inner contraction contours was 3D-printed using a MakerBot® Replicator 2X with ABS plastic material. The available printer volume was 9.7 inches long, 6.0 inches wide, and 6.1 inches tall with a heated print plate. The full contraction mold was too large for the 3D printer volume, so the contraction was split into three pieces. The layer thickness was set to 0.0039 inches (0.1 mm) to ensure that the surface of the contour mold would be smooth. Large 3D-printed parts tend to have trouble with shrinkage because heat is transferred away from the hot extruded material into the cooler ambient air. Often this can cause corners of the part to peel away from the print surface during printing. This was alleviated using "helper disks" (Figure 26) on all sharp corners of the part. Helper disks are round flat disks that are printed with the part to improve heat transfer on the corners and ensure the part sticks to the platform during printing. The part was also printed on a raft because the initial print layers would not stick to the print surface. The raft is simply a thicker print base that easily bonds to the print surface and ensures the first, fine-print layer can stick to the raft. The raft must be removed after printing, so the parts were oriented so that non-critical surfaces were printed on the raft. The MakerBot Replicator 2X has built-in default settings for coarse, medium, or fine surface roughness. All default settings for the fine detail were used with exception to the build plate temperature. The build plate temperature was increased to 125 degrees Fahrenheit to help ensure the part stuck to the build plate.

Print time for each section of the contraction mold was approximately 10 to 12 hours. The raft and helper disk sections were removed from the parts after printing was complete and any rough edges or surfaces were sanded smooth with a high-grit sandpaper. The three contraction sections were bonded together using acetone as the bonding agent. Some corners of the part were warped despite the author's efforts to prevent warping of the part on the build plate. Gaps created by the warped corners were filled with a plastic epoxy and sanded smooth using a high-grit sandpaper. The final mold of the contraction contours after filling and sanding is shown in Figure 26.

To cast the contraction nozzle, the contraction mold was placed inside the pipe bell housing as shown in Figure 27. The mold was placed on a flat plate with adjustable legs so that the molding process could be completed on a level surface. Prior to casting, the contraction mold was coated with a release agent to ensure it could be removed from the cast. Any holes in the leveling plate were covered to ensure that no casting material leaked out. The mold was placed in the center of the leveling plate and the nozzle housing was placed over the top of the mold. The mold position was adjusted by measuring the position of the rectangular end of the mold with respect to the inner edges of the round housing. Once the mold was properly positioned and the orientation was checked relative to the housing mounting holes, a clamp, shown in Figure 27, was devised using spare materials from the shop. A cross member was clamped to the nozzle housing and an adjustable screw was used to force the mold to remain in place during the casting process. A two-part, mineral-filled urethane casting resin from Smooth-On Inc. was used to cast the contraction inside the bell housing. The casting material set in approximately 2 hours but was left to cure overnight before sanding.

The casting process was not completed without difficulty. In hind-sight, the end of the mold should have been extended beyond the design length so that the casting material would have the proper geometric boundaries. Unfortunately, the 3D printed material shrinks as it cools and the nozzle mold was approximately 1/16th of an inch shorter than the housing. An extension was fabricated at the end of the nozzle mold just prior to casting to ensure that the nozzle exit geometry was accurately maintained. Furthermore, aligning the mold inside the housing was no easy task. A set

of pins could have been fabricated and pressed into the side of the housing to locate the mold during the casting process. Also, the release agent was applied to the mold outdoors during windy weather. The release agent did not stick to the nozzle mold well, and thus, the mold did not release easily from the nozzle housing. The nozzle mold was destroyed in the de-casting process. Finally, the end-cap that connects the test section to the nozzle housing was bolted in place. There were small gaps between the test section/end-cap and the end-cap/nozzle housing. Gaskets were used between the connections and the gaps were filled with an auto body filler. The cast and joints were sanded to a smooth finish using several grits of sand paper starting from coarse 50-grit to ensure the shape was correct and ending with 400-grit paper to ensure the surface was very smooth. The sanded surfaces were coated with spray paint to protect the surface. A comparison of the as-casted and finished nozzle contractions is shown in the lower left of Figure 27.

Analysis of Existing Wind Tunnel Diffuser

Subsonic wind tunnel flow quality is strongly dependent on the ability of the flow to stay attached during expansion in the diffuser and compression in the contraction. Since most of the wind tunnel was existing hardware that was used without modification, an analysis was performed to understand the flow quality that would be provided by the existing hardware. The diffuser turned out to be a critical component that likely causes separated flow in the tunnel. The following analysis (Lutz, 2017) is used to justify this claim.

The main diffuser (Figure 28) has an inlet diameter of approximately 3-inches and an outlet diameter of approximately 8-inches corresponding to areas of 7.1 and 50.3 square-inches, respectively. The diffuser length is approximately 30.5 inches. The diffuser wall angle (θ) can be calculated using trigonometry as 9.4 degrees. The ratio of outlet to inlet areas is 50.3/7.1=7.1. The non-dimensional length, L/D_{inlet} , is 30.5/3 = 10.2. Blevins (Blevins, 1986) provides diffuser curves based on the non-dimensional length and the area ratio as guidelines for diffuser flow quality. The UTSI blowdown tunnel diffuser characteristics are overlaid on Blevins' design curves in Figure 29. Here it can be seen that the tunnel likely operates in a region of appreciable to fully-developed stall, which by Blevins' definition, indicates that the flow may separate on one side of the tunnel wall near the diffuser throat. The non-dimensional length for the diffuser is in the range such that stalls are likely occurring on both diverging walls, but not at the parallel walls of the inlet. For fully-developed stall, there is likely a large eddy with reversed flow near the inlet of the diffuser. These types of separation are likely highly-turbulent and would cause large velocity and pressure fluctuations in the tunnel.

A flow-straightening honeycomb is installed downstream of the diffuser. However, discussions between the author and wind tunnel design experts (Lutz, 2017) indicate that the honeycomb will reduce vorticity generated by diffuser separation, but will do little to reduce the resulting thick boundary layer. Lutz suggests installing flow screens at the exit of the diffuser and a flow screen mid-length of the diffuser at an area ratio of 4:1 to ensure the flow remains attached to the walls of the diffuser as it progresses toward the wind tunnel contraction.

Instrumentation

High-response pressure instrumentation was used to measure the actuator performance in boundary layer and cavity flows. Steady-state pressures and temperatures were used to measure wind tunnel test conditions. Data acquisition was controlled using a National Instruments data

acquisition (DAQ) card SCXI-1102 for the high-response measurements and a National Instruments cDAQ9184 for the steady-state measurements. Data acquisition was controlled and viewable in real-time using the LabView software.

High-response Pressure Transducers

High-response pressure transducers were used to measure the fluctuations in the boundary layer downstream of the actuators in the tunnel floor. High-response pressure transducers were also used in the floors of the cavities tested with flow actuators. The high-response transducers were differential Kulite XCQ-093 models with a 5psid range. The transducers were checked using an acoustic calibrator device that produced a 114dB signal at 1kHz. The sensor was placed inside the device and the response was observed on the real-time display to ensure that the sensor responded at the correct frequency.

The high response transducers were installed in 0.134-inch OD stainless steel tubes. The transducers were inserted through the tubes, high-temperature RTV was placed around the tube opening and the transducer body, and the transducer was pulled back into the tube until the transducer face was flush with the end of the containing tube. The RTV created a seal between the transducer and the tube while keeping the transducer securely mounted in the tube. Tight-clearance holes were drilled in the floor of the wind tunnel for the stainless-steel tubes. The tubes were installed flush with the test section floor. RTV sealant was applied to the outside of the tubes and the outside of the test section floor to keep the tubes firmly mounted in place and the tunnel floor sealed.

The transducers were labeled PKxx where the “xx” is a two-digit channel identifier to locate the transducer in floor of the wind tunnel for initial testing. Ten Kulite transducers were used and the channel identifiers were 21 through 25 and 31 through 35. A schematic of the location of where each sensor was installed in the tunnel floor is shown at the bottom of Figure 30. Nine sensors were installed in the floor and the tenth sensor (PK24) was installed in the test section stilling chamber or outside of the test cell depending on the test objective. The high-response sensors were calibrated using a hand-pump pressure calibrator using 4 differential pressure points between 0 and 4 psid. The calibration for each of the 10 sensors is shown in Figure 30.

The transducers signals were acquired using a National Instruments SCXI data acquisition card in an SCXI-1000 chassis. Analog filtering was available on the card but could not be used because of the sample rate decimation required to stabilize the filter. Therefore, the data were oversampled by a factor greater than 2 and were digitally filtered after analog-to-digital conversion. The DAQ card maximum aggregate sample rate was 200 kHz, so each of the ten sensors were sampled at 20kHz (the highest sample rate possible) to ensure the data were oversampled as much as possible to prevent any analog-to-digital aliasing prior to digital filtering. Some early tunnel calibration runs and checkout runs were sampled at 10 kHz to reduce data file size for the calibration data. The data were acquired for greater than 10 seconds for each wind tunnel run. For tests involving a cavity in which only two sensors could be installed, the sample rate was increased to 20kHz.

The digital data were filtered using a 6-pole Butterworth low-pass filter with cut-off frequency of half the sampling rate. The data were filtered forward and backward to prevent phase shift. The data were digitally AC-coupled using a 2 Hz high-pass filter. The time series data were separated into 10 blocks of 4096 points and the Blackman-Harris window function was used to reduce

spectral leakage between frequency bins. The Fast Fourier Transform (FFT) was computed for each windowed block. For stationary (non-transient) data, the resulting frequency spectrum was averaged over all 10 blocks. For transient runs, the data were processed in each of the 10 blocks individual to provide a time-dependent frequency spectrum. The frequency domain power spectrum was converted to sound pressure levels using equation (80)

$$\mathrm{SPL} = 10\log_{10}\left(\frac{\mathrm{Pxx}}{\mathrm{P0^2}}\right), \tag{80}$$

where *Pxx* is the power spectrum as a function of frequency, *P0=2e-5* is the acoustic reference pressure in Pascals, and *SPL* is the sound pressure level in decibels for each high-response transducer.

Steady-state Sensors

Three steady-state, Rosemount pressure sensors were used to measure the pressure in the wind tunnel stilling chamber, the test section static pressure, and the test section total pressure. All steady-state pressures were acquired using a National Instruments 9219 card installed in the National Instruments cDAQ9184. All steady-state measurements were acquired at the maximum of 1 Hz and were sampled for the full 10 seconds of data acquisition needed for the high-response transducers. Ambient pressure was measured using a Ruska model 7000 Druck pressure sensor located approximately 5-feet from the wind tunnel. One type-K thermocouple was installed in the wind tunnel stilling chamber approximately 4-inches upstream of the wind tunnel flow conditioner at the 3 o'clock position when looking downstream.

All steady-state pressure sensors were calibrated using the same hand-pump pressure calibrator that was also used to calibrate the high-response sensors. The steady-state stilling chamber pressure was measured using a 0 to 100 psi gage-pressure Rosemount sensor. The stilling chamber static port was located approximately 4-inches upstream of the flow conditioner in the wind tunnel at the 10 o'clock position when looking downstream. The test section static pressure tap was located on the ceiling of the test section approximately 0.5 inches off-centerline and approximately 1 inch upstream of the test section exit. The test section static pressure was measured using a 0 to 20 psi differential-pressure Rosemount sensor. The static tap was connected to the Rosemount sensor using approximately 2 feet of hypodermic tubing. The test section total pressure was a pitot probe mounted on the test section exit. The inlet to the Pitot probe was located approximately on the centerline and 1 inch upstream of the test section exit. The test section total pressure was measured using a 0 to 50 psi differential-pressure Rosemount sensor which was also connected to the Pitot tube using hypodermic tubing. The results of the steady-state pressure calibrations are shown in Figure 31.

Wind Tunnel Operation

The wind tunnel is operated using a control regulator and diaphragm valve supplied by a high-pressure air bottle farm. The high-pressure line between the valve and the wind tunnel is a three-inch diameter flexible hose, approximately 30 feet in length. The control regulator is not co-located to the data acquisition controls, so tunnel operations require two people. One person manually controls the high-pressure supply regulator and a single person monitors test section conditions at the data acquisition station. When desired test conditions are achieved, the data acquisition

operator signals the pressure regulator operator to hold pressure constant. The data acquisition operator then acquires data. For runs where flow actuators are used, a third person is required to operate the actuator supply voltage and frequency. Once the desired actuator settings are achieved, the flow-actuator operator signals the data-acquisition operator to acquire data then move to the next test condition.

Since the high-pressure regulation is controlled with a diaphragm valve, a minimum supply pressure is required to break the seal on the diaphragm allowing air to flow. During the tunnel calibration, it was determined that approximately 40 to 50 psi is required to break the diaphragm seal and begin flow. This equated to approximately Mach 0.05 in the tunnel test section as a minimum available flow condition. The high-pressure air cools as it expands into the wind tunnel stilling chamber resulting in temperatures as low as -40 deg. F in the stilling chamber when the test section Mach number is approximately 0.7 to 0.8. Frozen condensate was visible on the outside of the wind tunnel expansion chamber at these conditions.

Wind Tunnel Calibration

The wind tunnel with installed test section was calibrated over the expected range of operating conditions from 0.05 to 0.8 test section Mach number. The test section Mach number was estimated using the ratio of the as-measured Pitot pressure with the as-measured static pressure and the associated isentropic relation shown in equations (66) through (68).

The first calibration run was a supply pressure sweep with continuous data acquisition to understand the range of supply pressure needed to operate the tunnel up to Mach 0.8 and to quantify any lags in the system. There were no observable pressure lags in the steady state measurements. The tunnel was then calibrated at 0.1 increments in Mach number from 0.1 to 0.8 with each point 10 seconds in length. Average steady-state values over the 10 seconds of data acquisition were used to calculate tunnel isentropic variables. The tunnel supply pressure vs. Mach number calibration is shown in Figure 32 and is nearly linear.

Data were acquired to quantify tunnel background noise using the nine high-response transducers installed in the tunnel floor. High-response data were taken at 10 kHz sample rate for the tunnel calibration. The data were processed according to the signal processing descriptions listed in the previous section. The sound pressure levels in the center of the test section are shown in the upper portion of Figure 33 as well as the sensor noise floor in the lower portion of the figure. At low Mach numbers, the spectrum below 1 kHz is dominated by noise as much as 20 to 30 dB above the broadband noise level. As the Mach number is increased, the noise broadens across the spectrum and is relatively flat, but as high as 125 dB. Also, there is a lesser-amplitude but significant broadband peak between 1 and 2 kHz. These noise sources are suspected to be caused by the high-pressure supply valve, the diffuser separation, and the upstream propagation of the acoustic jet noise at the exit of the test section into the ambient air.

High-response Pressure Instrumentation Uncertainty

The quoted uncertainty for the Kulite XCQ-093 transducer, including combined non-linearity, hysteresis, and repeatability, is a maximum of 0.5% of Full-Scale Output (FSO). The FSO of the transducers is 100 mV which corresponds to approximately 3.1 psi based on the calibration previously described. Multiplying the quoted uncertainty with the maximum pressure from the

calibration results in a maximum uncertainty of about +/-0.015 psi. The nominal peak pressure readings during the test were on the order of 1 psi. An uncertainty of +/-0.015 psi on peak levels of 1 psi results in peak pressure levels of 0.98 to 1.02 psi, or 170.5 dB to 170.9 dB. The difference in this range is about 0.4 dB which is a very low variation based on pure instrumentation uncertainty.

Several repeat runs were acquired at Mach 0.1 at various times during a test period of a couple of hours. The repeat data were averaged and the standard deviation calculated at each frequency bin to understand the repeatability of the data while accounting for the test condition set-point error, as well as the instrument uncertainty. A 95% confidence interval on the mean of the repeats provides an uncertainty-like estimate of where the mean lies. The 95% confidence interval was calculated using the equation

$$\overline{\mathrm{SPL}} - \frac{t_{n-1,\frac{\alpha}{2}}\sigma}{\sqrt{n}} < \overline{\mathrm{SPL}} < \overline{\mathrm{SPL}} + \frac{t_{n-1,\frac{\alpha}{2}}\sigma}{\sqrt{n}}.$$

The overbar indicates the average, $t_{n-1,\alpha/2}$ is the student's t-value for $n-1$ degrees of freedom (samples) at a confidence level $1-\alpha$, σ is the variance, and n is the number of samples. The 95% confidence interval simply provides a metric in which 95% of the observations will have an average value within the interval. Similarly, a prediction interval was estimated using the equation

$$\overline{\mathrm{SPL}} - t_{n-1,\frac{\alpha}{2}}\sigma\sqrt{1+\frac{1}{n}} < \overline{\mathrm{SPL}} < \overline{\mathrm{SPL}} + t_{n-1,\frac{\alpha}{2}}\sigma\sqrt{1+\frac{1}{n}}.$$

The prediction interval is an estimate of where future observations will lie and is a good indicator of data repeatability at a desired confidence level, in this case, 95%.

Results of the confidence and prediction interval estimates based on repeats of the data are shown in Figure 34. The left-side of the figure shows the repeat runs at Mach 0.1 over an afternoon of testing used for interval estimation. The right-side of the figure shows the mean of the repeats as the black solid line. The 95% confidence interval was averaged over all frequency bands and is estimated to be +/=0.68 dB from the mean. This value is shown in red in the figure. The 95% prediction interval was also averaged over all frequency bands and is estimated to be +/-1.5 dB from the mean. The prediction interval is shown in blue on the figure. This analysis indicates that any systematic changes greater than about 1 dB would be outside the uncertainty of the measurements and changes greater than about 1.5 dB would be greater than the observed repeatability in the data. Changes in the SPL caused by actuation would need to be greater than about 1 to 1.5 dB for the results to be statistically significant.

CHAPTER SIX COMPUTATIONAL FLUID DYNAMICS

Introduction

Computational Fluid Dynamics (CFD) was used to predict and visualize flow field parameters such as pressure, velocity, and vorticity to better understand the complex flow field. Models of the wind tunnel facility converging nozzle, the test section, and the test articles were created for use with the CFD code. CFD simulations were completed to study the operation of the wind tunnel, to study the detailed interactions between the flow and the actuators, and to study the potential for downstream flow control with the actuators. The following simulations were performed:

- The first simulation was a three-dimensional, unstructured grid, steady-state simulation of ¼ of the tunnel from stilling chamber to test section exit. This simulation was used to study and analyze tunnel flow quality and test-section Mach number uniformity as a comparative validation to the experimental calibration.
- The second simulation was a two-dimensional, structured grid, steady-state and time-accurate simulations of various rectangular cavity geometries. These simulations were used to validate the grid generation process, the solver numerical setup, and the turbulence model selection.
- The final simulations were two-dimensional, hybrid unstructured/structured grid, steady-state and time-accurate simulations of the wind tunnel test section and the cavity geometry. These simulations included moving boundaries to simulate the effect of the actuator on the flow field, including the unsteady flow structures generated by the motion of the actuators.

The setup and execution of each of these simulations will be described in this chapter. Results for the tunnel flow quality study and the validation cases will be detailed in this chapter. Results and discussion of the two-dimensional and three-dimensional flow actuation simulations will be discussed at the end of this chapter.

All simulations were executed using the small UTSI computer cluster GRAFX-CF. The computer cluster has two Intel® Xeon® E5-2670 processors each having a total of 8 cores with 2 threads each for a total of 32 processes. Each core had 32 GB of memory available. Windows Server 2008 R2 was the operating system installed on the computer cluster. Furthermore, the computer cluster was used by other students limiting the author to a maximum of 16 available processors. The limitations imposed by the available computer hardware were the driving factor for using two-dimensional CFD simulations to study the flow actuation research problem. Two-dimensional steady-state solutions could be run in a matter of hours, and three-dimensional steady-state solutions could be run overnight. However, cavity flows and moving-boundary flow actuation are time-dependent problems requiring small time steps to ensure the solution is properly incremented for appropriate convergence. Typical run times for two-dimensional, time-accurate cavity simulations with flow actuation simulations was approximately 4 to 5 days. Three-dimensional, time-accurate simulations were attempted on the UTSI computer hardware, however, a single case required approximately 10 days of computational time for approximately 0.05 seconds of useable solution.

The physical geometry of the flow actuators was not meshed because of their miniature sizes and the limited computational hardware available to the author. Instead, the motion of the actuator was modeled as a time-dependent, moving, boundary condition in the CFD simulation.

The student version of ANSYS Fluent software was used to perform the CFD simulations. Fluent is a cell-centered finite-volume CFD solver. For a cell-centered FV code, the flow properties are solved at the centers of the volumes bounded by the mesh nodes. Mesh nodes (or grid points) are specified by the user for the geometry in which the fluid flows. The fluid volume is discretized into small, finite volumes that must sum to the entire volume of the fluid domain being studied. The fluid solver integrates the equation for the general conservation law of a scalar variable (φ) around each finite volume in the fluid domain, equation (81) (ANSYS, 2016), where $\boldsymbol{A}$ is the surface area vector for a face of the volume (V), Γ_φ is the diffusion coefficient for φ, and S_φ is a source of φ per unit volume.

$$\int \frac{\partial \rho \phi}{\partial t} dV + \oint \rho \phi \boldsymbol{u} \cdot d\boldsymbol{A} = \oint \Gamma_\phi \nabla \phi \cdot d\boldsymbol{A} + \int S_\phi dV \tag{81}$$

The conservation law simply states that internal variations of φ inside the volume depend only on the source of φ inside the volume and the flux (transport) of φ across the surface(s), S (Hirsch, 2001). However, as Hirsch notes, not all scalars (such as pressure) conform to the conservation law, but fortunately, "the motion of a fluid is completely described by the conservation laws for the three basic properties: mass, momentum, and energy". The ANSYS Fluent solver applies the conservation equation to every discretized volume. The fluid domain is solved by discretizing the conservation equations for mass, momentum, and energy, which take the following algebraic form for any given cell (ANSYS, 2016),

$$\frac{\partial \rho \phi}{\partial t} V + \sum_f^{N_{faces}} \rho_f \boldsymbol{u}_f \phi_f \cdot \boldsymbol{A}_f = \sum_f^{N_{faces}} \Gamma_\phi \nabla \phi_f \cdot \boldsymbol{A}_f + S_\phi V \, .$$

The algebraic equations are solved numerically and the resulting solutions represent the average value of the scalar over the finite volume. For non-reacting, single-phase flows of interest, there are five scalar quantities that must be solved which are usually written as

$$\phi = \begin{vmatrix} \rho \\ \rho \boldsymbol{u} \\ \rho E \end{vmatrix} = \begin{vmatrix} \rho \\ \rho u \\ \rho v \\ \rho w \\ \rho E \end{vmatrix},$$

which are the scalar, conservative variables from the Navier-Stokes equations.

For the CFD solver to capture fine-resolution details associated with small-scale flows such as boundary layers or high-gradient areas such as shear layers, the geometry must be discretized with enough points that the fine-resolution details are not averaged or "smeared" out. This requires many layers of points near solid surfaces to capture boundary layer gradients or many points in a cavity to capture the shear layer detail. Furthermore, many flows of interest are time-dependent in nature and require the solution to be solved in time. For cavity flows of interest in this research, small time-steps are required to capture the acoustic wave propagation from the trailing edge to

the leading edge of the cavity which is ever so important for exciting cavity resonance. Small time-steps often lead to many thousands of iterations to capture as little as a fraction of a second of flow time. Finally, flows involving both small and large-scale turbulence require dense grids to produce useful results that can be used to analyze flow control situations. The student version of ANSYS limits the user to 512,000 grid points in the computational mesh. This limitation was overcome by reducing the computational domain to two dimensions for most of the problems solved in this research.

It is understood that turbulence, turbulent mixing, and certain features of cavity flows are fully three-dimensional in nature. However, there has been limited success modeling cavity flows with two-dimensional geometry (Larcheveque et al., 2007; Larcheveque, Sagaut, Mary, & Labbe, 2003). Two-dimensional simulations can still capture, with some success, the vortex production at the cavity leading-edge, the acoustic wave from the cavity trailing-edge, and the resonant cavity tones as will be shown in this chapter.

For this study, the author is primarily concerned with flow control of turbulent boundary layer and cavity flows. To capture the small perturbation effects such as Tollmien-Schlichting waves in boundary layers, LES or DNS simulations would be needed. However, the computational resources available to the author were extremely limited. Instead, a hybrid RANS/LES method called the Delayed Detached Eddy Simulation (DDES) was used with two-dimensional geometry to reduce the required computational time. The DDES turbulence model used in Fluent produces LES-like simulations in separated regions away from boundaries but models the turbulence in boundary layers using RANS turbulence models or wall functions. The "Delayed" part of the DDES model ensures that the RANS models are used throughout the boundary layer grids that are not fine enough to sustain turbulence even if the LES part of the model determines otherwise (ANSYS, 2016). There are five RANS turbulence models available for use with the DES model in Fluent: Spalart-Allmaras 1-equation model, the realizable k-ε model, the BSL k-ω model, and the Shear-Stress-Transport k-ω model. Only the Spalart-Allmaras model was used in the present research based on the results from the validation cases presented in the following sections. For separated regions, outside of boundary layers, the solution is resolved directly using the LES solver. Large turbulent structures generated at the leading edge of cavities are prime examples of the type of turbulence that can be directly solved using LES.

The Spalart-Allmaras turbulence model is a single, scalar-transport equation for the kinematic turbulent viscosity, $\tilde{\nu}$, that is solved with the five other conservation equations in the computational domain. The transport equation for the kinematic turbulent viscosity is (ANSYS, 2016)

$$\frac{\partial}{\partial t}(\rho\tilde{\nu}) + \frac{\partial}{\partial x_i}(\rho\tilde{\nu}u_i) = G_\nu + \frac{1}{\sigma_{\tilde{\nu}}}\left[\frac{\partial}{\partial x_j}\left\{(\mu + \rho\tilde{\nu})\frac{\partial\tilde{\nu}}{\partial x_j}\right\} + C_{b2}\rho\left(\frac{\partial\tilde{\nu}}{\partial x_j}\right)^2\right] - Y_\nu + S_{\tilde{\nu}}\,,$$

where the production of turbulent viscosity is G_v, the destruction of turbulent viscosity is Y_v, σ_v and C_{b2} are constants, and S_v is a user-defined source term. Modeling of the production and destruction terms is necessary and described in detail in the Fluent manual. The default values for the constants were used in all simulations, $\sigma_v=2/3$ and $C_{b2}=0.622$.

Wind Tunnel Calibration Check Using CFD

Several CFD simulations were completed to visualize the flow through the stilling chamber, contraction, and test section. Three-dimensional, RANS, steady-state, viscous solutions were completed using the ANSYS Fluent software. The SIMPLE pressure-velocity coupling scheme was used. The spatial discretization was second order upwind for the density, momentum, turbulent kinetic energy, specific dissipation rate, and energy. The PRESTO pressure discretization was used. Air was simulated as an ideal gas which required the addition of the energy equation. The *k-ω* 2-equation model with curvature correction was used to simulate turbulence. The pressure-outlet boundary condition was used for the test section exit plane. The pressure-inlet boundary condition was used for the stilling chamber inlet plane. Since the tunnel exhausts to ambient pressure, the operating pressure was set to ambient pressure at 70 degrees Fahrenheit. The inlet pressure was set to the total pressure gage values shown in Table 2 for each of the Mach numbers simulated. The turbulence levels at the inlet were specified using the turbulence intensity, equation (82), and turbulence length scale, equation (83), formulations. The hydraulic diameter was equal to the stilling chamber diameter and the Reynolds number based on hydraulic diameter was calculated using inlet properties estimated from one-dimensional flow calculations.

$$I = 0.16 Re_{D_h}^{-1/8} \tag{82}$$

$$l = \frac{0.07 D_h}{C_\mu^{3/4}} \tag{83}$$

The turbulent length scale was a constant 3.37 inches. The turbulent intensity for each target Mach number is also shown in Table 2. Approximately 3000 to 5000 solution steps were completed. The solutions of the continuity and momentum equations converged to residuals less than 1e-3 and 1e-5, respectively.

A grid resolution study was completed to ensure sufficient points were available to capture the boundary layer profile in the test section. Three grid resolutions were tested from 211,000 nodes to the limit of 512,000 nodes in the student version of the software. The boundary layer profile at the center of the test section was used to determine if the grid had converged. The boundary layer profiles for the medium and fine meshes were not significantly different, so the medium mesh was used for further CFD studies. The mesh is shown in Figure 35. For the three-dimensional, quarter-tunnel simulation, the first viscous layer was spaced from the wall about 6.9×10^{-4} inches from the wall providing a y+ value of about 10 at Mach 0.6 conditions.

Only one-quarter of the tunnel was needed to simulate the flow because the geometry is symmetric about the vertical and horizontal center planes as indicated in the figure. The viscous layers are also shown in the figure insets. The stilling chamber, contraction, and test section flow paths were combined into a single geometry prior to the gridding process. The inlet total pressures shown in Table 2 were calculated from the desired test section Mach number and one-dimensional gas dynamic relationships. The actual Mach number achieved in the CFD simulations was slightly lower. The test section Mach number from the CFD simulation (mass-averaged at a cross-section at the center of the test section) is shown in Figure 36 along with the 1-dimensional isentropic calculations for the test section Mach number and the Mach number calculated using a pitot pressure and static pressure during the tunnel calibration runs. The tunnel pressure ratio is the ratio

of stilling chamber pressure (P_t) to the test section exit static pressure (P_{exit}). The estimated uncertainty for the test section Mach number is also shown on the plot as dashed lines. The Mach number uncertainty was calculated using a Taylor Series Expansion of equation (72) and the manufacturer-rated accuracy of the Rosemount pressure sensors (+/- 0.125 psi for the total-pressure measurement and +/- 0.05 psi for the static-pressure measurement). The viscous, turbulent CFD results show the Mach number achieved in the test section in the CFD simulation for the given stilling chamber pressures is lower than estimated by the isentropic equations as well as the Mach number calculated from experimental measurements. The average ratio between the CFD average Mach number and the one-dimensional estimates is approximately 0.946, e.g. the test section Mach number from the CFD solution is about 5% low. The difference between the CFD and the test Mach number could be attributed to lack of grid fidelity or improper specification of the inlet boundary condition in the CFD which may cause the boundary layer thickness to be different in the CFD than in the real tunnel. Regardless of why the CFD mismatch is present, it is still satisfying to observe the high-quality agreement between the one-dimensional isentropic equations and the calculated tunnel Mach number.

Table 2. Inlet Boundary Conditions and Target Test Section Mach Number for Tunnel Calibration CFD Simulations

Stilling Chamber Total Pressure (psig)	**Target Test Section Mach Number**	**Turbulent Intensity (%)**
0.02	0.05	4.43
0.10	0.10	4.06
0.40	0.20	3.73
0.91	0.30	3.55
1.65	0.40	3.43
2.64	0.50	3.34
3.90	0.60	3.27
5.48	0.70	3.21
7.43	0.80	3.17
9.79	0.9	3.13

Contours and axial velocity vectors of the flow at the vertical symmetry plane of the tunnel are shown in Figure 37 for the test section Mach 0.5 case. Here it can be seen that the flow accelerates through the contraction to the desired Mach number in the test section. There is a small region of low-speed flow at the inlet of the contraction. However, upon closer inspection, the axial velocity vectors do not indicate there is flow separation or reversal. Further study with a fully 3D mesh and a time-accurate solution with DDES or LES simulation might be warranted for future flow quality assessments. Computational hardware necessary to produce simulations of this fidelity were not available to the author.

Validation Cases for Cavity Flow Simulations

It was decided that a thorough validation study was warranted before detailed simulations of the moving-boundary flow actuator CFD were accomplished. Two validation cases were explored to ensure that the grid generation methodology produced dense enough grids to capture the flow physics, and to ensure that the turbulence modeling and flow physics inputs were being used properly. A literature review was accomplished to find rectangular cavity experimental and computational data that could be used to validate the CFD simulation used for this research. Unfortunately, most of the literature lacked sufficient detail to fully model either the geometry or boundary conditions with enough confidence that differences between the literature and the CFD simulations could be adequately described. However, two cases were found with information relevant to the current research and will be detailed next.

Comparison of 2D Cavity Simulations with Larcheveque's Simulations and Forestier's Experiments

Larcheveque (Larcheveque et al., 2007; Larcheveque et al., 2003) and Forestier (Forestier, Geffroy, & Jacquin, 1999) published detailed computational and experimental results for deep cavities. Deep cavities are not the focus of the present research, however, Larcheveque and Forestier's work are the most detailed computational and experimental cavity databases that could be found at the time of this writing. This work was used as the primary validation for setting up the present CFD studies.

Background of Forestier's Experiment and Larcheveque's CFD Simulations

Forestier performed experiments to study the flow over a deep cavity (L/D=0.42) at Mach number 0.8. Forestier's experiment included measurements such as high-speed Schlieren, high-response pressure measurements, steady-state measurements, and two-component Laser-Doppler Velocimetry (LDV) system. Forestier's experiment was completed in a continuous-flow wind tunnel with a constant test-section cross section of 3.94-by-4.72 inches (100-by-120mm). Stagnation conditions were ambient pressure (14.2 psi) and ambient temperature (67.7 degrees F). The cavity model (L=1.97 in, D=4.72 in, W=4.72 in) was installed in the floor of the test section. The boundary layer was ensured to be turbulent by rough transition strips about 7.874 inches upstream of the cavity. Forestier provided measurements of the boundary layer velocity profile at 2.76 inches and 0.0394 inches upstream of the cavity. The free stream velocity was Ue=846.5 ft/s and the Reynolds number based on the cavity length was 860,000. High-response pressure measurements were acquired at 200 kHz per channel.

Larcheveque performed Large-Eddy Simulations that matched the experimental data of Forestier well. Larcheveque's computational geometry simulates the test section with cavity from Forestier's experiment. Interestingly, Larcheveque's computational geometry was a hybrid grid – two-dimensional above the cavity and three-dimensional near the floor and inside the cavity. The computational geometry begins about one cavity length upstream of the cavity and extends four cavity lengths downstream. A two-dimensional version of Larcheveque's computational geometry was used by the author for the validation case described in this section.

Fluent Validation Case and Comparison to Forestier's Experiments

A comparison of the geometry from Forestier's experiment, Larcheveque's simulations and the author's two-dimensional interpretation are shown in Figure 38. Larcheveque provided grid sizing recommendations which were followed for the two-dimensional grid-generation process. Nevertheless, a grid sizing study was completed to assess the sensitivity of the solution quality to grid density. Details of the medium grid are shown in Figure 39. Grid bias is introduced to ensure the points are packed near the confining walls. A fine grid was generated by doubling the number of points in each direction, and a coarse grid was generated by reducing the number of points by one-half in each direction.

Boundary conditions were matched to the conditions from Forestier's experiment. The velocity inlet boundary condition was used at the inflow face. The boundary layer profile reported by Forestier was interpolated to the fine grid points and used to define the velocity boundary. The temperature at the boundaries was set to 259 K which was determined from the Mach number (0.8) and by assuming the total temperature was equal to the stagnation temperature provided by Forestier. The walls were set to no-slip, adiabatic boundary conditions. The pressure at the outlet boundary condition was set to static pressure calculated from Mach number and stagnation pressure using the isentropic equations.

Comparison of the velocity profile at 0.0394 inches upstream of the cavity, as well as the velocity profile through the cavity shear layer, for Forestier's experiment and the three grid densities, are shown in Figure 40. There was a slight difference between the CFD results for the three grid densities and the difference cannot be easily seen in the figure. However, careful inspection of zoomed-in plots showed that the coarse grid produced slightly different velocity profiles at the cavity leading edge and through the shear layer. No difference could be seen between the medium and fine grids, so the medium grid was used for further time-accurate studies. Also, note that the grids are structured. Fluent is an unstructured code, but provides the option to build and simulate cases with structured meshes. The structured meshes require significantly less grid points to accurately describe the geometry and viscous layers which is important when using the student version of the Fluent software which limits the user to 512,000 nodes. Structured grids were used whenever possible for the CFD simulations.

Since LES turbulence modeling is not available in two-dimensional Fluent simulations, a study was performed to determine the effect of turbulence models on steady-state results. Steady-state, RANS solutions were run until the residuals for the discretized continuity, momentum, and energy equations dropped by six orders of magnitude, typically 3000 to 5000 iterations. Solution time for steady-state computations on 16 processors of the UTSI GRAFX-CF machine took approximately 20 minutes. Steady-state solutions are ideal for rapid parametric studies such as turbulence model studies since steady-state solutions can be executed and converged rather quickly. However, cavity flows are dynamic fields and must be simulated with time-accurate modeling to capture the edge tones and flow physics that drive cavity flow. Nevertheless, steady-state solutions are adequate for inspecting mean velocity fields.

Results from steady-state simulations for various turbulence models are shown in Figure 41 which also includes digitized data from Forestier's experimental results. The boundary layer profile as-measured 0.0394 inches upstream of the cavity leading-edge is shown in the upper left portion of the figure. The RSM, k-ω-SST and k-ε-realizable do not accurately capture the boundary layer

profile upstream of the cavity. All other turbulence models more accurately match the Forestier's reported boundary layer profile and the Spalart, Vorticity-based turbulence model matches the best with a maximum difference of ~0.5%. In fact, all Spalart models performed similarly and matched the experimental data well.

The lower half of Figure 41 shows velocity profiles through the cavity shear layer for different non-dimensional lengths along the cavity. Comparison of the simulations with different turbulence models and Forestier's experimental bring similar conclusions as the comparison to upstream boundary layer profiles. The Spalart model accurately captures the initial viscous diffusion of the velocity profile at x/L=0.2. Furthermore, the k-ε and RSM family of models do not accurately capture the diffusion effects that viscosity has on the velocity profile, especially as the flow progresses toward the back of the cavity. At x/L=0.4 and 0.6, the k-ε and RSM models show velocity profiles with sharp velocity gradients that haven't been smeared out by viscosity. Near the back of the cavity, the velocity has diffused into a nearly linear profile. None of the turbulence models showed enough diffusion to match the experimental data. However, the Spalart model, once again, shows the best agreement to the experimental data. Based on these results, the Spalart model was used for all further cavity CFD simulations, both steady-state and time-accurate.

Some results from the steady-state solution are shown in Figure 42. The contour plot shows the distribution of Mach number throughout the computational domain. Note that no turbulence or eddies can be observed because of the averaging of the Navier stokes equations provided by steady-state solutions. Nevertheless, the averaged shear layer across the cavity can be seen. The black vertical bars across the shear layer indicate the lines over which the data were extracted for comparison to Forestier's experiment. The centerline flow in the tunnel is Mach 0.8. Comparisons of the CFD simulation with Forestier's reported measurements are also shown in the figure. It is quite remarkable how close a two-dimensional CFD simulation can capture the measured shear layer from a real experiment.

Time-accurate simulations were performed using a hybrid LES/RANS turbulence model. The Spalart turbulence model was used to model turbulence with length scale smaller than could be captured by the grid and the Delayed Detached Eddy Simulation (DDES) was used to directly solve the larger-scale turbulent structures. The pressure-based solver was used for both steady-state and time-accurate simulations and is appropriate for subsonic applications. The spatial discretization of the governing equations was set up using the following configuration:

- gradient: Least-squares cell-based
- pressure: 2nd order
- density: 2nd order upwind
- momentum: 2nd order upwind (steady-state) or Bounded central difference (time-accurate)
- modified turbulent viscosity: 1st order upwind
- energy: 2nd order upwind.

Air was modeled as an ideal gas for the working fluid. The viscosity was constant and calculated using the ambient temperature and Sutherland's law. Steady-state solutions were used as initial conditions for the time-accurate solutions. For time-accurate solutions, several time steps were attempted ranging from $1x10^{-3}$ to $1x10^{-5}$ seconds. Only time steps smaller than $1x10^{-4}$ could accurately capture the oscillating and acoustic flow physics produced by the cavity. Therefore, a

fixed time step of $1x10^{-5}$ seconds was used for all time-accurate cavity flow simulations. The transient formulation was second order implicit.

The time-averaged Reynolds stress, $-\overline{u'v'}$ is the nonlinear Reynolds stress component, see equation (64), that couples the turbulent fluctuations to the mean flow in the two-dimensional simulation. (The Reynolds stress tensor is a 3x3 matrix but reduces to three components for a two-dimensional case). The *u'v'* Reynolds stress was averaged over 0.7 seconds of computational time for the time-accurate CFD simulation. Comparison of the Reynolds stress components to Forestier's experimental results is shown in Figure 43. These stresses are difficult for any CFD simulation to match with experimental data. Even Larcheveque's complicated simulation did not match Forestier's experiment exactly (Larcheveque et al., 2007). However, even the two-dimensional approximation used as a validation case for this research matches some of the characteristics of the stresses shown in Figure 43. Note that just downstream of the cavity leading-edge at x/L=0.2, the time averaged Reynolds stress has the same character as the experimental results. Inside the shear layer, the stress increases to about 0.02 for both the CFD simulation and the experimental data. However, away from the shear layer, the agreement is not perfect and the simulation shows less *u'v'* stress than the experiment. This is probably because there was much less mixing and entrainment by the shear layer on the mean tunnel flow and inside the cavity for the simulation. As the flow progresses downstream across the cavity, the *u'v'* stress dissipates quickly compared to Forestier's experiment. At x/L=0.8, there appears to be a slight variation in the *u'v'* stress compared to the experiment. However, these results are like Larcheveque's more complicated simulation results. Larcheveque's simulation also dissipated more quickly near the cavity trailing edge. However, Larcheveque's simulation retained most of the shape of that observed in the experimental data. The results of the present study are promising because it can be very difficult to match the Reynolds stress tensor in computational simulations (Larcheveque et al., 2003).

Next, a digital pressure measurement was sampled during the CFD simulation on the cavity leading-edge wall at $y/L = 0.7$ to compare to the pressure spectrum reported by Forestier. The time history of the pressure spectrum and the acoustic sound pressure levels are shown in blue in Figure 44. Forestier's spectrum was digitized from his report and overlaid in the figure. The first two Rossiter peaks are captured well by Forestier's measurement and the author's time-accurate simulations. The simulations show a higher base acoustic level which rolls off more quickly at the higher frequencies than that reported by Forestier. Specifics on window functions or digital filtering were not provided by Forestier. Despite the differences in broadband noise level, the two-dimensional CFD accurately predicts the frequency and SPL of the first and second Rossiter tones.

Finally, flow visualization results from the current CFD simulation, Larcheveque's CFD simulation, and Forestier's experimental data are shown in Figure 45. The contours for parts (b) and (c) represent the magnitude of the density gradient and are excellent ways to visualize large-scale turbulent structures. In all cases, the leading edge of the cavity produces a vortex which has travelled to approximately the middle of the cavity. Also, waves can be seen emanating from the leading edge of the cavity as well as the trailing edge. Larcheveque's simulation shows much finer granularity of turbulent structures than the current simulation because of his three-dimensional simulation and finer grid density.

These results have demonstrated the ability of the two-dimensional simulation to accurately capture (at least qualitatively if not quantitatively in some cases) the edge-tones, the shear layer profile, and the production and subsequent destruction of a vortex as it is generated from the cavity leading edge to its death at the trailing edge. These simulations are not perfect, but no simulation is. Enough of the flow features are captured that studies with flow actuation can be completed in two-dimensions despite the limited computational hardware available to the author.

Comparison of 2D Cavity Simulations with Radhakrishnan's Experiments

Radhakrishnan (Radhakrishnan, 2002) performed studies of shallow cavities using the UTSI blow-down wind tunnel with an 8x8-inch test section. He reported experimental spectra and CFD simulations at Mach numbers from 0.3 to 0.6. Some useful comparisons can be made above Mach 0.5 where the cavity tones are loud enough to overcome the tunnel noise. Cavity L/D ratios that were tested included 2.0, 2.5, 3.5, 4.5. Radhakrishnan used a flat plate with wedged-shaped leading edge in the test section to test his cavity models. The length of the plate was 25 inches and the distance from the plate leading-edge to the cavity leading edge was 11 inches. Dynamic pressure transducers were installed in the floor of the cavity to measure the cavity tones. Radhakrishnan reported boundary-layer profile measurements just upstream of the cavity as well as dynamic pressure spectra for each Mach number that was tested. Geometry for the L/D=2.5 cavity was chosen for validation of the CFD codes used in this research.

Fluent Validation Case and Comparison to Radhakrishnan's Experiments

The computational grid was developed based on the lessons learned from the Larcheveque/Forestier simulation. Therefore, a grid study was not completed for any other computational studies. Details of the computational grid used for the simulation to compare to Radhakrishnan's data are shown in Figure 46. Since Radhakrishnan's test section was much larger than the cavity model, it was decided not to model the entire test section in the CFD simulation because of limitations on computational hardware and grid size limitations imposed by the software. The 11-inch flat plate was modeled ahead of the cavity and 3.2 cavity lengths were modeled downstream. The grid was modeled as 3-inches in the vertical direction (about 1.6L) and the upper boundary condition was modeled as a pressure farfield condition with the Mach number of 0.6 specified parallel with the boundary. The left boundary condition was also set to a pressure farfield condition with Mach 0.6 flow specified normal to the boundary. The right boundary condition was set to a pressure outlet boundary condition which exhausted to ambient pressure.

A comparison of Radhakrishnan's measured boundary layer with the boundary layer extracted from the CFD simulation at 0.2362 inches upstream of the cavity leading edge is shown in Figure 47. The boundary layer from the simulation agrees well with the experimental data indicating the grid is of sufficient quality upstream of the cavity to capture the viscous layer.

Comparisons of the time history of a digital pressure measurement from the CFD simulation and Radhakrishnan's experimental data is shown in Figure 48. The time history from the simulation is shown on the left. Radhakrishnan did not report a time history for comparison. The sound pressure level spectrum is shown on the right for the CFD simulation (blue) and Radhakrishnan's experimental data (red). The CFD simulation does an excellent job predicting the experimental measurements and matches the classical Rossiter edge tone better than Radhakrishnan's experimental data. The peak tone observed in the CFD simulation is about 8 dB less than that

observed in Radhakrishnan's experiment. This is probably because there is a lesser harmonic of the first Rossiter tone being generated in the CFD simulation that is not observed in the experimental data. This sub-harmonic is a significant source of energy in the flow and appears to detract from the pure first mode Rossiter tone. Beyond the first-mode Rossiter tone, the CFD and experimental data agree well until the CFD simulation begins to roll-off because of the limited frequency bandwidth caused by only using 0.5 seconds of data for processing.

Visualization of one period of the cavity oscillation is shown in Figure 49. Again, this visualization leverages the magnitude of the density gradient to highlight the turbulent structures. At 0.1 seconds, a vortex begins to form at the leading edge of the cavity and the vortex from the previous cavity cycle begins to impact the aft cavity wall. By 0.1002 seconds the leading-edge vortex has formed and detached from the leading edge, and the previous-cycle vortex at the trailing edge has been broken down into smaller vortices and turbulence because of the local interactions with the rear bulkhead. A vortex is formed at the top of the cavity trailing edge and multiple smaller vortices are collected near the aft corner of the cavity. By 0.1004 seconds, the primary vortex has traversed to the middle of the cavity. Over this distance, the vortex has become significantly diffused, or "smeared out" by the viscous shear flow. At 0.1004 seconds, the flow interaction at the trailing edge of the cavity has produced several smaller vortices that are convected with the downstream boundary layer. At 0.1006 seconds, the primary cavity vortex has dissipated and grown enough that it fills the entire cavity and two trailing edge-vortices can be seen leaving the frame. At 0.1007 and 0.1008 seconds, the vortex begins to impact the trailing edge of the cavity starting the breakdown process. At the same time, a new leading-edge vortex can be seen forming to start the cyclical process over again.

Similarly, velocity vectors for the same cavity period are shown in Figure 50. Qualitatively, these are the similar to the velocity vectors computed by Radhakrishnan from PIV data; see Radhakrishnan's Figure 5.33 (Radhakrishnan, 2002). The vortices produced by the CFD simulation appear to be larger and with more intensity than those shown by Radhakrishnan. Some of the difference could be caused by differences in how the data were processed. Some of the difference is probably caused by the turbulence modeling choices. Nevertheless, the two-dimensional CFD simulations appear to capture the flow physics sufficiently to warrant further studies with moving-boundary flow actuator simulations.

Simulations for Flow Control Studies

Two-dimensional Tunnel Simulations used to Estimate Boundary Layer Characteristics

Two-dimensional simulations were completed using the ANSYS Fluent software with tunnel geometry from just downstream of the flow conditioning screen through the tunnel exit to determine the boundary layer characteristics at the location where the actuator would be installed. The following settings were used to configure the solver:

- air modeled as an ideal gas
- viscosity estimated from temperature using the Sutherland viscosity law
- viscous, Spalart-Allmaras 1-eqn turbulence model with curvature correction
- pressure-velocity coupled solver
- least-squares cell-based gradient

- pressure staggering option
- second order upwind spatial discretization for energy, density and momentum equations
- first order upwind spatial discretization for modified turbulent viscosity.

The two-dimensional geometry and mesh used for boundary layer characteristic estimation are shown in Figure 51. The geometry was not axisymmetric because of the circular to rectangular transition between the tunnel stilling chamber and test section. Therefore, the two-dimensional simulation represents a vertical centerline slice of the tunnel. A structured grid was used with enough points in the boundary layer to adequately capture the boundary layer profile. The pressure-inlet boundary condition was used at the stilling chamber inlet and the pressure-outlet boundary condition was used at the test section exit. The adiabatic, no-slip boundary condition was enforced on the tunnel walls, and symmetry was assumed at the tunnel centerline. A range of boundary conditions was used to investigate the flow field over the range of test-section Mach numbers between 0.1 and 0.53 as shown in Table 3. The solutions were executed until the residuals in the continuity, momentum, and energy equations dropped by six orders of magnitude which usually occurred within 1000 to 1200 iterations. The operating pressure, from which gage pressures are determined, was 99187.97 Pa and the total temperature was 291 K. The pressures are defined by $P_{abs} = P_{op} + P_{gauge}$.

Table 3. Pressure Boundary Conditions for Tunnel CFD Simulations

Mach Number	PT inlet, gauge (Pa)	PS exit, gauge (Pa)
0.1	736	-47.9
0.2	2743	-61.7
0.3	6282	-196
0.4	11355	449
0.53	20713	987

The vertical red line in Figure 51 represents the location of the leading edge of the actuator in the tunnel. This region was the line-surface along which velocity data were extracted from the simulations to characterize the boundary layer. Velocity profiles for the five Mach numbers are shown in Figure 52. The profiles are shown on a zoomed-in scale to demonstrate the difference between the velocity profiles at the various Mach numbers. As the Mach number increases (and therefore the Reynolds number) the boundary layer becomes thinner, as would be expected. Boundary layer characteristics derived from these profiles are discussed in the following chapter.

Two-dimensional Cavity Simulation without Flow Actuation (Baseline)

Grids were built with an extended test section for CFD runs in which the actuator was simulated because of the need for additional grid points near the actuator and in the cavity, and the limitations of the computing hardware and academic licensed software. The tunnel test section was extended in the upstream direction by approximately 12 inches to create enough straight-sectioned duct to allow the boundary layer to develop upstream of the cavity. The boundary layer characteristics

upstream of the cavity will not exactly match the estimated boundary layers from the full tunnel simulation, but they will be representative enough to study the cavity flow field. A picture of the hybrid structured/unstructured grid is shown in Figure 53. The tunnel height, cavity length and depth, and distance from cavity to tunnel exit were representative of the as-tested physical hardware (in two-dimensions). Structured grids were used wherever possible to minimize the number of grid points while maintaining high grid density in regions of large gradients such as the boundary layers on the floor/ceiling and inside the cavity. For all flow actuation runs, the spacing of the first grid point from the wall was approximately 0.00051 inches resulting in a y+ of 5 at test section conditions of Mach 0.5.

Like previously describe CFD simulations, the pressure-inlet and pressure-outlet boundary conditions were used at the inlet and exits of the domain. Adiabatic, no-slip walls were enforced on the ceiling, the floor, the actuator surfaces, the cavity walls, and the cavity floor. Only one test-section Mach number condition was executed because of the need to run time-accurate simulations for proper simulation of cavity physics and the limited computer hardware. A test section Mach number of 0.5 was the target test condition, and boundary conditions needed to achieve this Mach number for all cavity simulations were:

- Total temperature 30.7 degrees F
- Total pressure at the inlet (absolute) 17.11 psi
- Static pressure at the exit (absolute) 0.14 psi
- Non-reflecting acoustic wave model at the inlet and exit
- Turbulent intensity 2.95%
- Turbulent length scale 0.984 in.

These conditions result in a centerline test-section velocity of U=518 ft/s, with a convective time scale of t_{conv}=1.22x10^{-4} seconds to traverse the length of the cavity.

Solver settings for all cavity simulations were the same as those validated using the Larcheveque simulation and described previously. The Delayed, Detached Eddy Simulation (DDES), a hybrid RANS/LES turbulence model, was used for all time-accurate cavity simulations. The Spalart-Allmaras 1-equation model with curvature correction was used for RANS calculations. A time step of 1x10^{-5} seconds was used for all cavity simulations. A maximum of 20 sub-iterations were run at each time step or until the residuals of the energy, continuity, and momentum equations were reduced by six orders of magnitude, whichever came first. A minimum of 0.1 seconds of simulation time was used to calculate cavity acoustic spectra; solution start up transients were not used in the minimum 0.1 seconds. Steady-state solutions were used as the initial conditions for the time-accurate solutions. Simulations typically took 4 days to complete approximately 0.1 seconds of useable simulation time.

Instantaneous snapshots of the flow field for one cycle of the leading-edge vortex formation and subsequent impact with the cavity trailing-edge are shown in Figure 54. The contours represent the field in terms of the magnitude of the density gradient in which the large-coherent structures can be easily observed. At the *t=0.1495* second time-step, the formation of the vortex from the leading-edge shear layer can be seen. After only 1x10^{-4} seconds, the leading-edge vortex has grown significantly, and after only 2x10^{-4} seconds it has traveled half the length of the cavity. At *t=0.1498* seconds, the leading-edge vortex begins to interact with the turbulence created by the

impact of the previous vortex with the trailing edge. This interaction tends to smear-out and enlarge the vortex. At *t=0.15* seconds, vortex breakdown at the trailing edge creates new structures at the trailing edge of the cavity. These structures persist downstream of the cavity up to approximately three cavity lengths. By *t=0.151* seconds, the vortex has broken down and dissipates into smaller structures, and by *t=0.1502* seconds, a new vortex is formed at the leading-edge and the cycle begins again. Videos of these simulations showed a forward-propagating wave emanating from the trailing edge, interacting with the vortex formation at the leading-edge shear layer, and growing as the wave propagates forward. A picture of the flow field which has been zoomed-out to illustrate the forward propagating waves is shown in Figure 55. Also, the persistence of the turbulence downstream of the cavity can be seen in this figure.

Results of the time-accurate CFD simulations were captured as animated videos using contours of the magnitude of vorticity at each time slice. The video for the baseline, no-actuation, cavity flow field is provided in the attachment File 1. The flow direction is left to right in the video. The regions of zero vorticity are colored blue, and the regions of concentrated vorticity are shown as white. The video contains 0.7 milliseconds of flow simulation time which is approximately one cycle of the leading-edge vortex generation and convection cycle. Many interesting flow features can be observed in the video. First, the boundary layer upstream of the cavity can be seen to undulate as it interacts with the shear layer and vortex generation at the leading-edge of the cavity. Next, the leading-edge shear layer rapidly produces a region of concentrated vorticity. As the vorticity grows, it detaches from the leading-edge shear layer. The vorticity is then convected across the top of the cavity. The magnitude of the vorticity is dissipated as it convects across the cavity, but grows spatially. The region of concentrated vorticity reaches the cavity trailing edge at which point it breaks up; the highly-concentrated center region is forced into the lower, aft corner of the cavity while some of the spatially amplified vorticity convects along the surface downstream of the cavity. In the region downstream of the cavity, the vorticity interacts with the growing boundary layer producing regions of highly concentrated vorticity which is swept downstream and rapidly dissipates. Returning to the flow inside the cavity, the region of highly-concentrated vorticity that was forced into the lower, aft corner of the cavity is pulled toward the front of the cavity by the undulating region at the front of the cavity. The fluctuation of the leading-edge shear layer drives an oscillatory motion inside the cavity which entrains the fluid inside and outside of the cavity. As the region of concentrated vorticity moves upstream along the bottom of the cavity, it is entrained by the next vortex convected across the cavity opening and the process is repeated.

Contours of vorticity, velocity magnitude, and pressure were also inspected at each time slice. The contours of the magnitude of density gradient and the magnitude of the vorticity agreed well for determining the location and strength of turbulent structures. Pressure sampling on the floor of the cavity was performed as the solutions progressed. The time-histories of the pressure data were processed using the digital signal processing techniques described for the experimental data. Comparisons of the simulations with and without actuation will be presented at the end of this chapter.

Two-dimensional Cavity Simulations with a Single Actuator

Two regions of the tunnel floor boundary condition were used to prescribe motion that simulates actuator movement. These regions are line-surfaces in the two-dimensional geometry that define the boundary of the wind tunnel floor at the location where actuators would be installed. Both

regions were 0.591 inches in length, and there was half an actuator length between the tip of the upstream actuator and the base of the downstream actuator. The ANSYS Fluent software allows the user to define prescribed boundary motion which was used to rotate the two-dimensional boundary surfaces effectively simulating the top surface of the actuator motion. This technique was used instead of gridding the very thin actuator because of grid size limitations. The two regions simulate two, independent actuators with one placed upstream of the other. This arrangement demonstrates an additional level of flow actuation in which one upstream actuator produces disturbances that grow before the disturbance interacts with the second actuator and the cavity. Since the motion of the two actuators can be described independently, one simulation was completed in which only the motion of the actuator at the leading edge of the cavity was simulated, and one simulation was completed in which the both actuators were simulated in-phase with each other. The double-actuator motion simulation is described in the next section. The single-actuator motion simulation is described in this section.

Unstructured grids were needed above the simulated actuator boundaries to act as springs that absorb the motion of the actuator surfaces when the surfaces are moved. Inflation layers were used above the simulated actuator surfaces to match the upstream and downstream boundary layer grid spacing. The inflation layers were rigid and deformed with the moving actuator surfaces. The unstructured grid above the actuators was deformed and re-gridded as the actuator motion progressed.

The actuator motion was defined as rigid body rotation about the leading-edge of the actuator. A time-dependent sinusoidal driving signal defined at the cavity frequency and phase angle was used to specify the angular position of the actuator tip relative to the actuator leading-edge. The maximum actuator rotation was defined such that the tip of the actuator would remain below a height of 0.0197 inches from the floor of the tunnel. The limitation was chosen because this was the estimated maximum height of the tip of the physical actuators when they were installed in the tunnel and operated at resonance. No additional actuator maximum deflections were simulated because of the time required to produce a simulation.

The results from the time-accurate simulation were used as initial conditions for the actuator-motion simulations. Pressure spectra in the cavity from the no-actuation simulation were used to determine the frequency and phase angle at the dominant cavity tone. This frequency and phase angle were used to specify the motion of the actuator to ensure the actuator would operate in-phase with the cavity flow. Actuator motion was also attempted with out-of-phase driving signals, but the resulting solutions did not produce significantly different effects on the cavity flow field, probably because actuation was only attempted at the most stable cavity tone.

Results of holding the upstream actuator surface at rest while moving the simulated actuator surface at the cavity leading edge are shown in Figure 56. The flow field is shown using contours of the magnitude of density gradient for a subset of time slices during the simulation. A large turbulent structure is produced at the leading edge when the actuator reaches peak deflection. The large turbulent structure convects across the cavity opening where it quickly begins to interact with the cavity trailing edge. Large turbulent structures persist downstream of the cavity after the primary vortex breakdown occurs at the trailing edge. The large structures extend further into the flow field above the cavity and downstream of the cavity compared to the case without actuation. Although not shown in the figure, a forward-travelling wave was also observed and appeared to

be of greater intensity than the wave observed for the case without actuation. The actuator motion is synchronized to the observed pressure oscillation on the floor of the cavity that was observed in the simulation without actuation. This means that when a pressure peak is observed, the actuator motion should be at the maximum position. The actuator motion tended to produce leading-edge vortices about 25% faster than the case without actuation. This is observed by noting that the vortex generation, convection, and interaction with the trailing edge appears to take place over a time span of about t=0.003 seconds (or a non-dimensional time scale of t/t_{conv}=24.7) for the case with actuation (Figure 56) versus a time span of about t=0.004 seconds (or a non-dimensional time scale of t/t_{conv}=32.9) for the case without actuation (Figure 54).

A video of the time-accurate CFD results for the simulation with two actuators is provided in the attachment File 2. Again, the flow direction is left to right, the regions of zero vorticity are colored blue, the regions of concentrated vorticity are shown as white, and the video contains 0.7 milliseconds of flow simulation time, enough for one vortex convection cycle. Evidence of the simulated actuator motion can be observed by carefully inspecting the surface at the cavity leading-edge. Like the case without actuation, the undulation of the upstream boundary layer as well as the shear layer at the cavity leading-edge can be observed. However, simulated actuator motion is phase-locked with the peak pressure signal in the cavity causing a significant increase in the magnitude and spatial growth of the vortex prior to the separation of the vortex from the shear layer. The larger region of concentrated vorticity has several effects. First, as the large vortex convects across the cavity, the entrainment of the flow near the cavity floor into the vortex and shear layer is greatly enhanced. The small, undulating region near the cavity leading-edge that was observed in the baseline case without actuation is nearly eliminated resulting in more thorough mixing throughout the cavity. Second, the region of vorticity that is separated at the trailing edge of the cavity is also greatly enhanced. The spreading of the vorticity in the vertical direction is increased in the region downstream of the cavity when compared to the baseline case without actuation. Furthermore, as the vorticity dissipates downstream, the vertical depth at which the vorticity penetrates the free-stream persists.

Two-dimensional Cavity Simulations with Two Actuators

Motion for two simulated actuators was applied in a third CFD simulation to demonstrate multi-level actuation ability in which disturbances produced by the upstream actuator interact with the downstream actuator and the cavity. The motion of both actuators was in phase and defined by the frequency and phase of the dominant cavity tone observed from the baseline CFD simulation without actuation.

Flow field visualization, again using the magnitude of the density gradient, is provided in Figure 57. The tip of the upstream, simulated actuator surface is located at the left vertical edge of each flow field picture. The tip of the downstream actuator was, again, located at the leading-edge of the cavity. In the upper left flow-field picture, the large turbulent structure produced by the upstream actuator begins to enter the picture. At *t=0.2908* seconds, the leading turbulent structure reaches the leading edge of the cavity and begins to break up because of the downstream actuator motion and the interaction with the cavity flow field. At *t=0.2909* seconds, the results of the interaction are visible where a larger turbulent structure spans the cavity length, interacts with the leading-edge shear layer, and begins entraining flow at the aft, bottom corner of the cavity. The large structure then breaks up after another 0.0001 seconds and the process repeats in the remaining

images. Downstream of the cavity, large turbulent regions can be observed which extend even further into the free-stream flow than the simulation with only one actuator and the simulation without actuation.

A video of the time-accurate CFD results for the simulation with two actuators is provided in the attachment File 3. Again, the flow direction is left to right, the regions of zero vorticity are colored blue, the regions of concentrated vorticity are shown as white, and the video contains 0.7 milliseconds of flow simulation time, enough for one vortex convection cycle. Evidence of the simulated actuator motion can be observed by carefully inspecting the surface at the cavity leading-edge as well as the surface near the left-most vertical, white line. The dual-actuator simulation showed even more interesting results than the previous two simulations. The upstream actuator produces a compact region of concentrated vorticity. This large-scale structure is convected downstream where it interacts with the effects of the second actuator located at the cavity leading-edge. The magnitude of the vorticity in the first large-scale structure tends to dissipate rather quickly as it passes over the leading-edge actuator and shear layer at which point it becomes entrained with the second large-scale structure produced at the leading edge. This interaction creates a large region of elevated vorticity with spatial coverage even larger than was observed with the single-actuator simulation. The effect inside the cavity is different than the single-actuator case. The large structure entrains much of the undulating fluid inside the cavity, but does not reach as far into the forward corner of the cavity as the single-actuator case did. However, the dual actuator case provides additional entrainment of the flow above the cavity when compared to the previous cases (baseline without actuation and single actuator). Furthermore, the region downstream of the cavity shows the highest regions of concentrated vorticity and the largest penetration of elevated vorticity into the free-stream of all the simulations that were completed.

The results discussed thus far have provided a qualitative understanding of the flow field and the effects of a single, or multi-level actuator. Some comparisons and quantitative results are discussed in the next section.

Comparison of Cavity Simulation Results with and without Actuation

A qualitative comparison of flow fields using different field variables for the three simulations are shown in Figure 58. The top row was created from the simulation without actuation, the middle row corresponds to the simulation with only leading-edge actuation, and the bottom row corresponds to the simulation with two simulated actuators. The columns represent the various field parameters that were studied. The columns represent, from left to right, the magnitude of the density gradient, the magnitude of the vorticity vector, the magnitude of the velocity vector, and the pressure. Each contour represents an instant in time, and the time slices were chosen such that the leading-edge vortex was in approximately the same position.

Each parameter conveys somewhat different information. The persistence of the vorticity downstream of the cavity is most easily identified using the contour based on the magnitude of the vorticity vector. Applying single, leading-edge actuation increases the penetration of the vorticity into the free stream flow in the downstream region. The velocity field shows how the velocity is reduced in the free-stream above the actuators and is increased near the actuator tip when the actuators are active. The pressure field shows the classic, alternating high- and low-pressure distributions that are indicative of vortex shedding. Applying single, leading-edge actuation creates a large high-pressure region ahead of the cavity. The dual-actuator simulation produces two large

regions of high-pressure, but with an additional low-pressure region at the tip of the upstream actuator.

The turbulence kinetic energy, *K*, was used to quantitatively compare the distribution of turbulence inside and downstream of the cavity for the three simulations. The turbulence kinetic energy is defined by

$$K = \frac{1}{2}(\overline{u'u'} + \overline{v'v'} + \overline{w'w'}) ,$$

where the (*x*,*y*,*z*) components of velocity are (*u*,*v*,*w*), the primes indicate the fluctuating components of the Reynolds decomposition, and the overbars indicate the time-averaged quantities. The turbulence kinetic energy reduces to

$$K = \frac{1}{2}(\overline{u'u'} + \overline{v'v'})$$

for the two-dimensional simulations. All CFD solutions were time-averaged for a minimum of 0.1 seconds, starting from a statistically stationary flow in which start-up transients had already passed.

Comparisons of the turbulence kinetic energy (normalized by the square of free-stream average velocity) as a function of the vertical coordinate (normalized by upstream boundary-layer momentum thickness) are shown for the region inside the cavity in Figure 59. The CFD solutions were sampled along the line surfaces (line 1 and 2) shown at the top of the figure. The lines were positioned equidistant along the length of the cavity and extended into/above the cavity by one-half of the cavity depth. The turbulence kinetic energy for the three CFD simulations are shown in the lower part of the figure. The turbulence kinetic energy is higher in the forward part of the cavity for all three simulations because of the vorticity production at the leading-edge shear layer. The leading-edge simulated actuator produced the highest turbulence kinetic energy inside the cavity. The dual simulated actuator produced comparable turbulence kinetic energy inside the cavity, probably because the interaction of the upstream vortex with the downstream actuator breaks up the regions of intense vorticity and spreads them out over the cavity length resulting in a time-averaged value much like the no-actuation case. Furthermore, most of the turbulence kinetic energy produced by the dual actuator occurs near the cavity opening as opposed to within the cavity for the no-actuator case.

The effects of actuation on the region downstream of the cavity are shown in Figure 60. Four line-surfaces were used to query the CFD solutions downstream of the cavity. These were positioned at intervals of the cavity length as shown at the top of the figure. The turbulence kinetic energy is highest near the cavity trailing edge and it dissipates rapidly downstream. The addition of a single or multi-level actuation increased the peak turbulence kinetic energy by approximately 46% at 1 length downstream of the cavity. At 1 cavity length, downstream of the cavity trailing-edge, the single-actuator simulation increased the vertical (cross-stream) distance from the wall at which the turbulence kinetic energy was elevated (distance of penetration) by a factor of 2 (points A to B in the figure), and the dual-actuator simulation increased the distance of penetration by a factor of 2.8 (points A to C in the figure). By two cavity lengths, all solutions showed a dramatic reduction in normalized turbulence kinetic energy to about 0.01 or less. However, the single- and dual-actuators continue to increase the distance from the wall at which the turbulence kinetic energy is elevated, even at two, three, or four lengths downstream of the cavity despite the dissipation of the

turbulence kinetic energy in the downstream region. Both single- and dual-actuators provide at least 20% increase in normalized turbulence kinetic energy over the case without actuation. The dual-actuator simulation provides the highest increases as well as penetration into the free-stream flow that persists even at 4 lengths downstream of the cavity.

Finally, the acoustic spectra for the three CFD simulations with the addition of the acoustic spectrum derived from pressures measured experimentally on the floor of the cavity are shown in Figure 61. The CFD simulations were sampled at two places on the floor of the cavity located equidistantly from the cavity leading-edge and trailing edge. These points are illustrated at the circular markers in Figure 59. The data in Figure 61 correspond to the upstream location in the cavity. The thick red line represents the experimental data, which is discussed in further detail in the next chapter. The dashed vertical lines represent the Rossiter tones associated with this cavity geometry at the Mach 0.53 test condition. The green line represents the acoustic spectra derived from the time-dependent pressures in the CFD simulation without actuation. It is remarkable to note that the two-dimensional CFD accurately captures the frequency (as determined by the agreement with the first Rossiter tone) as well as the magnitude of the 160 dB Rossiter tone. The mismatch in frequency between the simulations and the test data is suspected to be related to a difference in the convective velocity at which the vortices pass over the cavity. It has been shown that a smaller time step for the simulation will reduce or eliminate the mismatch in frequency between cavity simulations and tests (Chapline & Birch). Unfortunately, a reduction in time-step of half (or more) would be needed, resulting in a time step on the order of 1x10-6 seconds and significantly increasing the time required to produce a solution. This would have prevented timely solutions on the computational hardware available to the author. The CFD simulations also show a peak at a sub-harmonic of the first Rossiter tone and a peak beyond the second Rossiter tone that are not observed in the test data.

The CFD results for the leading-edge simulated actuator and the simulated dual actuator are shown in blue and black lines, respectively, in Figure 61. The leading-edge actuator did not significantly increase the amplitude of the dominant first Rossiter tone; a finding that was also observed in experimental testing. This is likely because the dominant tone is the most stable and would require significant modification of the flow field to be perturbed. However, the dual, simulated-actuator results provide an increased amplitude of about 3 dB at the dominant first Rossiter tone. Apparently, the interaction and growth of the instabilities produced by two actuators is enough to significantly alter the cavity tones. Optimizing the tone amplification using phase control between the two actuators and the cavity would require many actuation combinations that would be best experimentally studied and refined with CFD simulation. This was outside of the scope of the current study and is recommended for future studies.

CHAPTER SEVEN FLOW ACTUATION TEST RESULTS AND DISCUSSION

Introduction

Wind tunnel tests were completed using the UTSI blowdown wind tunnel to study and evaluate the proposed actuators. The goal of the actuator experiment was to generate boundary layer flow disturbances which could grow and further couple with the cavity flow producing enhanced vertical flow structures for increased turbulence and mixing. Details of the test set up and the results of the tests are discussed in this chapter.

Several characteristic, non-dimensional frequencies are presented in this chapter. Non-dimensional frequencies related to the vortex shedding of the cavity leading-edge shear layer are shown by the symbol *R*. These may be interchangeably described as cavity Strouhal number, Rossiter tones, edge-tones, frequencies, or modes. This non-dimensional frequency is related to the cyclical process of leading-edge vortex convection across the open cavity. All non-dimensional Rossiter frequencies are based on the cavity length (*L*).

Non-dimensional frequencies associated with the three, fundamental cavity acoustic tones are given the symbol *A*. Each of the fundamental cavity acoustic tones is based on one of the cavity geometrical dimensions of the length (*L*), width (*W*), or depth(*D*), and the dimension used will be given in context. All cavity, fundamental-acoustic tones were calculated using equation (51).

Finally, the non-dimensional frequency for the actuator motion is based on the boundary-layer momentum thickness at the actuator leading-edge. Past research has shown that the most amplified instabilities in free shear layers scale with the non-dimensional frequency based on local boundary-layer momentum thickness (Michalke, 1972, 1977). Amplification of the free shear layer instabilities occurs for a non-dimensional frequency based on momentum thickness at the leading edge of the shear layer of about 0.013 (Samimy, Kim, Kastner, Adamovich, & Utkin, 2007). Non-dimensional frequencies for the actuator motion are given by the symbol K_{act}.

Furthermore, harmonics will be denoted by a leading integer and various modes will be denoted by a trailing integer. For example, the first Rossiter mode is *1R1,* the first harmonic of the first Rossiter mode is denoted by *2R1*, the tenth Rossiter mode is *1R10*, and so on. The same applies to the fundamental cavity acoustic modes.

There were no direct measurements of quantities from which boundary layer characteristics could be calculated during the wind tunnel tests because of lack of instrumentation and data acquisition channels. Therefore, representative boundary layer profiles were extracted from two-dimensional CFD simulations of the wind tunnel with geometry starting from the flow conditioning screen in the stilling chamber, through the nozzle contraction and test section, and terminating at the test section exit. Once the velocity profiles were extracted from the CFD solutions (at the location of the leading-edge of the actuator), boundary layer characteristics were calculated using equations (25), (26), and (32). The integrals were evaluated using backward finite-difference numerical integration method. Boundary layer characteristics for the Mach numbers tested during the wind tunnel tests are summarized in Table 4.

Table 4. Boundary layer characteristics at the leading-edge of the actuator.

Re/L	M	U	δ_{99}	δ*	θ	H	Reδ*	Reθ
10^6/ft	nonD	ft/s	in	in	in	nonD	nonD	nonD
0.70	0.1	116.3	1.33E-01	1.85E-02	1.33E-02	1.39	1083.3	778.1
1.46	0.2	214.9	1.28E-01	1.66E-02	1.25E-02	1.33	2023.3	1524.8
2.29	0.3	318.8	1.18E-01	1.46E-02	1.13E-02	1.29	2779.5	2158.5
3.17	0.4	419.0	1.13E-01	1.32E-02	1.04E-02	1.27	3498.4	2756.6
4.42	0.53	547.1	1.04E-01	1.21E-02	9.64E-03	1.26	4467.9	3549.8

Most actuation tests were accomplished with the actuator driving signal between 0 and 10 kHz, because of limitations in the data acquisition system when recording two or more high-frequency-response instrumentation channels. However, some higher, sample-rate signals were obtained with a single high-frequency-response instrument. Boundary layer actuation tests were accomplished at Mach 0.1 and 0.2, but cavity actuation tests were accomplished up to Mach 0.53. Using the range of frequencies and Mach numbers that were tested, along with the associated boundary layer momentum thickness, the actuator non-dimensional frequency (K_{act}) could be estimated. The range of actuator non-dimensional frequencies is summarized in Table 5.

Table 5. Actuator non-dimensional frequency (K_{act}).

Frequency	Mach Number				
Hz	0.1	0.2	0.3	0.4	0.53
1000	0.010	0.005	0.003	0.002	0.001
2000	0.019	0.010	0.006	0.004	0.003
4000	0.038	0.019	0.012	0.008	0.006
6000	0.057	0.029	0.018	0.012	0.009
8000	0.076	0.039	0.024	0.017	0.012
10000	0.095	0.048	0.030	0.021	0.015
20000	0.191	0.097	0.059	0.042	0.029

Experimental Set Up

Two experimental configurations were tested. For the first set of experiments, the largest actuator was installed on the flat floor of the tunnel and the response of the actuator was measured at tunnel conditions of Mach 0.1 up to Mach 0.5. (The flat-floor test was considered the baseline actuation test case.) Nine high-frequency-response pressure measurements were installed flush with the flat floor of the tunnel, downstream of the flow actuator, to measure the resulting unsteady effects of

the actuator on the flow. After the baseline, flat-floor tests were completed, a second experiment was conducted to evaluate and study the multi-level actuator plus cavity system. For the second set of experiments, a different floor section with a removable cavity (L/D=2.5) was installed. The cavity tones were measured using two high-frequency-response pressure measurements installed in the floor of the cavity. Cavity tones were measured during a tunnel-flow Mach sweep, from 0.1 up to a Mach number of 0.53, to establish the baseline cavity flow oscillations without actuation. A new, low-profile actuator bank was installed upstream of the cavity and the specific capability of the actuator to excite cavity instability was studied.

Flat-floor wind tunnel test setup

A photograph of the actuator installed in the wind tunnel test section for the flat plate test is shown in Figure 62. The test article used in this test was test article #5 (Figure 17) with an actuator tip length of 1.81 inches. A square piece of 0.003-inch shim steel was glued to the polycarbonate wind tunnel floor and the actuator was glued to the shim steel. The top piezo layer of the actuator was exposed to the flow during the flat-floor test. The bottom piezo layer of the actuator was glued directly to the shim steel on the tunnel floor.

The driving signal was supplied to the actuator via two 32-gage signal wires. One wire was soldered to the bottom piezo layer (prior to bonding to the tunnel floor) and one wire was soldered to the top piezo layer and was exposed to the flow for only the flat-floor test. The signal wires were run through a hole in the tunnel floor to allow the wires to be connected to the piezo driver. (The hole in the tunnel floor was plugged with plumber's putty during tunnel operations to prevent any flow leaks). A function generator was used to create an alternating driving signal. The function generator output was 10 volts. A linear amplifier (Piezo Systems' EPA-104-115) was used to drive the piezoelectric actuator devices. The linear amplifier has a maximum input voltage of 10 volts (which was supplied by the function generator), and a maximum output voltage of +/- 200 volts. However, only approximately 80 to 100 volts was needed to drive the actuator. An HP 3325A function generator was used to supply a 10-volt sinusoidal signal to the linear amplifier.

Nine high-response pressure measurements were installed flush to the tunnel floor as shown in Figure 62. The holes for the pressure instrumentation were centered in the tunnel test section floor and were spaced 0.5 inches apart in both directions. In nearly all cases tested, all the high-response pressure measurements showed comparable results with the only visible differences being channel noise that was consistent even when the tunnel was not operating. Furthermore, the center measurement (labeled PK33) was the least noisy among the group. Therefore, most of the test results shown in this section are taken from the PK33 measurement and are representative of all other measurements.

The first tunnel test run was accomplished to determine the range of supply pressures needed to achieve various test section Mach numbers. It was determined during the next tunnel run that there was an error in the facility data reduction when calculating Mach number. The error was corrected and the tunnel Mach number calibration points were re-tested. The results of these tunnel calibration runs were presented in Chapter Five.

During the first set of actuator tests, arcing was observed between tip of actuator and shim steel to which the actuator was mounted. A piece of insulating tape was placed under the actuator to prevent arcing, and testing was continued. Repeat testing was accomplished in attempts to

duplicate earlier test results. Unfortunately, the high-response pressure instrumentation excitation was not turned on before running the test. Despite not turning on the instrument excitation, a signal was still observed in the high-response pressures when the actuator was operated. A problem with the data acquisition was suspected, but after a thorough investigation, it was determined that a signal was being radiated from the actuator signal wires. The actuator signal wires were acting as a transmitting antenna when the actuator was powered, and the signal was contaminating all channels on the data acquisition system. The actuator signal wires were then twisted and shielded, and the wire shield was grounded to the facility. This fixed the signal contamination and testing proceeded once again.

Actuator frequency sweeps and tunnel Mach number sweeps were completed to look for actuator flow control coupling with the boundary-layer flow. Actuator frequency sweeps were accomplished between 0 and 10 kHz and flow control was observed using the high-response instrumentation. However, the signal was seriously aliased above 5 kHz because the data acquisition system was limited to 200 kHz aggregate sampling rate. With 10 high-response pressures, each could only be sampled at 20 kHz. At a sample rate of 20 kHz, the usable bandwidth is limited to the Nyquist frequency of 10 kHz. Any signal content above 10 kHz was aliased into the lower frequency bands. It was decided to reduce the number of pressure measurements from 10 to 1, and hence, increase sampling rate to the maximum available sampling rate of 200 kHz. Actuator tests were completed with frequency sweeps from 0 to 10 kHz and 0 to 20 kHz and actuator flow-control and coupling was observed in the collected data.

Following a successful flow control test with the flat plate configuration, it was decided to remove the flat plate configuration and install a custom-fabricated floor plate with a cavity configuration (Figure 63).

Cavity test setup

A photograph of the test section floor configured for the cavity test is shown in Figure 64. The cavity has dimensions of L=0.75 inches, D=0.3 inches, and W=1.5 inches for an L/D=2.5 and W/D=5. A rectangular hole was milled in a large section of the test-section floor to allow cavity blocks to be easily inserted and removed. The test section floor was machined out of aluminum and the cavity blocks were machined out of polycarbonate plastic. Actuators were installed upstream of the cavity leading edge and the actuator signal wires were run through a hole in the test section floor (the hole was plugged with plumber's putty during test operations).

Two high-response pressure measurements were installed on the centerline of the cavity/test section and were mounted flush with the floor of the cavity. The pressure measurements were spaced equidistant from the cavity leading-edge wall and the cavity aft-edge wall. The pressure instrumentation was bonded to the cavity using a clear RTV sealant to allow faulty instruments to be removed/replaced. It was desired to use a sampling rate of 200 kHz to observe high-frequency, small-scale disturbances, but unfortunately, the data acquisition system was limited. When using multiple high-response pressure instruments, the data acquisition system limits the user to 20 kHz sampling rate.

The first actuator that was tested was an actuator bank made from three of the configurations shown as test article #7, shown in Figure 4, chapter 3. This actuator was bonded to the test section floor using super glue, which unfortunately did not hold when the tunnel was brought on condition. The

first actuator bank was blown out of the tunnel and was destroyed. The second actuator that was tested was the same actuator that was used for the flat-floor test, test article #5 from Figure 17. Unfortunately, this actuator was damaged in attempts to run the tunnel on a new high-pressure air source (more details discussed below). The final actuator that was tested was of an improved design which made the actuator stronger and less susceptible to facility-generated failures.

The final actuator was bonded to the aluminum test section floor using epoxy. An actuator cover was also bonded to the aluminum test section floor upstream of the actuators and on top of the actuators to protect the actuators from high-speed flow, to seal any small gaps around the actuator and the floor, and to make the top of the actuator pack flush with the floor. The actuators were installed as far upstream of the cavity as the floor structure would allow resulting in approximately 0.25 inches between the tip of the actuator and the cavity leading edge. Placing the actuator tips upstream of the cavity, as opposed to coincident with the cavity leading edge, allows the small disturbances produced by the actuator to grow as the disturbances couple with the flow and protect the actuator from buffeting at the cavity leading edge.

A photograph of the final actuator bank is shown in Figure 65. There are three actuators made of 0.003-inch shim steel between two layers of 0.0075-inch piezoceramic sheets. The dimensions of the three actuators are those of bench test article #7 described in Figure 17. The top and bottom layers of piezoceramic are bonded to pieces of 0.003-inch shim steel with a tab on one end that is used to solder the ground wires. All layers were bonded together using a conductive super glue allowing the actuator to be conductive throughout. The base of each actuator was extended to allow the signal wire to be soldered to the shim steel instead of trying to directly solder wires to the piezoceramic or trying to sandwich the wires into the design. This arrangement has several benefits:

- it allows a low-profile actuator design with multiple actuators.
- minimum wiring is needed even when each actuator is wired in parallel.
- the maximum amplitude can be realized because the piezoceramic layers for each actuator are wired in parallel.
- there is no need to solder directly to the ceramic (which is difficult and resulted, in some cases, in over-stressing the ceramic leading to cracks).
- the actuator is robust because the piezoceramic and shim steel layers on top and bottom increase the stiffness of the final structure while maintaining the flexibility of the actuator tips.

The first cavity test without actuation occurred after the facility was reconfigured following a pressure regulator failure. Since the high-pressure air source was located in another facility, the pressure drop in the line was too great to maintain the mass flow rate needed to operate the tunnel at high Mach numbers. The maximum tunnel Mach number was reduced to 0.5 and the facility could only maintain the mass flow needed for this condition for approximately 5 to 10 seconds. This timeframe was not enough to perform research experiments where the actuator could be studied at different frequencies, so the facility staff decided to reconfigure the facility again to run from the high-pressure-air bottle farm. After the reconfigure, the pressure regulator had to be installed and removed at the bottle farm each time the wind tunnel was operated to prevent conflicts with other facilities.

Unfortunately, the first test that was run with high-pressure-air supplied from the bottle farm resulted in blowing water out of the high-pressure-air line and into the tunnel. The actuator and high-response pressure instrumentation were ruined. The actuator was removed and the pressure instrumentation were replaced (but the naming convention remained the same in the data acquisition system). The tunnel operating procedures were then changed so that the test article and tunnel floor were removed and the wind tunnel was operated for approximately 10 minutes at Mach number of 0.5 to evacuate any moisture from the high-pressure-air lines and the tunnel. Following tunnel moisture evacuation, the tunnel floor and test article were re-installed.

Flat-floor wind tunnel test results with actuation

The first series of flat floor tests with the actuator operating were accomplished by sweeping tunnel conditions by slowly opening the control valve continuously from minimum open to fully open. The actuator was operated at 100 volts peak-to-peak at discrete frequencies of 2, 3, 4, and 5 kHz. Only one actuator frequency was tested during a Mach sweep. The test procedure was to open the tunnel control valve to the minimum position, set the actuator frequency, then slowly open the tunnel control valve to fully open. When operated transiently, the tunnel produced screech tones near 3.8 kHz and 7.6 kHz in the low Mach number range. These screech tones generally disappeared if the test conditions were allowed to stabilize. The effect of the actuator could not be observed in the data for the 2, 3, and 4 kHz actuation tests. However, a faint actuation signal was visible in all 9 high-response pressure measurements when the actuator was operated at 5 kHz.

Results of the successful 5 kHz actuation during a Mach number sweep are presented in the spectrogram (or carpet plot) shown in Figure 66. These data were collected at a sample rate of 20 kHz giving a useful bandwidth of 10 kHz, per the Nyquist criterion. The horizontal axis is frequency with units of kHz. The color scale shows the Sound Pressure Level (SPL) in decibels which was defined in equation (80). There are two vertical axes, the first of which shows the time scale with units of seconds. The second vertical axis shows the sweep in test section Mach number. The low-frequency tunnel noise can be seen in the lower left corner of the plot. As the Mach number increases, the tunnel noise reaches a SPL of at least 130 dB and is broadband in nature. The tunnel screech tone and the first harmonic thereof can also be seen at the low Mach numbers at frequencies of 3.8 and 7.6 kHz. These tones are not the result of actuation and were continually encountered when changing tunnel test conditions with or without actuator operation. Finally, the actuation pressure response can be observed below Mach 0.3 as a vertical line with SPL of approximately 120 dB at 5 kHz frequency. Above Mach 0.3, the tunnel noise appeared to overcome the actuator pressure response.

Given the limited success of the actuator during the Mach sweep, and the inherent screech tones produced by the tunnel during transient operations, it was decided to study the actuator response at fixed Mach numbers between 0.1 and 0.3.

Results of an actuator frequency sweep from 0 to 10 kHz at a fixed Mach number of 0.11 are shown in Figure 67. A 10-second tunnel run at Mach 0.11 without the actuator operating is shown in Figure 67a. These results show the baseline noise level in the tunnel and that the test conditions are stationary in time, not having drifts in the mean or the standard deviation. A 10-second run is shown in Figure 67b in which the actuator was driven at 100 volts starting from rest at t=0 seconds and linearly sweeping frequency to 10 kHz at t=10 seconds by changing frequency by

approximately 1 kHz per second. (The function generator used for this test had analog frequency control. Therefore, the frequency sweep was manually controlled which explains the small waviness in the actuator pressure response.) Both carpet plots have a vertical axis of time, a horizontal axis of frequency, and colors defined by SPL in dB. All transient signals were separated into blocks of 2048 points and were windowed using a Blackman-Harris window of the same length. Blocks were overlapped by 75%, or 1536 points. The actuator pressure response can be seen beginning at an actuator non-dimensional frequency of approximately K_{act}=0.047, or 4.9 kHz. Also, as the actuation frequency gets closer to the Nyquist frequency of 10 kHz, the pressure signal is aliased where actuator responses at frequencies higher than 10 kHz are folded over to lower frequencies. Despite the aliasing and tunnel noise, a clear actuator response signal can be seen with amplitude near 130 dB.

The tunnel background noise was removed from the actuated-flow data to illuminate the actuation results. Removing the tunnel background noise from the plot is accomplished by taking the ratio of power spectrum of the run with actuation to the run without actuation, then converting to SPL using equation (84). Here, *Pxx* is the power spectrum of the run with actuation and *Pyy* is the power spectrum of the run without actuation.

$$\mathrm{SPL}_{\mathrm{actuation}} = 10\log_{10}\left(\frac{\mathrm{Pxx}}{\mathrm{Pyy}}\right) \tag{84}$$

The results of removing the tunnel background noise from the run with actuation are shown in Figure 68. The colors represent a delta-SPL above the tunnel noise floor. The actuator was driven for the entire 10 seconds beginning at rest and ending at 10 kHz at the end of the 10 second run. The actuator produces enough perturbation to be visible above the tunnel noise at approximately 4.9 kHz. The actuator response is clearly seen in Figure 68 to be approximately 40 dB above the tunnel background. The aliasing of the response can also be seen more clearly when tunnel background noise is removed.

A second set of 10-second runs with and without actuation were performed at Mach 0.2. These results are shown in Figure 69 and Figure 70. In Figure 69, the results are shown in an absolute-magnitude sense. A 10-second run without actuator operation was again acquired before actuation was started to ensure a good measure of the tunnel background noise at this test condition. Following the background noise run, actuation was again performed using approximately 100 volts and a frequency sweep from rest to 10 kHz over the 10-second data-acquisition span. At Mach 0.2, stronger tunnel tones in the low-frequency band can be clearly observed. Nevertheless, the actuator pressure response at approximately 0.5 inches downstream of the actuator tip can be seen in the right-half of Figure 69 and in the normalized version shown in Figure 70. Also, similar to the observations in the Mach 0.1 data, the effect of the actuator cannot be observed below a non-dimensional frequency of approximately K_{act}=0.036 at Mach 0.2 (or approximately 4 at Mach 0.1). Furthermore, there is no visible aliasing of the actuator response at Mach 0.2. This does not indicate the actuator pressure response is not aliased; it just cannot be observed above the background noise.

These results indicated that the actuator was working properly. However, there were two issues that warranted further study. First, because of the high tunnel background noise, actuation could not be observed clearly at low actuation frequencies. Second, since the most interesting actuation results could be clearly seen at higher frequencies, it was decided to use only one high-response

pressure measurement (PK33) and to change the data acquisition sampling rate to the maximum available of 200 kHz.

A repeat of the actuation test was performed with two 10-second runs, one run with an actuation sweep from rest to 10 kHz, and one run with an actuation sweep from rest to 20 kHz. The results of the actuation tests with sampling rate at 200 kHz are shown in Figure 71 and Figure 72. In Figure 71, the results are normalized by the tunnel background noise run without actuation as previously described. The higher data acquisition sampling rate allows more of the actuator flow response to be observed. The actuator not only creates pressure disturbances at frequencies which the actuator was driven, but also at harmonics as high as nine-times the actuator driving frequency. Beyond the ninth harmonic, the pressure disturbances become smaller and are not observable over the tunnel background noise. The disturbances created by the actuator are observable up to about 62 kHz or a non-dimensional frequency of approximately K_{act}=0.59. This demonstrates the ability of the actuator to produce pressure disturbances at much higher energy levels and amplitudes 30 to 40 dB higher than the background flow level. The pressure disturbances have coupled with the flow to reach a new flow state.

Results for an actuator sweep from 0 to 20 kHz are shown in Figure 71b, and the results are even more interesting than the first frequency sweep. Once again, the actuator has coupled with the flow to produce small-scale pressure disturbances at 9 to 10 times the actuation frequency. In fact, as the actuation frequency increases close to the 100 kHz Nyquist frequency, the pressure response becomes aliased like the data acquired at 20 kHz. Also like previous results, the amplitudes are at least 30 to 40 dB above the tunnel noise floor. Furthermore, since pressure responses are aliased beyond 200 kHz and are clearly folded back into the signal, the size of the disturbances is expected to be even smaller at the higher frequencies. Finally, the 0 to 20 kHz actuation sweep demonstrated another interesting feature: partial harmonics of the driving frequency also have amplitudes significantly higher than the background noise. These appear as small spots between the primary harmonics that show up as curved peaks on the carpet plot. The harmonics were investigated further by plotting a slice of the carpet plot at a constant time of t=7.86 seconds. The sliced results are shown in Figure 72. Here the pressure disturbance at the driving frequency is evident as the first peak at the lowest frequency. All other spikes are harmonics of the driving frequency. The 0 to 10 kHz frequency sweep is shown in Figure 72a. The flow coupling harmonics have clear peaks to the ninth harmonic. Similarly, the 0 to 20 kHz frequency sweep is shown in Figure 72b. Here, the harmonics and partial harmonics are also depicted and are clearly observable until the data begins to be aliased again in the 70 to 100 kHz frequency band. It is interesting to note that both actuator sweeps were performed at the same test conditions, but produced significantly different results. No partial harmonics were visible in the 0 to 10 kHz sweep, but were visible in the 0 to 20 kHz sweep. Also, the highest amplitude pressure disturbance for the 0 to 10 kHz sweep was at the driving frequency. Alternatively, the highest amplitude pressure disturbance for the 0 to 20 kHz sweep occurred at the third harmonic of the driving frequency. These results seem to indicate that there is a time-dependent effect on the stability of the flow caused by changing the actuation frequency. The flow stability appears to be sensitive to the rate of change of actuation frequency indicating that a faster increase in pressure disturbance produces more instabilities in the flow. These results tend to agree with equation (65) derived on page 35 in which the time-dependent change of velocity squared is related to the time-dependent change of pressure.

Cavity Test Results without Actuation

Measurements of the fluctuating pressure on the floor of the cavity are shown in Figure 73. The usual carpet plot is shown on the left side of the figure, but has some additional, cavity-related information. Again, the horizontal axis is the frequency in kHz, the colors represent sound-pressure-levels and the vertical axis is time in seconds with the corresponding Mach number. The Rossiter cavity tones have been overlaid and are denoted by R1, R2, and R3 which correspond to the first, second, and third Rossiter modes, respectively. The high-pressure-air supply valve was opened and the conditions were held for 10 seconds to ensure all systems were operating properly. Then the supply valve was slowly opened to the fully open position, achieving a Mach number of about 0.53. The cavity resonance tones began to stabilize around 22 seconds or a Mach number of 0.45. These are clearly visible as the yellow streak near the first Rossiter tone and the blurred yellow region near the second Rossiter tone. The first two cavity tones agree well with the first and second Rossiter tones. The first tone contains the highest amplitude, about 160 dB, which is well above the tunnel noise floor. The third Rossiter tone was not visible because the data acquisition system was limited to 20 kHz sampling rate putting the third Rossiter tone beyond the Nyquist frequency in the region of interest. Note that the Rossiter tones are not visible at the lower Mach numbers indicating that the flow is not being amplified or that the tunnel background noise is too high to observe the tones.

The right-half of Figure 73 shows a detailed view of the 7 seconds of operation at a Mach number of 0.53. The upper right shows the time history where the data appear stationary with a peak-to-peak amplitude of about 2 psid. The lower right portion of the figure shows the power spectrum in terms of sound pressure level as a function of frequency. Here, the Rossiter frequencies have been overlaid as well as the first-fundamental acoustic modes of the cavity based on the cavity dimensions (FD based on depth, FW based on width, FL based on length). This subset of the entire run clearly shows the strong, 160 dB peak in agreement with the first Rossiter tone indicating that the cavity "edge-tones" are dominating the flow. Note that the fundamental acoustic frequency for the cavity based on depth is the closest fundamental acoustic tone to any of the Rossiter tones.

Cavity with Actuation Test Results

The first actuator/cavity flow coupling test was planned to be accomplished at the Mach 0.53 condition where the strong, 160 dB cavity tone was observed in the previous test. However, the facility staff brought the tunnel online to Mach 0.3 and paused for nearly two-minutes to adjust communications from the data acquisition area to the high-pressure-air valve control area. An attempt to actuate the flow was attempted at this condition and will be discussed later. Once the facility staff brought the tunnel online to the Mach 0.53 condition, actuation was attempted by setting the actuator supply voltage to 100 volts, and the actuation frequency equal to the first Rossiter tone associated with this condition (about 3.4 kHz). Unfortunately, no response could be observed in the data when operating the actuator at this condition. The cavity resonance of 160 dB near 3.4 kHz was observed, but changing the actuator voltage amplitude, frequency, or phase delay did not result in a change of the cavity resonance. Other frequencies near the second or third Rossiter tones were also attempted to no avail. It is suspected that the cavity resonance at Mach 0.53 of 160 dB and 3.4 kHz is very stable and would require significantly large disturbances to perturb the cavity into a higher resonant mode or to attenuate the stable mode. Furthermore, at Mach 0.53, the convective velocity is very high and any disturbances produced by the actuators

are quickly swept downstream. This likely prevented the disturbances from growing enough to be able to attenuate or amplify the cavity resonance when the actuators were positioned near the leading-edge of the cavity. Moving the actuator well upstream of the cavity may provide enough distance for the disturbances to grow enough to influence the cavity flow field.

Despite the failed actuation test at the higher Mach number and more stable cavity resonant condition, the actuators were still successful at producing flow disturbances that significantly perturbed the flow field. Consider the results presented in Figure 74 which show the results of the tunnel startup run with actuation during a stable pause near the end of the startup run. Here, two carpet-plots are shown. The left plot represents the data acquired from the pressure instrument (PK33) located on the floor closest to the leading edge of the cavity and the right plot represents the data from the instrument (PK21) located on the floor closest to the trailing edge of the cavity. Similar to previous data presentations, the colors represent sound pressure level in dB, the horizontal axis is the frequency in Hz, and the vertical axes are time in seconds and the associated test section Mach number. The typical tunnel noise associated with the facility is clearly present once again in the lower frequency bands. The cavity Rossiter edge-tones are overlaid as black lines and labeled R1, R2, and R3 for the first, second, or third-mode tones. The second pressure instrument, PK21, shown on the right of the figure, has a significant amount of noise in the 4.2 kHz band. The noise was at a frequency near the Rossiter tone of interest, was not observed in the first pressure instrument (PK33), and caused the data from PK21 to be unusable. Further analysis was accomplished using only the PK33 transducer.

Near the end of the test run shown in Figure 74, there is a small patch of yellow where the actuator was operated. This region shows a broad-band spike in the data on the order of 125 dB which is significantly higher than the region surrounding the spot in both the frequency and time axes. Further study into the actuation region was completed to ensure that the signal was not being contaminated by noise and the actuation results were real.

The time history plot of PK33 during the tunnel startup run and subsequent holding at Mach 0.3 is shown in Figure 75. The time history is shown in blue and three slices are highlighted in distinct colors. The time slice over which the actuator was operating is highlighted in red, and time slices before and after the actuation are shown in black and green, respectively. Each of these three slices were run through the signal processing algorithms to produce a sound pressure level vs. frequency plot. Once again, the first three Rossiter tones are overlaid, as well as the cavity first-mode fundamental acoustic frequencies.

For the time slice before actuation (black line), there is a strong peak near 0.5 kHz corresponding to the tunnel noise followed by a second spike just under 4 kHz, then a small broader-band hump at about 4.3 kHz with SPL of 116 dB. These small humps were recognized to be close to a Rossiter tones for the cavity at this condition and it was decided to attempt flow control actuation. The resulting spectrum for the time slice when the actuator was operating is shown in red. The actuator produced a peak in the spectrum around 4.3 kHz of approximately 124 dB, about 8 dB higher than without actuation. The peak is also broader indicating that the instabilities created by the actuation have a wider range of sizes than were present in the flow without actuation. Furthermore, a change in flow state can also be seen near the 10-kHz frequency band. Unfortunately, the signal processing limits the results to 10 kHz, but there is a distinct rise in amplitude near the third Rossiter tone when the second tone is excited using the actuator. When the actuator was turned off, the flow

returned to the previous state. Note that the closest fundamental cavity acoustic tone to any of the Rossiter tones is the tone based on cavity width. It is the experience of the author, and others (Bauer & Dix, 1991b) that when the natural width tone is close to a Rossiter tone, the cavity resonance is very unstable. This is probably because cavity flows are three-dimensional in nature, and shear-flow stability is sensitive to cross-stream disturbances.

Following the successful flow actuation at Mach 0.3, a series of stationary runs were attempted at Mach 0.1 and 0.2. Data points were acquired for 10 seconds with the actuator operating at a constant frequency for the entire 10 seconds. This provided a stable flow condition from which many FFT averages could be obtained to produce frequency resolution on the order of 1 Hz.

Pressure spectra on the floor of the cavity for the actuation runs at Mach 0.1 for six different actuation frequencies around the fourth-, fifth-, and sixth-mode Rossiter tones are shown in Figure 76. These results were observed when the cavity was in the upstream position (0.25 inches between actuator tips and cavity leading edge). In each case, the actuator produces a clear tone (blue lines) in the cavity that was not present without actuation (red lines). The largest amplitude cause by actuation resulted when the actuator was operated near the fifth-mode Rossiter tone, or 5 kHz with a magnitude of 111 dB (approximately 15 dB of amplification) where a tone was not observable without actuation. Similar results can be observed when the actuator frequency was increased to 5.1 kHz (amplitude of 110 dB or increase of 20 dB above non-actuated case) and 5.2 kHz (amplitude of 108 dB or 20 dB above non-actuated case). In both cases, two clear tones are generated by the actuator near both the fifth- and sixth-mode Rossiter tones. This demonstrates that the actuator, operating at a single frequency, excites the boundary layer upstream of the cavity, couples with the shear layer, and produces disturbances that can excite cavity tones at multiple frequencies. The results were similar when decreasing actuation frequency from 5 kHz to 4.9 kHz. Multiple tones were clearly excited by the flow coupling. Reducing the actuation frequency to 4.8 kHz and 4.7 kHz resulted in less excitation and flow coupling, and further reduction of actuation frequency resulted in no observable tones or flow coupling. This seems to indicate that there was some physical phenomenon that allowed the actuation to couple with the flow near the fifth- and sixth-mode Rossiter tones.

Inspection of the cavity acoustic tones sheds some light on why the cavity flow field was unstable and easily excitable near the 5-kHz band at Mach 0.1. Following Rona's analysis, the cavity flow field is prone to resonance when a cavity acoustic resonance mode matches a component of the harmonic series of any Rossiter mode. The intercepts of the quantity $1\text{-}oR_m/A_n = f(M_\infty)$ define the Mach numbers at which the Rossiter (R_m) and fundamental acoustic (A_n) Strouhal numbers resonate (m and n are integer mode numbers and o is an integer harmonic) (Rona, 2007). The Rona quantity is shown in Figure 77 for various Rossiter and fundamental cavity acoustic modes relevant to the actuation test at Mach 0.1 with the cavity in the upstream position. Three plots are shown in the figure; one plot for each fundamental cavity dimension. The black horizontal lines indicate the zeros of the Rona quantity and the black vertical lines represent the Mach number at which actuation was tested. The solid and dashed lines represent the Rona curves for Rossiter modes 4,5, and 6 and the fundamental acoustic modes 1, 2, and 3. The crossings of the horizontal black lines with the Rona quantities are the areas of interest. Based on the results shown in Figure 76, the actuator driving signal is closest to the fifth Rossiter tone. For the cavity fundamental-acoustic mode based on cavity length, there is not significant coupling between the cavity length mode and nearby Rossiter modes. It is also clear that the fundamental cavity acoustic mode based on cavity

depth does not amplify with the nearby Rossiter tones as indicated by the large distance between the Rona curves and the horizontal black line at Mach 0.1. However, inspection of the first-mode fundamental cavity acoustic mode based on cavity width shows that this mode couples with the fifth Rossiter tone at the Mach 0.1 test condition. This analysis seems to indicate that, even though these tones were not visible in the spectrum when the actuator was stationary, they are highly unstable and easily controlled by the actuator. Comparable results were obtained at the Mach 0.3 and 0.2 cases and were also observed when the cavity was placed in the downstream position.

Pressure spectra on the floor of the cavity (installed in upstream position) for the actuation runs at Mach 0.2 and three different actuation frequencies around the fourth-mode Rossiter tone are shown in Figure 78. Actuation at 7.3 kHz produced a 2 to 3 dB excitation of the R4 tone. Increasing the actuation frequency to 7.4 kHz resulted in a 5 dB increase at the R4 tone as well as a 5 dB increase at the R2 tone. This indicates that the actuator produced coupling with the cavity flow field not only at the driving frequency, but sub-harmonics of that frequency also. Increasing the actuation frequency to 7.5 kHz resulted in only a 5 dB increase at the R4 tone. Actuation was also tested near the R1, R2, R3, and R5 frequencies, but no change in cavity flow field was observed. Inspection of the Rona curves in Figure 79 reveals that, at the Mach 0.2 condition with the cavity in the upstream position, there are two possible couplings that are being excited by the actuator. The first possible mode that was excited is the coupling between the R5 and the A1 modes for the cavity length. This curve crosses zero at almost exactly the Mach 0.2 test condition indicating that the R5 mode should be easily excitable. However, the pressure spectra do not show tone amplification near the R5 frequency. Further inspection reveals that the cavity width mode is, once again, the likely mode that is being excited by the actuator. The Rona curves for the R3/A1 tone, the R4/A2, and the R2/A1 tone are close to zero at the test Mach number. Furthermore, the R4/A2 and R2/A1 tones have almost identical Rona curves which indicates that these tones are closely coupled and that perhaps the R4/A2 tone is simply the first harmonic of the R2/A1 tone, i.e. R4/A2 = 2(R2/A1). This explains why the R2 tone was excited when the actuator was driven at the R4 frequency. Examination of the cavity fundamental acoustic mode based on cavity depth reveals that there is likely no sensitivity of these modes to actuation at the tested Mach number of 0.2.

Even more interesting results were obtained when the cavity was removed and re-installed in the downstream position which locates the actuator tip about 4.25 inches from the cavity leading edge. Actuation results at the Mach 0.1 test condition for the cavity located in the downstream position are shown in Figure 80. The actuator was first driven at 4.8 kHz which was close to the R5 tone and created successful amplification of cavity tones when the cavity was installed in the upstream position. However, results of actuation were very different when the cavity was located further downstream of the actuator. When driven at 4.8 kHz, cavity tones were excited, not at the fifth Rossiter tone, but near the seventh-, ninth-, and tenth- Rossiter tones. Furthermore, the amplitude of the excited tones was much greater for the downstream cavity position than the upstream position. Near the R7 tone, the amplitude was increased by 10 dB, near the R9 tone, the amplitude was increased by 27 dB, and near the R10 tone, the amplitude was increased by 5 dB. These results indicate that the disturbances produced by the actuator grew as they convected toward the cavity coupling with the cavity flow to produce large-amplitude excitations in the cavity flow field. Comparable results were obtained when the actuator was operated at 4.5 kHz. As much as 25 dB of excitation between the R7 and R8 tones was achieved with additional excitation at the R9 and between the R9 and R10 tones of about 8 dB in amplitude. Inspection of the Rona curves at the

Mach 0.2 test condition indicates that the likely acoustic modes that are coupled with the Rossiter tones where excitation occurred were, again, the cavity fundamental acoustic mode based on the cavity width. The Rona curves for this condition are shown in Figure 81. The intersection of the curves with the horizontal line near Mach 0.1 indicate that the R8 and R9 tones are coupled with the A1 tone for the cavity length to produce an unstable cavity flow field. Furthermore, the R7, R8, and R9 tones are coupled with the A2 cavity tone based on cavity width. It is hypothesized that the large cavity amplification that was observed when the cavity was located further downstream from the actuator is because of the alignment of many of the higher-level Rossiter tones with multiple cavity acoustic modes.

Again, comparable results were observed when the actuator was operated at 6.387 kHz (near the R4 mode) in Mach 0.2 flow with the cavity in the downstream position. Amplification of tones between Rossiter modes is clearly observed in Figure 82. At this condition, the cavity amplification is about 15 dB at 7.6 kHz (or 2 times the driving frequency) and about 17 dB at 3.8 kHz (or a little more than half the driving frequency). The amplification of the cavity flow field is broad-band in nature between the R4 and R5 tones, perhaps because of significant coupling that is contributing from the proximity to both tones. Like the Mach 0.1 case, inspection of the Rona curves indicates that the actuator is likely coupling with multiple Rossiter and cavity fundamental acoustic tones. The intersection of the Rona curves with the horizontal lines in Figure 83 indicates the actuator is likely coupling with the R6/A1 and R5/A1 tones for the acoustic tones based on cavity length, as well as the R3/A1 and R5/A3 tones for the acoustic tones based on cavity width. Again, the cavity fundamental acoustic mode based on the cavity depth does not appear to influence the cavity resonance. The amplification and excitation of tones observed in Figure 82 is likely of higher amplitude and broader frequency than previously observed results because of the multiple Rossiter tones as well as the multiple cavity tones that the actuator disturbances interact with when they grow in the boundary layer and couple with the cavity shear layer.

These results indicate that the flow conditions where fundamental acoustic tones couple with Rossiter edge-tones were very unstable and could be controlled by small disturbances produced from the three-actuator bank upstream of the cavity leading edge at Mach numbers of 0.1, 0.2, and 0.3. Placing the cavity further downstream from the actuator bank resulted in significantly higher amplification of cavity tones because of the growth of the instabilities produced by the actuator. At the Mach 0.53 condition, the actuator was unable to produce a change in flow state when the actuator was operated at the frequency of the dominant Rossiter tone, probably because of one or more of the following:

- The dominant Rossiter tone was close to the cavity fundamental tone based on cavity depth which is not the most unstable combination.
- The dominant Rossiter tone was very stable at Mach 0.53 and would require significant energy input to perturb the flow away from the stable state.
- The convective velocity was too high for the small disturbances produced by the actuator to grow enough to affect the stable cavity tone when the actuator was placed only 0.25 inches upstream of the leading edge of the cavity.

CHAPTER EIGHT CONCLUSION

A multi-level, flow-control actuator was developed and tested in a relevant flow environment. Two piezoceramic plates are used to drive a thin steel material in sinusoidal motion. The actuator design included provisions for multiple actuators driven by a single piezoceramic pair. The actuator design has several benefits over other flow actuator designs:

- The design enables a low-profile actuator.
- The design enables multiple actuators to be driven on a single pair of piezoelectric crystals and a single power source.
- Minimum wiring is needed even when each actuator is wired in parallel.
- The maximum amplitude can be realized because the piezoceramic layers for each actuator are wired in parallel.
- There is no need to solder wires directly to the ceramic (which is difficult and can over-stress the ceramic).
- The layered architecture increases the stiffness of the final structure while maintaining the flexibility at the actuator tips.
- The power requirements to drive a bank of actuators are minimal.

The actuators were tested for the ability to create instabilities in boundary layers and for the ability to control cavity flow by coupling the excited boundary layer flow with the cavity flow. Actuation results were measured in a subsonic wind tunnel using high-response Kulite pressure instrumentation. Flow actuation and coupling tests were completed at test conditions of Mach 0.1, 0.2, 0.3, and 0.53 and Reynolds numbers based on momentum thickness from 778 to 3550. Three configurations were tested:

- the actuator in the boundary layer of the wind tunnel floor,
- the actuator located approximately 22 momentum thicknesses (or 0.25 inches) upstream of the leading-edge of a L/D=2.5 rectangular cavity, and
- the actuator located approximately 371 momentum thicknesses (or 4.25 inches) upstream of the leading-edge of the same L/D=2.5 rectangular cavity.

Experimental Results

When tested in boundary-layer flow only, the actuator creates pressure disturbances at frequencies which the actuator was driven and at harmonics as high as nine-times the actuator driving frequency. Amplitudes of the disturbances produced by the actuator were 30 to 40 dB higher than the background flow level. Beyond the ninth harmonic, the pressure disturbances become smaller and are not observable over the tunnel background noise. The disturbances created by the actuator couple with the boundary layer flow and are observable up to about 62 kHz or a non-dimensional frequency of approximately K_{act}=0.59.

The boundary-layer tests were completed using two actuator frequency sweep rates of 1 kHz/sec and 2 kHz/sec. The measured pressure disturbances were different for the two frequency sweep rates when test conditions were held constant. Partial harmonics of the driving frequency with amplitudes significantly higher than the background noise were observed for the 2 kHz/sec frequency sweep rate but were not observed for the 1 kHz/sec sweep rate. Furthermore, the highest

amplitude pressure disturbance for the 0 to 10 kHz sweep was at the driving frequency, but the highest amplitude pressure disturbance for the 0 to 20 kHz sweep occurred at the third harmonic of the driving frequency. These results seem to indicate that there is a time-dependent effect on the stability of the flow caused by changing the rate of actuation frequency.

A bank of three actuators was designed, fabricated, and tested for the ability to excite instabilities in cavity flows by producing disturbances in the upstream boundary layer that couple with the cavity flow. Actuation response was measured using two high-response pressure transducers in the floor of the cavity. Cavity actuation tests were completed at Mach numbers of 0.1, 0.2, 0.3, and 0.53. The Rossiter "edge-tones" of the cavity were used as starting points for selecting actuator driving frequencies.

Actuator operation did not produce amplified cavity oscillations at all Rossiter tones. The actuator was unable to produce a change in flow state when the actuator was operated at the frequency of the dominant Rossiter tone, probably because of one or more of the following:

- The dominant Rossiter tone was close to the cavity fundamental tone based on cavity depth (which is not the most unstable combination).
- The dominant Rossiter tone was very stable at Mach 0.53 and would require significant energy input to perturb the flow away from the stable state.
- The convective velocity was too high for the small disturbances produced by the actuator to grow enough to affect the stable cavity tone when the actuator was placed only 22 momentum thicknesses (or 0.25 inches) upstream of the leading edge of the cavity.

Examination of the cavity fundamental acoustic mode based on cavity depth reveals that there is likely no sensitivity of depth modes to actuation.

Significant flow coupling and subsequent cavity oscillation amplification occurred when the actuator driving signal matched the frequency at which a Rossiter edge-tone couples with a fundamental cavity acoustic tone. The most unstable and most easily controlled tones were those in which a Rossiter tone couples with the fundamental acoustic tone based on cavity width. Amplification of cavity oscillations also occurred at actuation frequencies near a Rossiter tone that couples with the fundamental acoustic tone based on cavity length. No amplification was observed near Rossiter tones that couple with the depth-based, fundamental, cavity acoustic tone.

The cavity oscillation amplifications were stronger when the actuator was located approximately 371 momentum thicknesses (or 4.25 inches) upstream of the cavity leading-edge than when the actuator was 22 momentum thicknesses (or 0.25 inches) upstream of the cavity leading-edge. These amplifications are likely of higher amplitude and broader frequency than previously observed results because of the multiple Rossiter tones as well as the multiple cavity tones that the actuator disturbances interact with when they grow in the boundary layer and couple with the cavity shear layer. These results indicate that certain flow conditions, where a fundamental acoustic tone(s) couple with a Rossiter edge-tone(s), were very unstable and easily controlled. A clear tone was not present in non-actuated cases at the frequencies where actuation produced significant cavity oscillation amplification.

To the author's knowledge, this study is the first experiment demonstrating that cavity acoustic and Rossiter edge-tone coupling can have a significant impact on amplification of cavity flow-field instabilities. Rona (Rona, 2007) analytically demonstrated the potential for instability

amplification by cavity acoustic and Rossiter edge-tone coupling, and this work validates that such a coupling can have profound impacts to the cavity flow field. While the coupling may not naturally excite amplifications, it does, however, create an unstable system which can be easily modified and sustained by flow control methods.

Computational Results

The simulated actuators produced large structures that extend further into the flow field above the cavity and downstream of the cavity than the baseline case (without actuation). The turbulence kinetic energy is higher in the forward part of the cavity for all three simulations because of the vorticity production at the leading-edge shear layer. The leading-edge simulated actuator produced the highest turbulence kinetic energy inside the cavity. The dual simulated actuator produced comparable turbulence kinetic energy to the baseline (non-actuator) case when compared inside the cavity. This is probably because the interaction of the upstream vortex with the downstream actuator breaks up the regions of intense vorticity and spreads them out over the cavity length resulting in a time-averaged value much like the no-actuation case. Furthermore, most of the turbulence kinetic energy produced by the dual actuator occurs near the cavity opening as opposed to within the cavity for the no-actuator case. This results in additional entrainment from the free stream flow and could provide useful for mixing enhancement.

The addition of a single or multi-level actuation increased the peak turbulence kinetic energy by approximately 46% at 1 cavity length downstream of the cavity. At 1 cavity length, downstream of the cavity trailing-edge, the single-actuator simulation increased the vertical (cross-stream) distance from the wall at which the turbulence kinetic energy was elevated (distance of penetration) by a factor of 2, and the dual-actuator simulation increased the distance of penetration by a factor of 2.8. By two cavity lengths downstream of the cavity trailing-edge, all solutions showed a dramatic reduction in normalized turbulence kinetic energy to about 0.01 or less. However, the single- and dual-actuators continue to increase the distance from the wall at which the turbulence kinetic energy is elevated, even at two, three, or four lengths downstream of the cavity despite the dissipation of the turbulence kinetic energy in the cavity downstream region. Both single- and dual-actuators provide at least 20% increase in normalized turbulence kinetic energy over the case without actuation. The dual-actuator simulation provides the highest increases as well as penetration into the free-stream flow that persists even at 4 lengths downstream of the cavity.

The two-dimensional CFD accurately captures the frequency (as determined by the agreement with the first Rossiter tone) as well as the magnitude of the oscillating pressures inside the cavity that produce the dominant 160 dB Rossiter tone. The leading-edge actuator did not significantly increase the dominant first Rossiter tone which agrees with the experimental findings. However, the dual-simulated-actuator results provide an increased amplitude of about 3 dB at the dominant first Rossiter tone. The interaction and growth of the instabilities produced by two actuators in the streamwise direction is enough to significantly alter the stable cavity tones.

Conclusions

Actuator in Boundary Layer Flow

- The actuator generated controlled, oscillating pressure disturbances in boundary layer flows.

- Pressure-disturbance frequencies measured downstream of the actuator were as high as nine-times the actuator driving frequency.
- Pressure disturbances measured downstream of the actuator were 30 dB to 40 dB higher in amplitude than the background flow "noise" level.
- A time-dependent effect on the stability of the flow can result from changing the rate of actuation frequency.

Actuator with Cavity

- Actuator operation did not produce amplified cavity oscillations at the dominant, most-stable Rossiter tone.
- Significant cavity flow-amplification can be achieved when the actuator driving frequency matches a Rossiter frequency and a fundamental cavity acoustic frequency simultaneously (this may be the first experimental validation of Rona's analytical model).
- The most unstable and most easily controlled instability is one where the actuator and Rossiter frequencies align with the width-based acoustic frequency.
- The second most unstable and easily controlled instability is one in which the frequencies align with the length-based acoustic frequency.
- There was no observable sensitivity to frequencies which align with depth-based acoustic tones.
- Amplifications of cavity pressure oscillations increased when disturbances had more distance to grow, i.e. the actuator was located further upstream from cavity leading edge.

Computational Modeling

- Two-dimensional CFD can be used to accurately capture the frequency as well as the magnitude of the oscillating pressures inside the cavity.
- Actuation at the cavity leading-edge did not significantly increase the dominant first Rossiter tone, which agrees with the experimental findings.
- A series of actuators may produce significant disturbances that can amplify the most stable Rossiter tone (two actuators in series).
- The magnitude of the turbulence kinetic energy in the region inside and downstream of the cavity can be significantly increased by use of the multilevel actuator/cavity configuration. This could lead to enhanced mixing for combustion applications.
- The region of elevated turbulence inside and downstream of the cavity can be significantly expanded using a multilevel actuator/cavity configuration. This could also lead to enhanced mixing for combustion applications.

Future Work

The work described herein has shown that small, light, piezoceramic actuators can produce disturbances in the boundary layer upstream of a cavity that couple with the cavity flow and produce larger levels of turbulence in the cavity flow field as well as downstream of the cavity. A multi-level actuator is envisioned in which the downstream flow produced by the actuator/cavity coupling can grow/couple with other flow fields of interest. Additional experimental and

computational work could be completed to demonstrate the ability of the proposed multi-level actuator to produce additional coupling with other flow fields such as jets, and in other flow conditions such as supersonic or hypersonic flows.

The two-dimensional CFD performed to support this research should be extended to three-dimensions in the future using a high-performance supercomputer. It is well understood by the author that turbulence is a fully three-dimensional flow characteristic that cannot be adequately captured using two-dimensional simulations. A three-dimensional simulation with proper grids for the actuators should be used to fully investigate the flow field produced by the triangular shapes.

Furthermore, additional computational studies should be performed to investigate the flow fields at conditions where the Rossiter and cavity acoustic Strouhal numbers match to produce unstable flows. The experiments showed that these conditions were most easily controlled by the actuators and could produce large-amplitude disturbances in the cavity. Computational studies associated with the cavity acoustic modes would need to be fully three-dimensional because of the sensitivity of the cavity flow to the Strouhal number based on cavity width.

A constant time step was used for all CFD simulations in this work. The ANSYS Fluent software has an adaptive time step option. However, the adaptive time step option is not available for second-order-time-accurate simulations. If a combination of settings could be found to allow the use of an adaptive time step, while retaining second-order accuracy, then the time to produce a solution could be significantly reduced while maintaining accurate results.

Additional work could be completed to optimize cavity tone amplification or amplification of downstream turbulent fluctuations using phase control between the two actuators with measurements in the cavity and/or downstream of the cavity. This type of study would require many actuation combinations that would be best experimentally studied and refined with CFD simulation. Furthermore, quantification of the high-frequency-response pressures downstream of the cavity and subsequent comparison to measurements inside the cavity could lead to additional understanding of the flow control properties of the multi-level actuator. Tests such as this would require significant data acquisition capabilities in both number of channels and sample rate that were not available to the author.

The structural resonance of the actuator was studied during the bench test, but the actuator shape was not optimized to take advantage of structural resonance. It was shown that alignment of the actuator driving frequency, a Rossiter tone, and a width- or length-based acoustic mode can produce a significant instability in the cavity flow. If a design could be realized such that the actuator resonates structurally at the Rossiter and acoustic tones, further increases in turbulence production could be achievable. Furthermore, if the actuator geometry could be adaptable in real time to produce structural resonance (and therefore maximum actuator amplification), then the actuator could resonate with the Rossiter and acoustic tones at nearly any condition.

While not discussed in this work, Rona generated three-dimensional mode-shape plots of various acoustic modes inside a rectangular cavity. Future studies could be accomplished to investigate the reason for the sensitivity of the cavity flow field to width-based acoustic modes through the lens of Rona's mode-shape plots. These investigations may shed some light on the coupling between Rossiter tones and width- and length-based acoustic modes as well as the lack of sensitivity to depth-based acoustic modes.

Finally, the limited instrumentation used in this research could be expanded to include an assessment of boundary layer profiles at various locations in the test section, a flow-quality survey at the test section inlet, and optical measurement techniques (such as shadowgraph or PIV) to quantify flow-field parameters inside and downstream of the cavity. The impact of tunnel flow quality on the measurements of this experiment are unknown. However, the measured oscillating pressures inside the baseline cavity agree well with Rossiter's model providing a level of confidence to the work.

LIST OF REFERENCES

Abdelhamed, A. S. (2015). Design optimization of three dimensional geometry of wind tunnel contractions. *Ain Shams Engineering Journal, 6*, 281-288.

ANSYS. (2016). ANSYS Fluent: Theory Guide. Canonsburg, PA ANSYS.

Bai, H., Zhou, Y., Zhang, W., Xu, S., Wang, Y., & Antonia, R. (2014). Active control of a turbulent boundary layer based on local surface perturbation. *Journal of Fluid Mechanics*.

Bansal, R. K. (2005). A Textbook of Fluid Mechanics and Hydraulic Machines.

Batikh, A., Baldas, L., Caen, R., Ghozlani, W., & Kourta, A. (2010). Experimental Characterization of Sub-millimetric Fluidic Actuators: Application to Boundary Layer Separation Control. *Experimental Heat Transfer*.

Batill, S. M., & Hoffman, J. J. (1984a). *Aerodynamic Design of High Contraction Ratio, Subsonic Wind Tunnel Inlets.* Paper presented at the 22nd AIAA Aerospace Sciences Meeting.

Batill, S. M., & Hoffman, J. J. (1984b). Aerodynamic Design of Three-Dimensional Subsonic Wind Tunnel Inlets. *AIAA Journal, 24*(2), 268-269.

Bauer, R., & Dix, R. (1991a). *Engineering Model of Unsteady Flow in a Cavity*. (AEDC-TR-91-17). Tullahoma, TN: Arnold Engineering Development Center.

Bauer, R., & Dix, R. (1991b). *Engineering Model of Unsteady Flow in a Cavity*. Retrieved from Arnold Engineering Development Center:

Bechert, D. W. (1982). Excited Waves in Shear Layers (pp. 150). Berlin: Institut fur Experimentelle Stromungsmechanik.

Bell, J. H., & Metha, D. (1988). Contraction design for small low-speed wind tunnels: NASA.

Benjamin, T. B. (1962). Theory of the Vortex Breakdown Phenomenon. *Journal of Fluid Mechanics, 14*, 593-629.

Blackwelder, R., Liu, D., & Jeon, W. (1998). velocity perturbations produced by oscillating delta wing actuators in the wall region. *Experimental Thermal and Fluid Sciences*.

Blevins, R. D. (1986). *Applied Fluid Dynamics Handbook*.

Bruce, R. J., & Mundell, A. R. (2003). Low speed wind tunnel tests on the 1303 UCAV concept: QINETIQ/FST.

Burke, S., & Hubbard, J. (1987). Active Vibration Control of a Simply Supported Beam Using a Spatially Distributed Actuator.

Calautit, J. K., Chaudhry, H. N., & Hughes, B. R. (2014). A validated design methodology for a closed-loop subsonic wind tunnel. *Journal of Wind Engineering and Industrial Aerodynamics, 125*, 180-194.

Caylor, M. J., & Batill, S. M. (1984). *An Experimental Study of High Contraction Ratio, Subsonic Wind Tunnel Inlets.* Paper presented at the 13th Aerodynamic Testing Conference.

Chapline, R., & Birch, T. (2012). *The aero-acoustic environment within the weapons bay of a generic UCAV*. Paper presented at the 30th AIAA Applied Aerodynamics Conference, New Orleans, LA.

Chiekh, M., Bera, J., & Sunyach, M. (2011). Synthetic jet control for flows in a diffuser: vectoring, spreading and mixing enhancement. *Journal of Turbulence*.

Cumbo, L. (1996). *Stability of boundary free shear flows: the effects of diffusion.* (Master of Science), Lehigh University. (Paper 448)

D. Inman, A. E. (2011). *Piezoelectric Energy Harvesting Modelling and Application* (1st ed.): John Wiley and Sons.

Davidson, P. A. (2015). *Turbulence An Introduction for Scientists and Engineers*. New York: Oxford University Press.

Dix, R., & Bauer, R. (1993, Jan 11-14, 1993). *Engineering Model Predictions of Aeroacoustic Amplitudes in a Weapons Cavity.* Paper presented at the 31st AIAA Aerospace Sciences Meeting, Reno, NV.

Dix, R., & Bauer, R. (2000). *Experimental and theoretical study of cavity acoustics*. (AEDC-TR-99-4). Tullahoma, TN: Arnold Engineering Development Center.

Donaldson, C., & Sullivan, R. D. (1962). Examination of the solutions of the Navier-Stokes equations for a class of three- dimensional vortices. Part 2: Velocity and pressure distributions for unsteady motion. In N. J. Aeronautical Research Associates Of Princeton Inc (Ed.).

Donaldson, C. D. (1960). *Examination of the solutions of the Navier- Stokes equations for a class of three- dimensional vortices*: Princeton, N. J.: Aeronautical Research Associates of Princeton, Inc.

Doolan, C. J. (2007). Numerical Evaluation of Contemporary Low-Speed Wind Tunnel Contraction Designs. *Journal of Fluids Engineering, 129*, 1241-1244.

Faler, J. H., & Leibovich, S. (1978). An experimental Map of the Internal Structure of a Vortex Breakdown. *Journal of Fluid Mechanics, 86*(2), 313-335.

Felderman, E. J., Chapman, R., Jacocks, J. L., Horn, D. D., & Bruce, W. E. (1996). High-Pressure Arc Heater Development and Modeling: Status and Requirements. *Journal of Propulsion and Power, 12*(6), 1044-1052.

Flaherty. (2013). *Investigation of cavity flow using fast-response pressure sensitive paint.* Paper presented at the 51st AIAA Aerospace Sciences Meeting.

Forestier, N., Geffroy, P., & Jacquin, L. (1999). *Flow over cavities in transonic regime: a test case for numerical simulations.* Paper presented at the 1st International Symposium on Turbulence Shear Flow Phenomena, Santa Barbara.

Fowler, W. (2010). Analysis and Comparison of Effects of an Airfoil or a Rod on Supersonic Cavity Flow.

Freitas, P. (2014). Numerical Simulation of Compressible Flow Over a Deep Cavity.

Givogue, G., Fowler, W., & Vakili, A. (2011). An Experimental Investigation of 2-D Cylinders Affecting Supersonic Cavity Flow.

Gostintsev, Y. (1968). Flow stability of an ideal swirling fluid in a tube. *Fluid Dyn, 3*(6), 33-34. doi:10.1007/BF01022872

Gutmark, E. (1997). *Shear-Flow Role in Combustion Control.* Paper presented at the 28th Fluid Dynamics Conference.

Hall, J. L. (1985). *An Introduction to Vortex Breakdown and Vortex Core Bursting*. Retrieved from Ottawa, Canada:

Hall, M. G. (1967). A New Approach to Vortex Breakdown. *Heat Transfer Fluid Mechanics*, 319-340.

Heller, H., Holmes, D., & Covert, E. (1971). Flow-Induced Pressure Oscillations in Shallow Cavities. *Journal of Sound and Vibration*.

Hirsch, C. (2001). *Numerical Computation of Internal and External flows. Fundamentals of Numerical Discretization* (Vol. 1): Wiley.

Hoghooghi, H., Ahmadabadi, M. N., & Manshadi, M. D. (2016). Optimization of a subsonic wind tunnel nozzle with low contraction ratio via ball-spine inverse design method. *Journal of Mechanical Science and Technology, 30*(5), 2059-2067.

Hoyt, N. C., Kang, M. F., Lee, K. L., Kharraz, A., Kadambi, J., & Kamotani, Y. (2013). Study of Steady and Dynamic Behavior of Gas Core of Passive Cyclonic Separator for Space Applications. *Microgravity Science and Technology, 25*(3), 187-200.

Huang, C., & Hu, C. (2013). Three-dimensional analyses of stress singularities at the vertex of a piezoelectric wedge. *Applied Mathematical Modeling*.

Hudec, M. (2013). Modeling and control of a piezoelectric actuator for active and adaptive optics.

Hussein, H., Shtern, V., & Hussain, F. (1997). *Control of Vortex Breakdown Using Vortex Generators*. Paper presented at the AIAA 4th Shear Flow Conference.

Jabbal, M., Liddle, S., Potts, J., & Crowther, W. (2012). Development of Design Methodology for Synthetic Jet Actuator Array for Flow Separation Control Applications.

Jacobson, S., & Reynolds, W. (1998). Active control of streamwise vortices and streaks in boundary layers. *Journal of Fluid Mechanics, 360*, 179-211.

Jeon, W., & Blackwelder, R. (2000). Perturbations in the wall region using flush mounted piezoceramic actuators. *Experiments in Fluids*.

Jimenez, J. (2013). *Free Shear Flows*. School of Aeronautics. Universidad Politecnica de Madrid. Retrieved from http://torroja.dmt.upm.es/area_alumnos/Introduccion_a_la_turbulencia/shear.pdf

Jones, J. P. (1960). The Breakdown of Vortices in Separated Flow: Dept. Aero. Astro., University of Southampton.

Khorrami, M., & Grosch, C. (1989). *Temporal Stability of Multiple Cell Vortices*. Paper presented at the AIAA 2nd Shear Flow Conference, Tempe, AZ.

Khorrami, M. R. (1989). A Study of the Temporal Stability of Multiple Cell Vortices. Langley, VA: NASA.

Klebanoff, P. S. (1955). Characteristics of turbulence in boundary layer with zero pressure gradient.

Knuth, W. J., Chiaverini, M. J., & Gramer, D. J. (2001). USA Patent No.

Knuth, W. J., Chiaverini, M. J., & Gramer, D. J. (2003). USA Patent No.

Knuth, W. J., Crawford, R., & Litchford, R. (1993). *Integrated Modular Propulsion for Launch Vehicles*. Paper presented at the 29th Joint Propulsion Conference and Exhibit.

Knuth, W. J., Gramer, D. J., Chiaverini, M. J., & Sauer, J. A. (1998a). *Development and testing of a vortex-driven, high-regression rate hybrid rocket engine*. Paper presented at the 34th AIAA/ASME/SAE/ASEE Joint Propulsion Conference and Exhibit, Cleveland, OH.

Knuth, W. J., Gramer, D. J., Chiaverini, M. J., & Sauer, J. A. (1998b). *Experimental investigation of a vortex-driven high-regression rate hybrid rocket engine*. Paper presented at the 34th AIAA/ASME/SAE/ASEE Joint Propulsion Conference and Exhibit, Cleveland, OH.

Knuth, W. J., Gramer, D. J., Chiaverini, M. J., & Sauer, J. A. (2002). Solid-Fuel Regression Rate Behavior of Vortex Hybrid Rocket Engines. *Journal of Propulsion and Power, 18*(3), 600-609.

Knuth, W. J., Gramer, D. J., Chiaverini, M. J., Sauer, J. A., Whitesands, R. H., & Dill, R. A. (1998). *Preliminary CFD Analysis of the Vortex Hybrid Rocket Chamber and Nozzle Flow Field*. Paper presented at the 34th AIAA/ASME/SAE/ASEE Joint Propulsion Conference & Exhibit, Cleveland, OH.

Komerath, N. M., Hegde, U. G., & Strahle, W. C. (1985). Turbulent Static Pressure Fluctuations Away from Flow Boundaries. *AIAA Journal, 23*(9), 1320-1326.

Lada, C., & Kontis, K. (2010). Experimental Studies on Transitional and Closed Cavity Configurations Including Flow Control. *Journal of Aircraft*.

Lada, C., & Kontis, K. (2011). Experimental Studies of Open Cavity Configurations at Transonic Speeds with Flow Control. *Journal of Aircraft*.

Larcheveque, L., Sagaut, P., & Labbe, O. (2007). Large-eddy simulation of a subsonic cavity flow including asymmetric three-dimensional effects. *Journal of Fluid Mechanics, 577*, 105-126.

Larcheveque, L., Sagaut, P., Mary, I., & Labbe, O. (2003). Large-eddy simulation of a compressible flow pas a deep cavity. *Physics of Fluids, 15*(1), 193-209.

Lastra, M. R., Fernandez, J. M., & Vega, M. G. (2013). Novel design and experimental validation of a contraction nozzle for aerodynamic measurements in a subsonic wind tunnel. *Journal of Wind Engineering and Industrial Aerodynamics, 118*, 35-43.

Liepmann, H. W., & Roshko, A. (1993). *Elements of Gas Dynamics*: Dover.

Loewen, R. (2008). Analysis of Cavity Flow and the Effects of a Rod in Crossflow.

Ludweig, H. (1961). *Contribution to the Explanation of the Instability of Vortex Cores Above Lifting Delta Wings* (AVA/61 A01). Retrieved from

Lutz, R. (2017, January 10, 2017). [UTSI Wind Tunnel].

Ma, R., Slaboch, P., & Morris, S. (2009). Fluid mechanics of the flow-excited Helmholtz resonator. *Journal of Fluid Mechanics*.

Michalke, A. (1972). The instability of free shear layers. *Progress in Aerospace Sciences, 12*, 213-216. doi:http://dx.doi.org/10.1016/0376-0421(72)90005-X

Michalke, A. (1977). *Instability of a compressible circular free jet with consideration of the influence of the jet boundary layer thickness*. Retrieved from NASA, United States:

Mikhail, M., & Rainbird, W. (1978). *Optimum design of wind tunnel contractions.* Paper presented at the 10th Aerodynamic Testing Conference.

Nakamura, Y., Leonard, A., & Spalart, P. R. (1985). *Vortex Breakdown Simulation*. Paper presented at the AIAA 18th Fluid Dynamics and Plasmadynamics and Lasers Conference, Cincinnati, OH.

Nolan, D. S. (2012). Three-dimensional instabilities in tornado-like vortices with secondary circulations. *J. Fluid Mech., 711*, 61-100. doi:10.1017/jfm.2012.369

Parhi, S., & Nath, G. (1997). The growth of perturbations associated with the linear stability of inviscid fluid flows. *Applied Mathematics and Computation, 81*(1), 23-30. doi:10.1016/0096-3003(95)00299-5

Paschereit, C. O., Terhaar, S., ĆOsiĆ, B., & Oberleithner, K. (2014). Application of linear hydrodynamic stability analysis to reacting swirling combustor flows. *Journal of Fluid Science and Technology, 9*(3), JFST0024-JFST0024. doi:10.1299/jfst.2014jfst0024

Perng, S., & Dolling, D. (2001). Suppression of Pressure Oscillations in High-Mach-Number Turbulent, Cavity Flow. *Journal of Aircraft*.

PiezoTechnology. (2014). Piezoelectric Ceramic Products. Fundamentals, Characteristics and Applications.

Radhakrishnan, S. (2002). *An Experimental and Numerical Study of Open Cavity Flows.* (Doctor of Philosophy), The University of Tennessee Knoxville.

Raman, G. (1997). Using Controlled Unsteady Fluid Mass Addition to Enhance Jet Mixing. *AIAA Journal*.

Rigney, S. J. (1988). *Water Tunnel Simulation of the Internal Flow of a Segmented Arc Heater.* (M.S.), University of Tennessee.

Rona, A. (2007, 2007). *The acoustic resonance of rectangular and cylindrical cavities.* Paper presented at the 28th AIAA Aeroacoustics Conference.

Rossiter, J. E. (1966). Wind-Tunnel Experiments on the Flow over Rectangular Cavities at Subsonic and Transonic Speeds.

Samimy, M., Kim, J., Kastner, J., Adamovich, I., & Utkin, Y. (2007). Active Control of a Mach 0.9 Jet for Noise Mitigation Using Plasma Actuators. *AIAA Journal, 45*(4), 890-901.

Saprkaya, T. (1995). *Vortex Breakdown and Turbulence*. Paper presented at the AIAA 33rd Aerospace Sciences Meeting and Exhibit, Reno, NV.

Sargison, J. E., Walker, J. G., & Rossi, R. (2004). *Design and calibration of a wind tunnel with a two-dimensional contraction.* Paper presented at the 15th Australasian Fluid Mechanics Conference, The University of Sydney, Sydney, Australia.

Schlichting, H., & Gersten, K. (1999). *Boundary Layer Theory* (8th Ed.): Springer.

Schubauer, G. B., & Skramstad, H. K. (1948). Laminar-boundary-layer oscillations and transition on a flat plate ; NACA Technical Reports. In S. National Bureau Of (Ed.).

Shi, H. (2013). A piezoelectric pseudo-bimorph actuator. *Applied Physics Letters*.

Sipp, D. (2012). Open-loop control of cavity oscillations with harmonic forcings. *Fluid Mechanics, 708*, 439-468.

Smith, A. O. (1975). High-Lift Aerodynamics. *Journal of Aircraft, 12*(6), 501-530.

Sullivan, J., Hubbard, J., & Burke, S. (1996). Modeling approach for two-dimensional distributed transducers of arbitrary spatial distribution. *J. Acoust. Soc. Am.*

Takahashi, H., Liu, F., Palaviccini, M., Oyarzun, M., Griffin, J., Ukeiley, L., & Cattafesta, L. (2011). Experimental Study of Adaptive Control of High-speed Flow-induced Cavity Oscillations. *Fluid Science and Technology, 6*(5), 701-716.

Tennekes, H., & Lumley, J. L. (1972). *A First Course in Turbulence*. Cambridge: MIT Press.

Trinh, H. P., Knuth, W., & Michaels, S. (2000). *Evaluation of Vortex Chamber Concepts for Liquid Rocket Engine Applications* (20010020208). Retrieved from

Tsai, G., & Yang, J. (1993). Pressure fluctuations in correlation with velocity fluctuations in turbulent wake flow. *Experiments in Fluids, 15*(6), 462-463.

Vakili, A., Eramo, R., & Tennent, S. (1993). *Increasing and Decreasing the Stability of a Confined Vortex by Forcing*. Paper presented at the AIAA 24th Fluid Dynamics Conference, Orlando, FL.

Vakili, A., Fowler, W., Loewen, R., Thiemann, C., Fetterhoff, T., & Meganathan, A. (2014). Cavity Flow Control Experiments and Simulations. *Journal of Physics*.

Vakili, A., & Gauthier, C. (1994). Control of Cavity Flow by Upstream Mass-Injection. *Journal of Aircraft*.

Vakili, A., Tennent, S., & Panchapakesan, N. (1996). *An Experimental Study of Confined Multicell Vortex Flows*. Paper presented at the AIAA 34th Aerospace Sciences Meeting and Exhibit, Reno, NV.

Vakili, A. D. (1993). *An Investigation on the Influence of Forced Disturbances on the Arc-Heater Flow* (AF F40600-92-K-0001). Retrieved from

Vakili, A. D., & Gauthier, C. (1991). Control of Cavity Flow by Upstream mass Injection.

Vladimirov, V. (1983). Stability of ideal incompressible flow with constant vorticity in an elliptic cylinder. *J Appl Mech Tech Phys*, *24*(4), 555-560. doi:10.1007/BF00907907

White, F. (1991). *Viscous Fluid Flow* (2nd ed.): McGraw Hill.

Zaman, K. B. M. Q., & Hussain, A. K. M. F. (1980). *Turbulence Suppression in Free Shear Flows by Controlled Excitation*. Paper presented at the AIAA 13th Fluid & Plasma Dynamics Conference, Snowmass, CO.

Zhang, K., & Naguib, A. (2008). *Effect of Cavity Width on Self-sustained Oscillations in a Low-Mach-number Cavity Flow*. Paper presented at the 38th Fluid Dynamics Conference.

Zhuang. (2006). Supersonic cavity flows and their control. *AIAA Journal*, *44*(9).

APPENDICES

Appendix 1: Figures

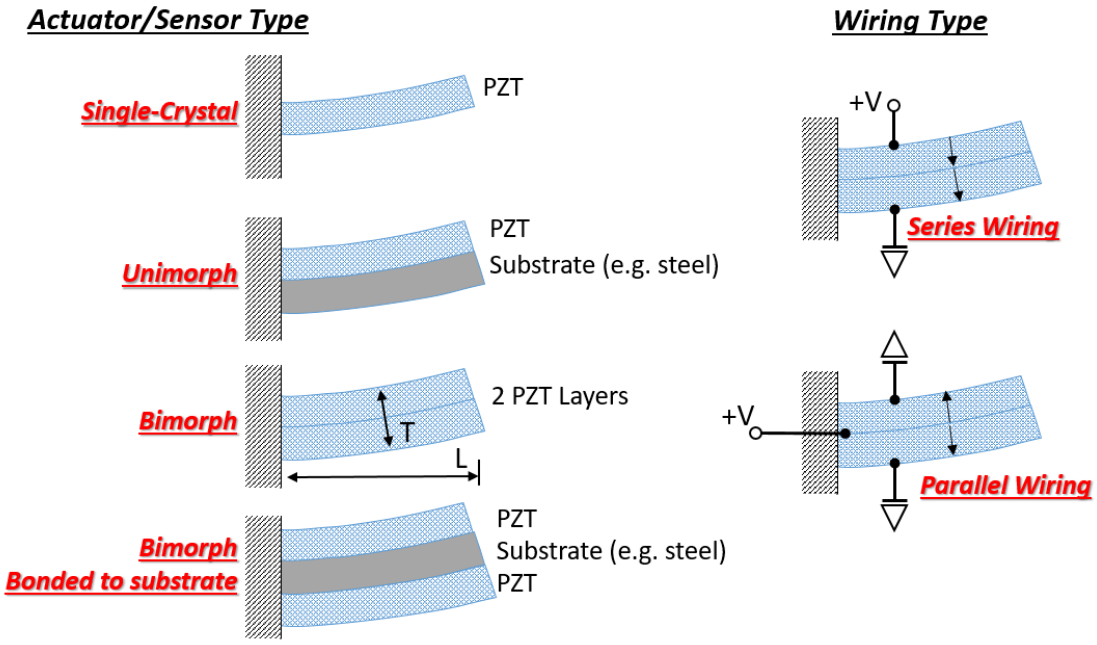

Figure 1. Example piezoelectric actuator/sensor types.

Left – four types of cantilever-beam piezoelectric actuators. Right – Two types of wiring schemes for piezoelectric actuators.

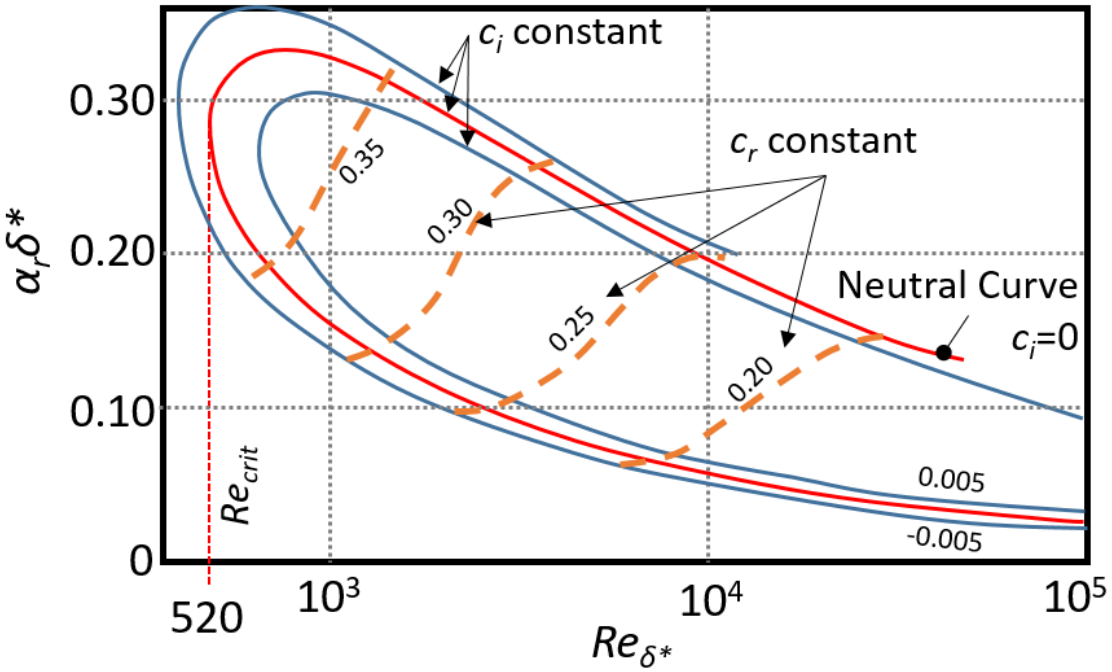

Figure 2. Temporal stability curves for Blasius flat-plate boundary layer flow.

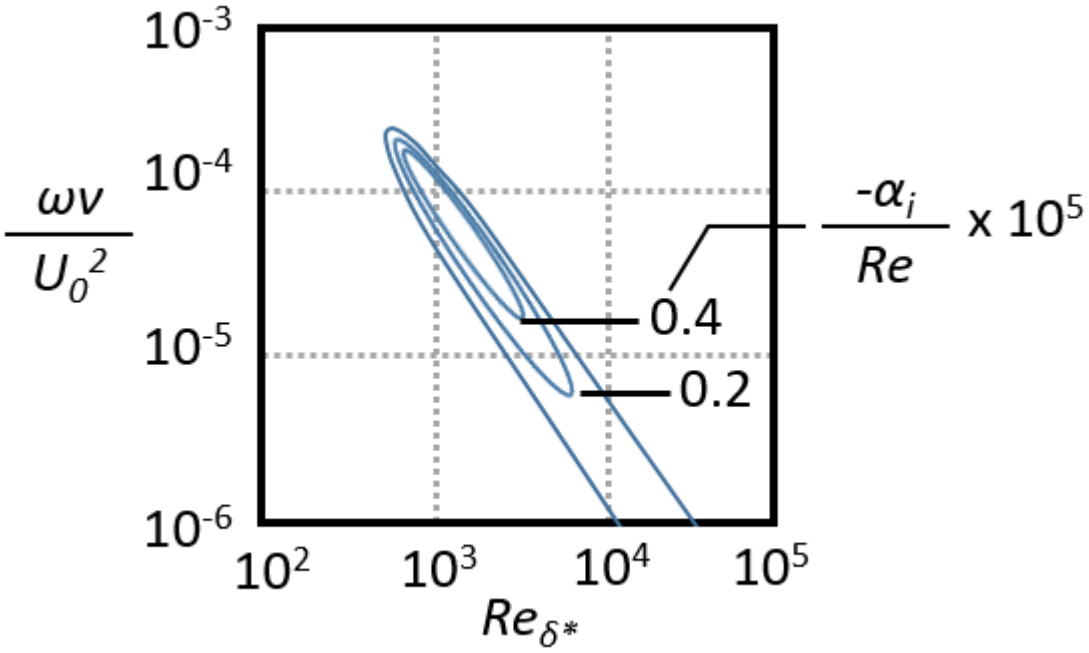

Figure 3. Spatial stability curves for Blasius flat-plate boundary layer flow.

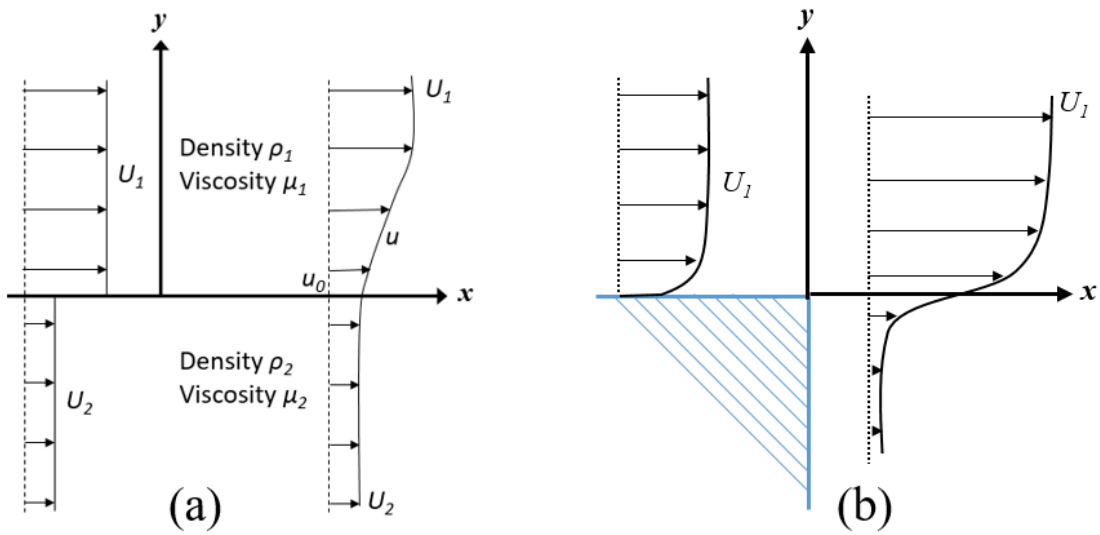

Figure 4. Shear layer terms and coordinates.

a) a free-shear layer, b) a shear layer downstream of an aft-facing step.

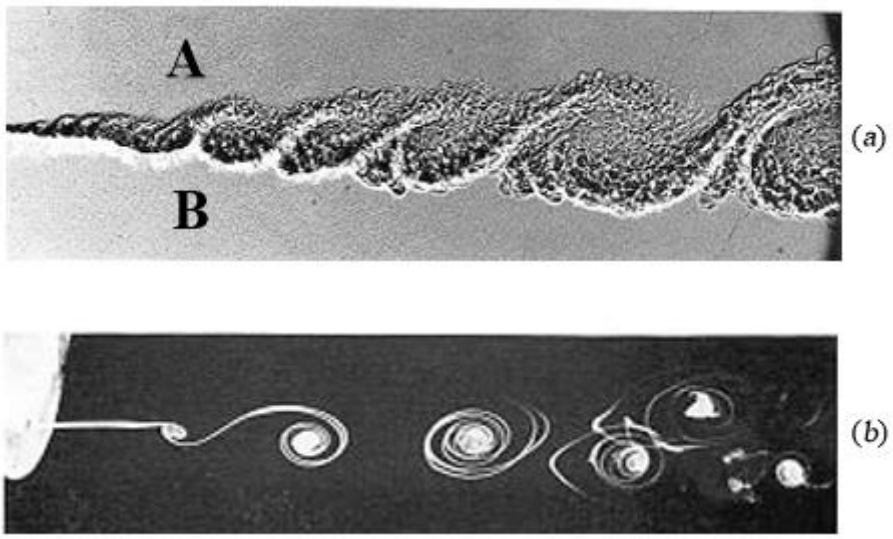

Figure 5. Flow visualization of turbulent structures.

(a) Turbulent shear layer at high Reynolds number between two streams of different gases. The Reynolds number based on the velocity difference and on the maximum visual thickness is Re ≈ $2x10^5$. (b) Initial development of a low Reynolds number velocity discontinuity Re ≈ 7,500. Reproduced from (Jimenez, 2013).

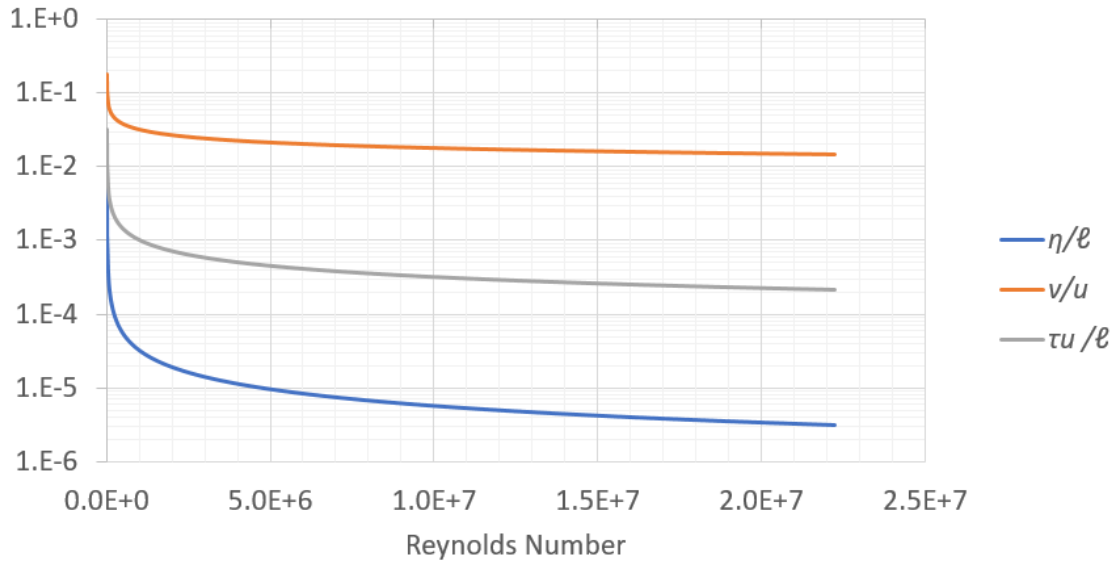

Figure 6. The microscales of turbulence.

Values normalized by large-scale quantities, and shown as a function of Reynolds number. The length scale is η, the velocity scale is v, and the time scale is τ.

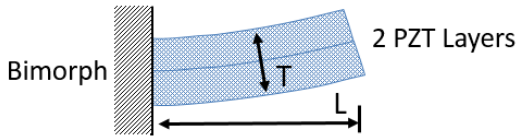

Figure 7. Simple, one-dimensional, bimorph, cantilever beam actuator.

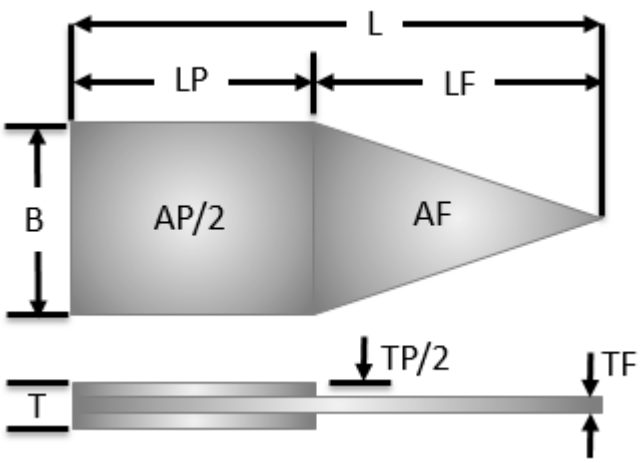

Figure 8. Actuator dimensions.

B-base length, L-total length, LP-length of piezo, LF-length of flapper, T-total thickness, TP-thickness of piezo, TF-thickness of flapper, AP-area of piezo, AF-area of flapper

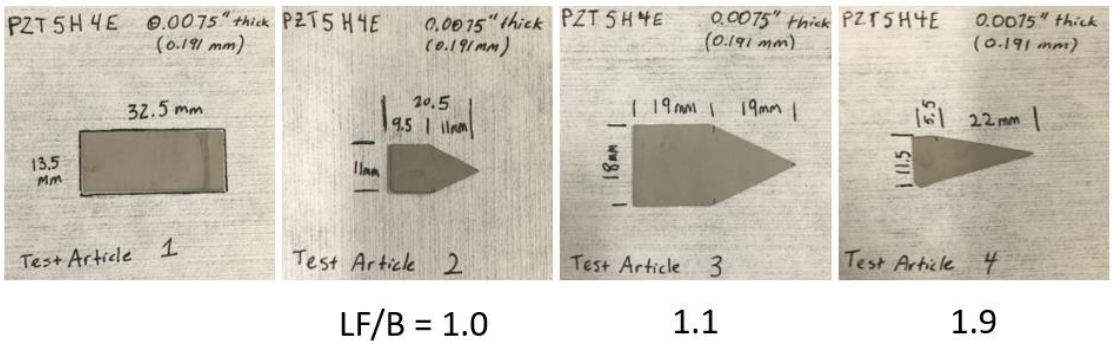

Figure 9. Single-crystal actuator test articles.

From left to right – rectangular actuator, small delta-wing actuator, large delta-wing actuator, and high-aspect-ratio delta-wing actuator.

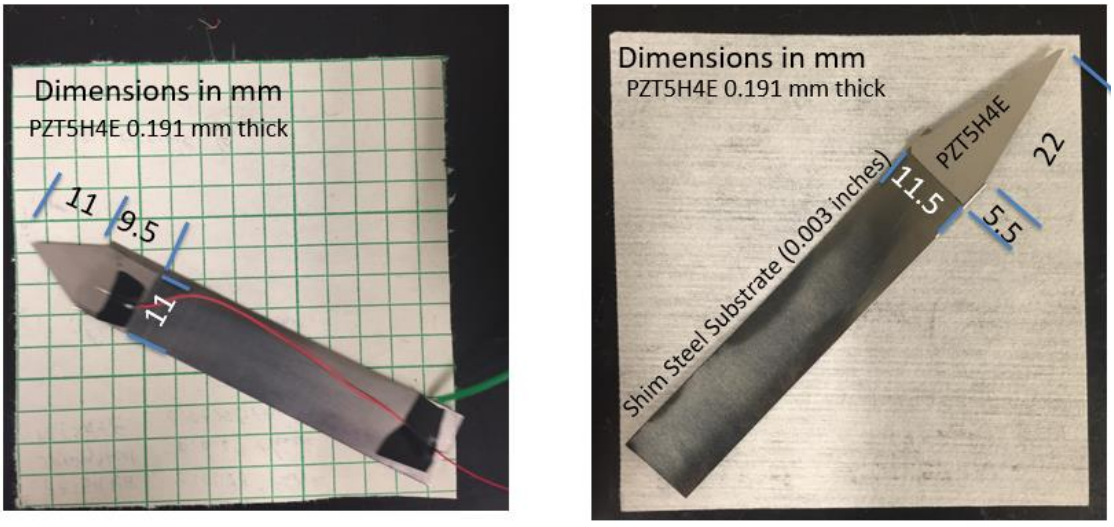

Figure 10. Unimorph actuator test articles.

Left – small delta-wing actuator. Right- high-aspect-ratio delta-wing actuator.

LF/B = 1.667

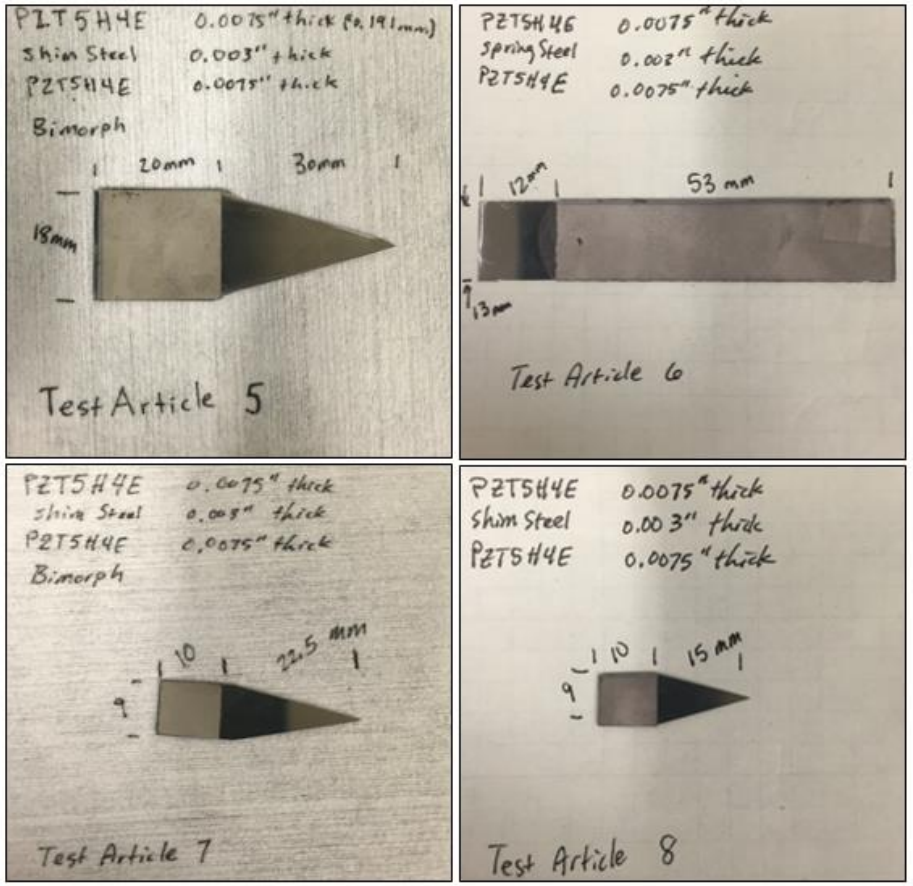

LF/B = 0.92

LF/B = 2.5

LF/B = 1.667

Figure 11. Bimorph actuator test articles.

Upper left – the baseline actuator used for this research. Upper right – a bimorph, rectangular actuator variant. Lower left – the baseline shape used for actuator bank development. Lower right – the smallest actuator fabricated and tested.

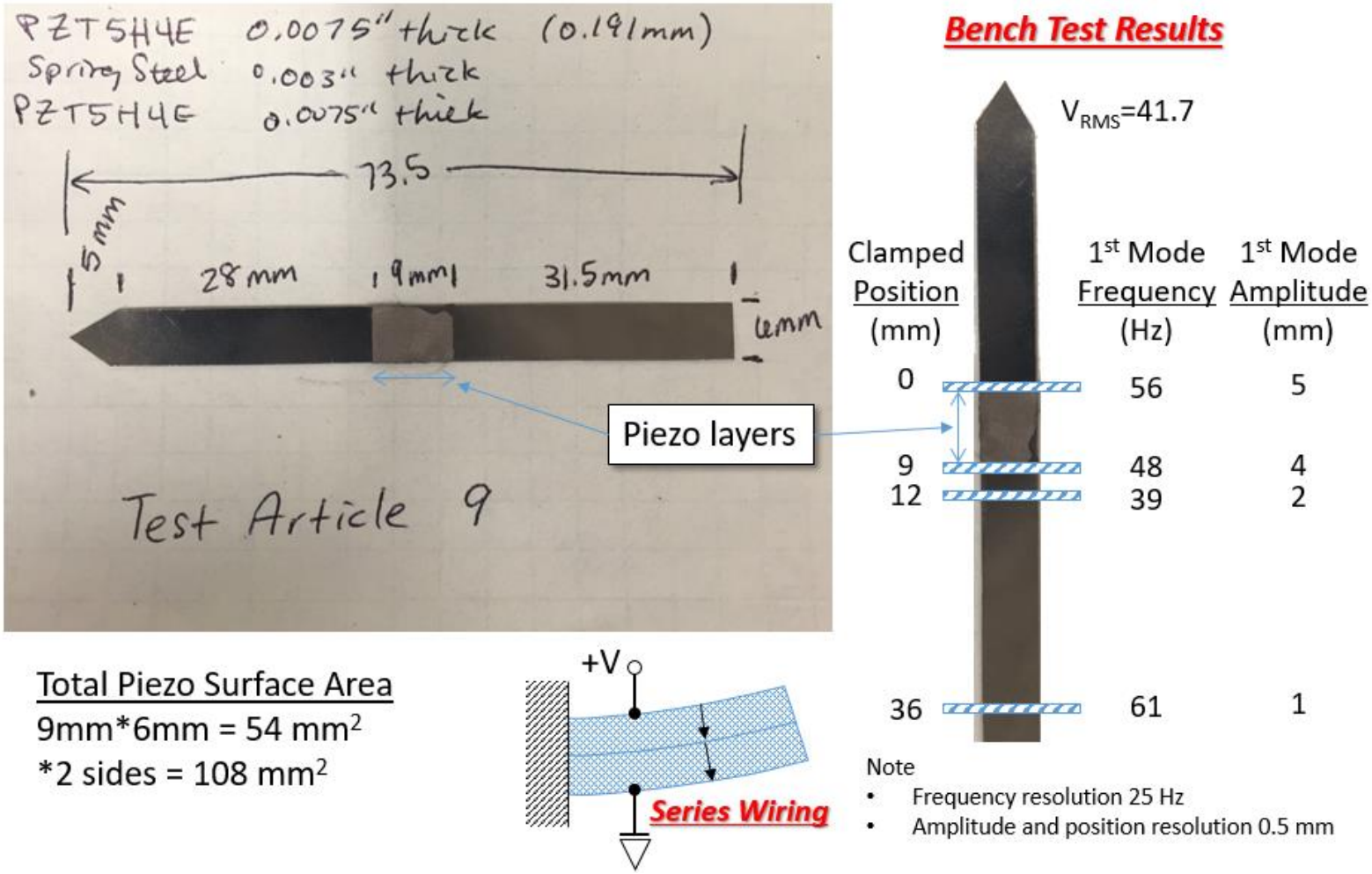

Figure 12. Bimorph actuator test articles with additional tunability.

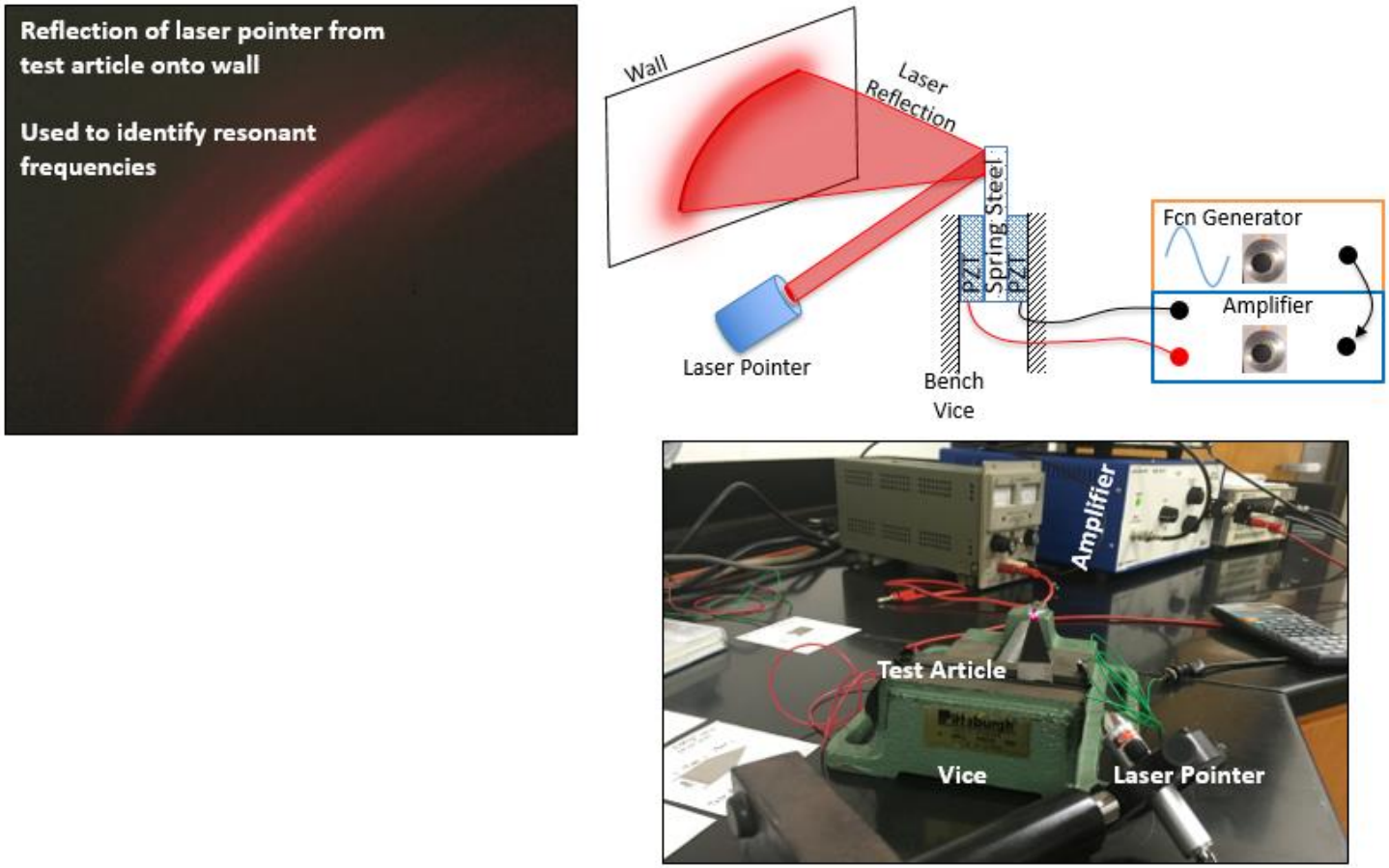

Figure 13. Bench test setup.

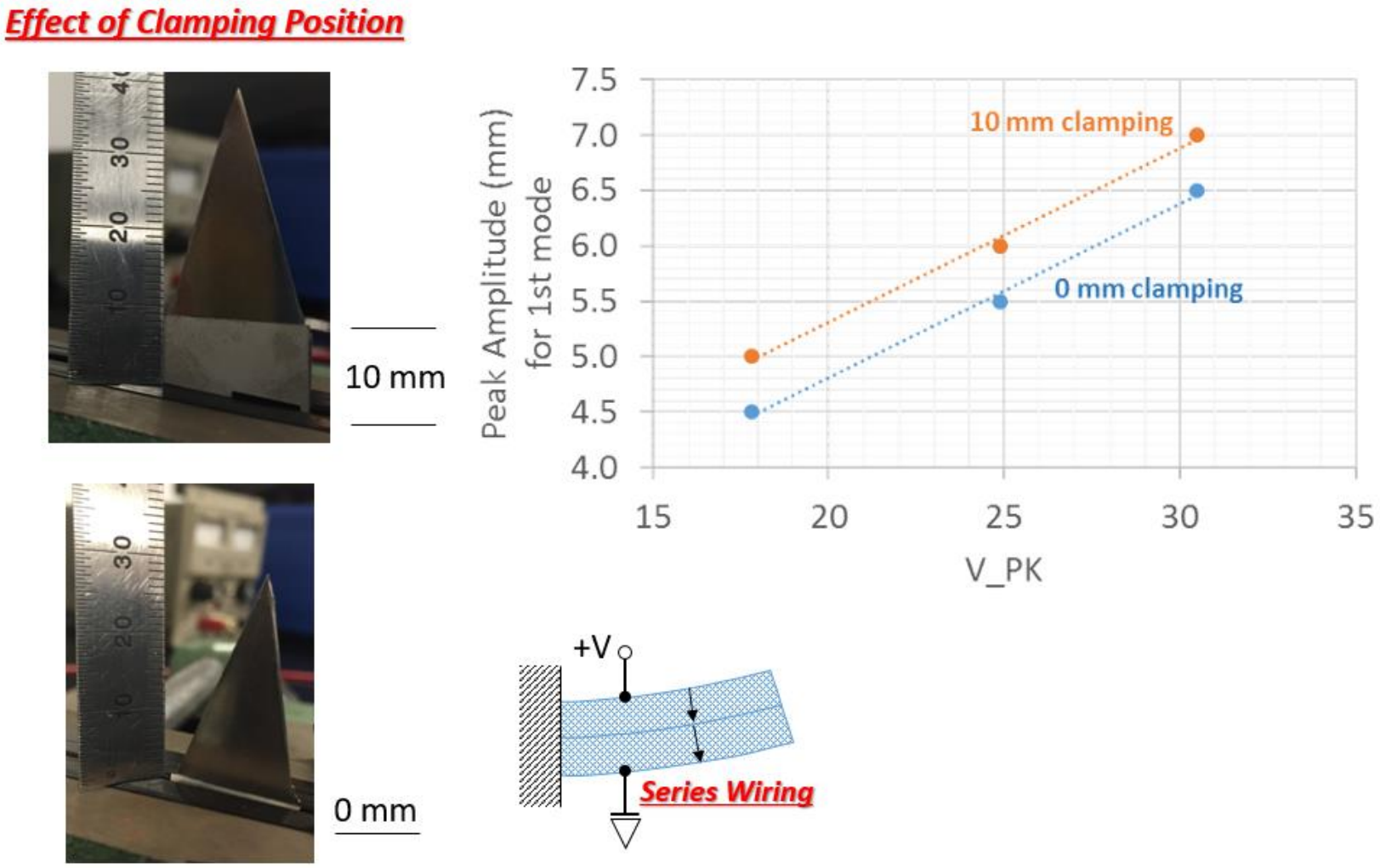

Figure 14. Effect of clamping position on tip deflection at first mode frequency for test article 5.

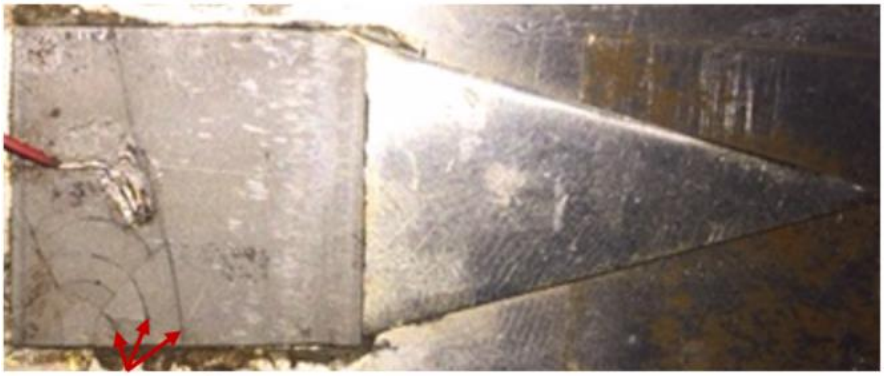

Figure 15. Example of stress cracks in an actuator.

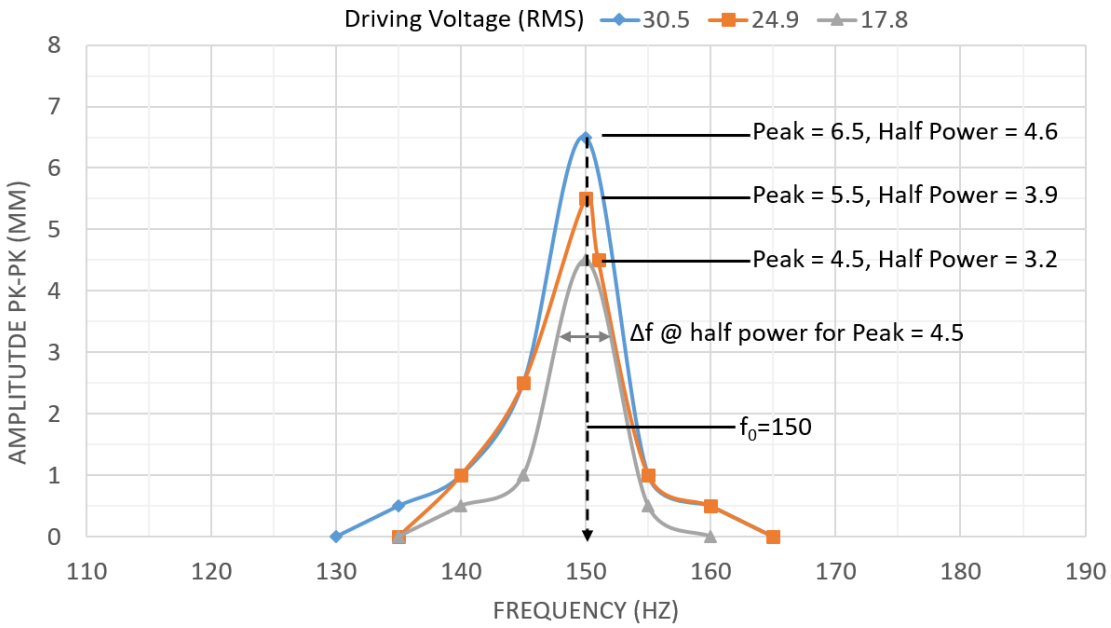

Figure 16. Measured frequency response for test article 5.

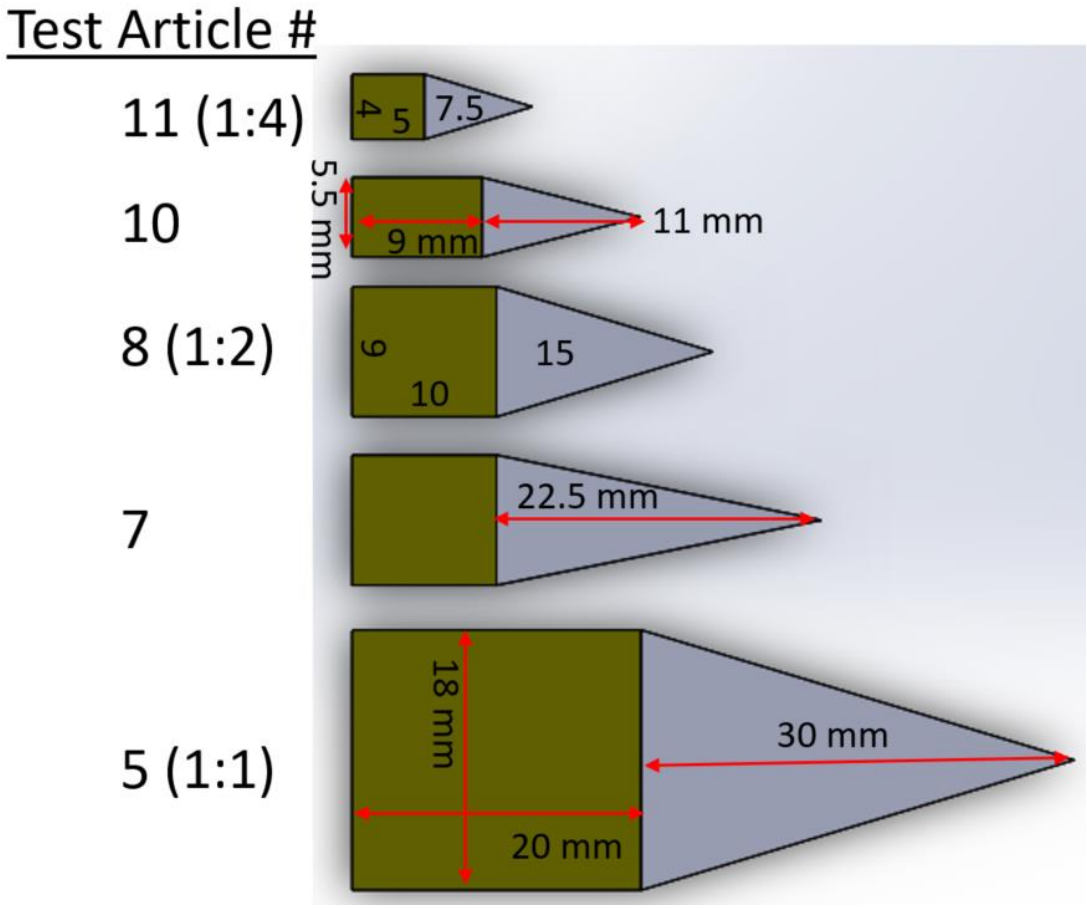

Figure 17. Variations in the shape of test article 5.

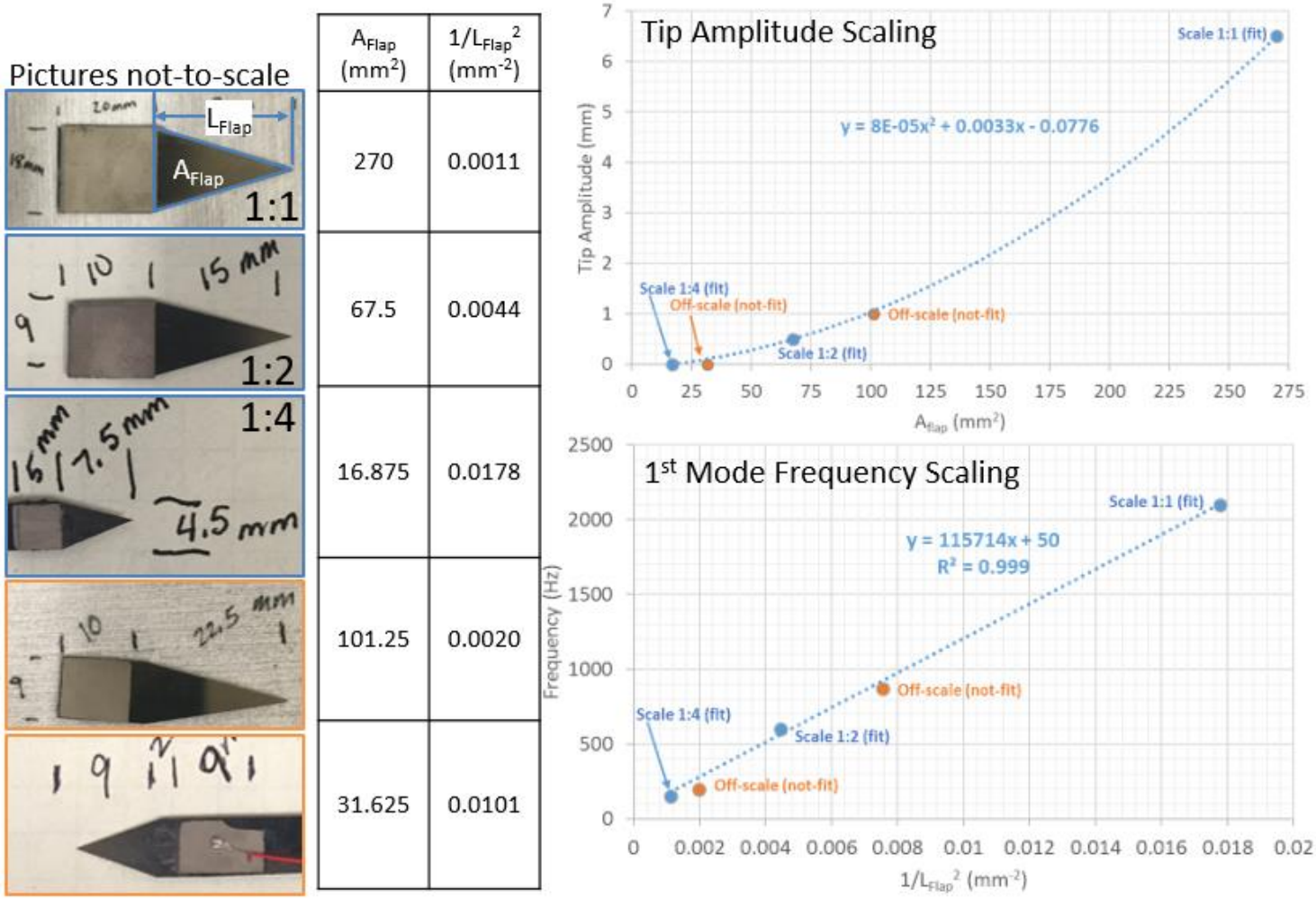

Figure 18. Numerical model for actuator scaling.

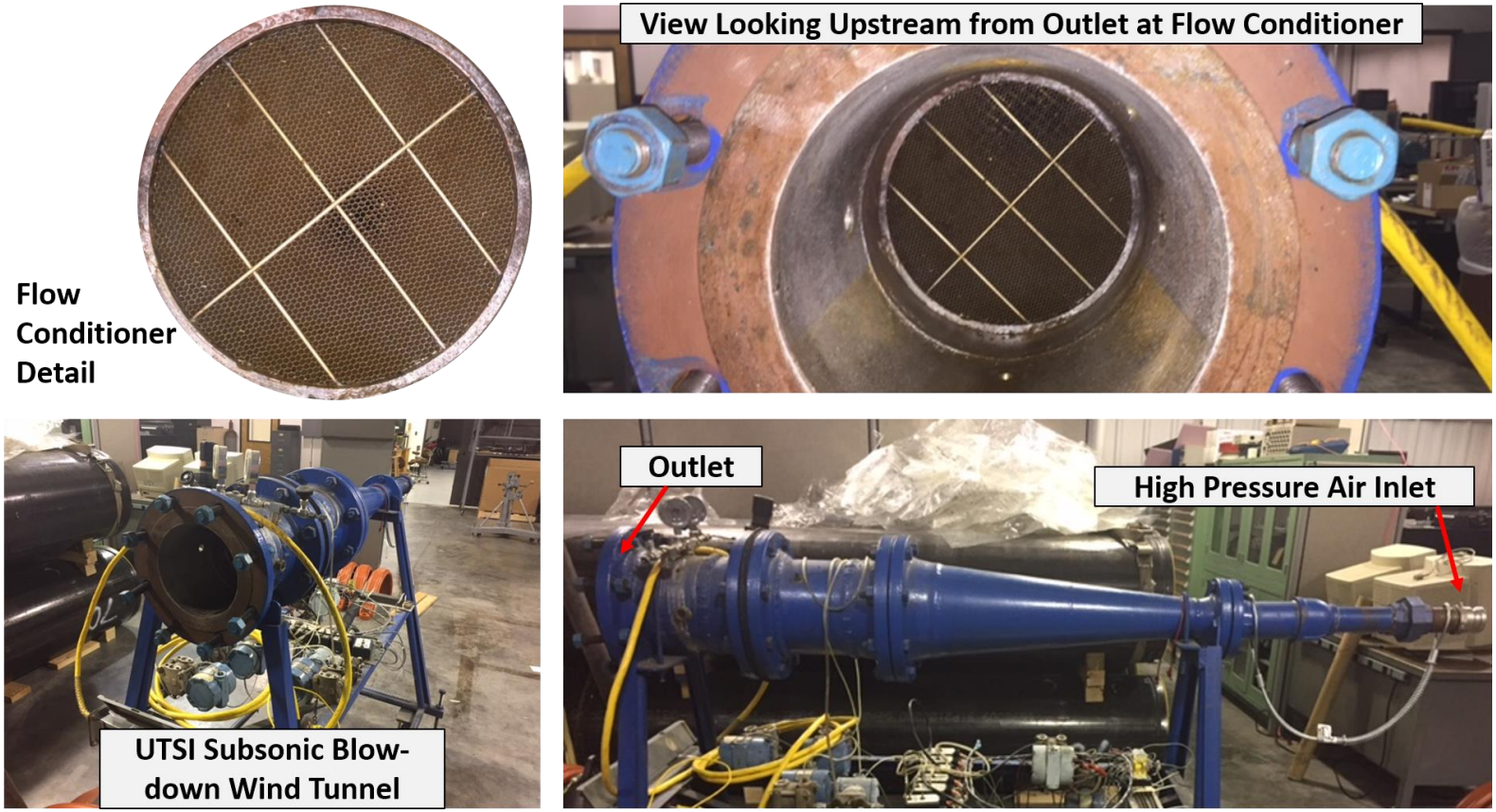

Figure 19. UTSI subsonic blowdown wind tunnel.

Upper – photographs of the flow-conditioning screen. Lower left – photograph of the downstream section of the wind tunnel. Lower right – side-view of the length of the wind tunnel.

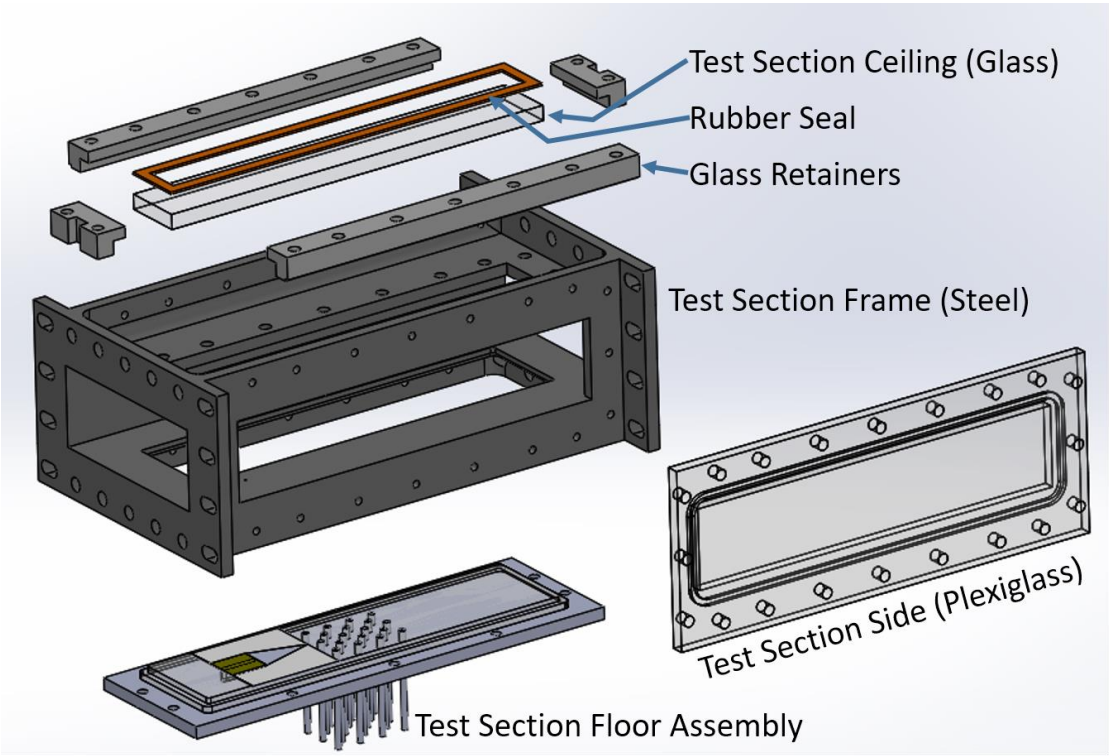

Figure 20. Exploded view of test section assembly.

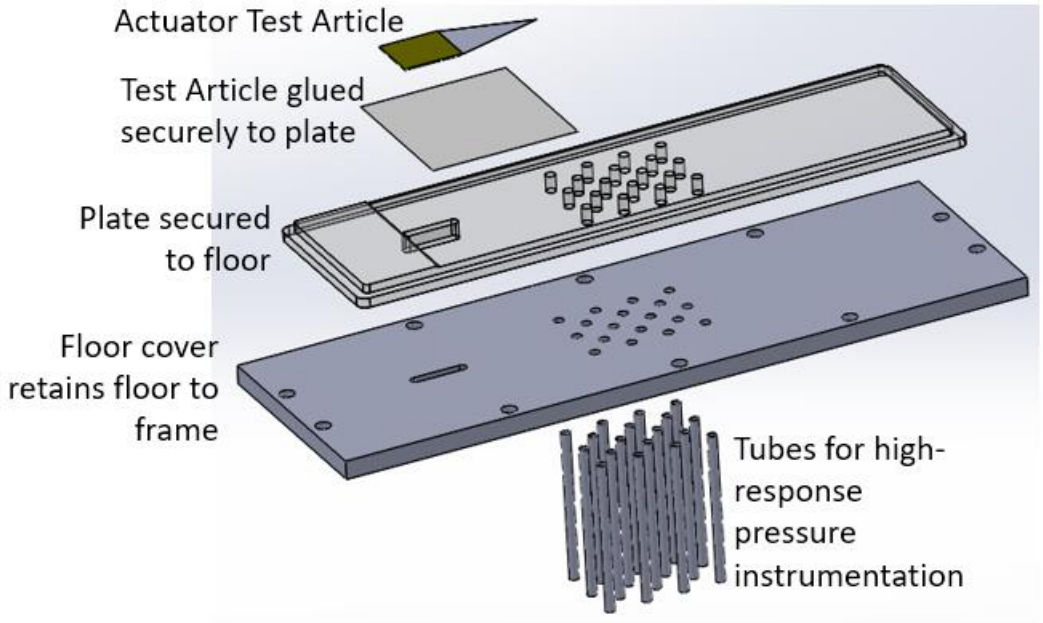

Figure 21. Exploded view of test section floor assembly.

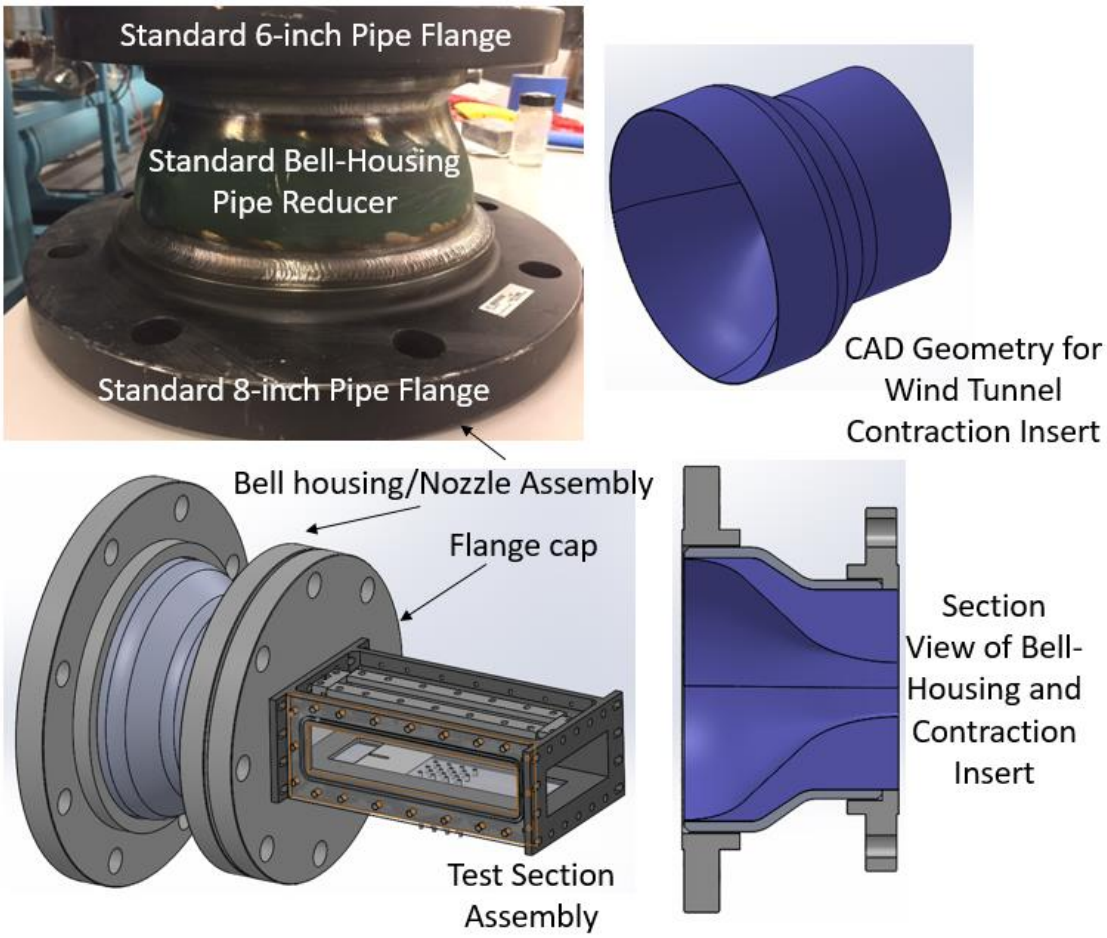

Figure 22. Wind tunnel contraction section.

Upper left – the standard bell-housing reducer and flanges used to house the nozzle contraction. Upper right – a CAD model of the internal nozzle-contraction flow-path. Lower left – a CAD assembly of the test section attached to the flange cap. Lower right – a cross-section view of the assembled nozzle contraction.

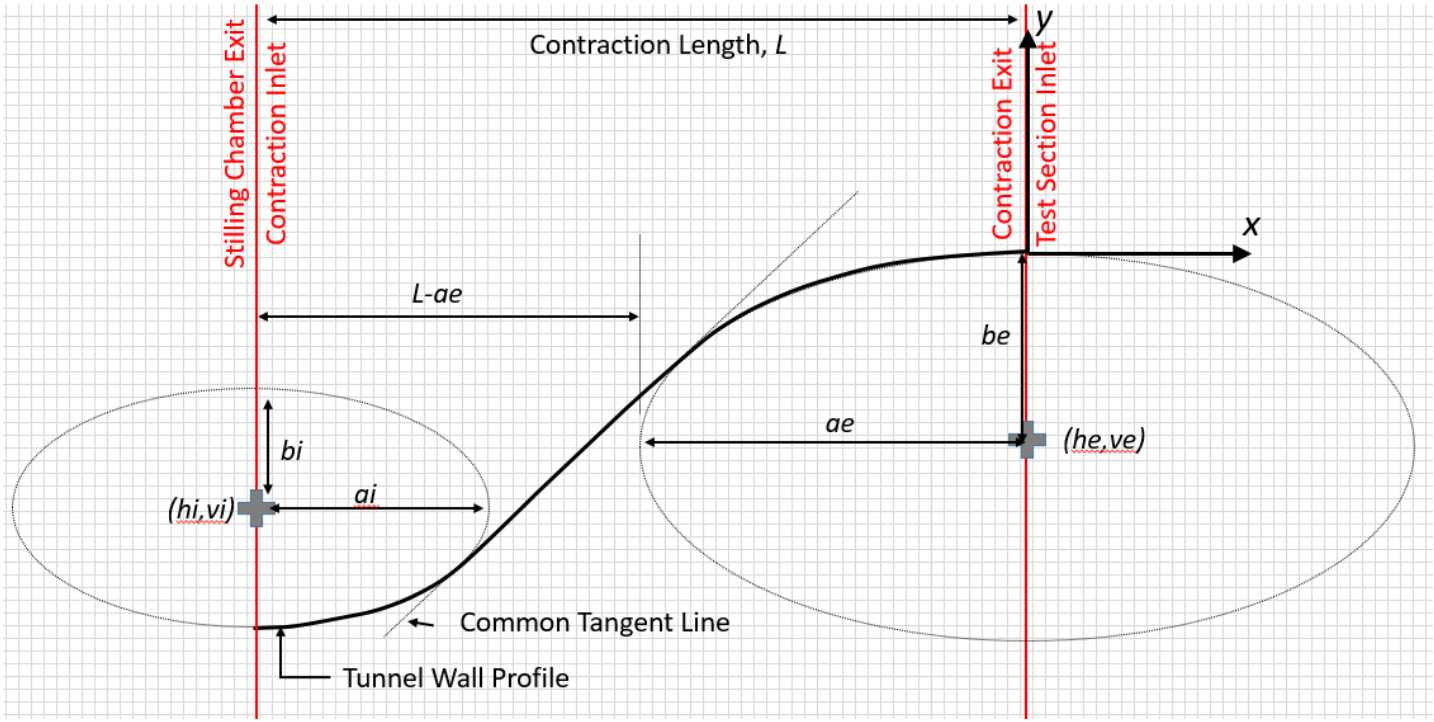

Figure 23. Elliptical nozzle contour definition.

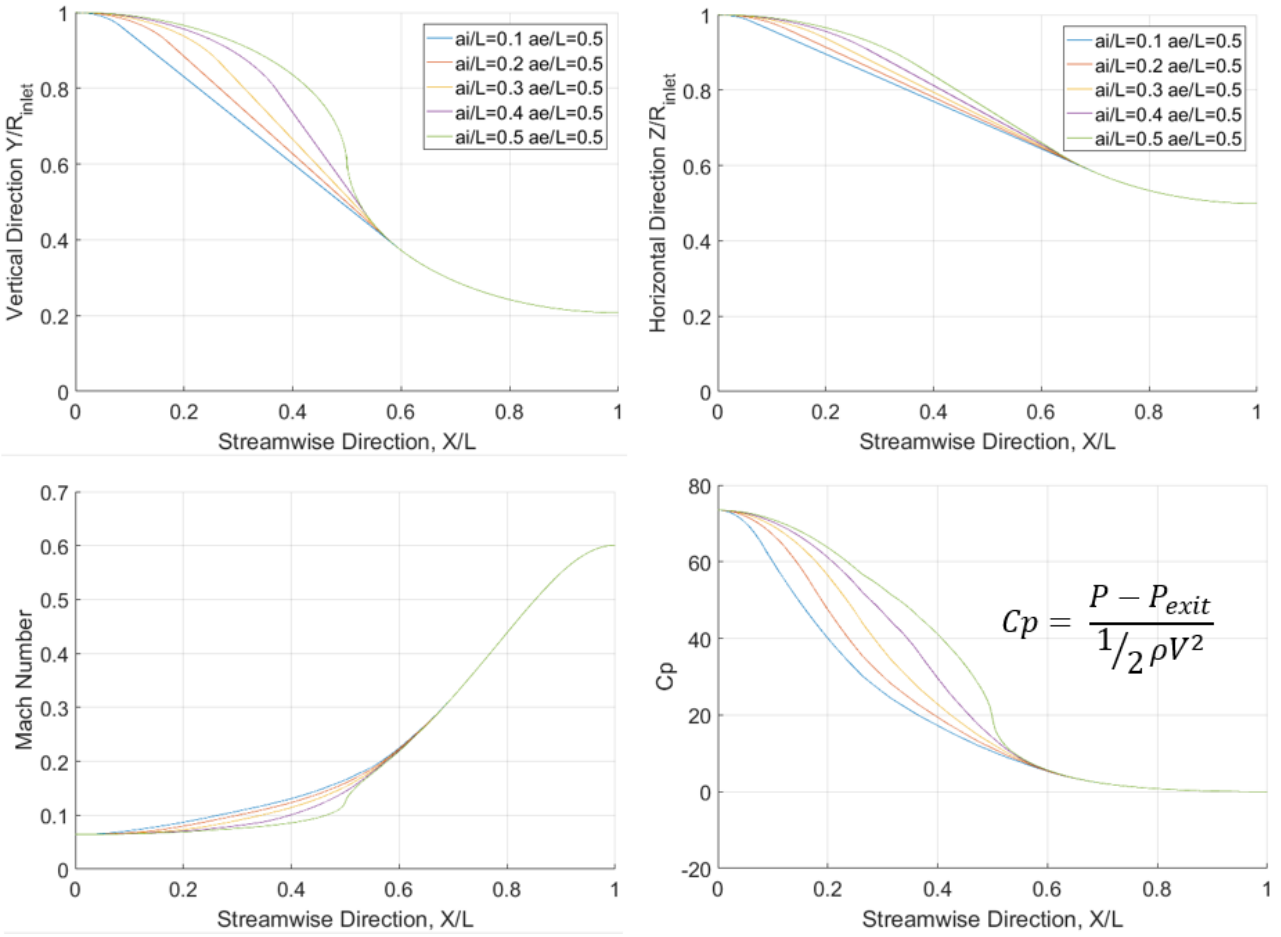

Figure 24. Example parametric studies of inlet length, ai.

Upper left – profiles in the vertical direction vs. streamwise direction. Upper right – profiles in the horizontal direction vs. the streamwise direction. Lower left – centerline Mach number profile vs. streamwise coordinate. Lower right – centerline pressure coefficient vs. streamwise direction.

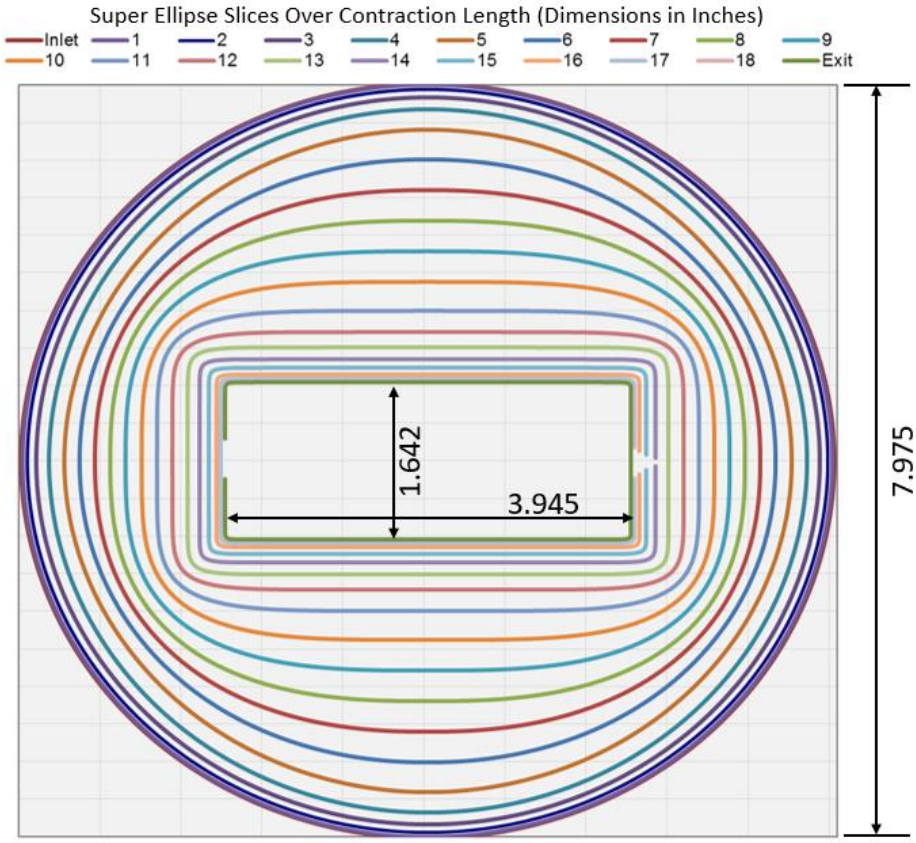

Figure 25. Super ellipse slices over contraction length.

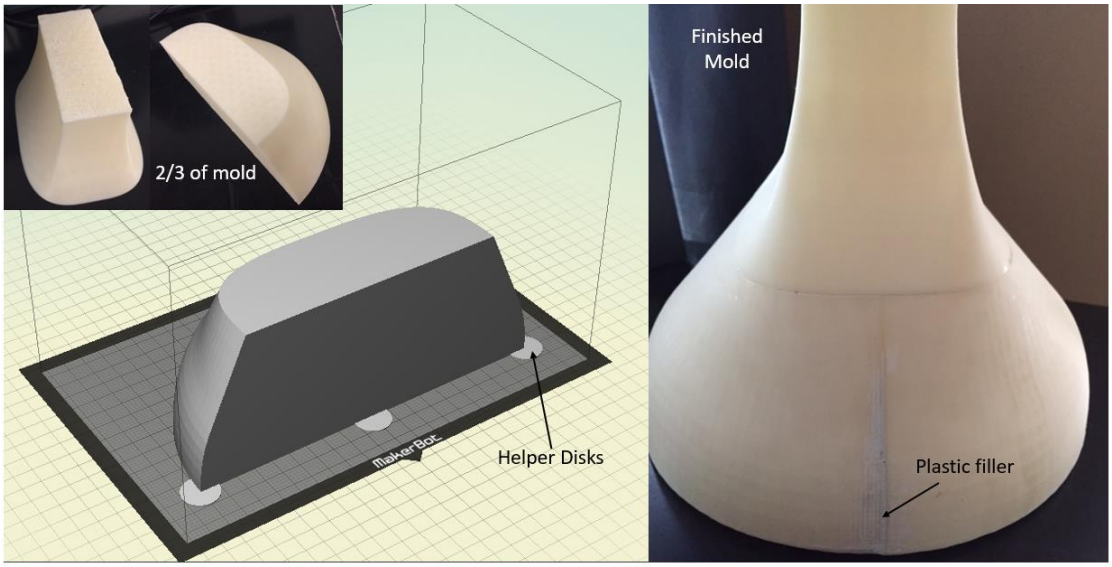

Figure 26. 3D-Printed contraction mold.

Left – CAD view of nozzle part inside print volume. Left inset – example nozzle parts before joining. Right – assembled nozzle contraction mold.

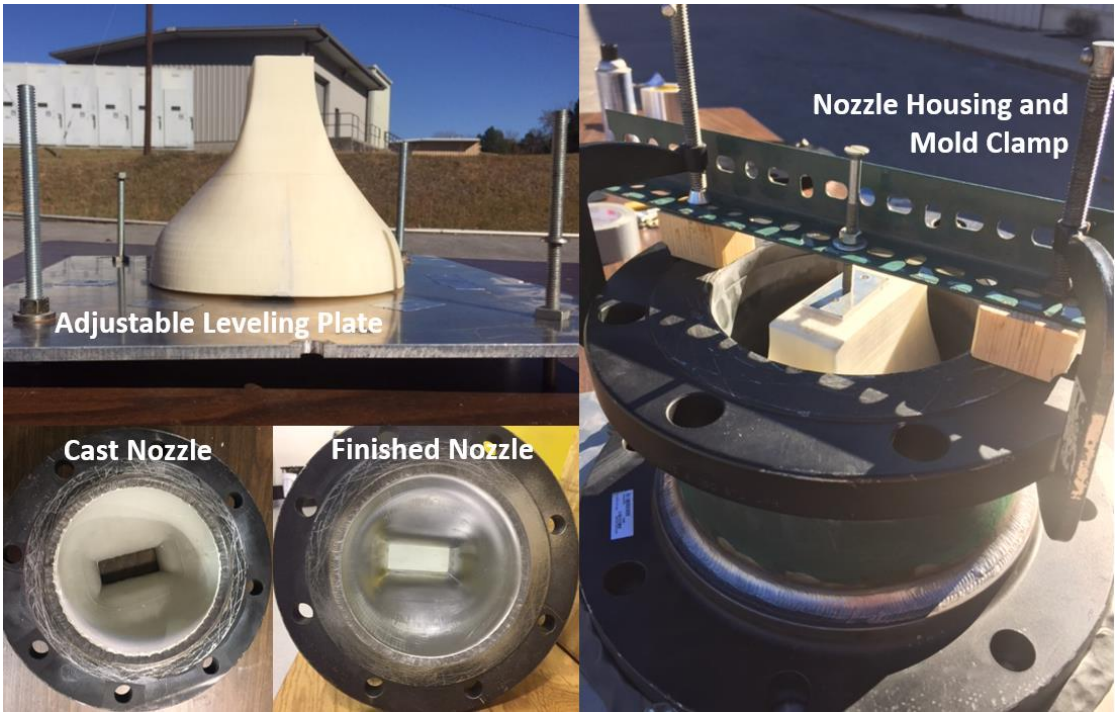

Figure 27. Nozzle contraction casting.

Upper left – photograph showing the nozzle mold placed on the leveling plate before casting. Right – photograph of the nozzle mold and housing before casting. Lower left – before/after photographs of the cast nozzle and smoothed/painted/finished nozzle.

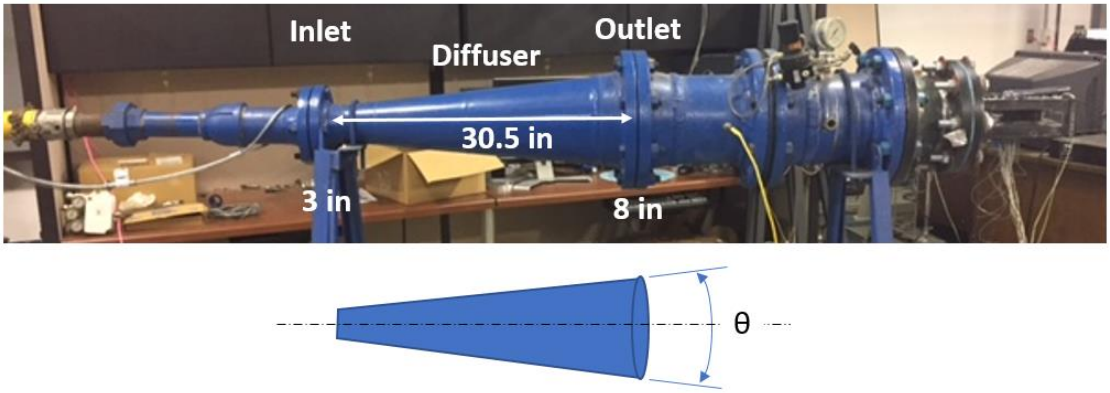

Figure 28. UTSI tunnel diffuser geometry.

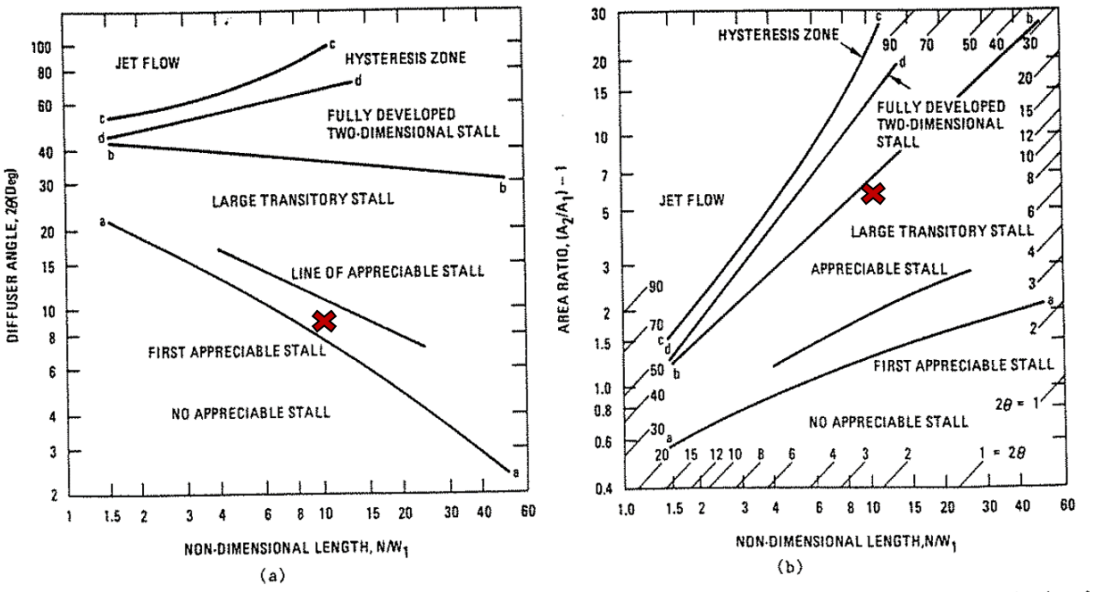

Figure 29. Stall regimes for two-dimensional straight-walled diffusers.

Part (a) and part (b) are equivalent. The red X is the UTSI blowdown tunnel diffuser. The diffuser operates in the stall region. Reproduced and modified from (Blevins, 1986).

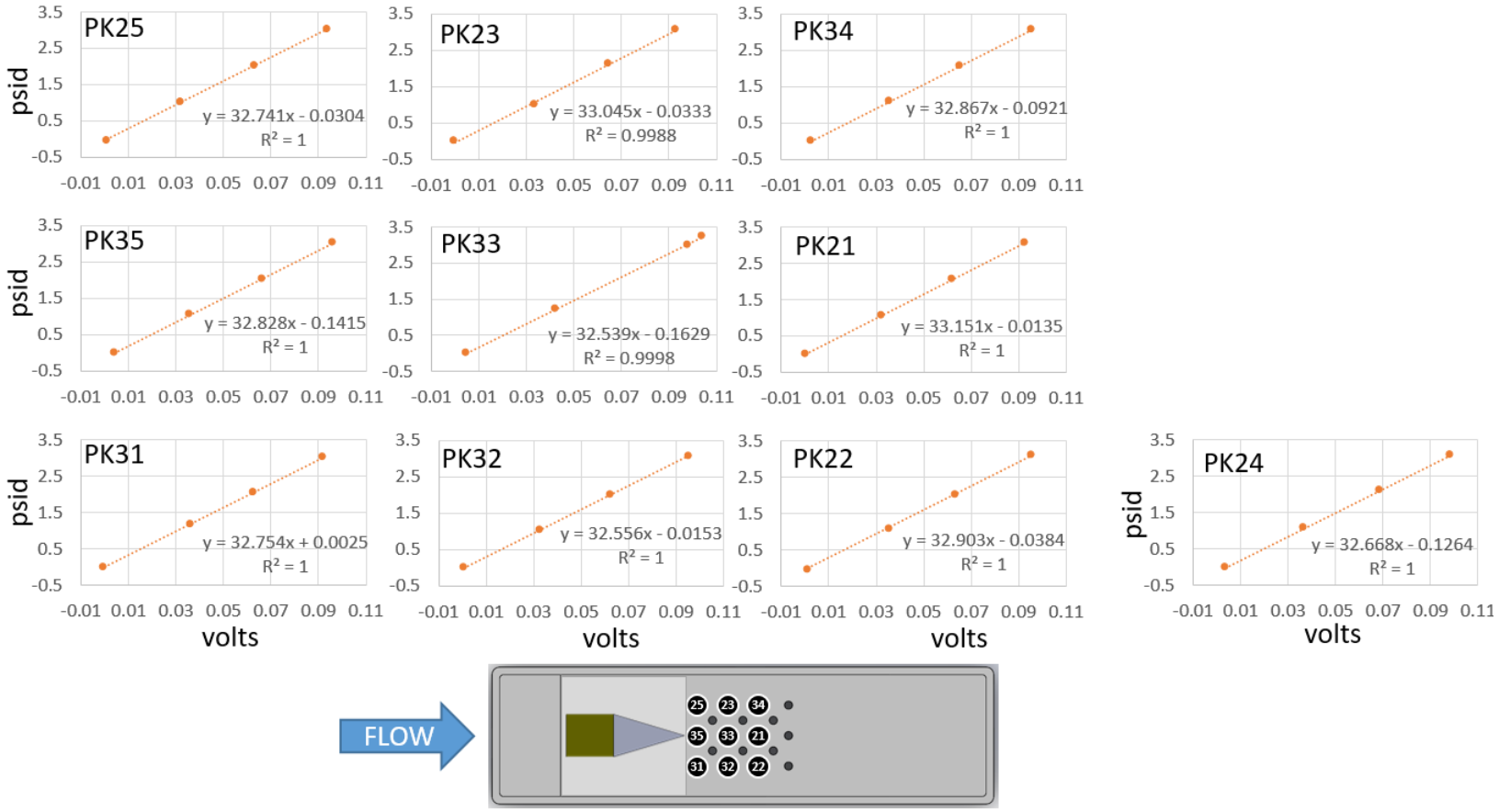

Figure 30. Calibrations for high-response transducers and installed locations in test section floor.

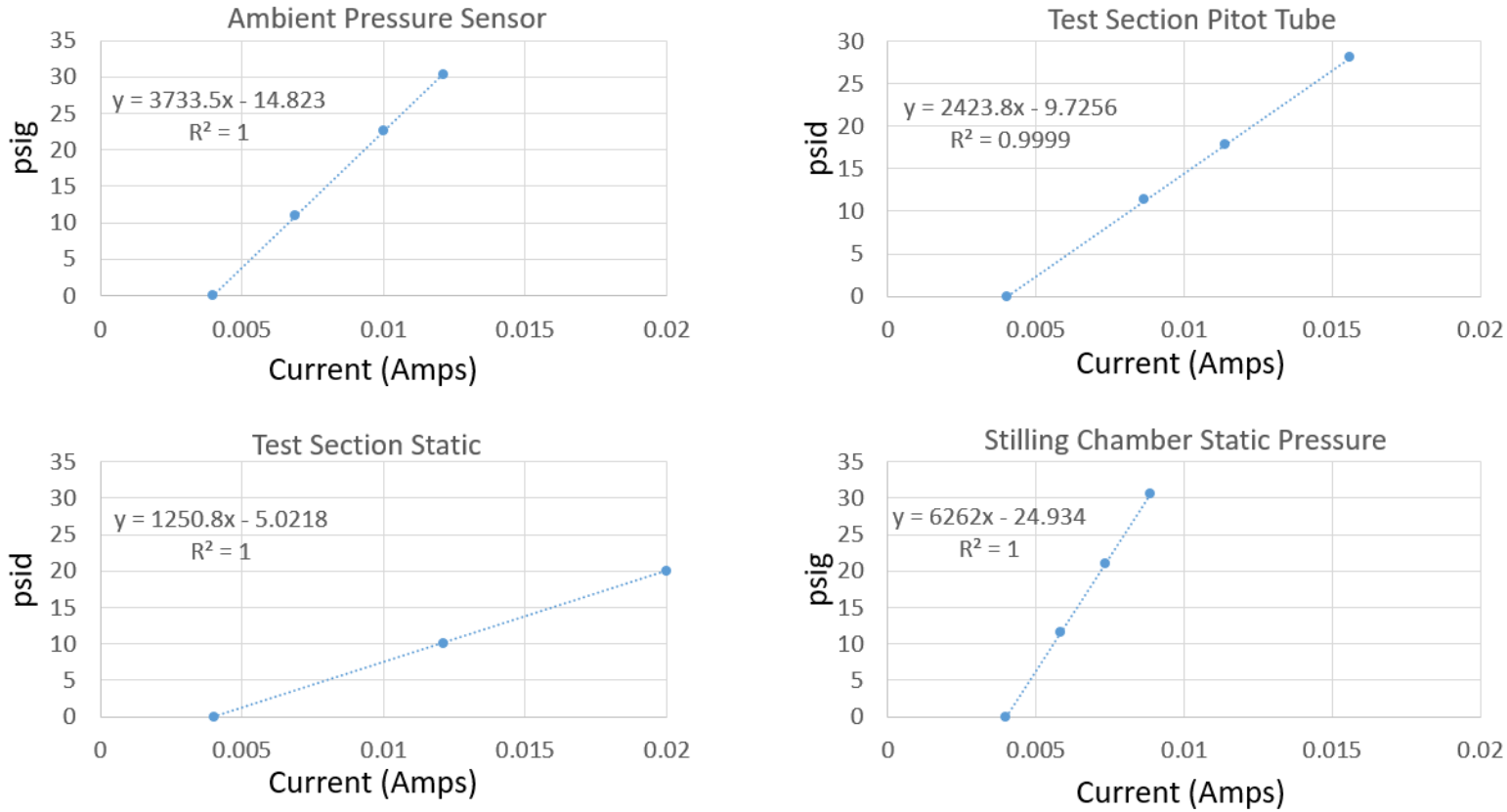

Figure 31. Calibrations for steady-state pressure sensors.

Upper left – calibration for the ambient pressure sensor. Upper right – calibration for the test-section total pressure sensor. Lower right – calibration for the stilling chamber static pressure sensor. Lower left – calibration for the test-section static pressure sensor.

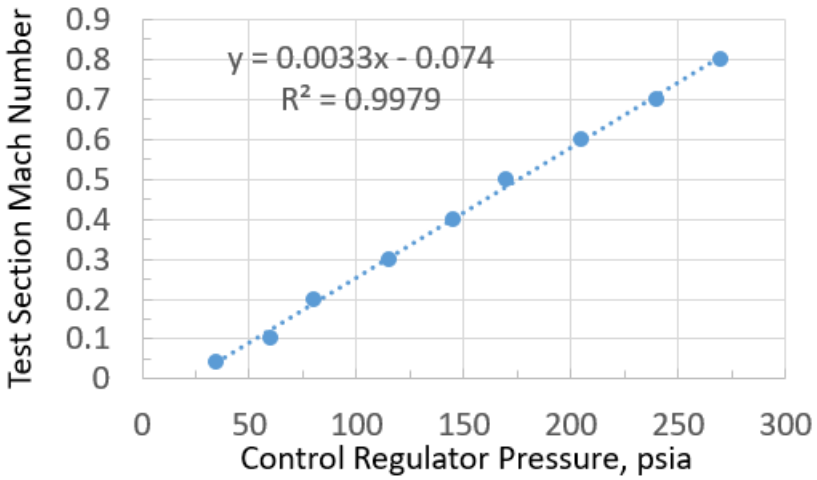

Figure 32. Tunnel supply pressure and test section Mach number correlation.

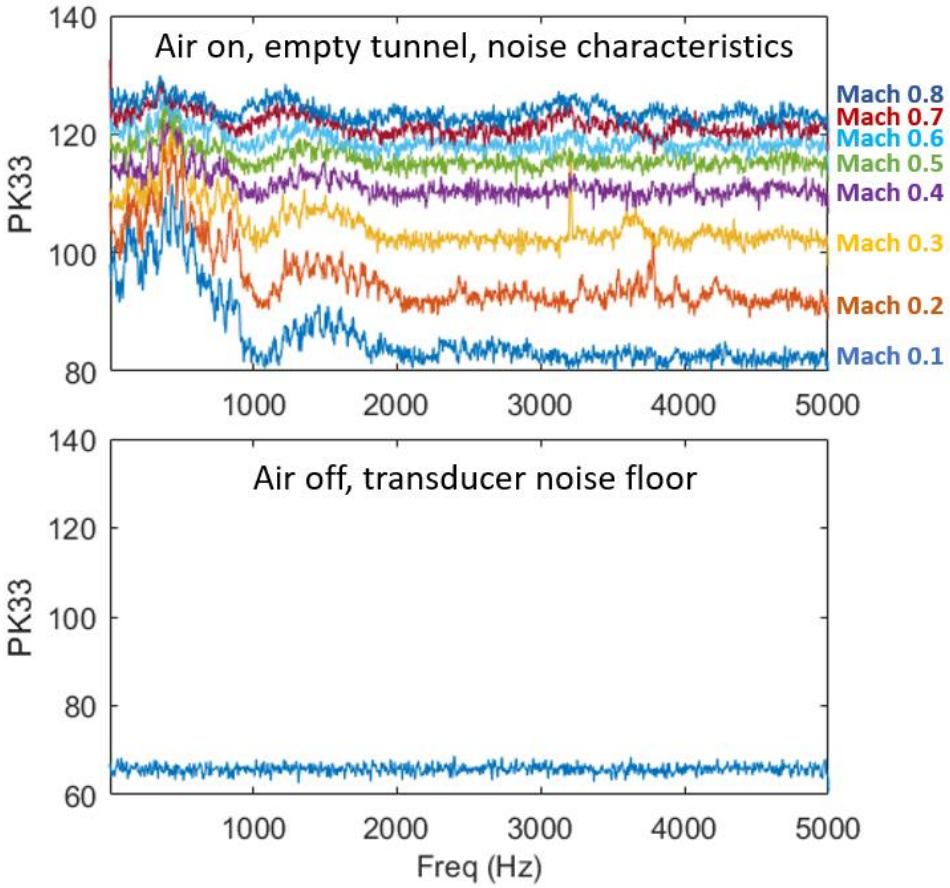

Figure 33. Tunnel noise levels from calibration.

Lower – typical noise-floor of a high-response pressure measurement with no flow in the tunnel. Upper – typical noise-floor for a high-response pressure measurement with the tunnel flowing at the indicated Mach numbers. Units in decibels.

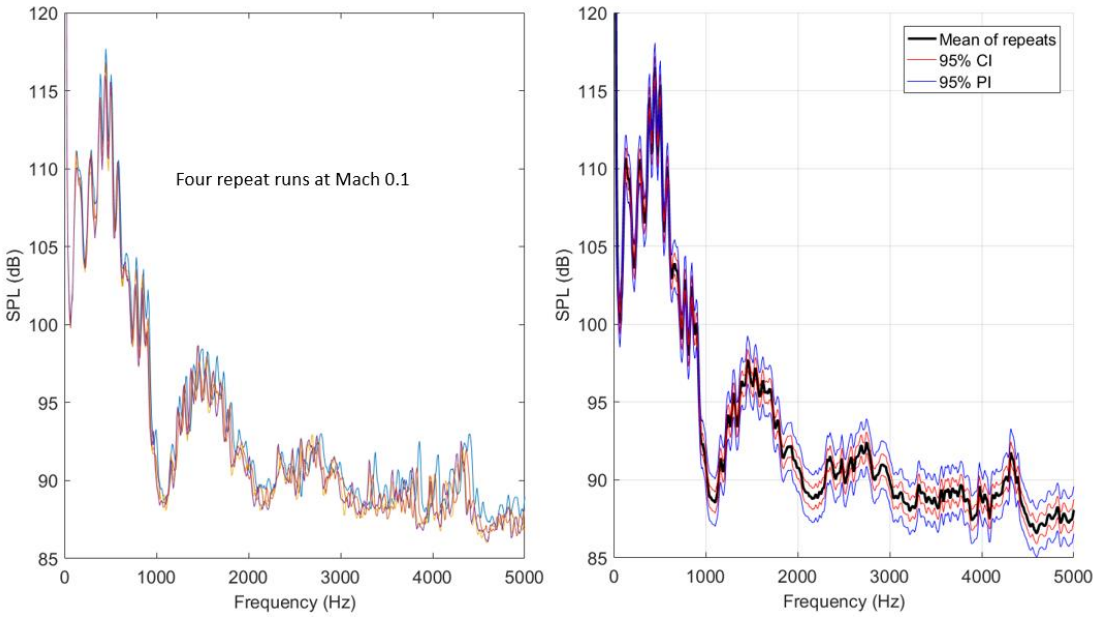

Figure 34. Estimates of the data uncertainty and data repeatability using the confidence and prediction intervals based on repeat runs.

Left – four repeat runs at Mach 0.1 test conditions. Right – the mean of the repeat runs with 95% confidence (CI) and prediction (PI) intervals overlaid.

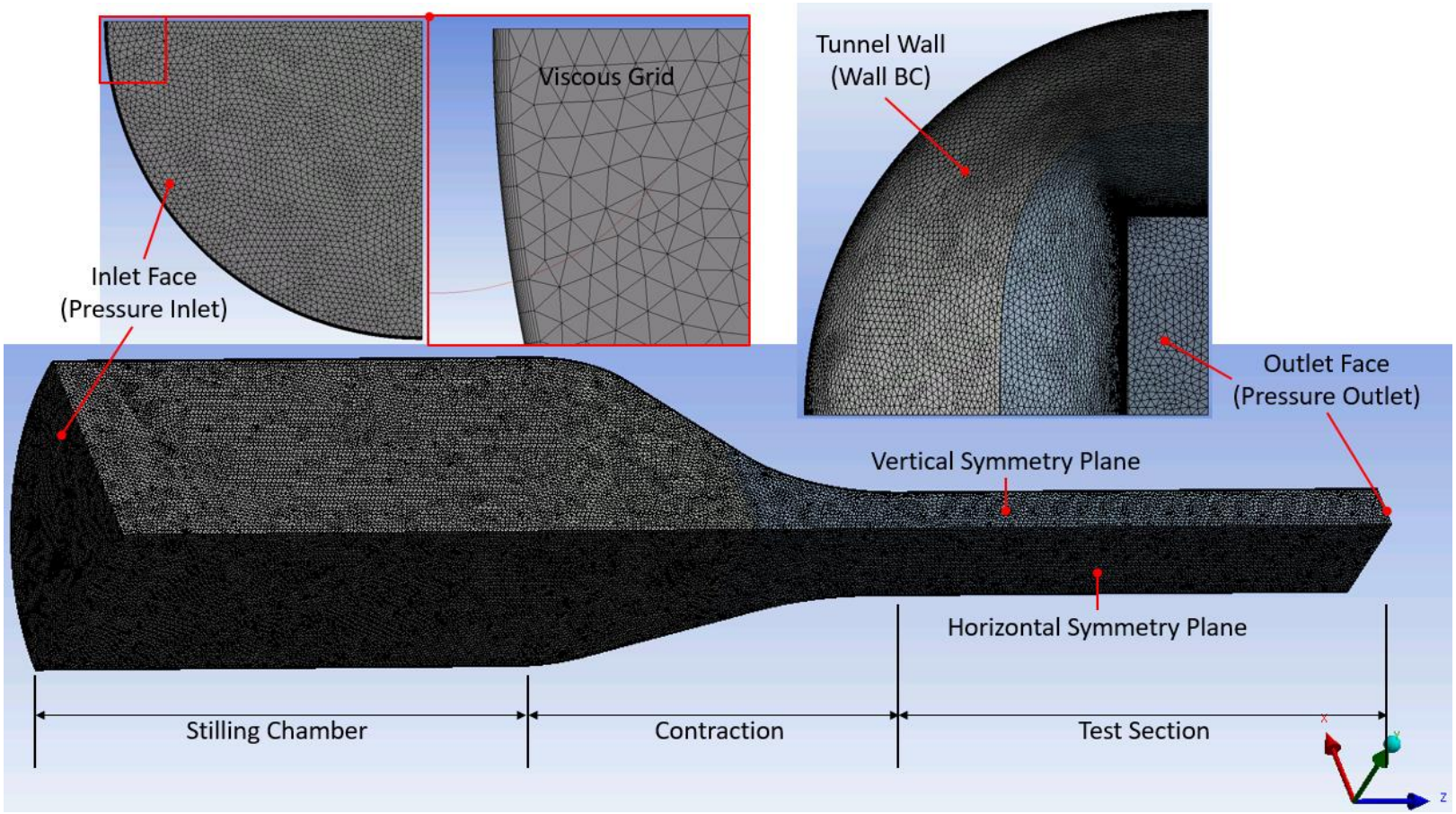

Figure 35. CFD Mesh for tunnel quarter.

Upper left – viscous grid details. Upper right – pressure outlet and nozzle contour details. Lower – centerline view of the CFD geometry.

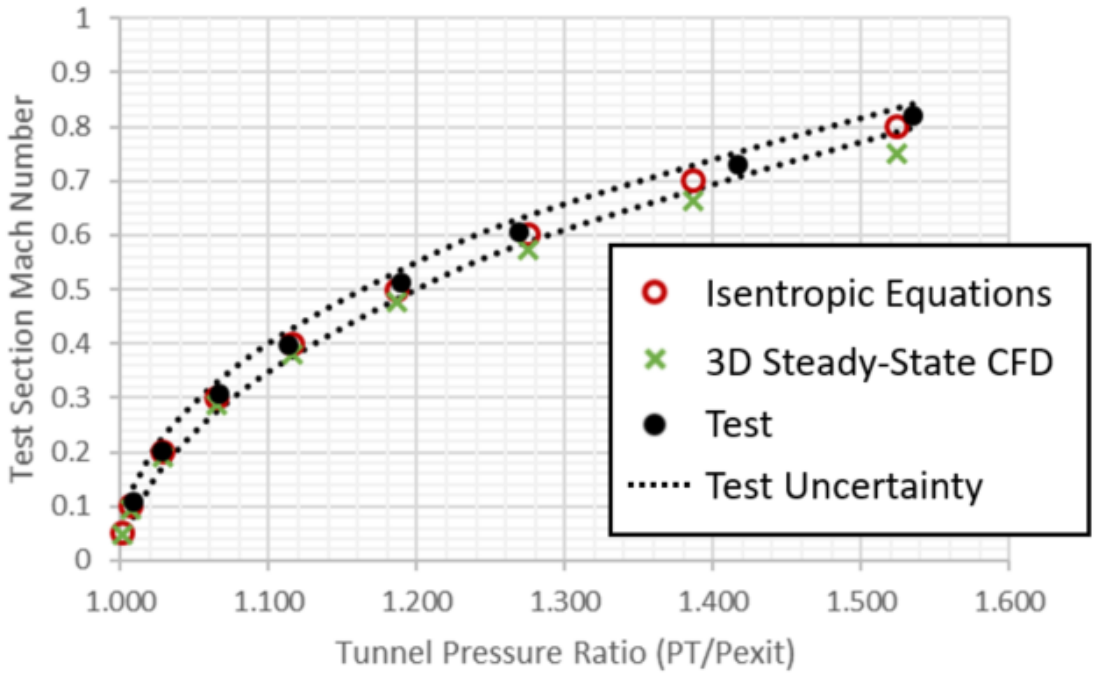

Figure 36. Calibration curves from isentropic equations, CFD, and test.

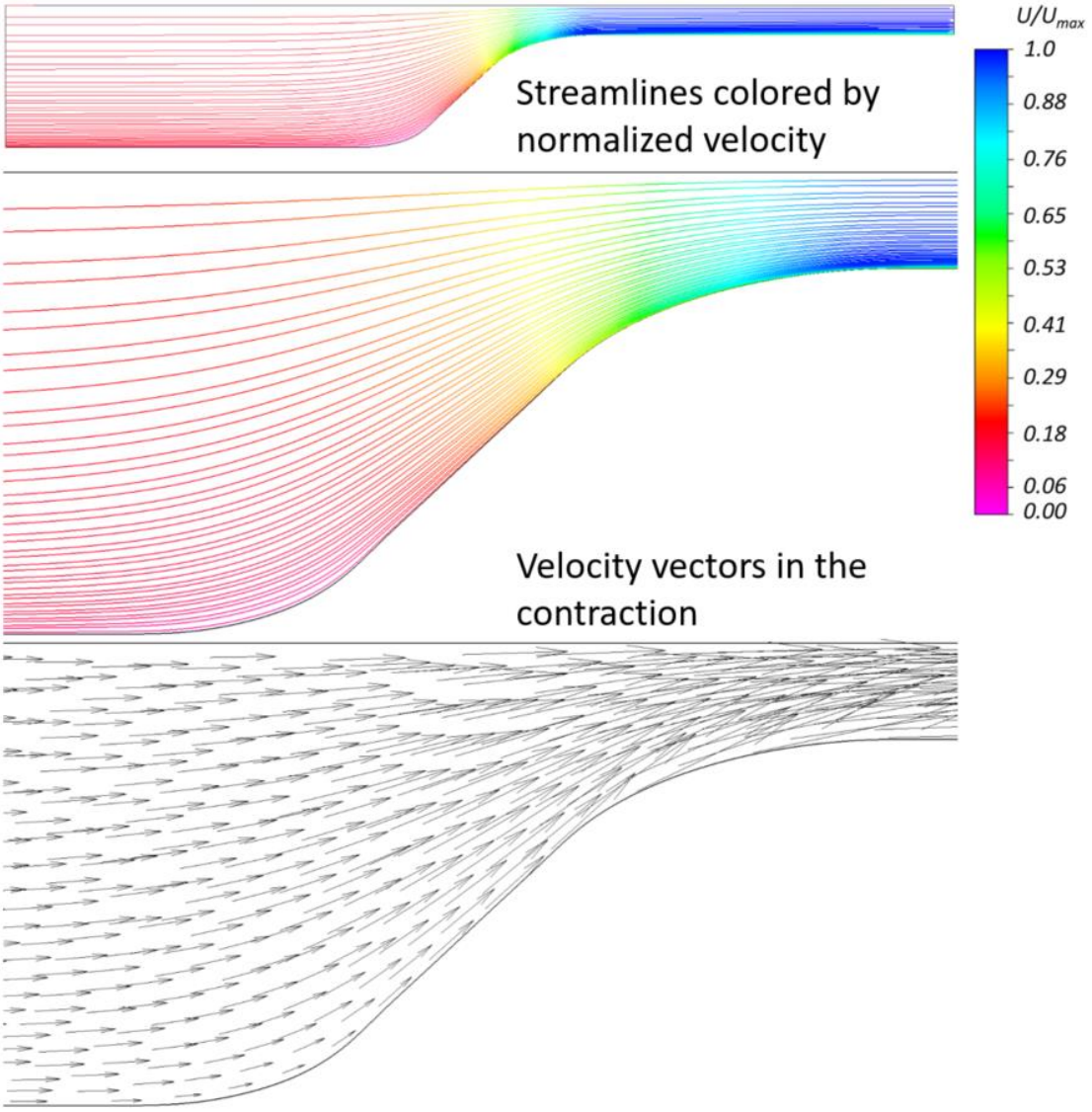

Figure 37. Velocity vectors and streamlines on the vertical tunnel centerline plane.

Forestier's Experimental Domain

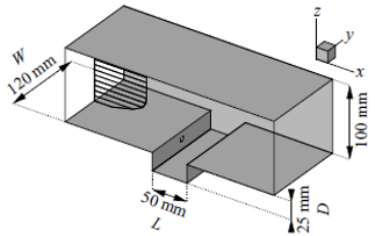

Larcheveque's Computational Domain

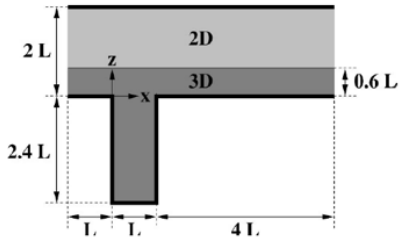

FIG. 1. 2D mesh dimensions.

2D Fluent Computational Mesh

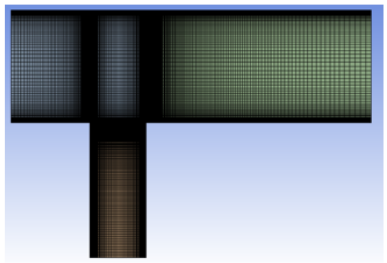

Figure 38. Comparison of cavity geometries.

Left - Forestier's experimental geometry. Middle - Larcheveque's computational geometry. Right - two-dimensional geometry used to validate fluent grid generation and physics setup procedures.

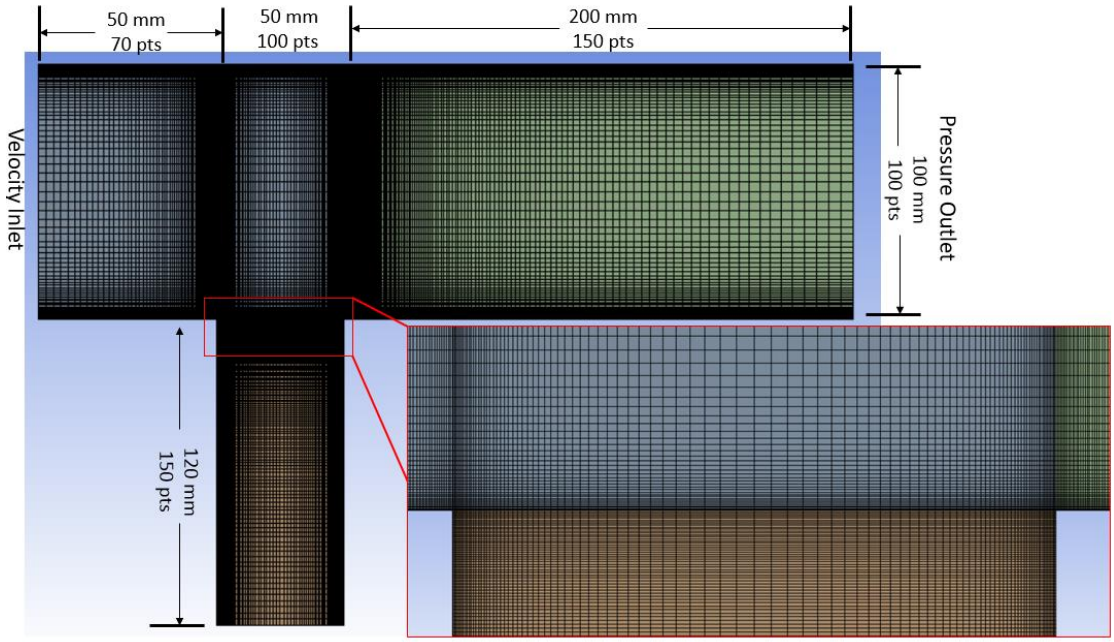

Figure 39. Medium Grid Details

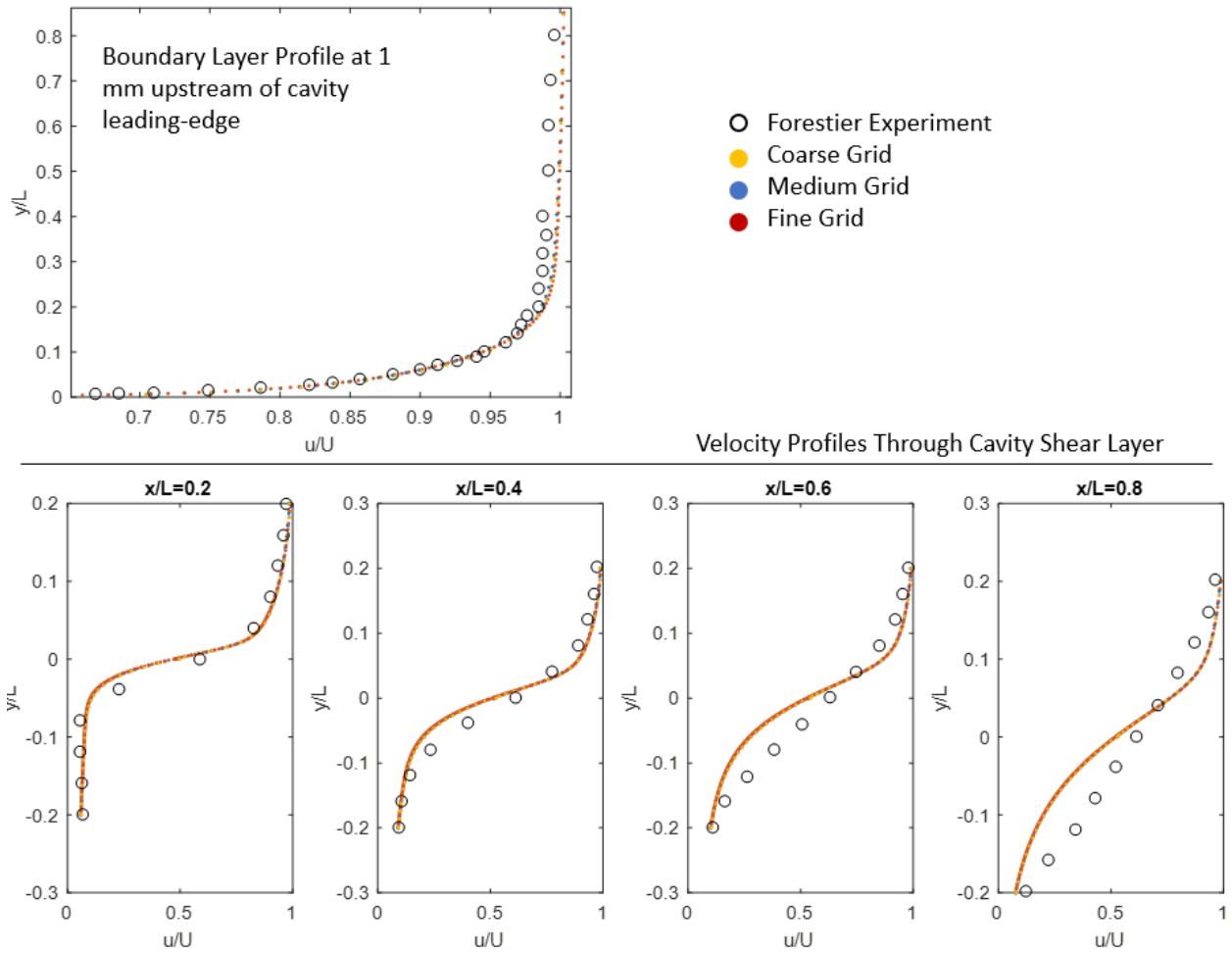

Figure 40. Comparison of Three Grid Densities with Forestier's Experimental Results

Upper – boundary layer profile upstream of cavity leading-edge. Lower – velocity profiles inside the cavity.

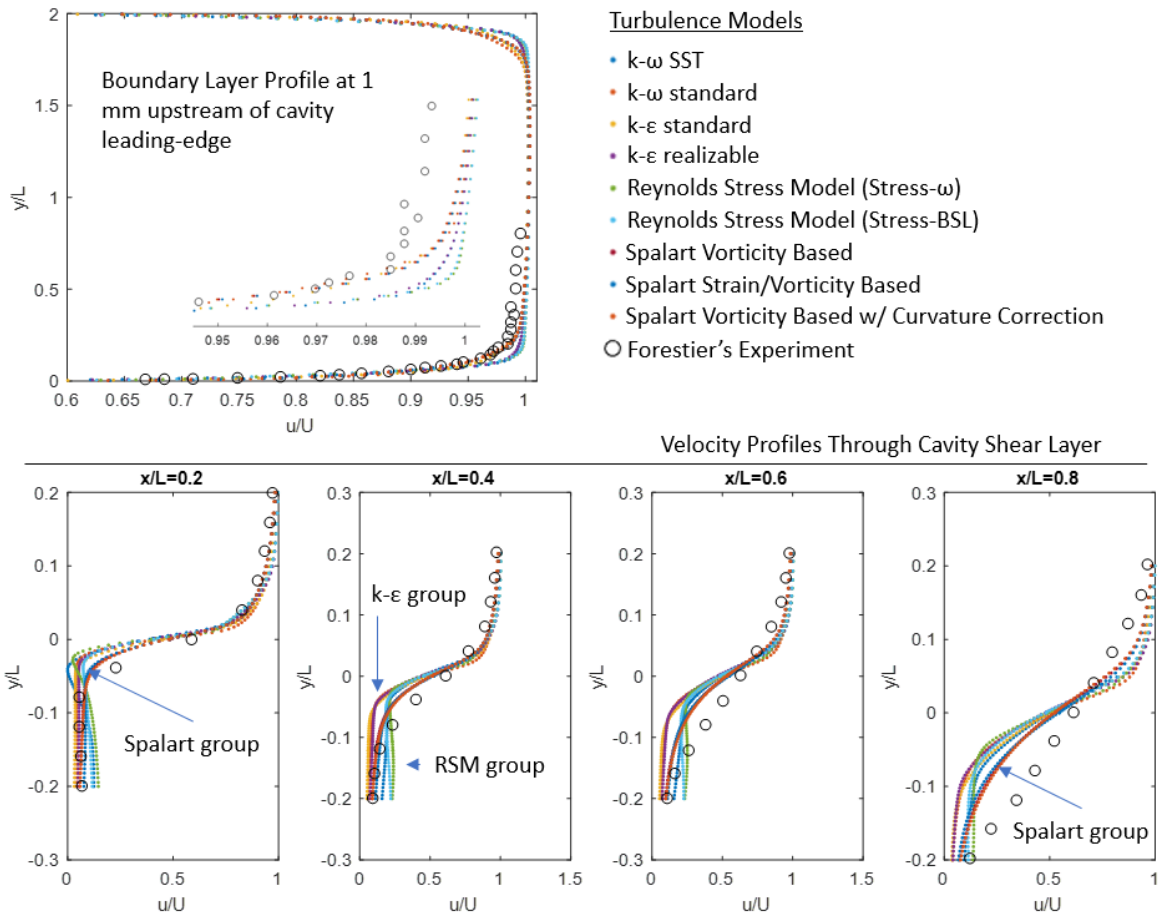

Figure 41. Comparison of Various Turbulence Models Available to a Fluent User for a 2D Simulation.

Comparisons for the cavity geometry of Larcheveque and Forestier.

Upper – boundary layer profiles upstream of cavity leading-edge. Lower – velocity profiles inside the cavity.

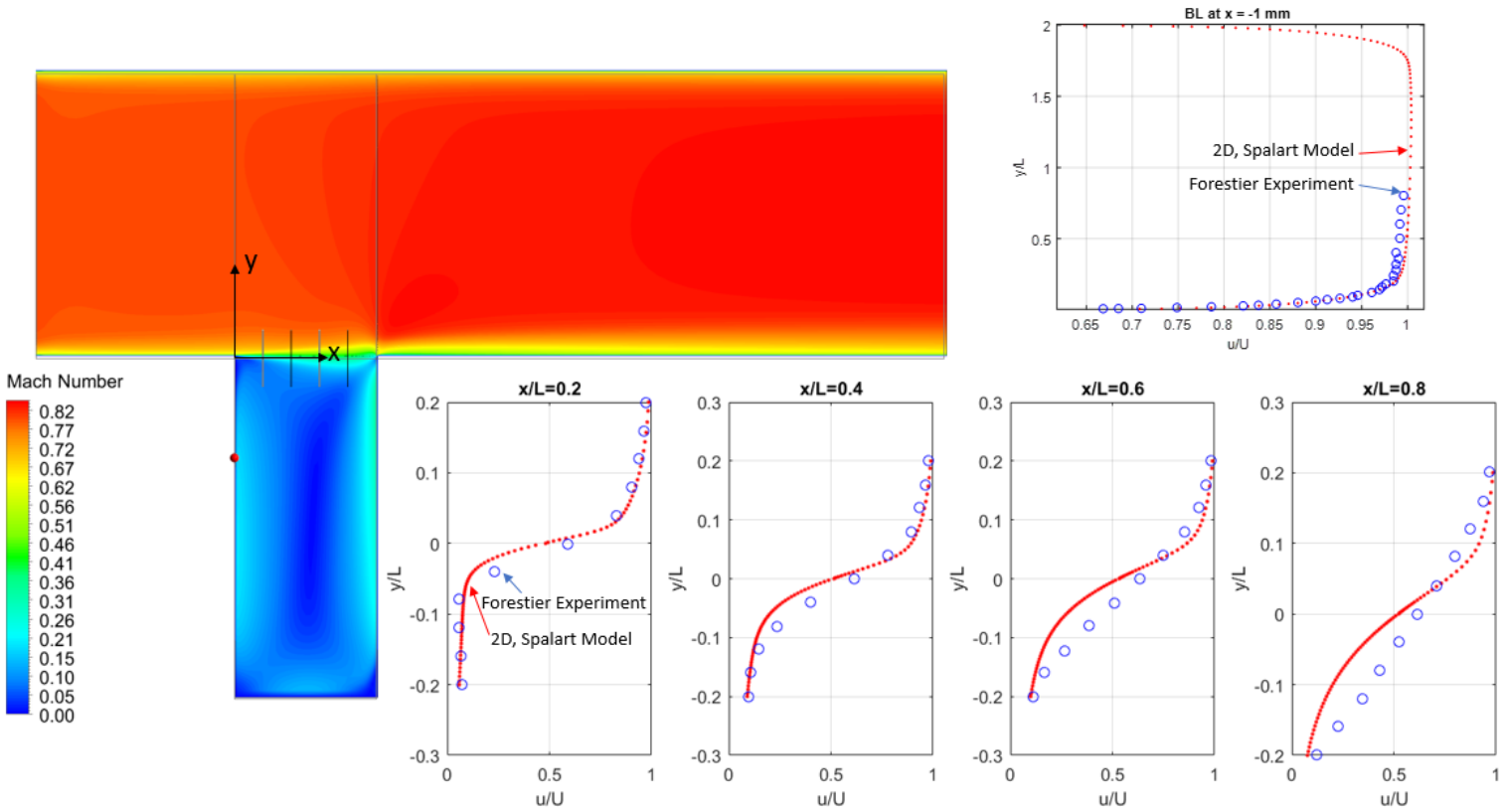

Figure 42. Steady-state results from simulation of Larcheveque and Forestier cavity experiment.

Left – Computational domain showing the Mach number distribution. Upper right – boundary layer profile comparison with experiment at a location just upstream of the cavity leading-edge. Lower right – comparisons of velocity profiles in the cavity for CFD and experiment.

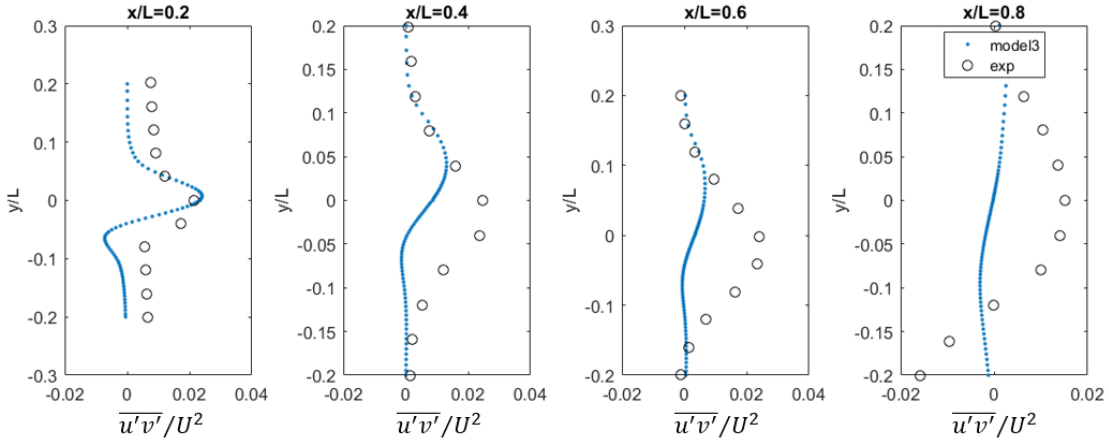

Figure 43. The u'v' Reynolds stress through the cavity shear layer for the time-accurate CFD simulations.

Simulations of Larcheveque's and Forestier's experiment. Values averaged over 0.7 seconds of simulation time. Distance from cavity leading edge increasing from left plat to right plot.

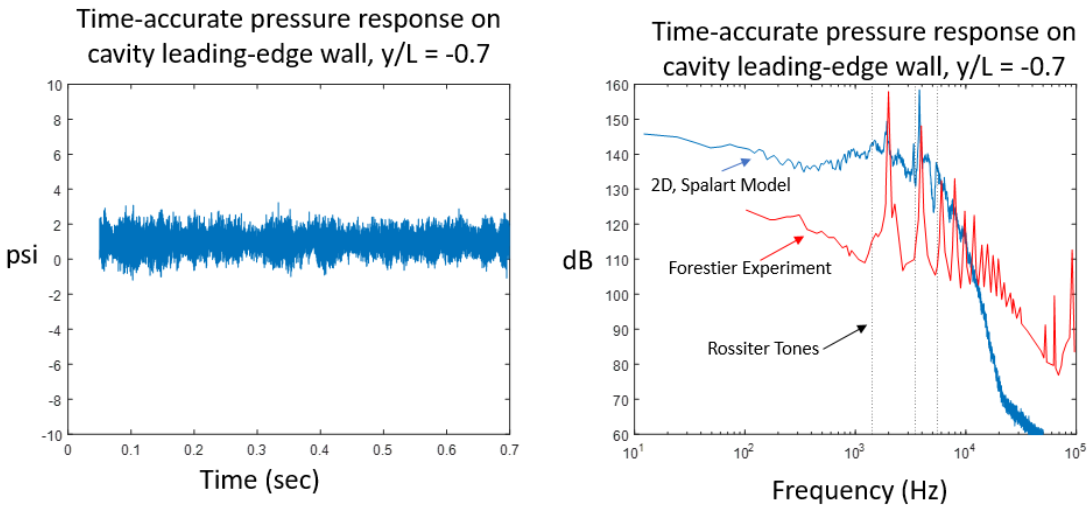

Figure 44. Pressure time history and sound pressure level (SPL) spectra.

Data represent the two-dimensional CFD simulation of Forestier's experiment and comparison to Forestier's reported SPL spectra. Left is time-history of pressure on cavity leading-edge wall (CFD only). Right is pressure spectra at cavity leading-edge wall (CFD and experiment).

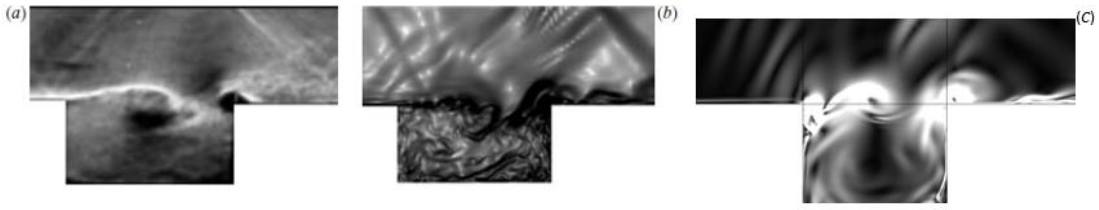

Figure 45. Comparison of flow visualization across the cavity.

(a) Experimental fast Schlieren view of Forestier experiment. (b) filled isolevels of the magnitude of the density gradient from Larcheveque simulations. (c) filled isolevels of the magnitude of the density gradient from the author's Fluent simulation. (a) and (b) reproduced from Larcheveque (Larcheveque, Sagaut, & Labbe, 2007).

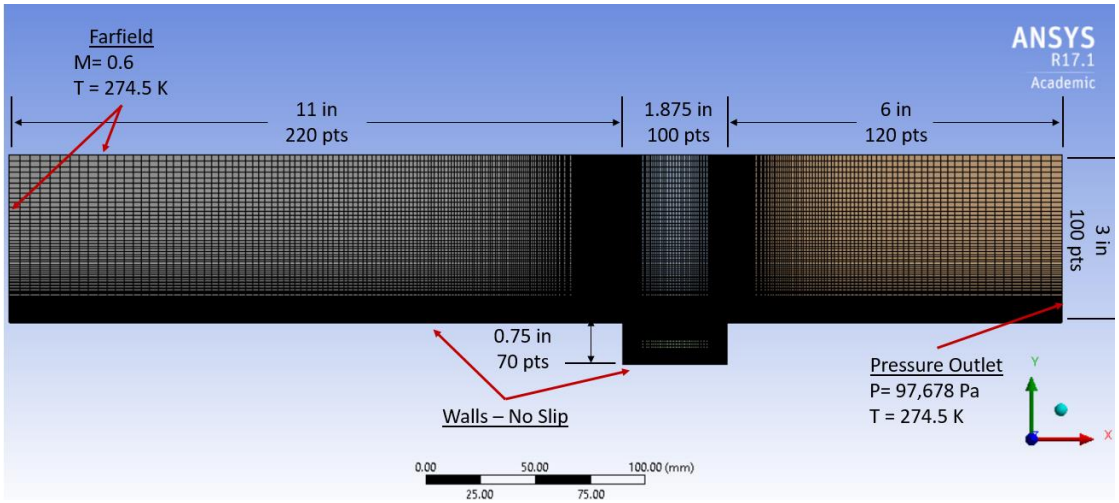

Figure 46. Computational domain used in CFD simulation of Radhakrisnan's experiment.

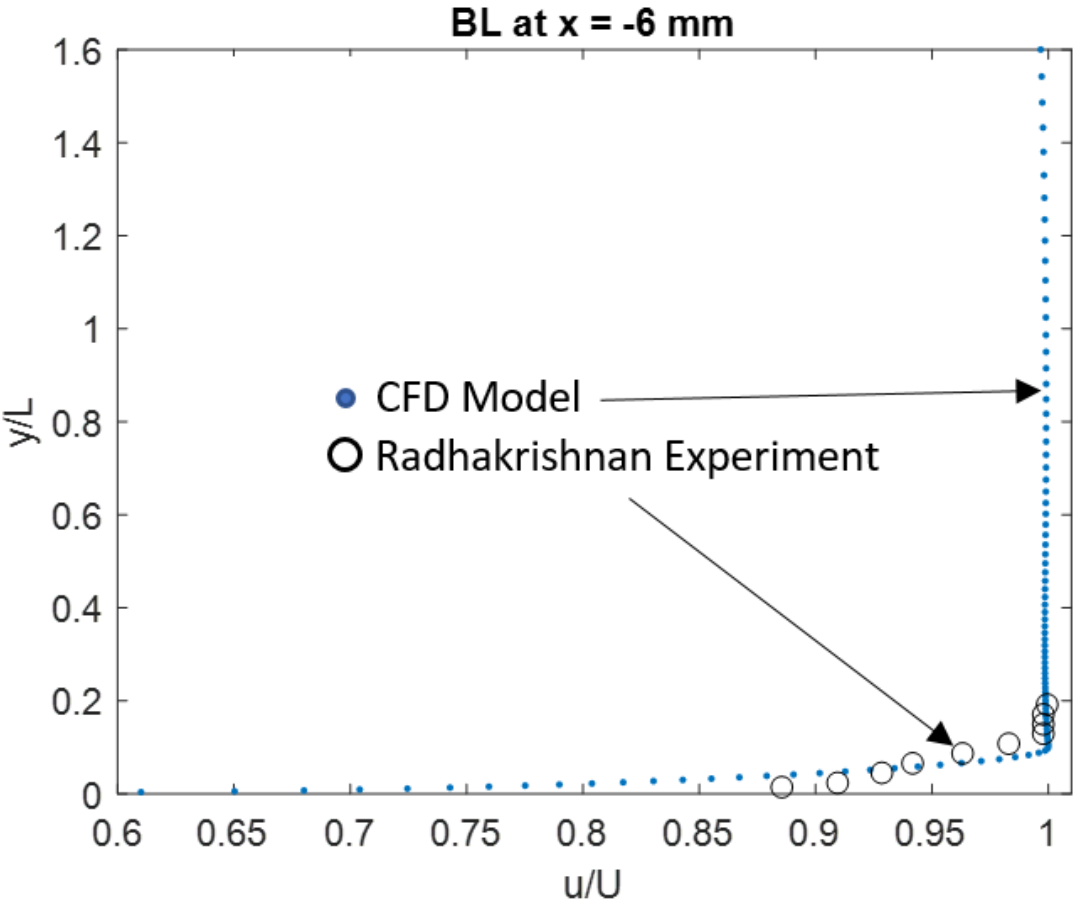

Figure 47. Comparison of boundary layer upstream of cavity leading edge in CFD simulation and Radhakrishnan's experimental data.

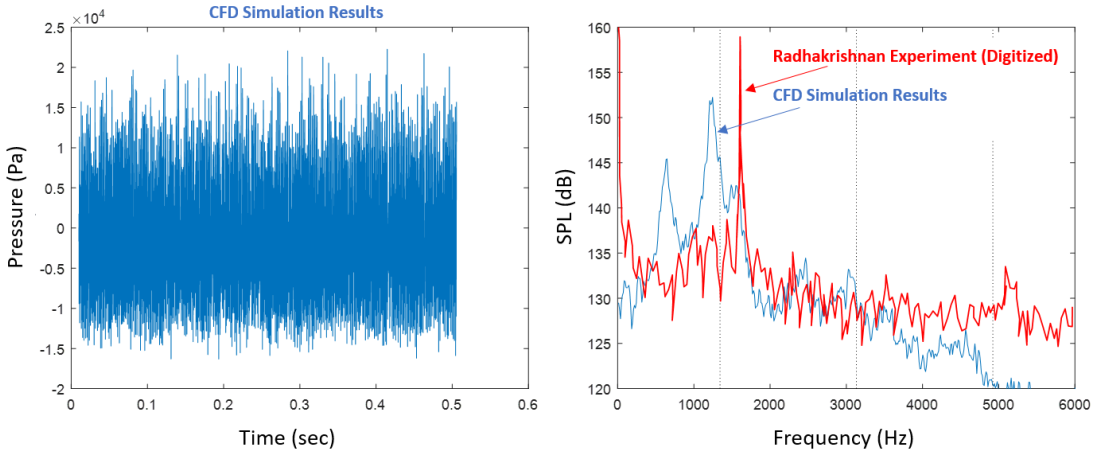

Figure 48. Time-accurate CFD results for simulation of Radhakrisnan's experiment.

Left – time history of a digital pressure measurement on the floor of the cavity. Right Comparison of sound pressure level (SPL) spectrum from 0.1 seconds of CFD simulation time and Radhakrishnan's experimental SPL spectrum.

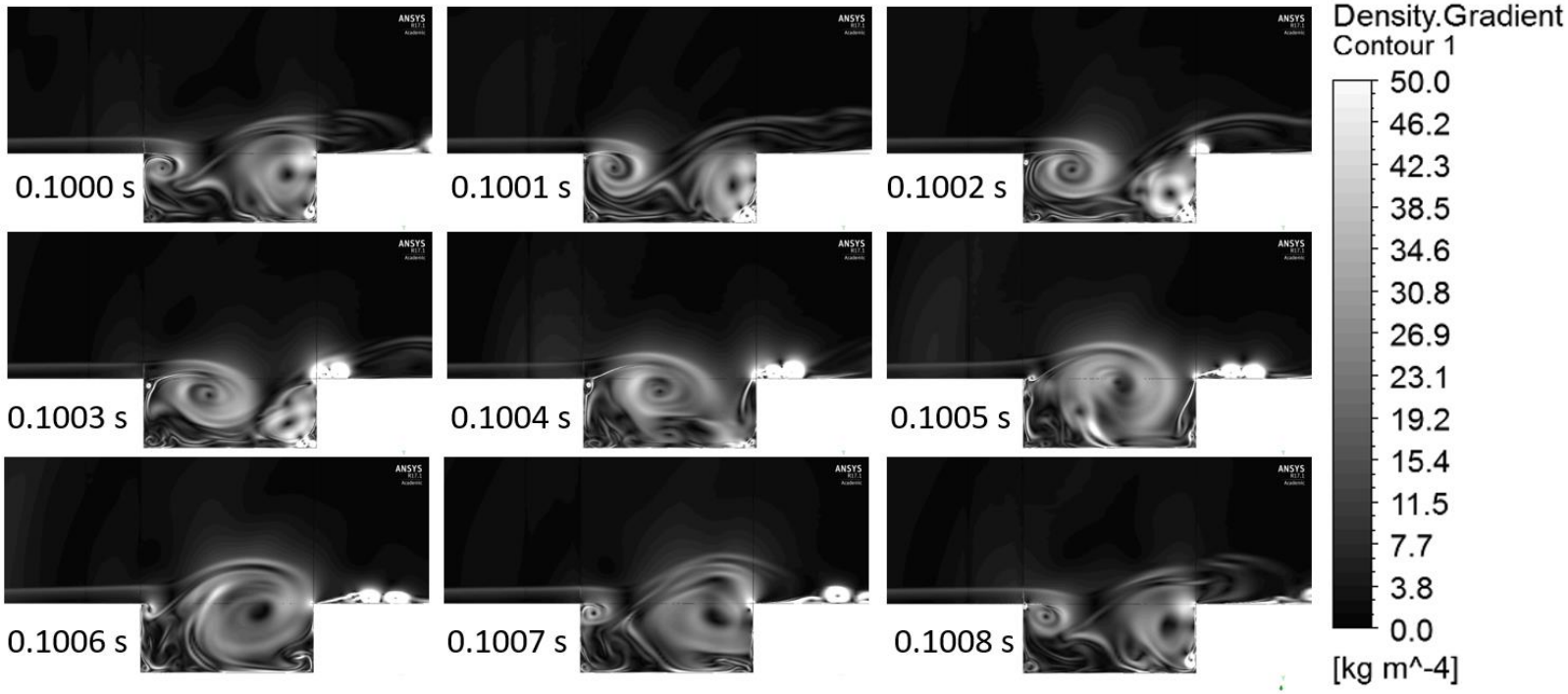

Figure 49. Flow visualization using the magnitude of density gradient for CFD simulation of Radhakrishnan's experiment.

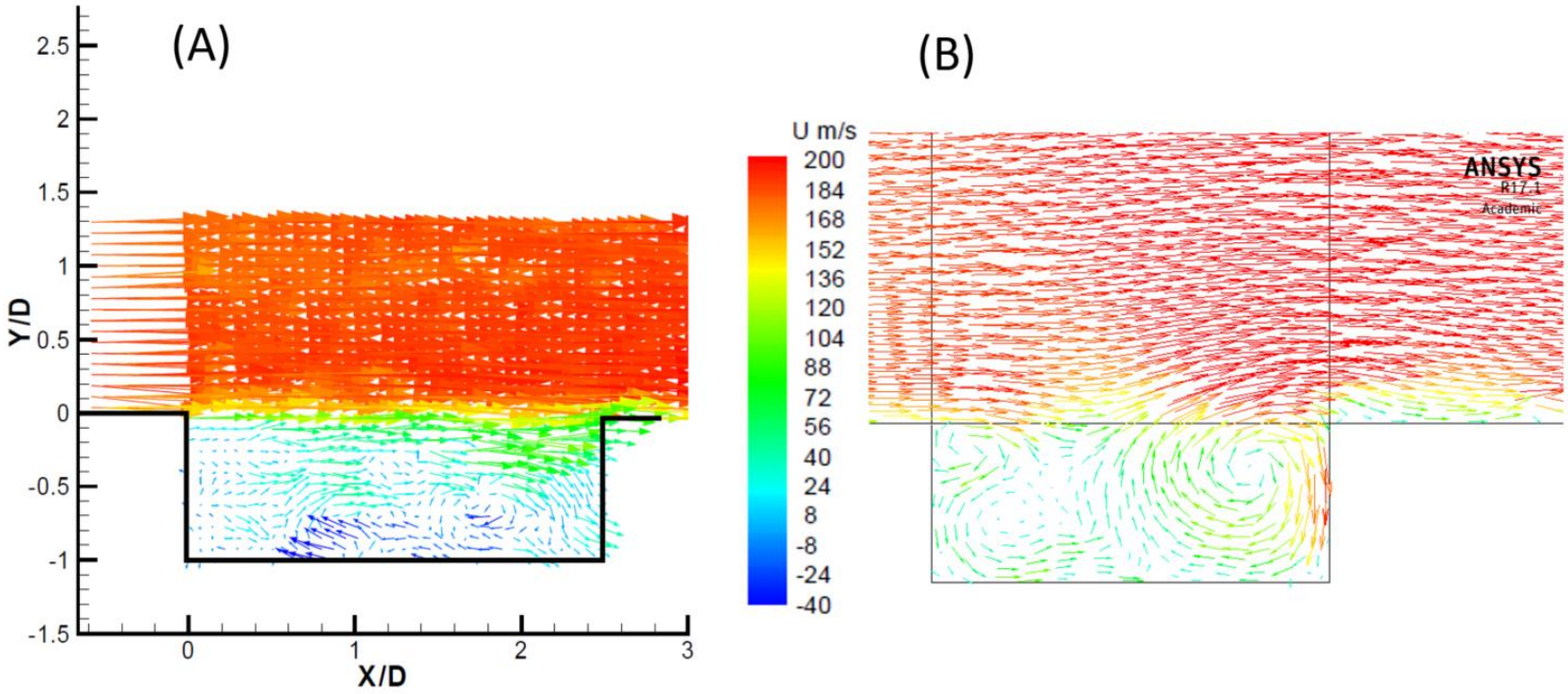

Figure 50. Qualitative comparison of instantaneous velocity vectors from Radhakrishnan's experiment to CFD validation case.

A) Sample of Radhakrishnan's experimental data shown as velocity vectors colored by velocity magnitude at an instant in time. Two vortex regions can be seen inside the cavity. B) Sample from time-accurate CFD solutions from validation check cases showing velocity vectors colored by velocity magnitude at an instant in time. Two vortex regions of greater extent and higher velocity can be seen inside the cavity.

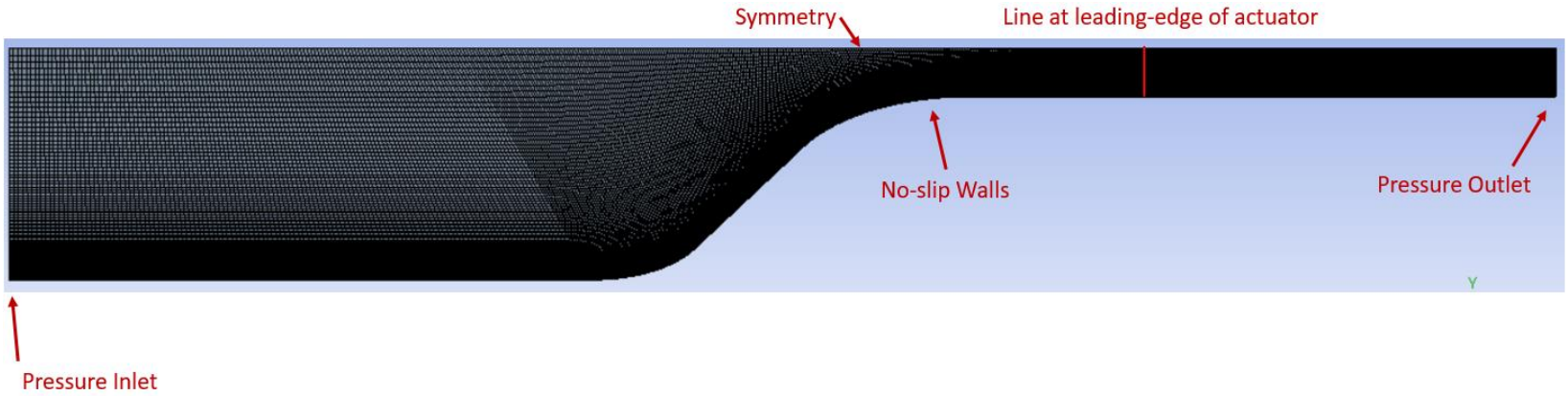

Figure 51. Computational grid used for boundary-layer study.

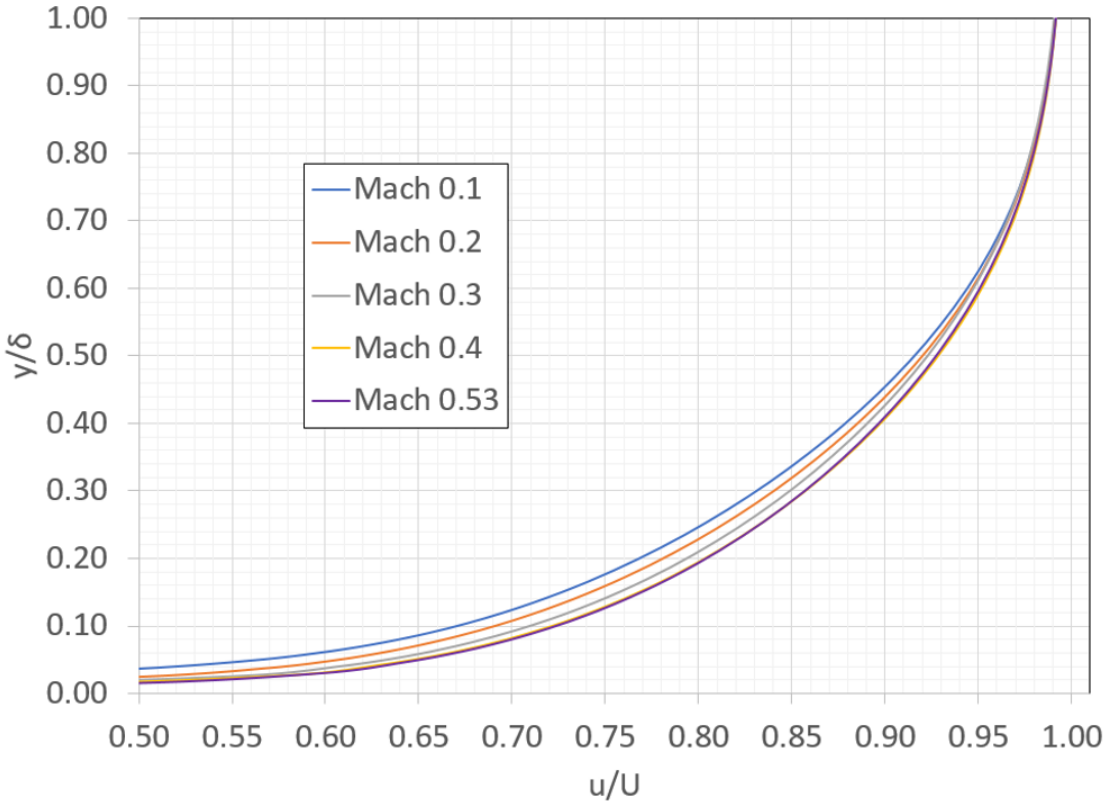

Figure 52. Boundary layer profiles extracted from CFD solutions at various Mach numbers at the location of the leading-edge of the actuator.

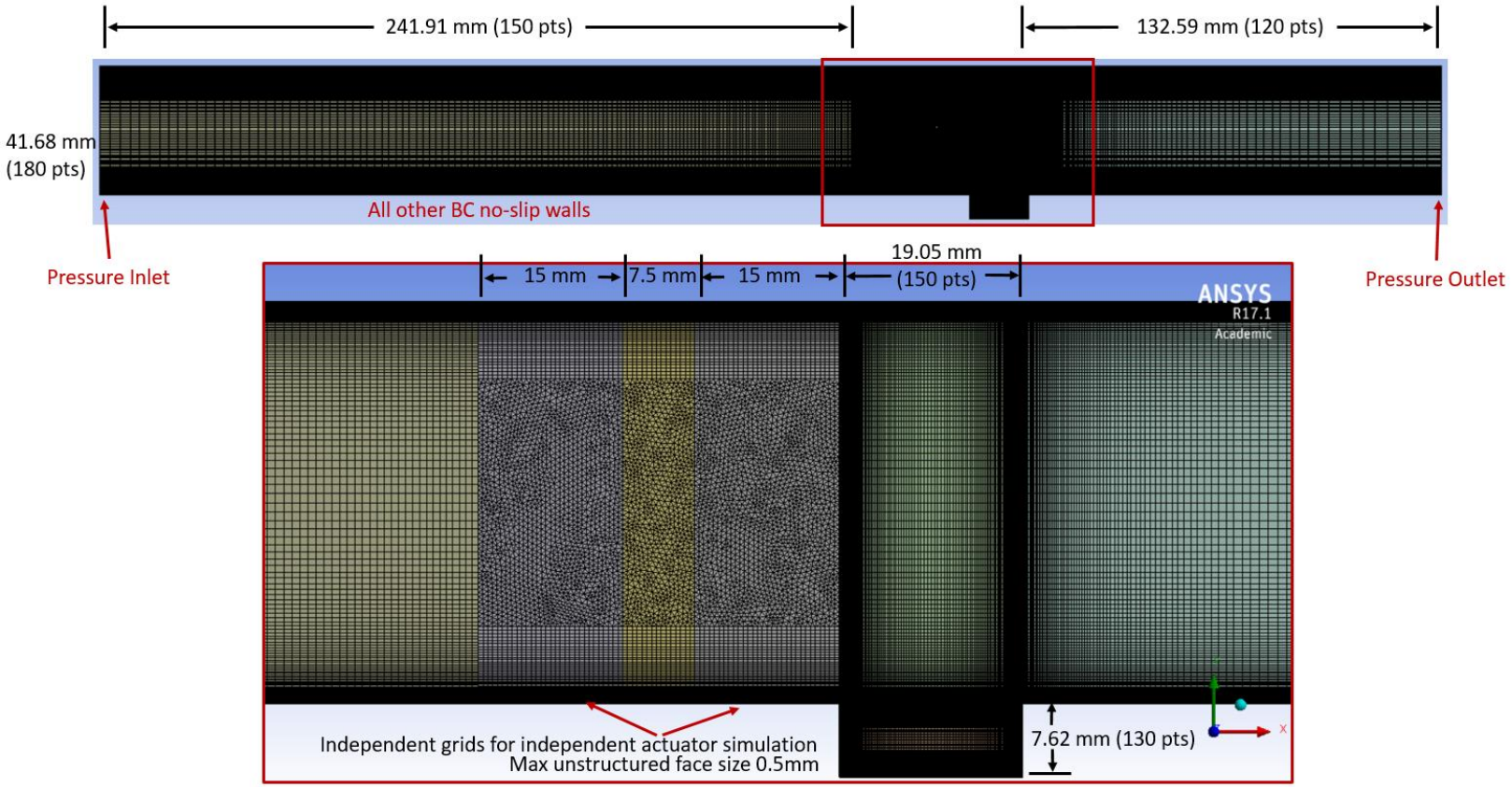

Figure 53. Computational grid used to study cavity flow and actuator/cavity flow coupling.

Upper – the full computational domain. Lower – detail view of the grid density and structure near the cavity. The hybrid structured/unstructured grid allows independent control of two simulated actuators.

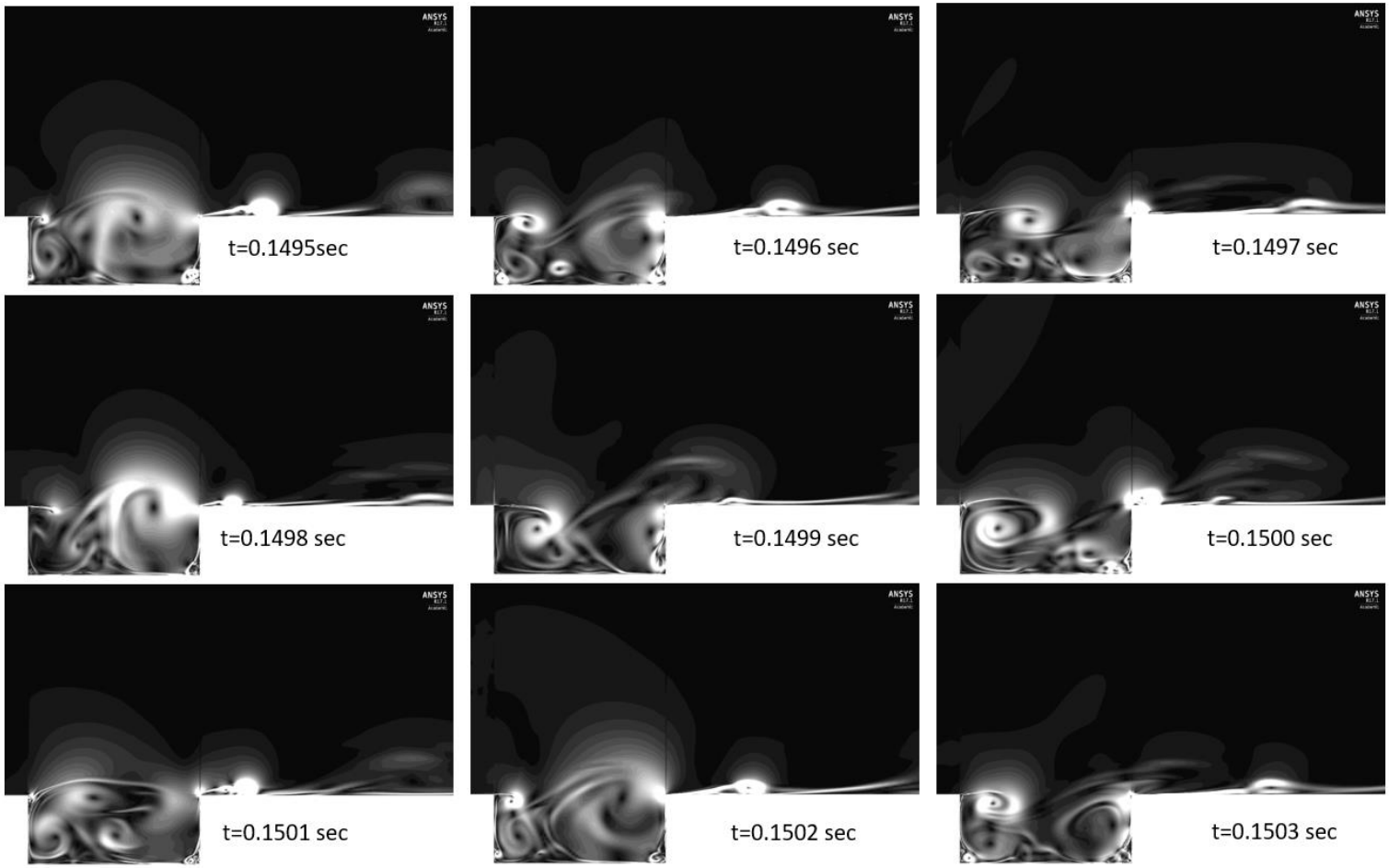

Figure 54. Cavity flow field visualization using the magnitude of the density gradient for approximately one convective cycle of the cavity without simulated flow actuation.

Figure 55. Cavity flow field visualization using the magnitude of the density gradient illustrating the cavity flow field, the forward-propagating wave, and the turbulence downstream of the cavity.

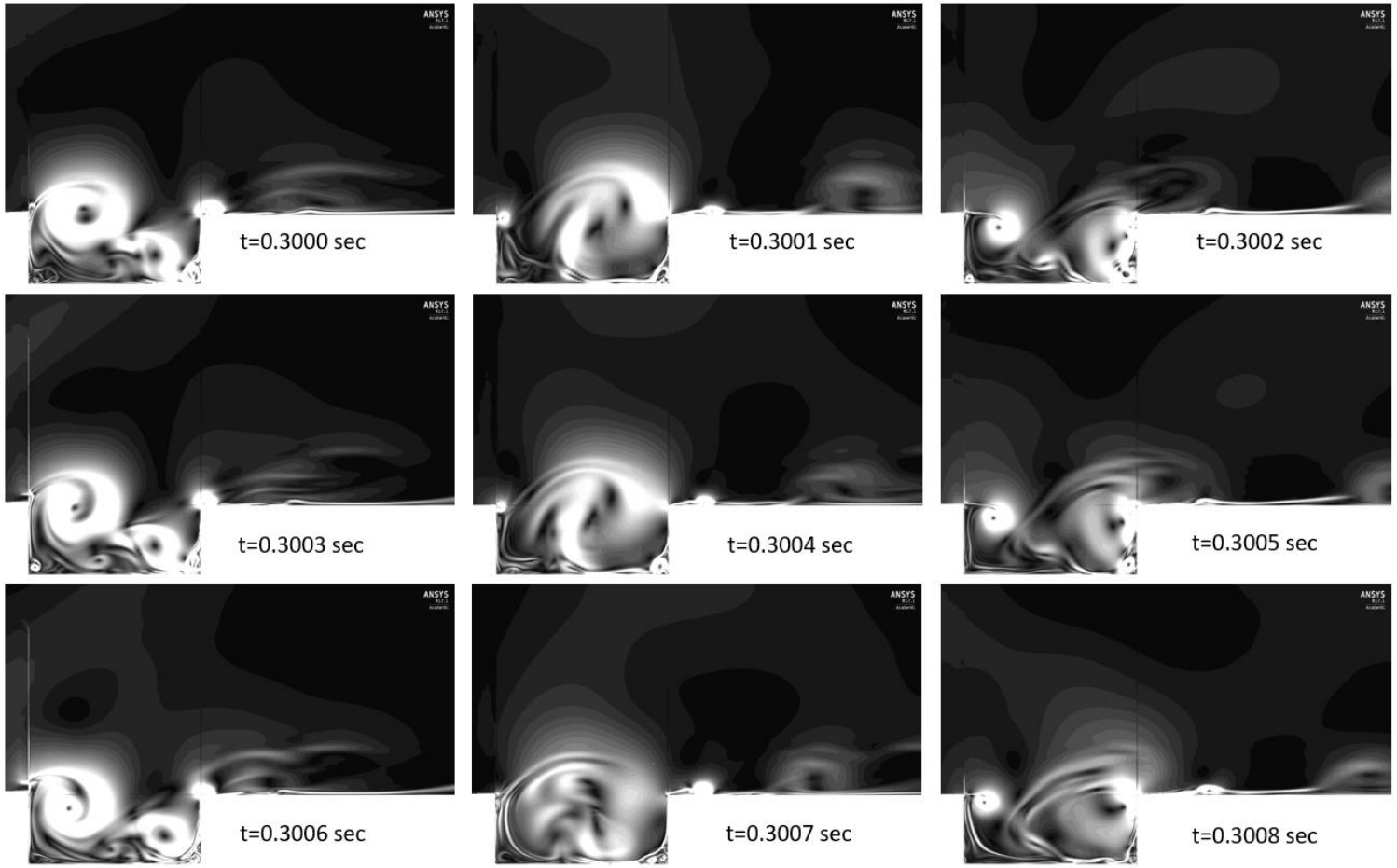

Figure 56. Cavity flow field visualization using the magnitude of the density gradient for approximately one convective cycle of the cavity with simulated flow actuation at the cavity leading-edge.

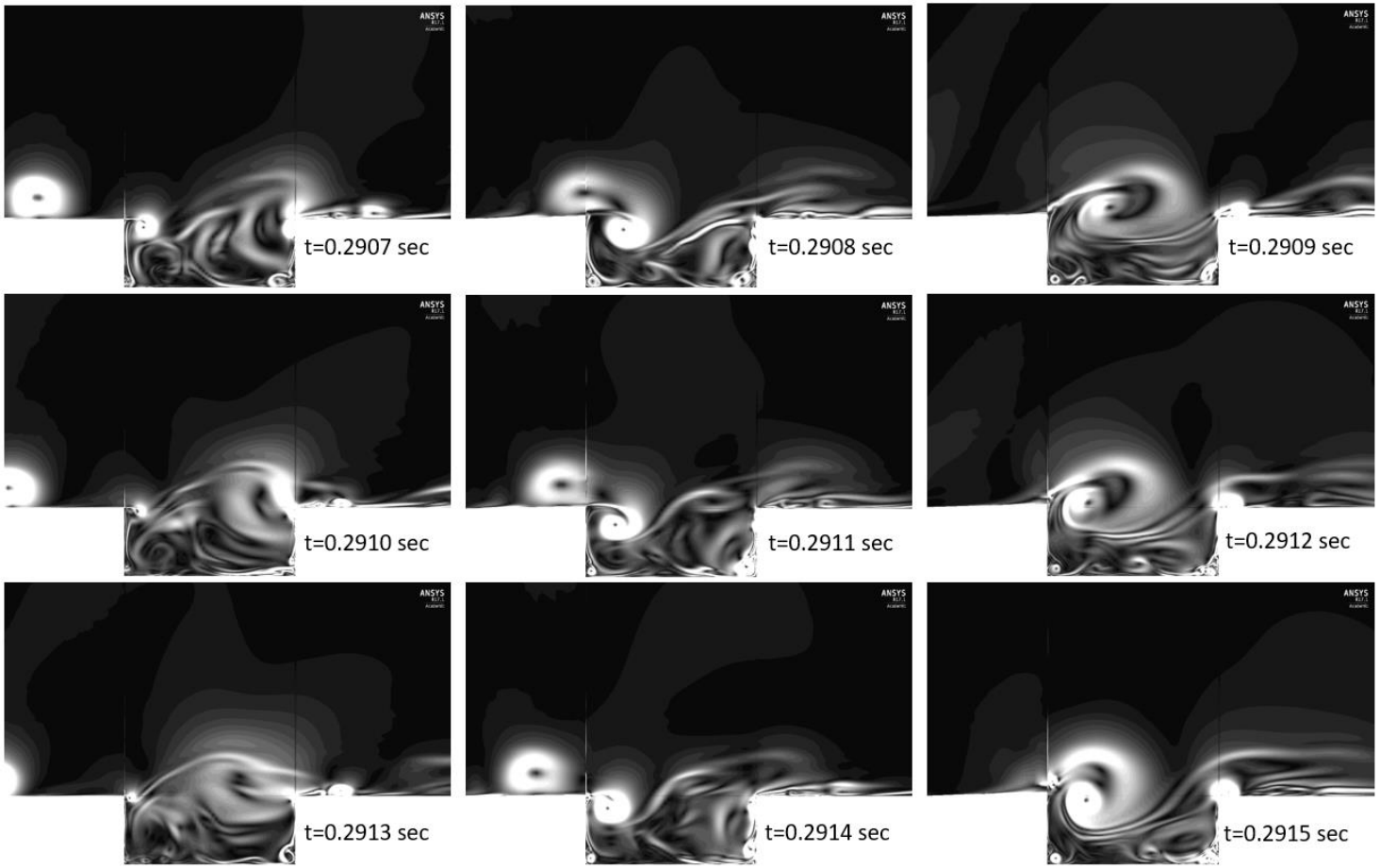

Figure 57. Cavity flow field visualization using the magnitude of the density gradient for approximately one convective cycle of the cavity with simulated multi-level flow actuation at the cavity leading-edge and upstream of the cavity.

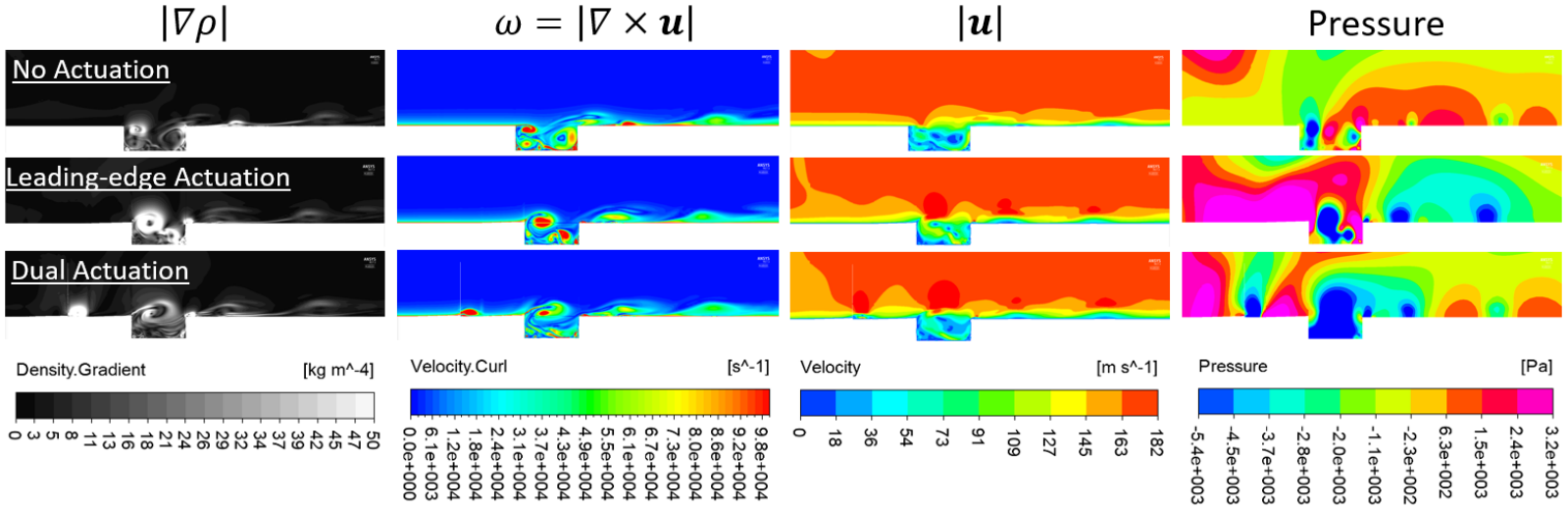

Figure 58. Comparison of cavity flow fields with and without actuation using various flow field parameters.

Top row – without actuation. Middle row – with leading-edge actuation. Bottom row – dual actuators in series. Left column – flow field contours colored by the magnitude of the density gradient. Second column from left – flow field contours colored by the magnitude of the vorticity vector. Third column from left – flow field contours colored by the magnitude of the velocity vector. Right column – flow field contours colored by pressure.

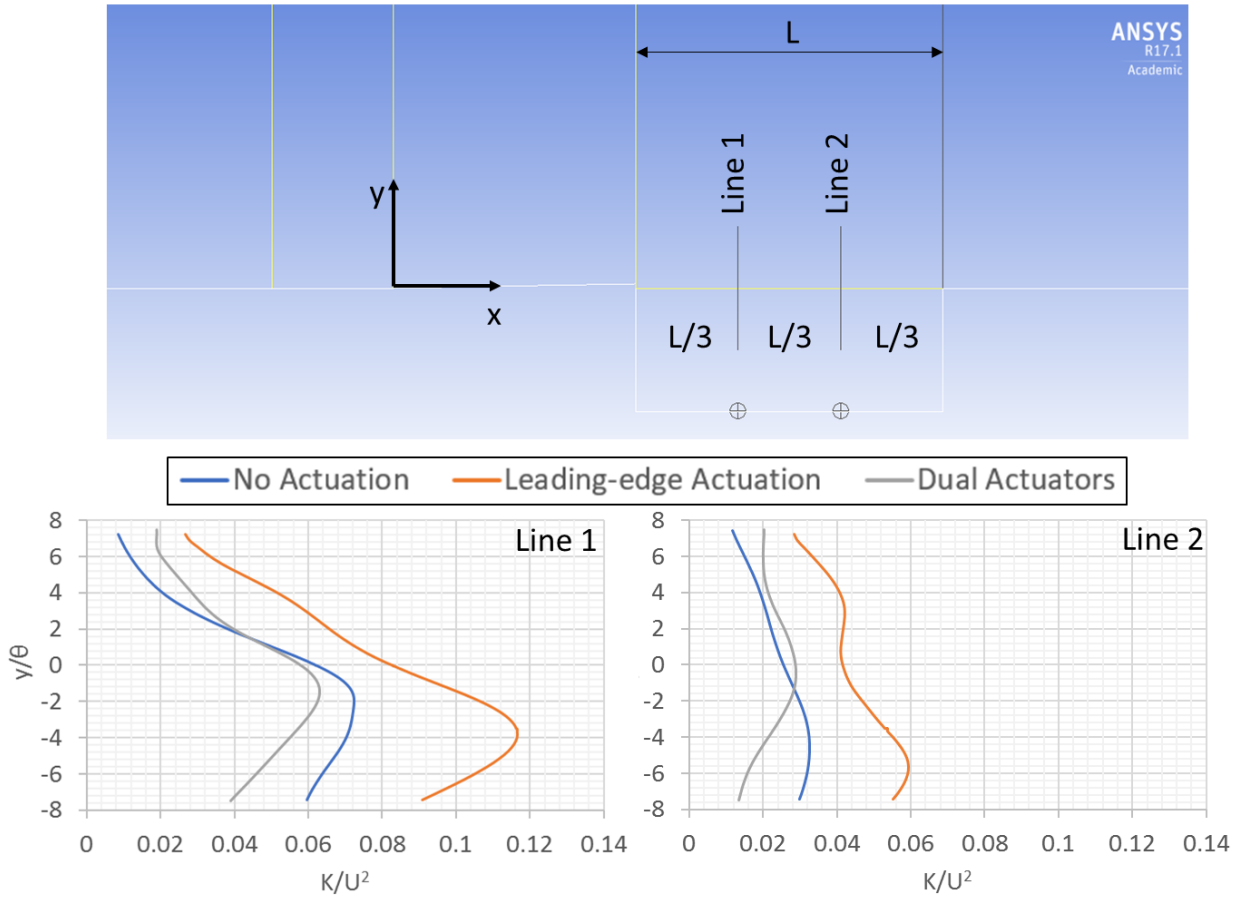

Figure 59. Comparison of turbulent kinetic energy (K) across the cavity shear layer at two locations for CFD solutions with and without flow actuator simulations.

Upper – geometry indicating location of sampled data inside the cavity. Lower – sampled turbulence kinetic energy at the locations specified in the upper schematic.

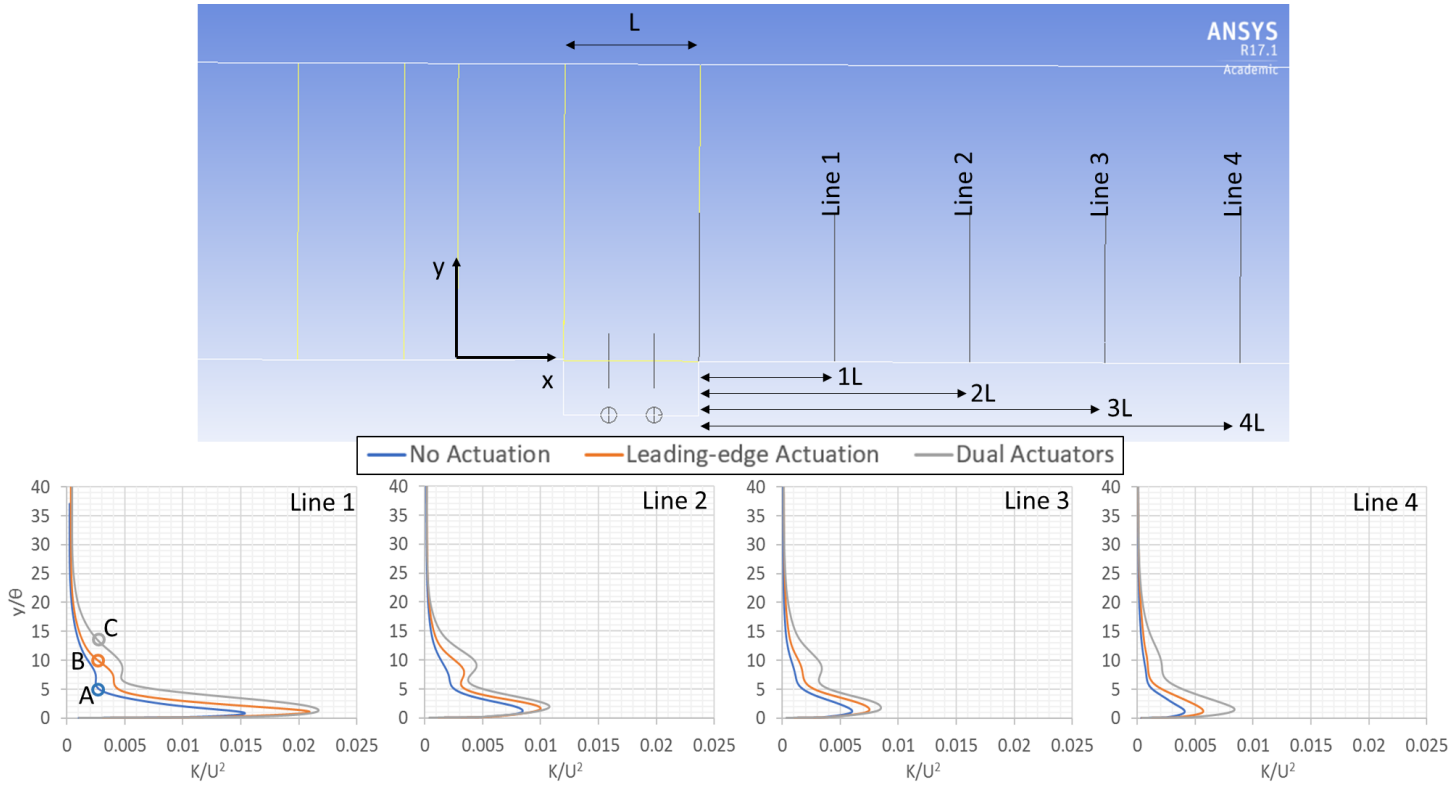

Figure 60. Comparison of turbulent kinetic energy (K) downstream of the cavity for CFD solutions with and without flow actuator simulations.

Upper – geometry indicating location of sampled data downstream of the cavity. Lower – sampled turbulence kinetic energy at the locations specified in the upper schematic.

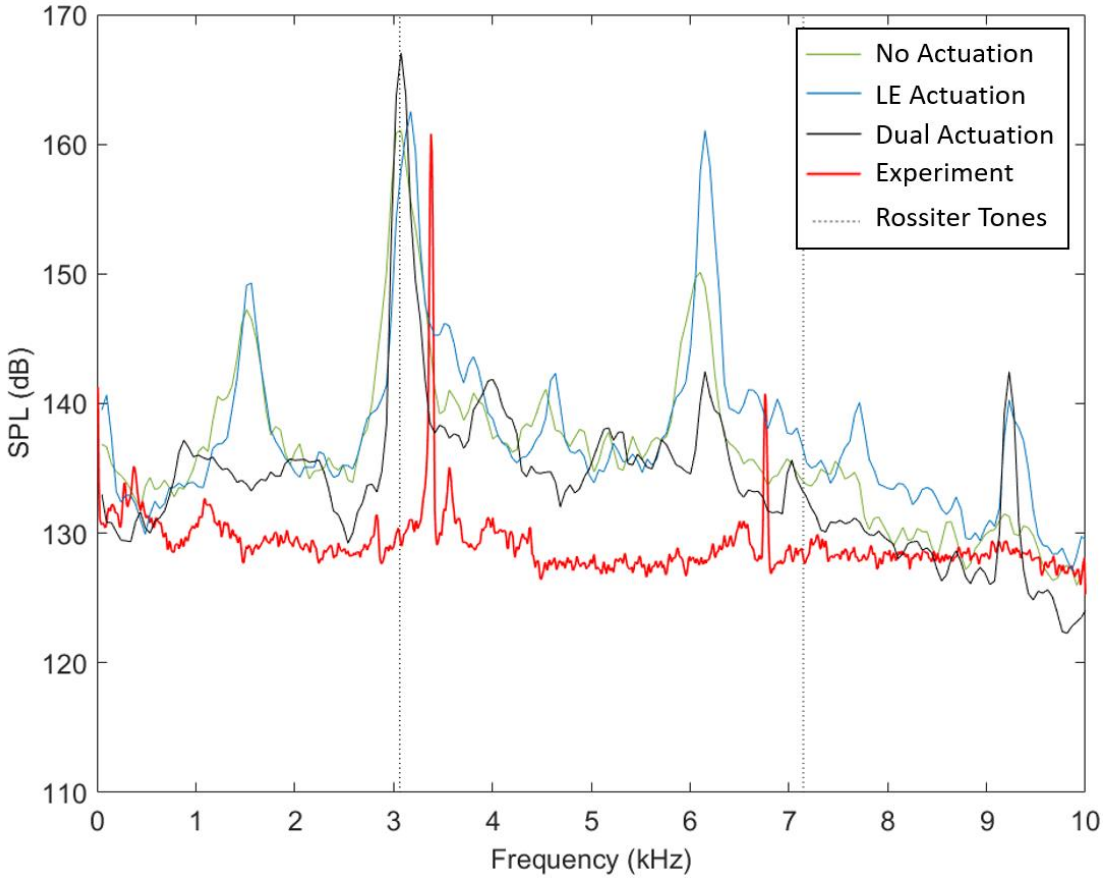

Figure 61. Comparison of acoustic spectra for digitally-sampled pressures on the cavity floor for CFD solutions with and without actuator simulations.

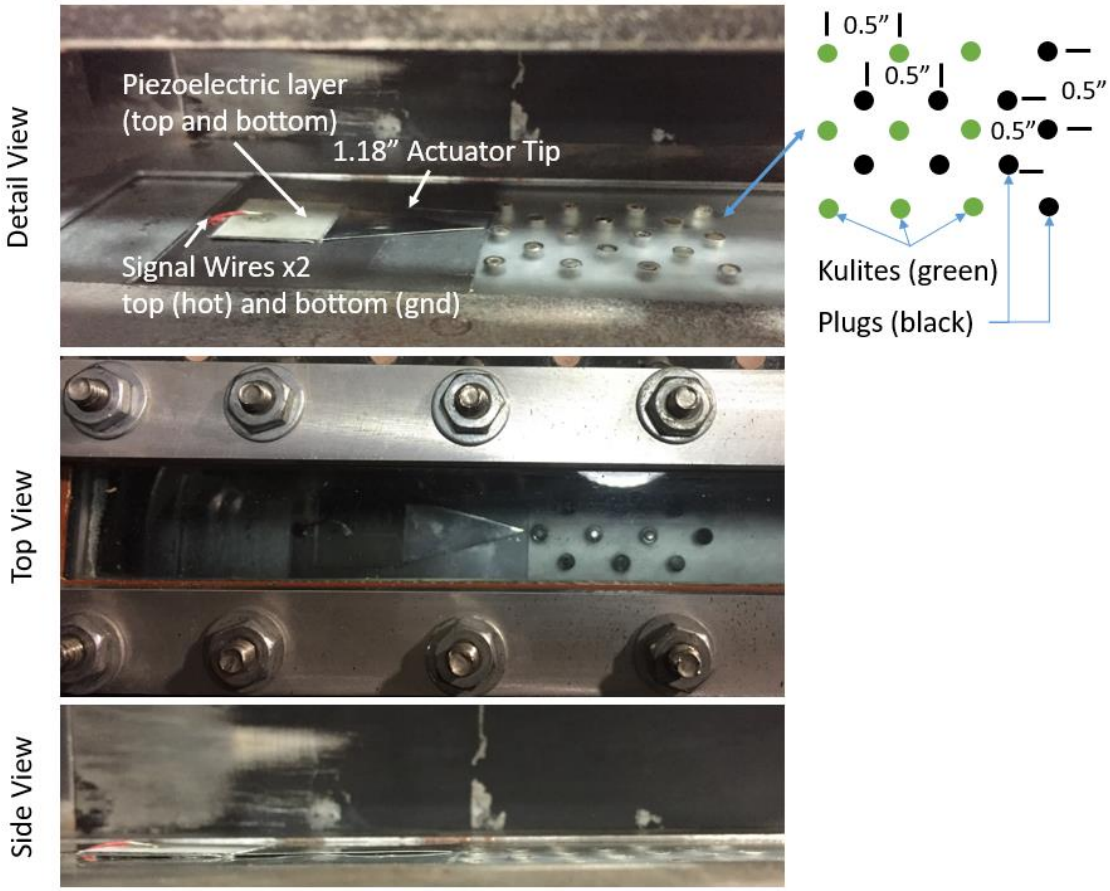

Figure 62. Actuator installed in test section for flat-floor test.

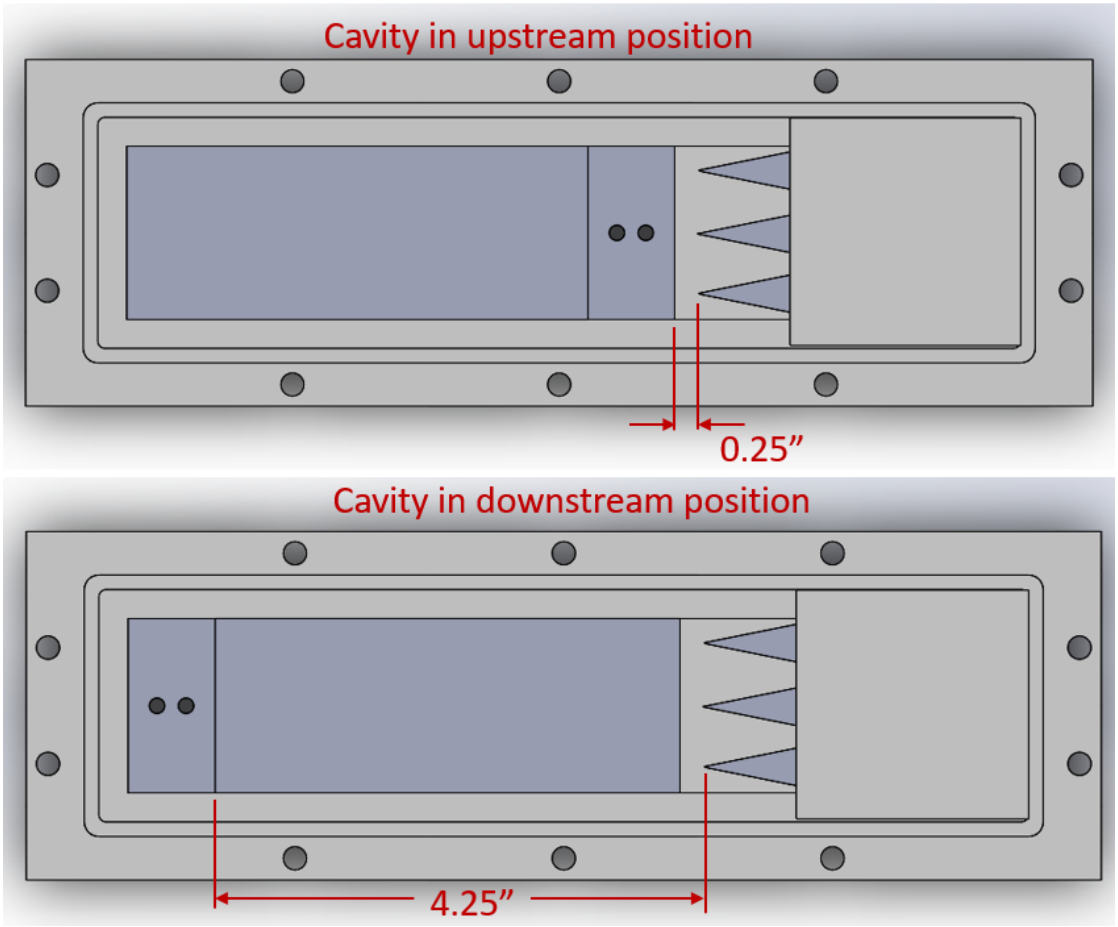

Figure 63. Test section cavity insert in the upstream and downstream positions.

Upper – cavity placed in the upstream position. Lower – cavity placed in the downstream position. Flow is from right to left.

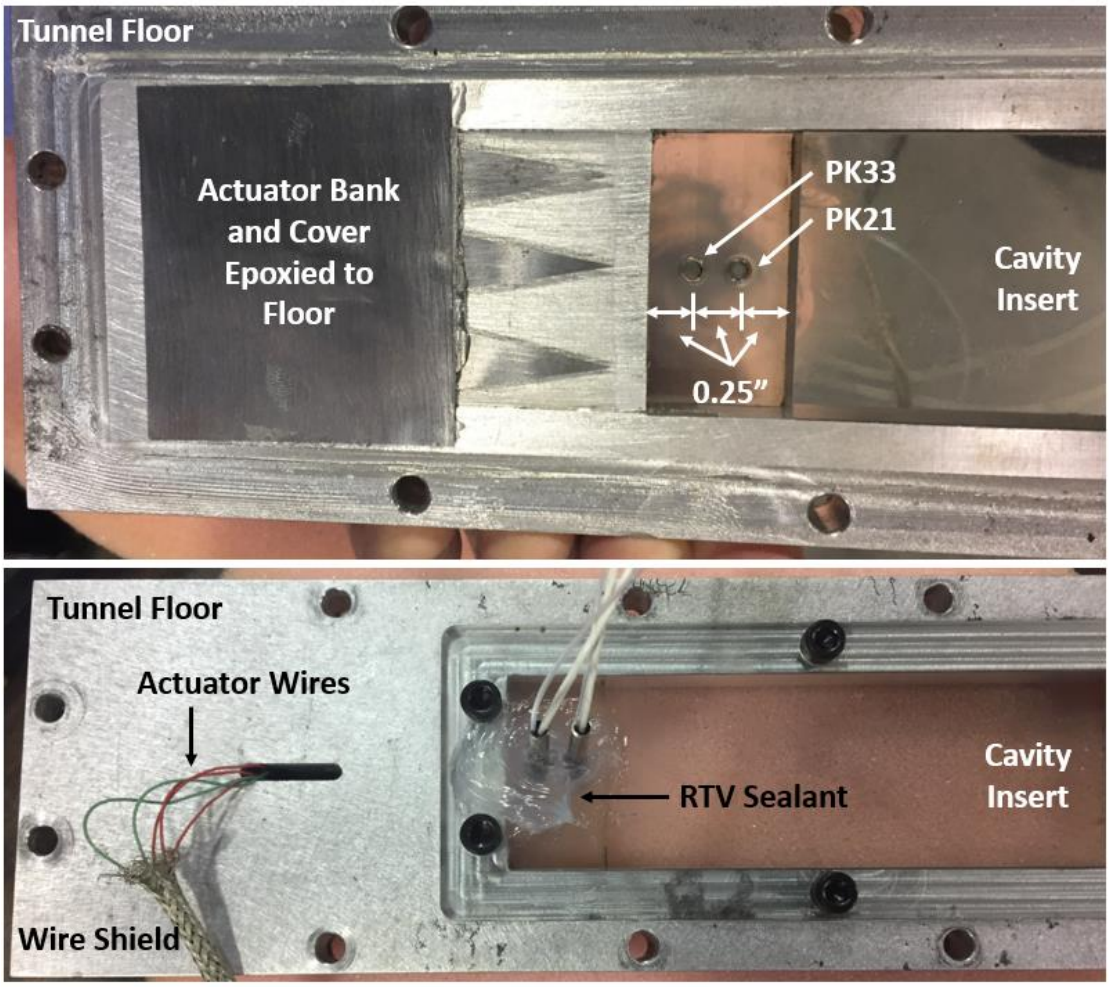

Figure 64. Picture of tunnel floor section with cavity insert and installed actuator bank.

Upper – Top view of the cavity experiment. Flow is from left to right. Lower – bottom view of the cavity experiment.

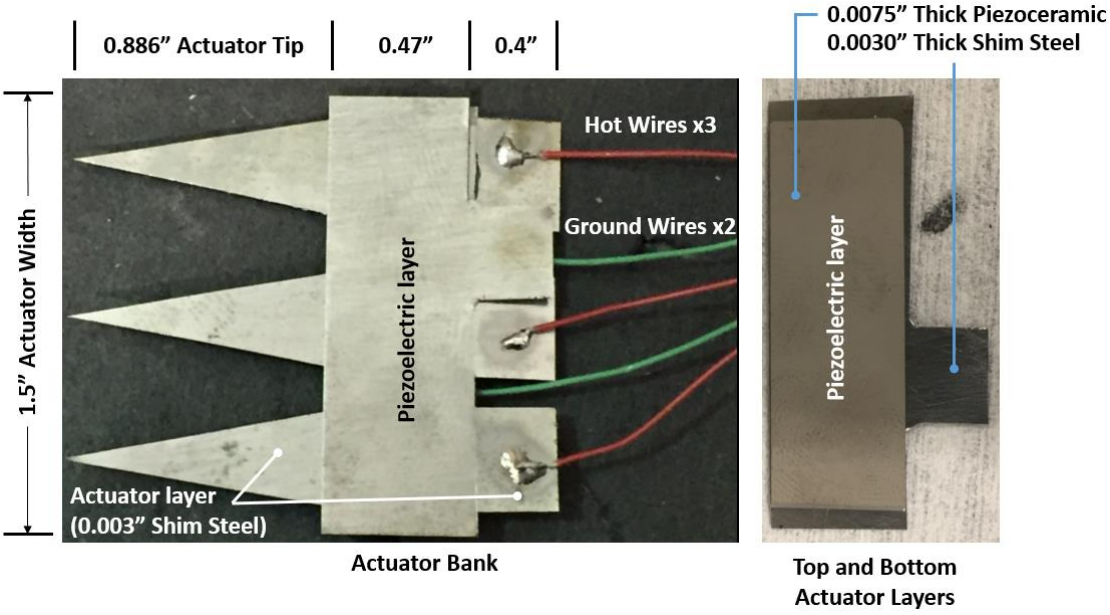

Figure 65. Final actuator bank design.

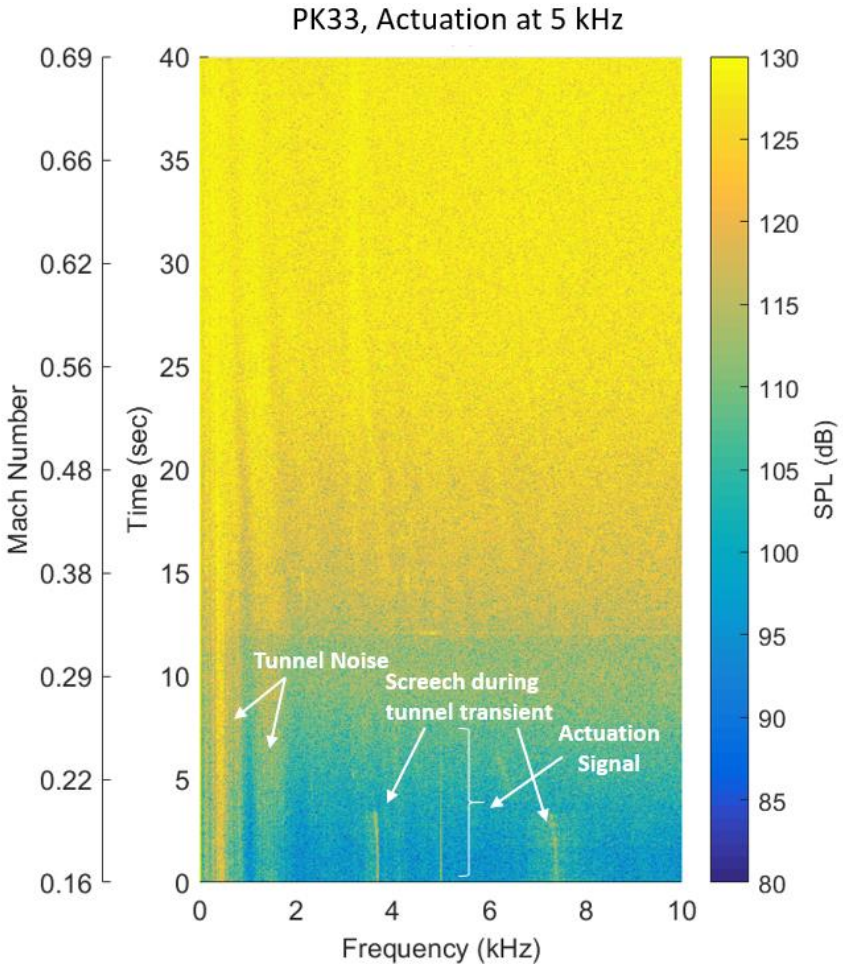

Figure 66. Tunnel Mach number sweep with actuator operation at 5 kHz.

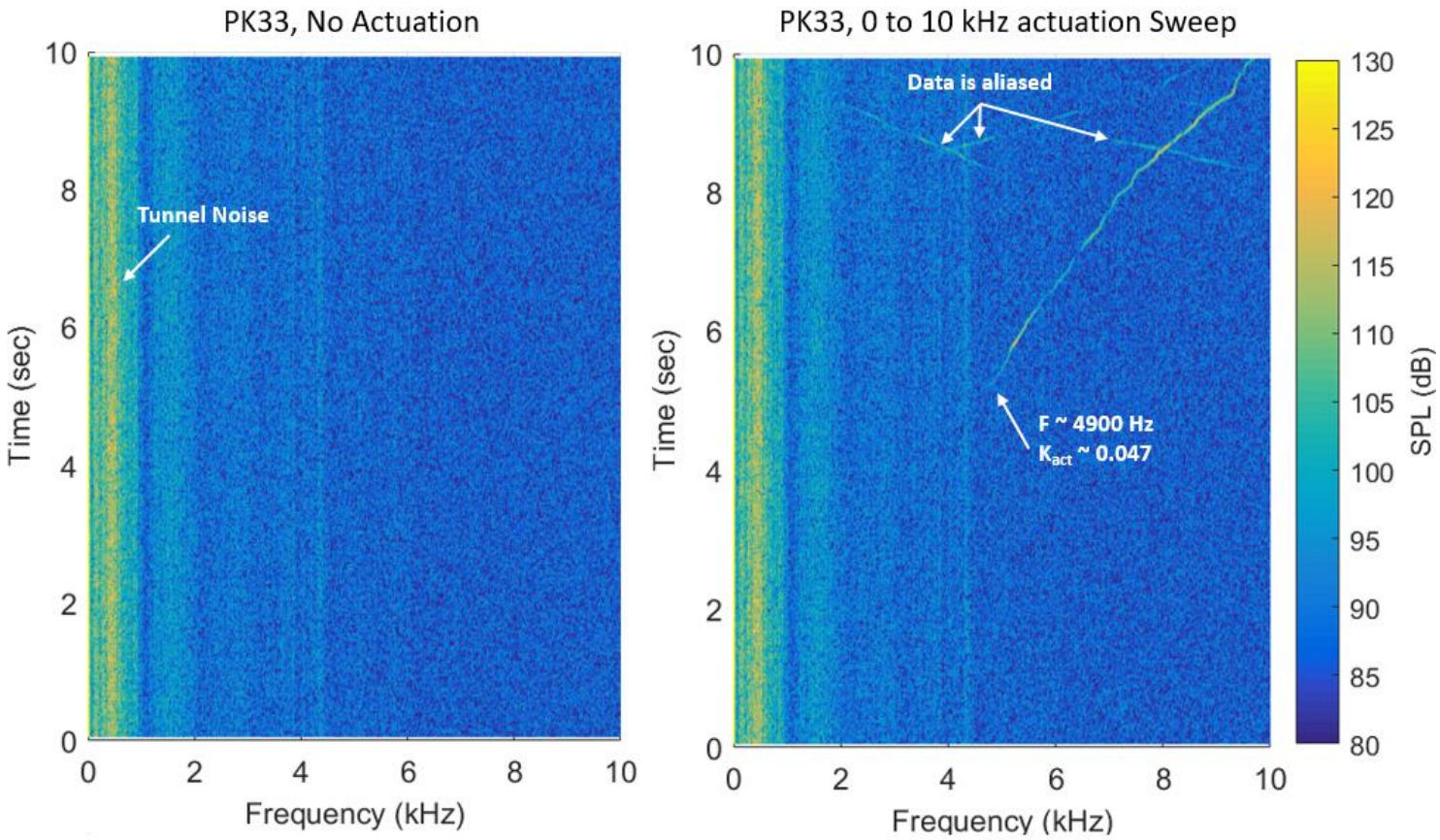

a) no actuation b) with actuation sweep

Figure 67. Spectrograms of measured high-response pressure signal at Mach 0.11.

PK33 shown (~ 0.5 inches downstream of actuator tip) at Mach 0.11. Sampling rate was 20 kHz. Left – Measured pressure at PK33 without actuation. Right – Measured pressure at PK33 with actuation frequency sweep from 0 to 10 kHz.

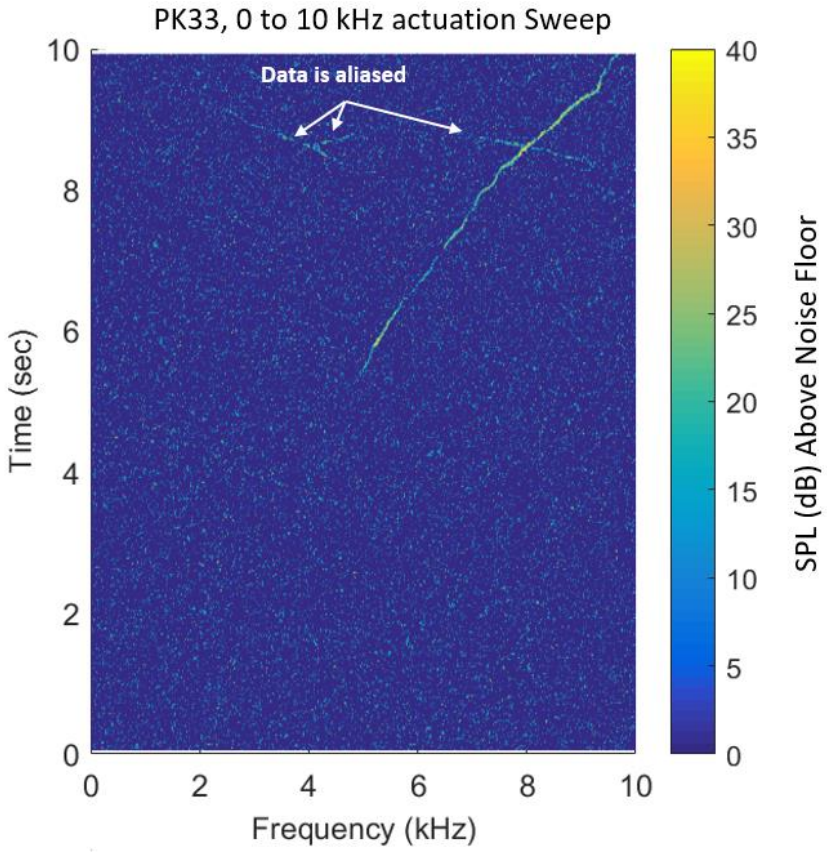

Figure 68. Spectrogram of measured high-response pressure signal normalized by tunnel noise at Mach 0.11.

PK33 shown (~ 0.5 inches downstream of actuator tip) at Mach 0.11 with actuator frequency sweep from 0 to 10 kHz. Sampling rate was 20 kHz. Data has been normalized by tunnel background noise. Sound Pressure Levels in decibels above tunnel background noise without actuation.

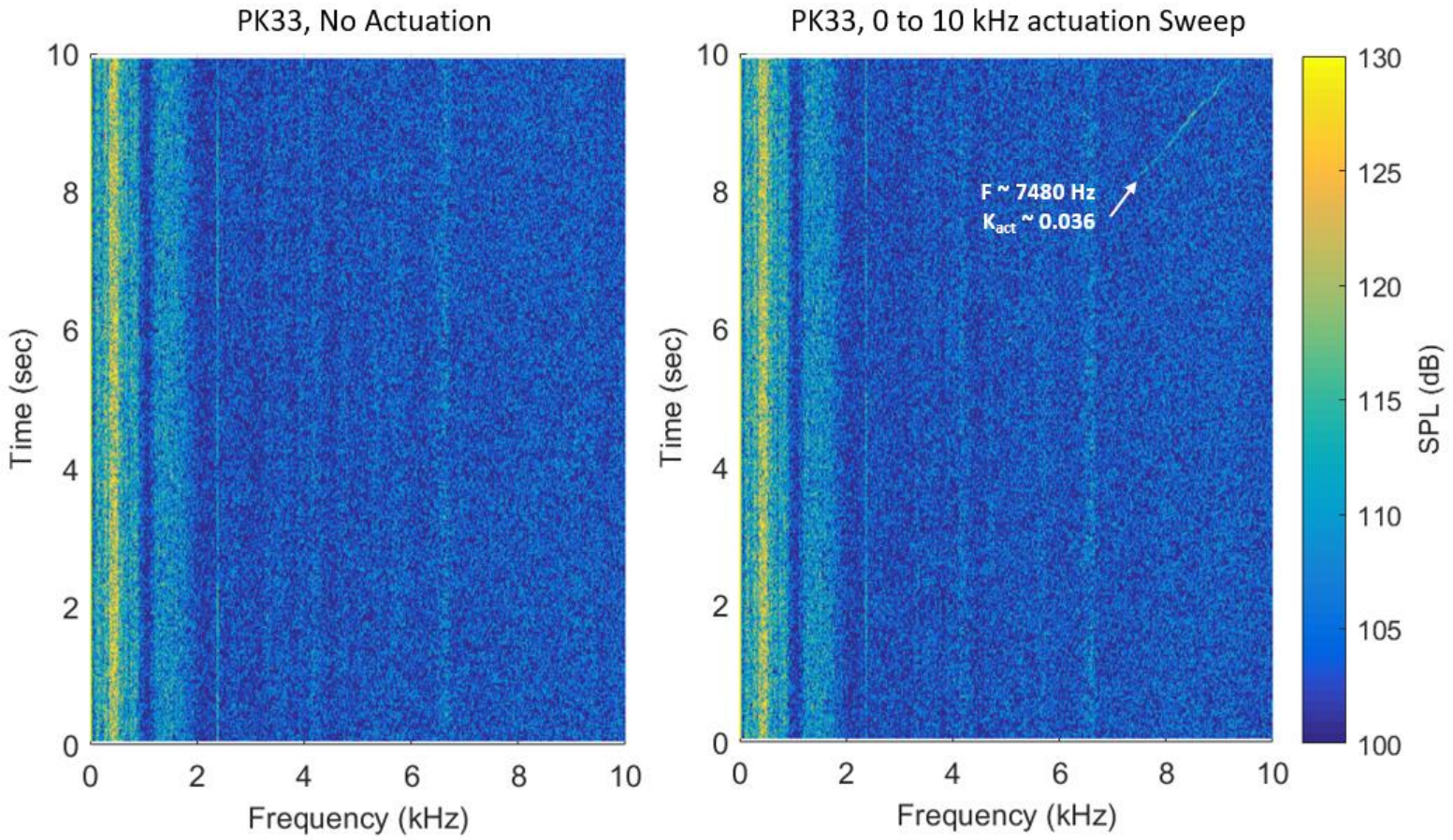

a) no actuation b) with actuation sweep

Figure 69. Spectrograms of measured high-response pressure signal at Mach 0.2.

PK33 shown (~ 0.5 inches downstream of actuator tip) at Mach 0.2. Sampling rate was 20 kHz. Left – Measured pressure at PK33 without actuation. Right – Measured pressure at PK33 with actuation frequency sweep from 0 to 10 kHz.

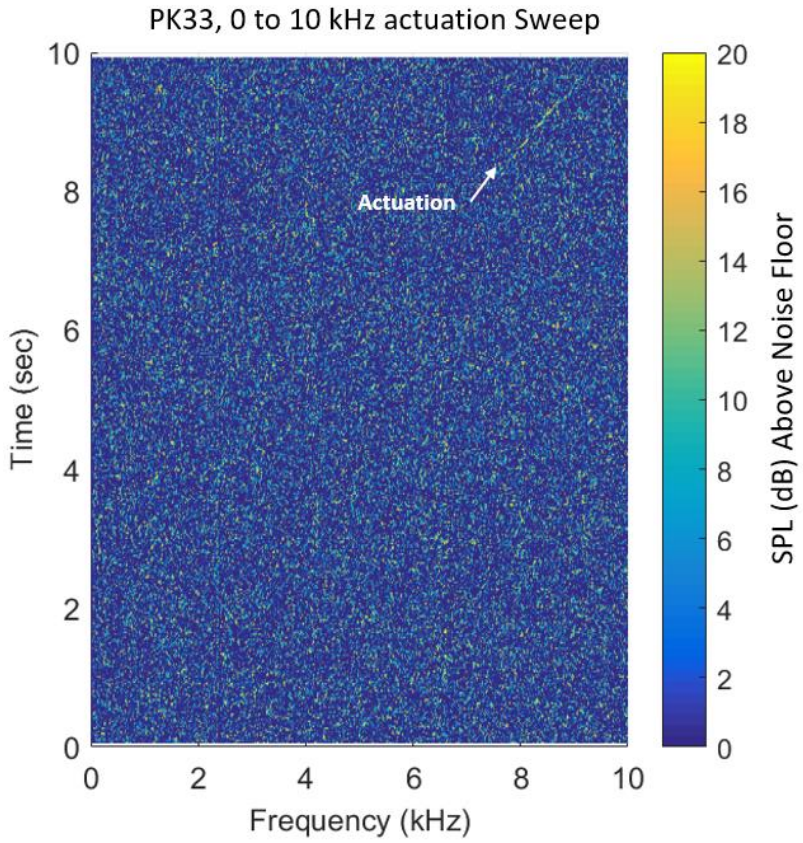

Figure 70. Spectrogram of measured high-response pressure signal normalized by tunnel noise at Mach 0.2.

PK33 shown (~ 0.5 inches downstream of actuator tip) at Mach 0.2 with actuator frequency sweep from 0 to 10 kHz. Sampling rate was 20 kHz. Data has been normalized by tunnel background noise. Sound Pressure Levels in decibels above tunnel background noise without actuation.

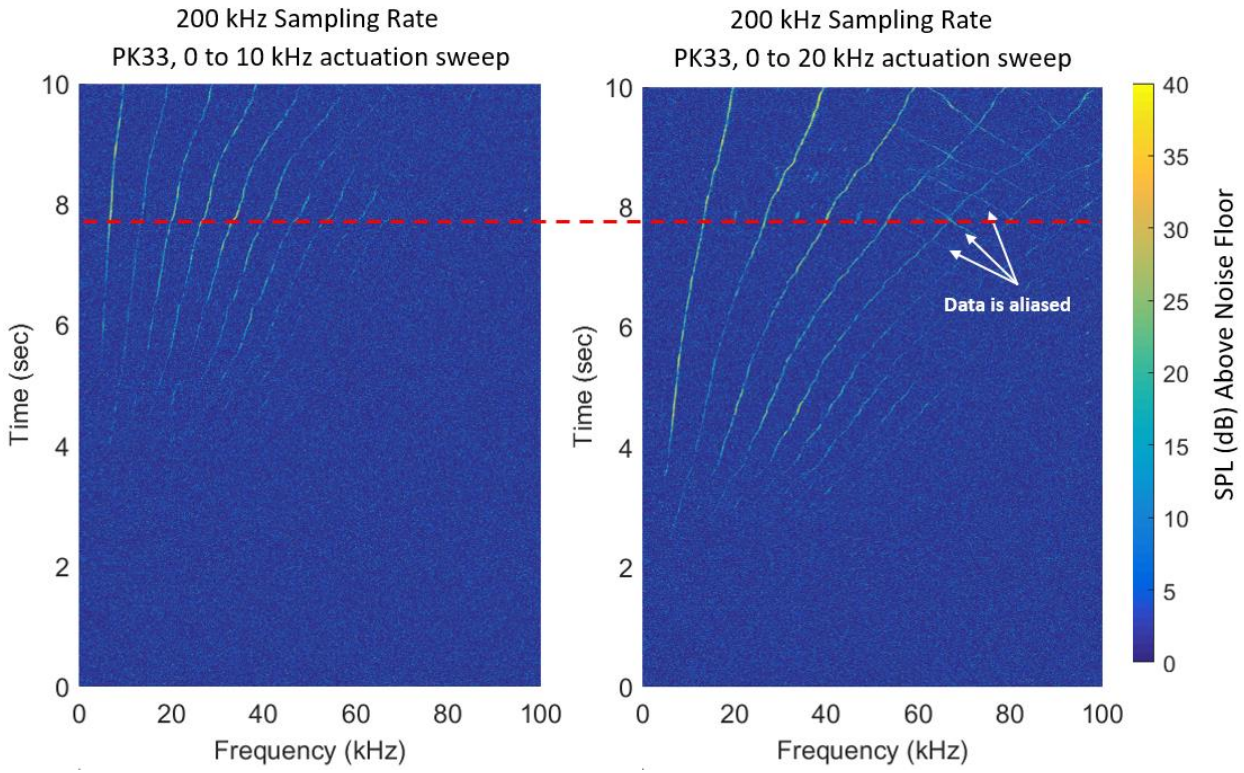

a) Actuation sweep from 0 to 10 kHz b) Actuation sweep from 0 to 20 kHz

Figure 71. Spectrograms of measured high-response pressure signal using high-sample-rate data.

PK33 shown (~ 0.5 inches downstream of actuator tip) at Mach 0.12. Left is actuator frequency sweep from 0 to 10 kHz. Right is actuator frequency sweep from 0 to 20 kHz. Sampling rate was 200 kHz. Data has been normalized by tunnel background noise. Sound Pressure Levels in decibels above tunnel background noise without actuation. Red dashed line is approximately 7.8 seconds into the sweep from which subsequent figures were made.

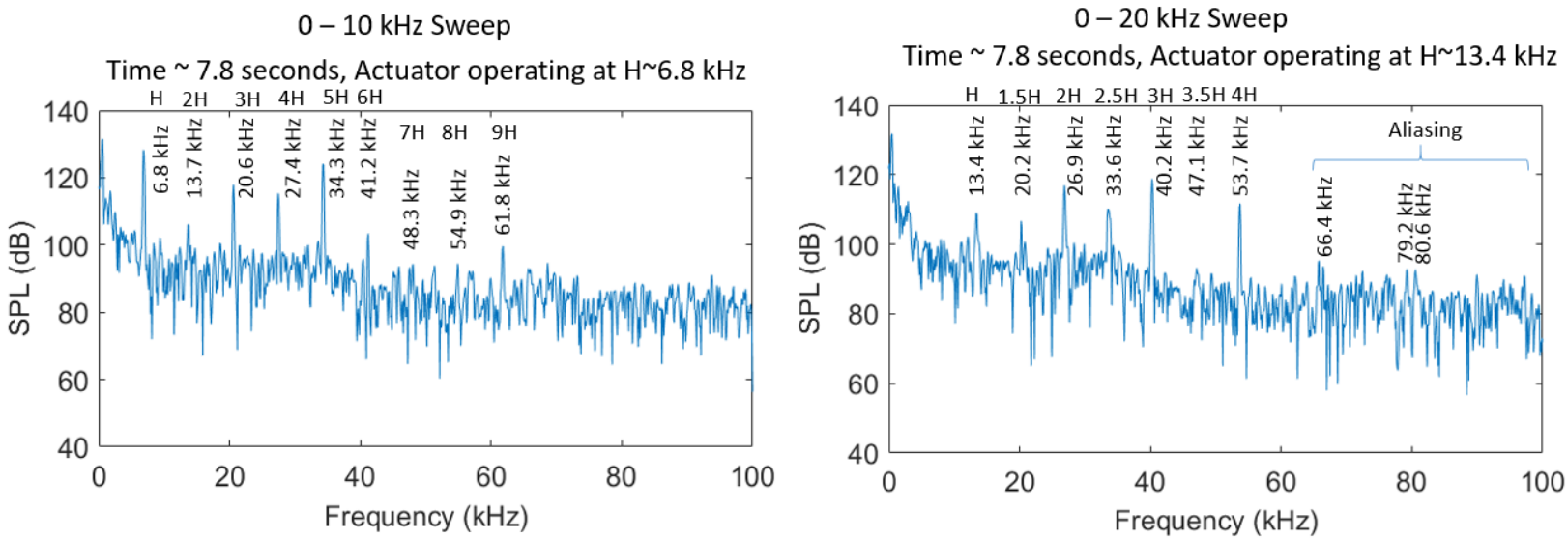

a) Actuation sweep from 0 to 10 kHz

b) Actuation sweep from 0 to 20 kHz

Figure 72. Power spectrum at 7.8 seconds during the 10-second actuation runs at Mach 0.12.

Data sampled at 200 kHz. Left is actuator frequency sweep from 0 to 10 kHz. Right is actuator frequency sweep from 0 to 20 kHz. Actuator driving frequency is denoted by H.

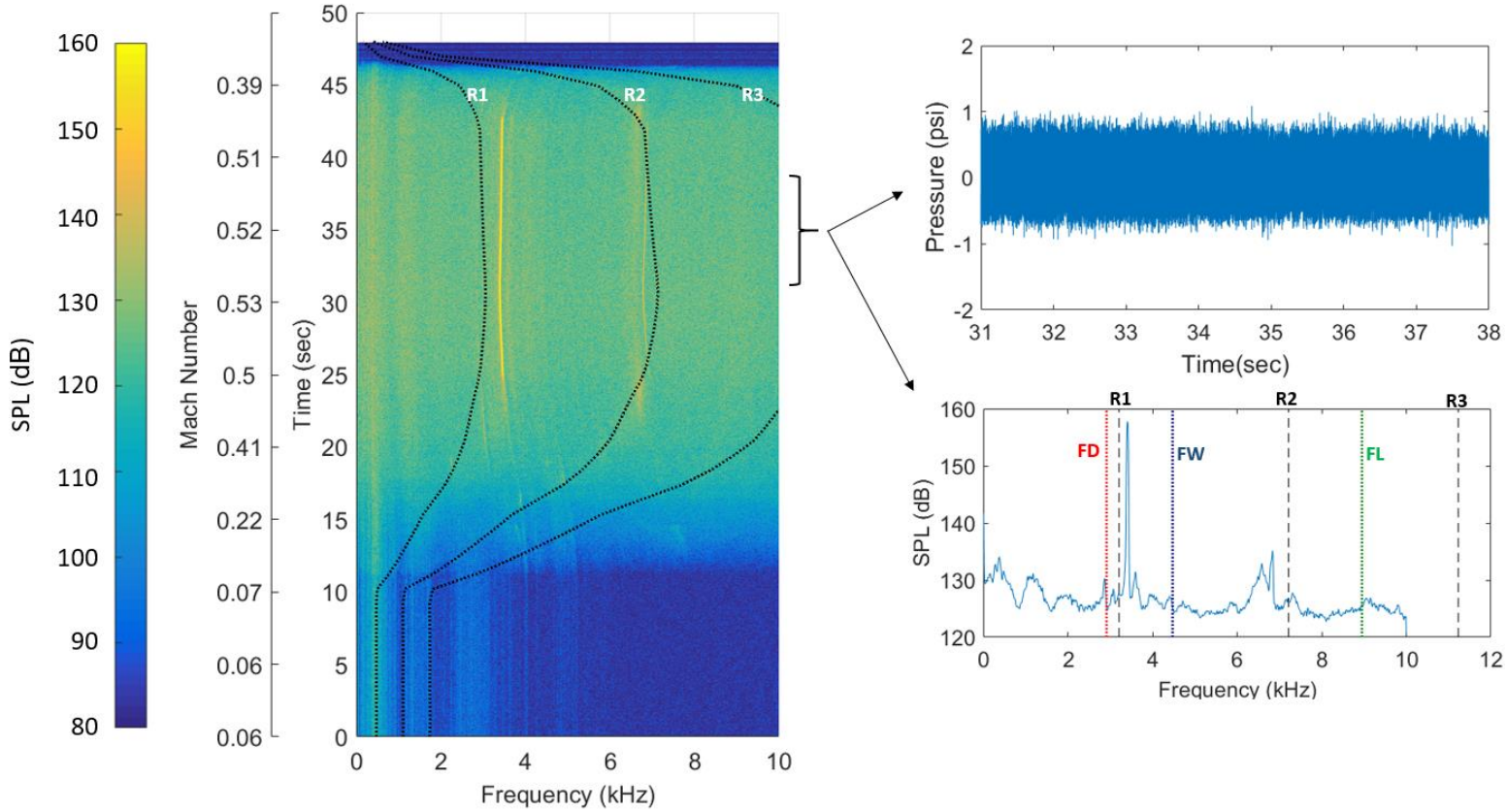

Figure 73. Results from cavity test without flow actuation.

Tunnel Mach number sweep from 0 to 0.53 and back to 0. Left – waterfall plot of the sound pressure level on the floor of the cavity. Right – a subset of data near the Mach 0.53 condition where the top plot is the time history and the bottom plot is the frequency spectrum.

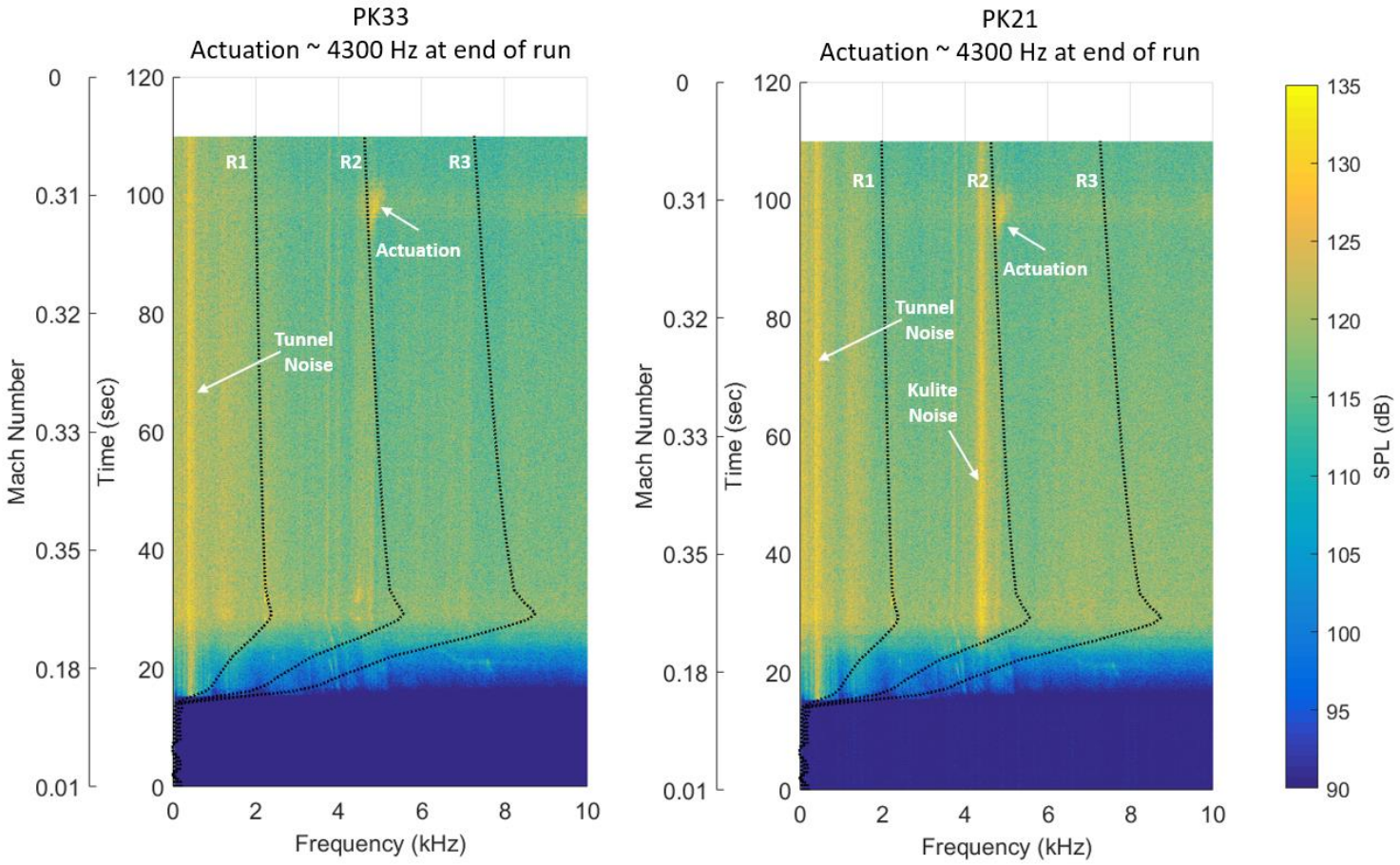

Figure 74. Results from cavity test with approximately 8-seconds of actuator coupling with the flow.

Left – results from the upstream sensor on the floor of the cavity. Right – results from the downstream sensor on the floor of the cavity.

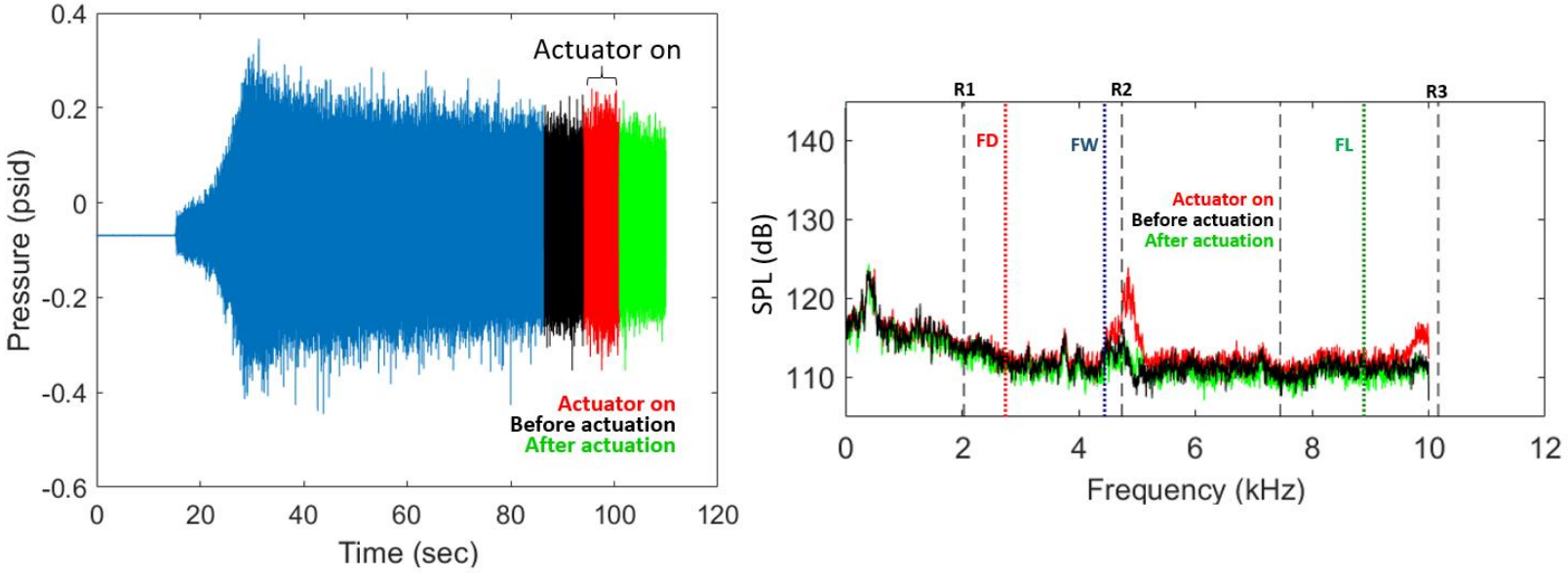

Figure 75. Details of cavity test with actuation.

Left – time history of the run highlighting where actuator operation occurred. Right – power spectrum of the highlighted timeframes showing the effect of with/without flow actuation.

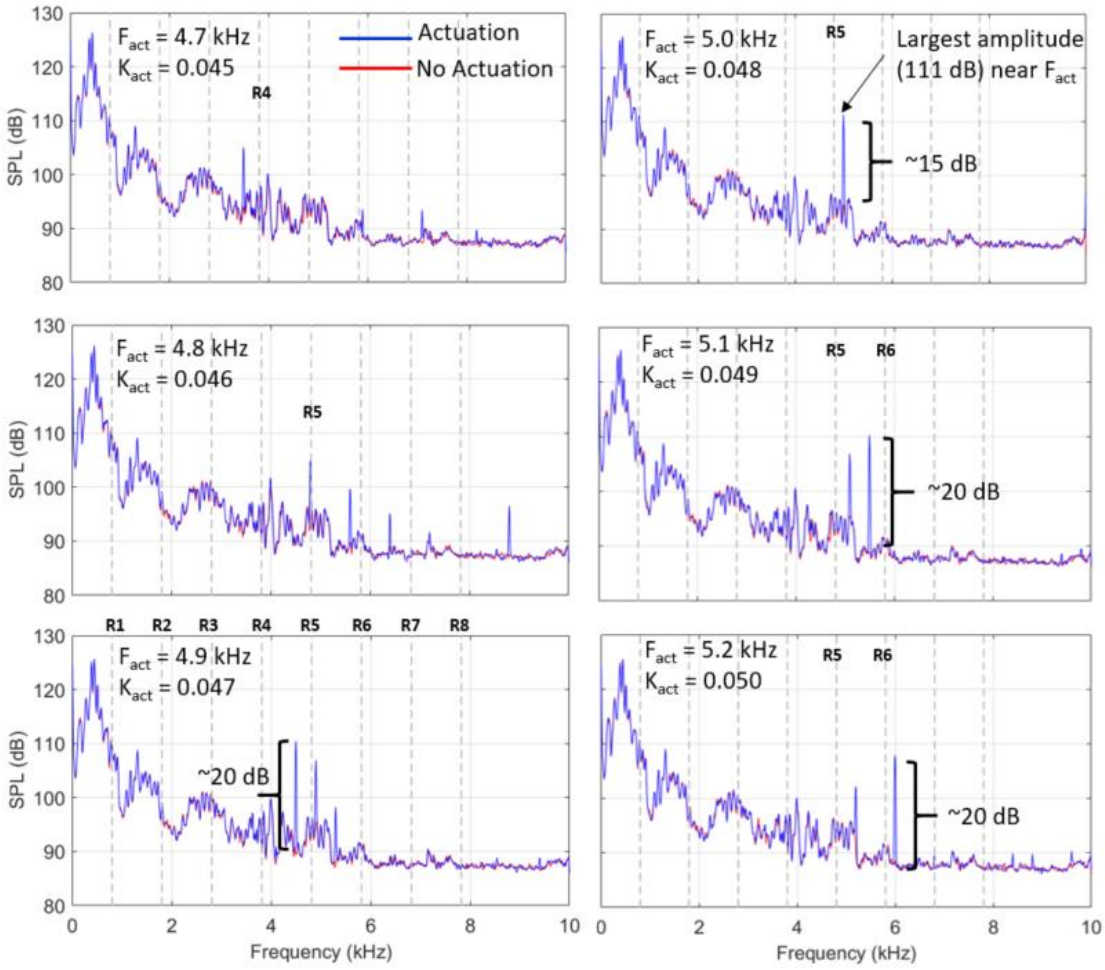

Figure 76. Cavity actuation results at Mach 0.1 test conditions and six actuator driving frequencies. Cavity in upstream position.

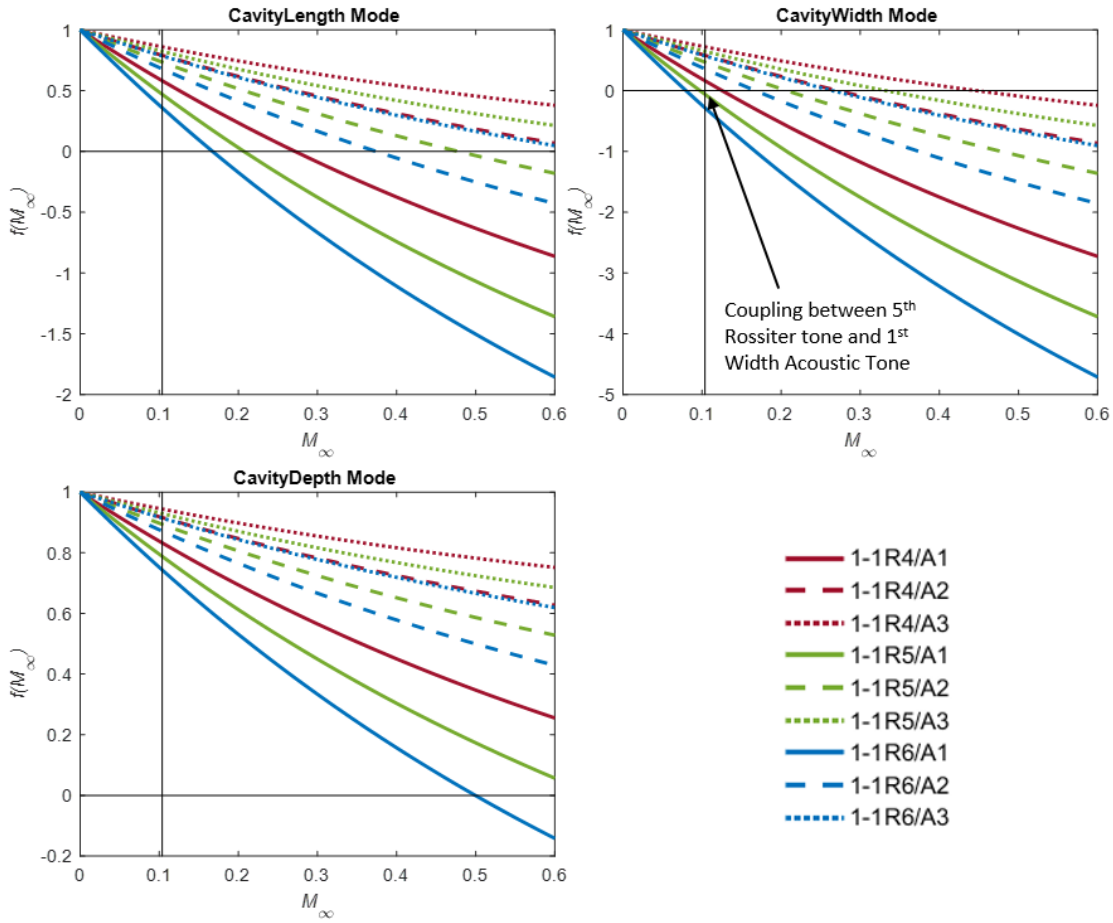

Figure 77. Coupling of cavity acoustic and cavity Rossiter tones near actuator frequency at Mach 0.1 test conditions. Cavity in upstream position.

Upper left – length-based cavity acoustic modes. Upper right – width-based cavity acoustic modes. Lower left – depth-based cavity acoustic modes.

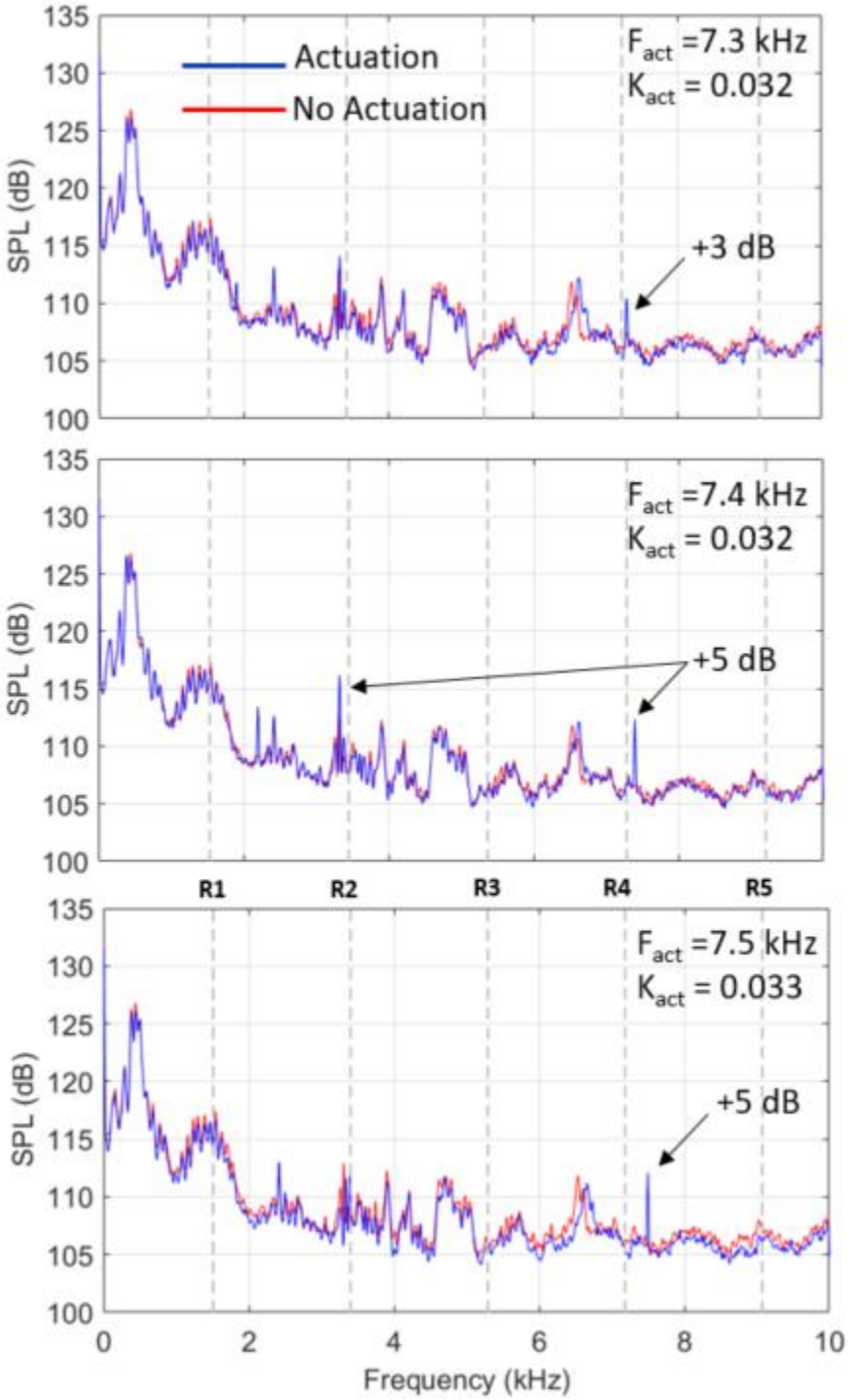

Figure 78. Cavity actuation results at Mach 0.2 test conditions and three actuator driving frequencies. Cavity in upstream position.

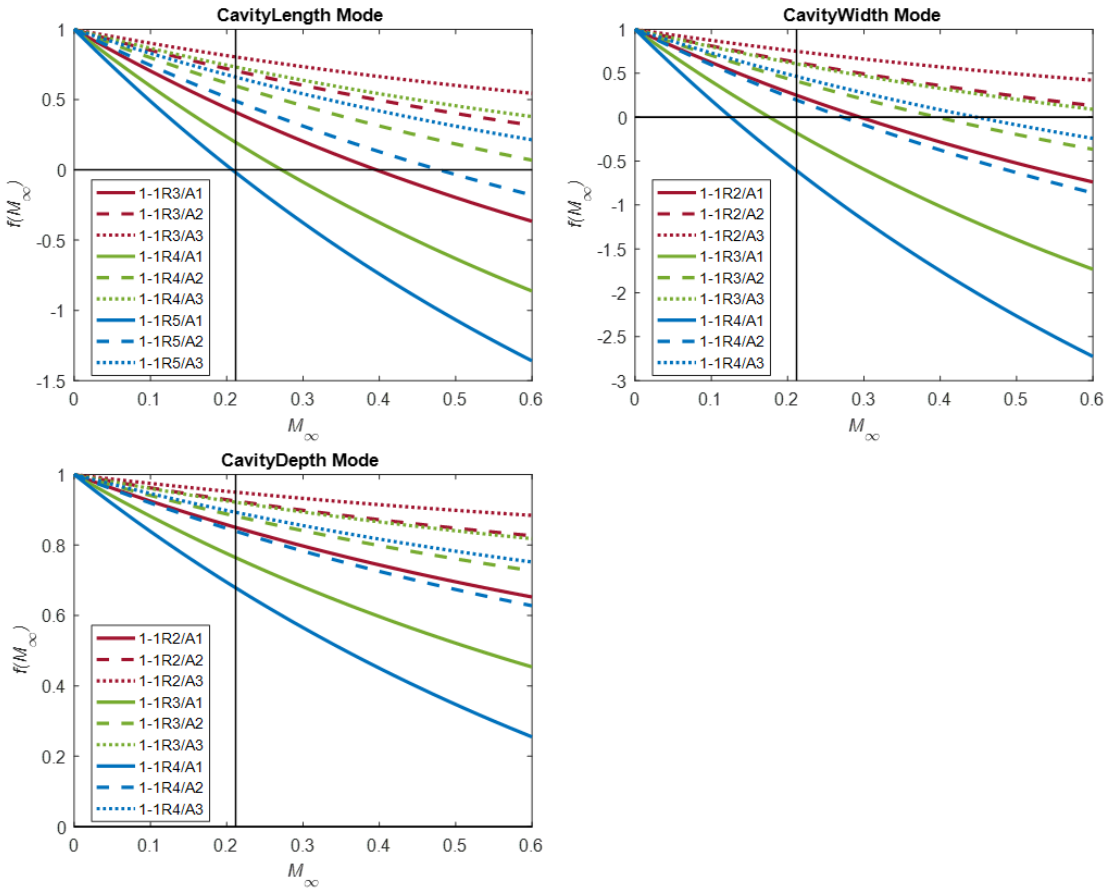

Figure 79. Coupling of cavity acoustic and cavity Rossiter tones near actuator frequency at Mach 0.2 test conditions.

Upper left – length-based cavity acoustic modes. Upper right – width-based cavity acoustic modes. Lower left – depth-based cavity acoustic modes. Cavity in upstream position for all plots.

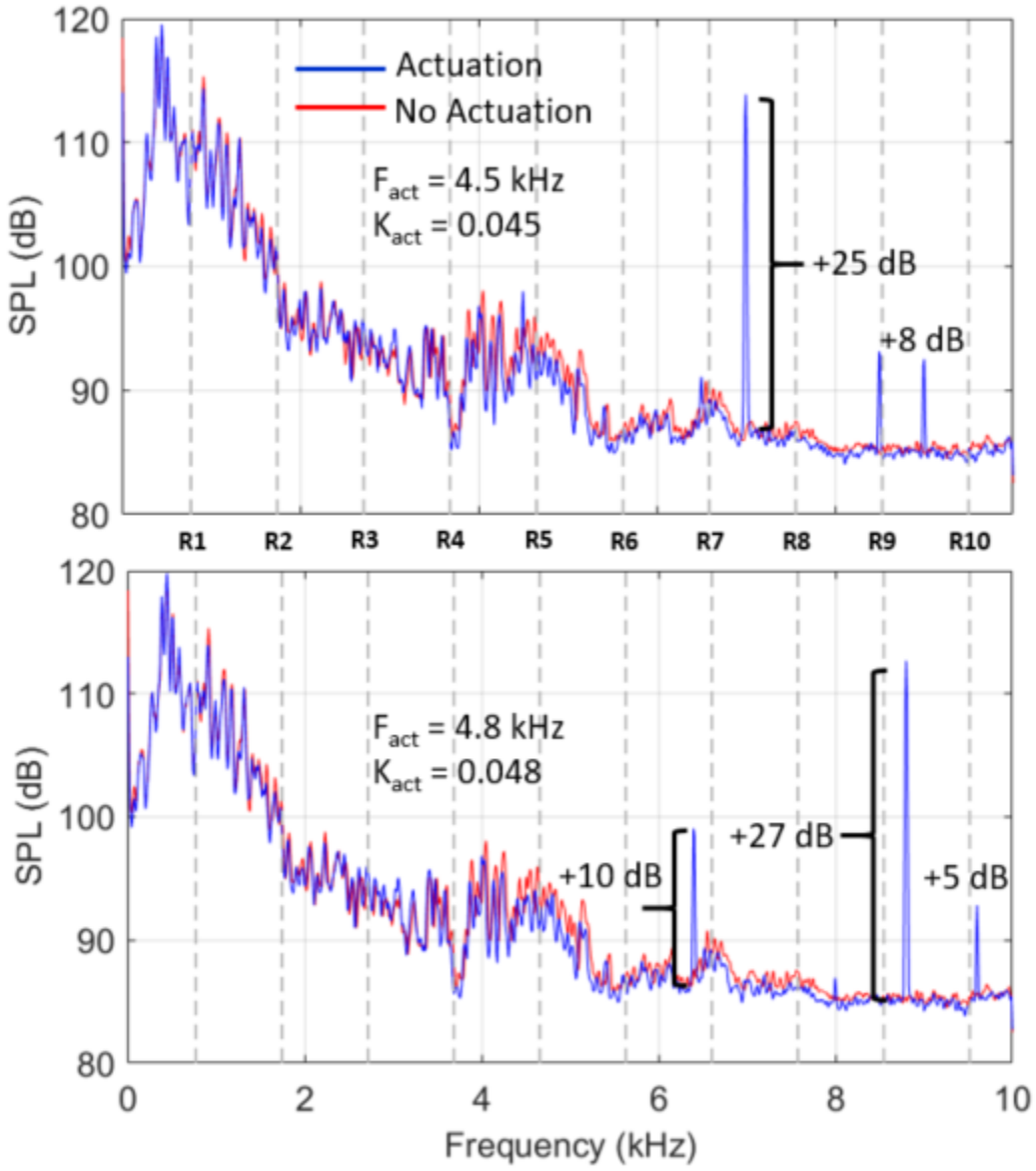

Figure 80. Cavity actuation results at Mach 0.1 test conditions and two actuator driving frequencies. Cavity in downstream position.

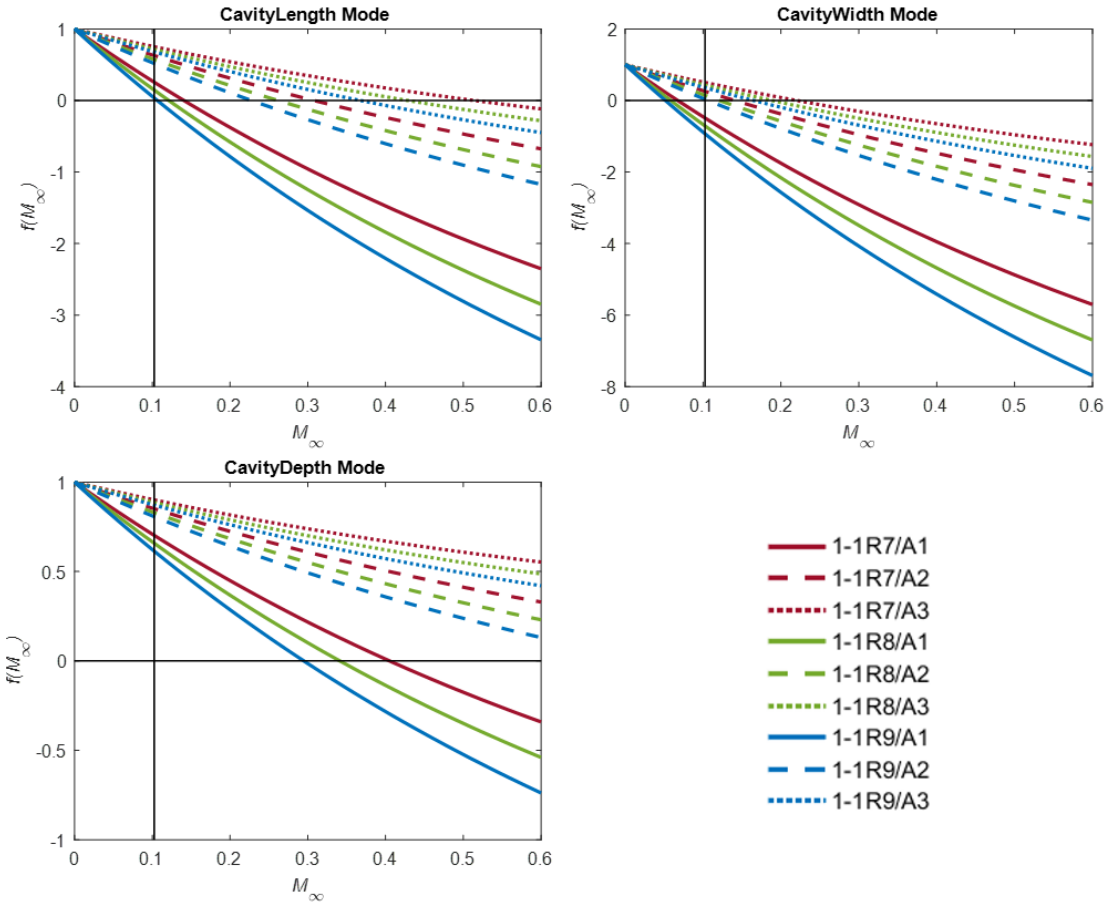

Figure 81. Coupling of cavity acoustic and cavity Rossiter tones near actuator frequency at Mach 0.1 test conditions.

Upper left – length-based cavity acoustic modes. Upper right – width-based cavity acoustic modes. Lower left – depth-based cavity acoustic modes. Cavity in downstream position.

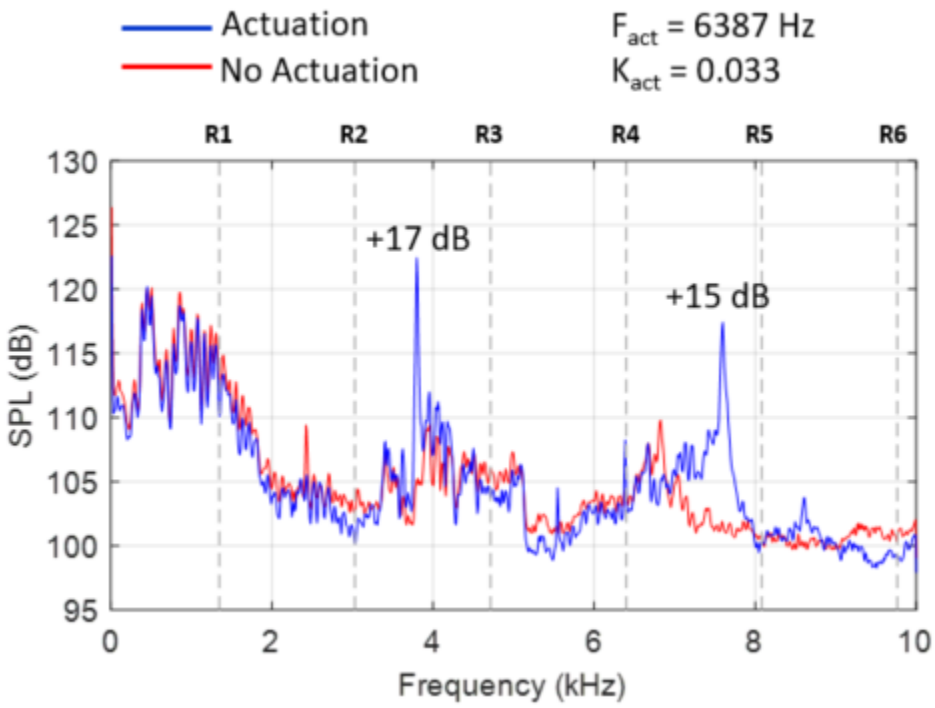

Figure 82. Cavity actuation results at Mach 0.2 test conditions and one actuator driving frequency. Cavity in downstream position.

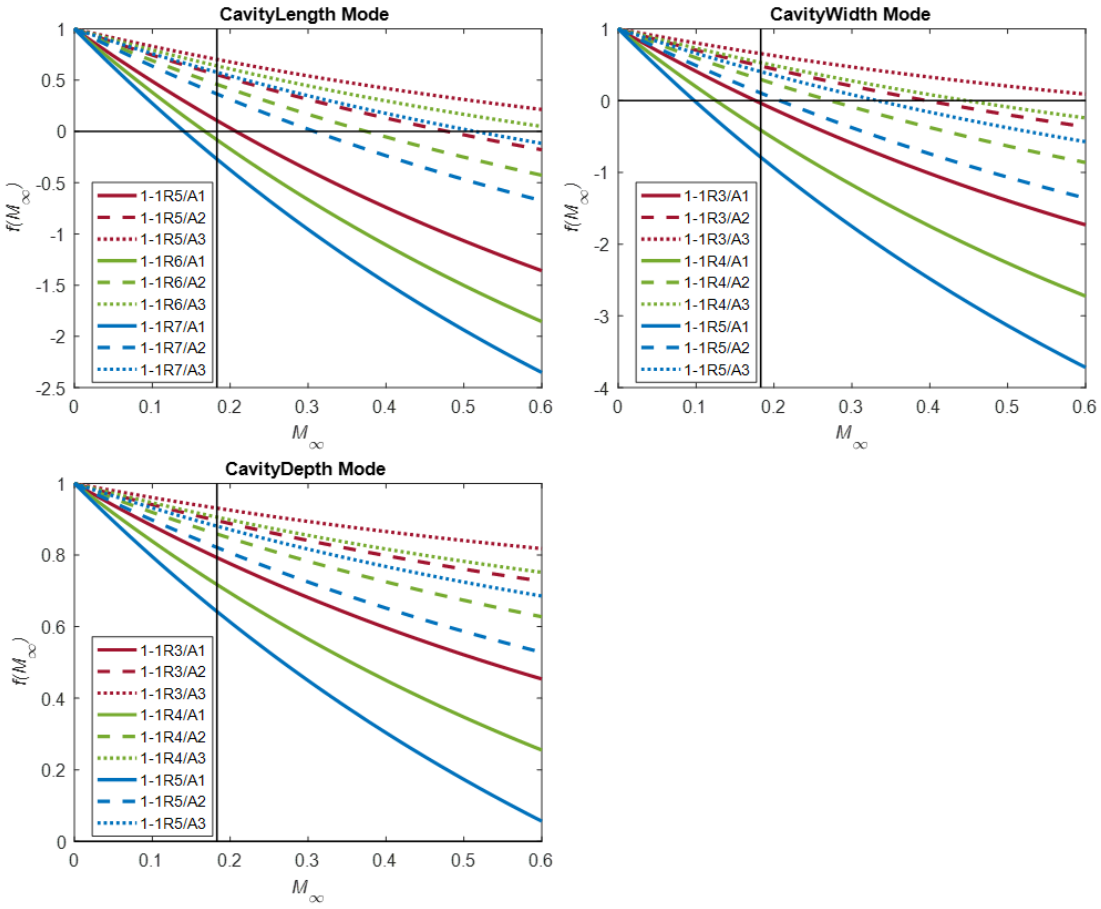

Figure 83. Coupling of cavity acoustic and cavity Rossiter tones near actuator frequency at Mach 0.2 test conditions.

Upper left – length-based cavity acoustic modes. Upper right – width-based cavity acoustic modes. Lower left – depth-based cavity acoustic modes. Cavity in downstream position.

Appendix 2: Data Processing Code

Batch Processing Code

A MATLAB code was written to convert test data from the data-acquisition file format (TDMS) into MATLAB files (MAT). The MATLAB-based TDMS file readers provided by National Instruments were used to interface the MATLAB code to the TDMS files. The batch-conversion process was completed using the MATLAB code shown below.

```
% Script to batch-process TDMS data into mat-files for use with other
% processing scripts

% Select file(s) to process
[Files,PathName,FilterIndex] = uigetfile('*.tdms', …
                                         'Choose Raw Data', …
                                         'MultiSelect','on');
if isnumeric(Files)
   disp('User Cancelled')
   return
elseif ischar(Files)
   Files = {Files};
end

% Set up options for reading TDMS files
cons.DDC_FILE_NAME                    =  'name';
cons.DDC_FILE_DESCRIPTION             =  'description';
cons.DDC_FILE_TITLE                   =  'title';
cons.DDC_FILE_AUTHOR                  =  'author';
cons.DDC_FILE_DATETIME                =  'datetime';
cons.DDC_CHANNELGROUP_NAME            =  'name';
cons.DDC_CHANNELGROUP_DESCRIPTION     =  'description';
cons.DDC_CHANNEL_NAME                 =  'name';

% Initialize some empty structures for writing data to
DataHR = struct('Fs',0,'NSamples',0,'Time',0,'Names',[],'Values',0);
DataSS = struct('Fs',0,'NSamples',0,'Time',0,'Names',[],'Values',0);
for i=1:length(Files)
   filename = Files{i};
   % Read the file
   dataStruct = readTDMS(fullfile(PathName,filename),cons,false);

   % Parse sample rates.
   Fs_dyn = double(dataStruct.Data.DynamicPressureSensors.Fs);
   Fs_ss  = double(dataStruct.Data.StaticPressureSensors.Fs);

   % Create the time vectors
   Nsamples_dyn = size(dataStruct.Data.DynamicPressureSensors.ChanVals, 1);
```

```
tmax_dyn = Nsamples_dyn / Fs_dyn;
t_dyn = linspace(0,tmax_dyn,Nsamples_dyn);
Nsamples_ss = size(dataStruct.Data.StaticPressureSensors.ChanVals, 1);
tmax_ss = Nsamples_ss/Fs_ss;
t_ss = linspace(0,tmax_ss,Nsamples_ss);

% Remove zeros from steady-state pressures
try
   zeroNames = dataStruct.Data.Zeros.Names;
   zeroVals  = dataStruct.Data.Zeros.Values;
   zeroValsSS = zeroVals{strcmp('Static',zeroNames)};
   for j = 1:length(zeroValsSS)
      dataStruct.Data.StaticPressureSensors.ChanVals(:,j) = …
      dataStruct.Data.StaticPressureSensors.ChanVals(:,j) - zeroValsSS(j);
   end
catch
   disp('Could not apply zeros')
end

% Calculate average steady-state values
%   PT   - pitot pressure at test section exit, psid
%   PS   - static pressure near test section exit, psid
%   Pamb - local ambient pressure, psid
%   PC   - tunnel chamber pressure, psid
%   TTC  - thermocouple temperature in stilling chamber, deg F
indPT   = strcmp('Pitot Tube', …
            strtrim(dataStruct.Data.StaticPressureSensors.ChanNames));
indPS   = strcmp('Test Section',  …
            strtrim(dataStruct.Data.StaticPressureSensors.ChanNames));
indPamb = strcmp('Ambient Manual',  …
             strtrim(dataStruct.Data.StaticPressureSensors.ChanNames));
indPC   = strcmp('Stilling Chamber', …
            strtrim(dataStruct.Data.StaticPressureSensors.ChanNames));
indTTC  = strcmp('Stilling Chamber', …
             strtrim(dataStruct.Data.TemperatureSensors.ChanNames));
PT   = dataStruct.Data.StaticPressureSensors.ChanVals(:,indPT);
PS   = dataStruct.Data.StaticPressureSensors.ChanVals(:,indPS);
Pamb = dataStruct.Data.StaticPressureSensors.ChanVals(:,indPamb);
PC   = dataStruct.Data.StaticPressureSensors.ChanVals(:,indPC);
TTC  = dataStruct.Data.TemperatureSensors.ChanVals(:,indTTC);

% Steady-state pressures are differential from ambient pressure
PT   = PT + Pamb;
PS   = PS + Pamb;
PC   = PC + Pamb;
```

```
    % Calculate test section variables
    MT = sqrt( ((PT./PS).^(0.4/1.4)-1) * 2/0.4 );
    MC = sqrt( ((PC./PS).^(0.4/1.4)-1) * 2/0.4 );
    TSC = (TTC+459.67) ./ (1 + 0.4/2*MC.^2) - 459.67;
    TST = (TTC+459.67) ./ (1 + 0.4/2*MT.^2) - 459.67;

fprintf(1,'\n############################################################\n')
    fprintf(1,'%s \n',filename)
    fprintf(1,'MT = %.2f\n',mean(MT));
    fprintf(1,'MC = %.2f\n',mean(MC));
    fprintf(1,'TSC = %.1f F\n',mean(TSC));
    fprintf(1,'TST = %.1f F\n',mean(TST));
    fprintf(1,'PAMB = %.1f psia\n',mean(Pamb));
    fprintf(1,'PT = %.1f psia\n',mean(PT));
    fprintf(1,'PS = %.1f psia\n',mean(PS));
    fprintf(1,'PC = %.1f psia\n',mean(PC));

fprintf(1,'############################################################\n')

    % Get channel names
    channelNames = strrep(dataStruct.Data. …
                          DynamicPressureSensors.ChanNames, ...
                          'Dynamic Sensor ','PK');

    % Populate Structures for saving to mat files
    DataHR.Fs          = Fs_dyn;
    DataHR.NSamples = Nsamples_dyn;
    DataHR.Time        = t_dyn(:);
    DataHR.Names       = channelNames;
    DataHR.Values      = dataStruct.Data.DynamicPressureSensors.ChanVals;
    DataSS.Fs          = Fs_ss;
    DataSS.NSamples  = Nsamples_ss;
    DataSS.Time        = t_ss(:);
    DataSS.Names       = {'PT','PS','PC','PAMB','TTC','TST','TSC','MT','MC'};
    DataSS.Values      = horzcat(PT(:),PS(:),PC(:),Pamb(:), …
                                 TTC(:),TST(:),TSC(:),MT(:),MC(:));

    % Save processed data to mat file
    place = fullfile(pwd,'matfiles_batch',strrep(filename,'.tdms','.mat'));
    save(place,'DataSS','DataHR')
end
```

Plotting Code for Generating Carpet Plots

A MATLAB code was used to generate the carpet plots, for example, as shown in Figure 67. The code did not require any peculiar software and made use of standard MATLAB packages such as “spectrogram”. Nevertheless, the carpet-plotting code is provided for reference.

```
% Plot a spectrogram of frequency vs. time
clear all; clc;
% Font size for all axes and labels
fsize = 14;
% Limits for colorscale
colorlims = [80 130];
% Flag for plotting steady-state data
plotSS = 0;
% Add a supplementary y-axis
addSuppYAxis = 1;
addAxisName = 'MT';
addAxisDesc = 'Mach Number';
% Add a supplementary x-axis
addSuppXAxis = 1;
% Flag for normalizing wavelength
normWaveL = 1;
% Length of actuator for flat floor runs
% normL = 30/25.4; % mm to in
% Length of actuator for cavity runs
normL = 22.5/25.4; % mm to in
% Flag for normalizing frequency
normFreq = 1;
% Flag for overlaying dots for Rossiter tones
% Flag for determining if this is a cavity run so the program
% can use a different length of scaling
isCavity = 1;
cavL = 0.75/12; % inches to ft
gammaRoss = 0.25;
k = 0.57;
% Channels to process
doThese = {'PK33'};
% Signal processing options
N = 2048;
w = window(@blackmanharris,N,'periodic');
overlappct = 75;
noverlap = N*overlappct/100; % Number of samples to overlap
% Reference pressure for SPL calculation
P0 = 2e-5 * 0.000145038; % Pa to psi
% END OF INPUTS ----------------------------------------------------------
```

```
% Prompt user for data file and load it
[FileName,PathName,FilterIndex] = uigetfile('*.mat');
load(fullfile(PathName,FileName))

% Calculate speed of sound in the boundary layer
indTT = strcmp(DataSS.Names,'TST');
TTall = DataSS.Values(:,indTT);
TT = mean(TTall) + 459.67;
sndspd = sqrt(1.4*1716*TT); % ft / sec
indMT = strcmp(DataSS.Names,'MT');
allM = DataSS.Values(:,indMT);
MT = mean(allM);
Vinf = sndspd * MT;
Vall = sqrt(1.4*1716*(TTall+459.67)) .* allM;

for i=1:length(doThese)
   fig = figure('color','white','units','normalized','position',[0.1,0.1,0.4 0.8]);
   ind = strcmp(doThese{i},DataHR.Names);
   [s,f,t,ps] = spectrogram(DataHR.Values(:,ind), w, noverlap, N, DataHR.Fs,
'power');
   % Converts matlab decibels to sound pressure level
   dB = 10*log10(ps./P0^2);
   ax = axes('parent',fig);
   surf(f,t,dB','edgecolor','none')
   view(2)
   caxis(colorlims)
   hc = colorbar();
   title(doThese{i})
   ylabel(hc,'SPL (dB)')
   ylabel(ax,'Time (sec)')
   xlabel(ax,'Frequency (kHz)')
   % This changes x-axis tick labels from Hz to kHz. Ticks will remain in
   % Hz
   xtl = cellfun(@str2double,get(ax,'xticklabels'));
   set(ax,'xticklabels',arrayfun(@num2str,xtl/1000,'uniformoutput',false))

   if addSuppYAxis
      % Add Mach number to the vertical axis
      indSupp = strcmp(DataSS.Names,addAxisName);
      VAL = DataSS.Values(:,indSupp);
      cpos = get(ax,'position');
      set(ax,'position',[cpos(1)+0.15 cpos(2) cpos(3)-0.15 cpos(4)])
      cpos = get(ax,'position');
      axcompleft=0.2;
```

```
        ledge = cpos(1);
        redge = cpos(3)+cpos(1);
        totwid = redge-ledge;
        xpos = ledge-axcompleft*totwid;
        v_ax = axes('position',[xpos, cpos(2), cpos(3)*.015, cpos(4)]);
        set(v_ax,'yaxislocation','left');
        set(v_ax,'color',get(gcf,'color'));
        set(v_ax,'box','off');
        set(v_ax,'xtick',[]);
        % Find times where ticks should be located
        timeTicks = get(ax,'ytick');
        valTicks = interp1(DataSS.Time,VAL,timeTicks);
        valTicks(isnan(valTicks)) = 0;
        set(v_ax,'ylim',get(ax,'ylim'))
        set(v_ax,'ytick',timeTicks)
        set(v_ax,'yticklabels',round(valTicks,2));
        ylabel(v_ax,addAxisDesc)
    end
    if addSuppXAxis
        moveFact = 0.05;
        freq = get(ax,'xtick'); % 1/sec
        waveL = sndspd ./ freq; % sndspd in ft/sec
        if normWaveL
            if isCavity
                waveL = waveL / (cavL);
                wavestr = 'Wavelength / Cavity Length';
            else
                waveL = waveL / (normL/12); % normL in inches, waveL in ft
                wavestr = 'Wavelength / Actuator Length';
            end
        else
            wavestr = 'Wavelength (ft)';
        end
        cpos = get(ax,'position');
        set(ax,'position',[cpos(1) cpos(2)+moveFact cpos(3) cpos(4)-moveFact])
        cpos = get(ax,'position');
        if exist('v_ax','var')
            vpos = get(v_ax,'position');
            set(v_ax,'position',[vpos(1) vpos(2)+moveFact vpos(3) vpos(4)-
moveFact])
        end
        axcompbot=moveFact;
        bedge = cpos(2);
        tedge = cpos(2)+cpos(4);
        totwid = tedge-bedge;
```

```
        ypos = bedge-axcompbot*totwid;
        h_ax = axes('position',[cpos(1), ypos, cpos(3), cpos(4)*.015]);
        set(h_ax,'xaxislocation','bottom');
        set(h_ax,'color',get(gcf,'color'));
        set(h_ax,'box','off');
        set(h_ax,'ytick',[]);
        set(h_ax,'xlim',get(ax,'xlim'))
        set(h_ax,'xtick',get(ax,'xtick'))
        set(h_ax,'xticklabels',round(waveL,1));
        xlabel(h_ax,wavestr)
    end
    if normFreq
        moveFact = 0.15;
        freq = get(ax,'xtick'); % 1/sec
        if isCavity
            St = freq * cavL / Vinf;
        else
            St = freq * (normL/12) / Vinf;
        end
        cpos = get(ax,'position');
        set(ax,'position',[cpos(1) cpos(2)+moveFact cpos(3) cpos(4)-moveFact])
        cpos = get(ax,'position');
        if exist('v_ax','var')
            vpos = get(v_ax,'position');
            set(v_ax,'position',[vpos(1) vpos(2)+moveFact vpos(3) vpos(4)-
moveFact])
        end
        axcompbot=moveFact;
        bedge = cpos(2);
        tedge = cpos(2)+cpos(4);
        totwid = tedge-bedge;
        ypos = bedge-axcompbot*totwid;
        h_ax = axes('position',[cpos(1), ypos, cpos(3), cpos(4)*.015]);
        set(h_ax,'xaxislocation','bottom');
        set(h_ax,'color',get(gcf,'color'));
        set(h_ax,'box','off');
        set(h_ax,'ytick',[]);
        set(h_ax,'xlim',get(ax,'xlim'))
        set(h_ax,'xtick',get(ax,'xtick'))
        set(h_ax,'xticklabels',round(St,1));
        xlabel(h_ax,'Strouhal Number')
    end

end
```

```
if isCavity
   R1 = Vall./(cavL) .* (1-gammaRoss) ./ …
         ( ( allM ./ (1 + 0.4/2*allM.^2).^0.5) + 1/k);
   R2 = Vall./(cavL) .* (2-gammaRoss) ./ …
         ( ( allM ./ (1 + 0.4/2*allM.^2).^0.5) + 1/k);
   R3 = Vall./(cavL) .* (3-gammaRoss) ./ …
         ( ( allM ./ (1 + 0.4/2*allM.^2).^0.5) + 1/k);
   R4 = Vall./(cavL) .* (4-gammaRoss) ./ …
         ( ( allM ./ (1 + 0.4/2*allM.^2).^0.5) + 1/k);
   R5 = Vall./(cavL) .* (5-gammaRoss) ./ …
         ( ( allM ./ (1 + 0.4/2*allM.^2).^0.5) + 1/k);
   R6 = Vall./(cavL) .* (6-gammaRoss) ./ …
         ( ( allM ./ (1 + 0.4/2*allM.^2).^0.5) + 1/k);
   axRoss = axes();

plot(axRoss,R1,DataSS.Time,'linestyle',':','linewidth',1.5,'marker','none','color','k')
   hold(axRoss,'on')

plot(axRoss,R2,DataSS.Time,'linestyle',':','linewidth',1.5,'marker','none','color','k')

plot(axRoss,R3,DataSS.Time,'linestyle',':','linewidth',1.5,'marker','none','color','k')

plot(axRoss,R4,DataSS.Time,'linestyle',':','linewidth',1.5,'marker','none','color','k')

plot(axRoss,R5,DataSS.Time,'linestyle',':','linewidth',1.5,'marker','none','color','k')

plot(axRoss,R6,DataSS.Time,'linestyle',':','linewidth',1.5,'marker','none','color','k')
   set(axRoss,'ylim',get(ax,'ylim'), 'xlim',get(ax,'xlim'), 'ytick',[], 'xtick',[], …
               'box','off', 'position',get(ax,'position'), 'color','none')
end

% Go back and change all font sizes to the correct size
allAxesInFigure = findall(fig,'type','axes');
for i = 1:length(allAxesInFigure)
   thisAx = allAxesInFigure(i);
   set(thisAx,'fontsize',fsize);
   ylabH = get(thisAx,'ylabel');
   xlabH = get(thisAx,'xlabel');
   set(ylabH,'fontsize',fsize);
   set(xlabH,'fontsize',fsize);
end

if plotSS
   % Plot steady-state data too
   for i=1:length(DataSS.Names)
```

```
        if strcmp(DataSS.Names{i},'MT')
            figure;
            plot(DataSS.Time,DataSS.Values(:,i))
            xlabel('Time (sec)')
            ylabel(DataSS.Names{i})
        end
        if strcmp(DataSS.Names{i},'TTC')
            figure;
            plot(DataSS.Time,DataSS.Values(:,i))
            xlabel('Time(sec)')
            ylabel(DataSS.Names{i})
        end
    end
end
```

MATLAB Code for Normalizing Carpet Plots by Tunnel Noise

Removing tunnel noise from the data was accomplished by the process described in (84. The MATLAB code used to implement this procedure and produce carpet plots is provided next.

```
% Plot a carpet plot of the difference between two signals as a function of
% dB = f(F,t)

clear variables; clc;
% Font size for all axes and labels
fsize = 14;
% Limits for colorscale
colorlims = [0 40];

titlestr = 'Mach 0.10, Fs 20kHz, 0-6 kHz sweep';
file1 = fullfile(pwd,'matfiles_batch','Apr 03 13_58_20  HSWT Data.mat');
file2 = fullfile(pwd,'matfiles_batch','Apr 03 14_14_03  HSWT Data.mat');
channelName = 'PK34';
dbmin = 5;
% Add a supplementary y-axis
addSuppYAxis = 1;
addAxisName = 'MT';
addAxisDesc = 'Mach Number';
% Add a supplementary x-axis
addSuppXAxis = 1;
% Flag for normalizing wavelength
normWaveL = 1;
normL = 30/25.4; % mm to in
```

```
% Flag for normalizing frequency
normFreq = 1;
% Specify some signal processing options
N = 2048;
w = window(@blackmanharris,N,'periodic');
overlappct = 75;
noverlap = round(N*overlappct/100); % Number of samples to overlap

% Load both sets of data into memory
F1 = load(file1);
F2 = load(file2);

% Calculate speed of sound in the boundary layer
indTT = strcmp(F2.DataSS.Names,'TTC');
TT = F2.DataSS.Values(:,indTT);
TT = mean(TT) + 459.67;
sndspd = sqrt(1.4*1716*TT); % ft / sec
indMT = strcmp(F2.DataSS.Names,'MT');
MT = mean(F2.DataSS.Values(:,indMT));
Vinf = sndspd * MT;

% find corresponding data values from each file for requested channel
ind1 = strcmp(channelName,F1.DataHR.Names);
ind2 = strcmp(channelName,F2.DataHR.Names);
chan1= F1.DataHR.Values(:,ind1);
chan2= F2.DataHR.Values(:,ind2);
Fs1  = F1.DataHR.Fs;
Fs2  = F2.DataHR.Fs;

% Compute spectrograms
[s1,f1,t1,ps1] = spectrogram(chan1, w, noverlap, N, Fs1, 'power');
[s2,f2,t2,ps2] = spectrogram(chan2, w, noverlap, N, Fs2, 'power');

% Compute the relative level between the two tests (in decibels)
dB = 10*log10(ps2./ps1);
% Filter out some of the noise
dB(dB<dbmin) = -60;

% Display the resulting relative SPLs
fig = figure('color','white','units','normalized','position',[0.1,0.1,0.4 0.8]);
ax = axes('parent',fig);
surf(f1,t1,dB','edgecolor','none')
view(2)
caxis(colorlims)
hc = colorbar();
```

```
xlabel(ax,'Frequency (kHz)')
ylabel(ax,'Time (sec)')
% This changes x-axis tick labels from Hz to kHz. Ticks will remain in
% Hz
xtl = get(ax,'xtick');
set(ax,'xticklabels',arrayfun(@num2str,xtl/1000,'uniformoutput',false))

title(ax,strcat(titlestr,', ',channelName))
if addSuppYAxis
   % Add Mach number to the vertical axis
   indSupp = strcmp(F2.DataSS.Names,addAxisName);
   VAL = F2.DataSS.Values(:,indSupp);
   cpos = get(ax,'position');
   set(ax,'position',[cpos(1)+0.15 cpos(2) cpos(3)-0.15 cpos(4)])
   cpos = get(ax,'position');
   axcompleft=0.2;
   ledge = cpos(1);
   redge = cpos(3)+cpos(1);
   totwid = redge-ledge;
   xpos = ledge-axcompleft*totwid;
   v_ax = axes('position',[xpos, cpos(2), cpos(3)*.015, cpos(4)]);
   set(v_ax,'yaxislocation','left');
   set(v_ax,'color',get(gcf,'color'));
   set(v_ax,'box','off');
   set(v_ax,'xtick',[]);
   % Find times where ticks should be located
   timeTicks = get(ax,'ytick');
   valTicks = interp1(F2.DataSS.Time,VAL,timeTicks);
   set(v_ax,'ylim',get(ax,'ylim'))
   set(v_ax,'ytick',timeTicks)
   set(v_ax,'yticklabels',round(valTicks,2));
   ylabel(v_ax,addAxisDesc)
end
if addSuppXAxis
   moveFact = 0.05;
   freq = get(ax,'xtick'); % 1/sec
   waveL = sndspd ./ freq; % sndspd in ft/sec
   if normWaveL
      waveL = waveL / (normL/12); % normL in inches, waveL in ft
      wavestr = 'Wavelength / Actuator Length';
   else
      wavestr = 'Wavelength (ft)';
   end
   cpos = get(ax,'position');
   set(ax,'position',[cpos(1) cpos(2)+moveFact cpos(3) cpos(4)-moveFact])
```

```
    cpos = get(ax,'position');
    if exist('v_ax','var')
       vpos = get(v_ax,'position');
       set(v_ax,'position',[vpos(1) vpos(2)+moveFact vpos(3) vpos(4)-moveFact])
    end
    axcompbot=moveFact;
    bedge = cpos(2);
    tedge = cpos(2)+cpos(4);
    totwid = tedge-bedge;
    ypos = bedge-axcompbot*totwid;
    h_ax = axes('position',[cpos(1), ypos, cpos(3), cpos(4)*.015]);
    set(h_ax,'xaxislocation','bottom');
    set(h_ax,'color',get(gcf,'color'));
    set(h_ax,'box','off');
    set(h_ax,'ytick',[]);
    set(h_ax,'xlim',get(ax,'xlim'))
    set(h_ax,'xtick',get(ax,'xtick'))
    set(h_ax,'xticklabels',round(waveL,2));
    xlabel(h_ax,wavestr)
end
if normFreq
    moveFact = 0.15;
    freq = get(ax,'xtick'); % 1/sec
    St = freq * (normL/12) / Vinf;
    cpos = get(ax,'position');
    set(ax,'position',[cpos(1) cpos(2)+moveFact cpos(3) cpos(4)-moveFact])
    cpos = get(ax,'position');
    if exist('v_ax','var')
       vpos = get(v_ax,'position');
       set(v_ax,'position',[vpos(1) vpos(2)+moveFact vpos(3) vpos(4)-moveFact])
    end
    axcompbot=moveFact;
    bedge = cpos(2);
    tedge = cpos(2)+cpos(4);
    totwid = tedge-bedge;
    ypos = bedge-axcompbot*totwid;
    h_ax = axes('position',[cpos(1), ypos, cpos(3), cpos(4)*.015]);
    set(h_ax,'xaxislocation','bottom');
    set(h_ax,'color',get(gcf,'color'));
    set(h_ax,'box','off');
    set(h_ax,'ytick',[]);
    set(h_ax,'xlim',get(ax,'xlim'))
    set(h_ax,'xtick',get(ax,'xtick'))
    set(h_ax,'xticklabels',round(St,1));
    xlabel(h_ax,'Strouhal Number')
```

```
end

% Go back and change all font sizes to the correct size
allAxesInFigure = findall(fig,'type','axes');
for i = 1:length(allAxesInFigure)
   thisAx = allAxesInFigure(i);
   set(thisAx,'fontsize',fsize);
   ylabH = get(thisAx,'ylabel');
   xlabH = get(thisAx,'xlabel');
   set(ylabH,'fontsize',fsize);
   set(xlabH,'fontsize',fsize);
end
```

Code Used to Produce Acoustic Reinforcement Curves (Rona Curves)

The curves used to identify acoustic reinforcement ((51) of the Rossiter edge-tones and the intercepts of the quantity, $1\text{-}oR_m/A_n = f(M_\infty)$, were produced using the MATLAB code shown below.

```
function Ross_acoustic_Reinforcement()
% Plot maps of the ratio of acoustic to rossiter strouhal numbers

% Constants
L = 0.75/12; % ft
W = 1.5/12; % ft
D = 0.3/12; % ft
alph = 0.25;
Kc = 0.57;

M = 0:0.01:0.6;
TToTS = 1 + 0.5*(1.4-1)*M.^2;

% Overlay some test data
% Apr 03 14_16_43 reversed cavity
RangeRossL = 5:7;
RangeL = 1:3;
oL=1;
RangeRossW = 3:5;
RangeW = 1:3;
oW=1;
RangeRossD = 3:5;
RangeD = 1:3;
oD = 1;
test_M = 0.183;

% Plot the curves and overlay test data
```

```
plot_control_curves(oL, RangeRossL, RangeL, 'Length', test_M);
plot_control_curves(oW, RangeRossW, RangeW, 'Width', test_M);
plot_control_curves(oD, RangeRossD, RangeD, 'Depth', test_M);

  function plot_control_curves(o,RangeRoss,RangeAcoustic,modestr,test_M)
    cols = [161 19 46
            118 171 47
            0 113 188
            137 117 255
            253 190 61
            243 12 255
            8 247 255]/255;
    lins = {'-','--',':'};

    %
    hf = figure('color','w','units','normalized','position',[0.2 0.05 0.3 0.4]);
    ax = axes('parent',hf);
    hold(ax,'on')
    box(ax,'on')
    j=0;
    for iRoss = RangeRoss
      j =j+1;
      if j>size(cols,1), j=1; end

      St_Ross = (iRoss - alph) ./ ( M./sqrt(TToTS) + 1/Kc );
      jj=0;
      for i = RangeAcoustic
        jj=jj+1;
        if jj>3, jj=1; end
        switch lower(modestr)
          case 'length'
            el = i;
            m = 0;
            n = 0;
          case 'width'
            el = 0;
            m = i;
            n = 0;
          case 'depth'
            el = 0;
            m = 0;
            n = i;
          otherwise
            error('Unknown mode string')
        end
```

```
            St_acoustic = sqrt(TToTS) ./ M * …
                                sqrt( (el/2)^2 + (m/2*L/W)^2 + (n/2*L/D)^2 );
            FofM = 1 - o*St_Ross ./ St_acoustic;
            plot(M,FofM,'displayname', …
                  sprintf('1-%dR%d/A%d',o,iRoss,i), …
                  'linewidth',2,'linestyle',lins{jj},'color',cols(j,:));
        end
    end
    legend('show','location','best')
    xlabel(ax,'\it{M_{\infty}}')
    ylabel(ax,'\it{f(M_{\infty})}')
    plot(get(ax,'xlim'),[0 0],'linewidth',1,'color','k')
    title(ax,strcat('Cavity ',modestr,' Mode'))
    plot([test_M, test_M],get(ax,'ylim'),'linewidth',1,'color','k')
end
```

VITA

Brian Adam Binkley was born in Hendersonville, TN. He completed his undergraduate degree in Mechanical Engineering at Tennessee Technological University in 2007. He began part-time graduate studies at the University of Tennessee Space Institute in 2008 while working at the Arnold Engineering Development Complex. He received his Master of Science degree in Mechanical Engineering in May 2011 and the Doctor of Philosophy degree in August 2017.